Transient Stability Assessment of Hybrid Distributed Generation Using Computational Intelligence Approaches

By

OLULOPE PAUL KEHINDE

THIS THESIS IS SUBMITTED TO THE DEPARTMENT OF ELECTRICAL ENGINEERING, UNIVERSITY OF CAPE TOWN, IN COMPLETE FULFILMENT OF THE REQUIREMENTS FOR THE DEGREE OF DOCTOR OF PHILOSOPHY

FEBRUARY 2014

UNIVERSITY OF CAPE TOWN
IDYUNIVESITHI YASEKAPA • UNIVERSITEIT VAN KAAPSTAD

DEPARTMENT OF ELECTRICAL ENGINEERING
UNIVERSITY OF CAPE TOWN
CAPE TOWN

Declaration

I hereby:

(a) Grant the University free license to reproduce the above thesis in whole or in part, for the purpose of research;

(b) Declare that:

(i) The above thesis is my own unaided work, both in conception and execution, apart from the normal guidance of my supervisor. Where collaboration with other people has taken place, or material generated by other researchers is included, the parties and/or materials are indicated in the acknowledgements or are explicitly stated with references as appropriate.

(ii) Except as stated below, neither the substance nor any part of the thesis has been submitted in the past, or is being, or is to be submitted for a degree at this University or any other University.

(iii) I am now presenting the thesis for examination for the Degree of PhD.

…… …….

PAUL KEHINDE OLULOPE Date

Acknowledgements

Let me first and foremost thank God for His protection and inspiration throughout the course of this research. He is indeed the source of my strength and wisdom. He owns everything in my life. May His name be praised forever amen.

I also want to express my heartfelt thanks to my wife and children for their prayers, support and encouragement. I will never forget the role of mother, friend, companion, helper my wife played throughout the course of the research.

Special thanks to my main supervisor Prof Komla Folly for his words of encouragement and his supervisory role. His encouraging words helped a great deal to keep me motivated and challenged me when the need arose throughout my research.

I would like to express my appreciation to Prof Kumar Venayagamoorthy of Missouri Science and Technology, USA for his advice. My stay in the Missouri Science and Technology Institute in the USA under his leadership was very productive and inspiring. His encouragement and diligence challenged me to always aspire to perform to my full professional ability.

My mother (Mrs Theresa Olulope), without whom I would not have been here. I appreciate every bit of the training giving to me at every stage of my life. My extended family, in-laws and all my colleagues in my working place; you are all appreciated for your supports and encouragements.

My friends and research colleagues in the Intelligent and Power Group played the roles of team mates that will not be easily forgotten.

To my intimate twins brother (Taiwo Olulope), your assistance in putting many things in order at home is highly appreciated.

My sincere and heartfelt gratitude goes to my co-pastors (Pastor C.E Okafor, Bro Ilesanmi Oluwafemi), Christian brothers in ministry as well as the entire Redeemed Christian Fellowship, UCT, Redeemed Christian Church of God, Latter House Parish, Cape Town, The Living Spring Revival and Truth Ministry Ire Ekiti, My parish pastor (Pastor. & Pastor. Mrs Adelusi), Pastor and Pastor Mrs Oduwole, my prayer partner (Dr

Seun Oyekola, Dr & Mrs Femi Olaofe, Mr Oluwaseun Ogunmodimu), Dr & Dr Mrs Herbert Melariri, Mr Ereola Aladesanmi, Pastor and Dr Mrs Tayo Boyinbode, Mr & Dr Mrs Victoria Ikoro and Mr and Mrs Tejumade Ogundipe.

Finally, my appreciation will not be complete without mentioning the assistance and permission of my employer, the University of Ado Ekiti, now the Ekiti State University, Ado–Ekiti and the University of Cape Town postgraduate funding office for providing financial support.

Abstract

Due to increasing integration of new technologies into the grid such as hybrid electric vehicles, distributed generations, power electronic interface circuits, advanced controllers etc., the present power system network is now more complex than in the past. Consequently, the recent rate of blackouts recorded in some parts of the world indicates that the power system is stressed. The real time/online monitoring and prediction of stability limit is needed to prevent future blackouts.

In the last decade, Distributed Generators (DGs) among other technologies have received increasing attention. This is because DGs have the capability to meet peak demand, reduce losses, due to proximity to consumers and produce clean energy and thus reduce the production of CO_2. More benefits can be obtained when two or more DGs are combined together to form what is known as Hybrid Distributed Generation (HDG). The challenge with hybrid distributed generation (HDG) powered by intermittent renewable energy sources such as solar PV, wind turbine and small hydro power is that the system is more vulnerable to instabilities compared to single renewable energy source DG. This is because of the intermittent nature of the renewable energy sources and the complex interaction between the DGs and the distribution network. Due to the complexity and the stress level of the present power system network, real time/online monitoring and prediction of stability limits is becoming an essential and important part of present day control centres.

Up to now, research on the impact of HDG on the transient stability is very limited. Generally, to perform transient stability assessment, an analytical approach is often used. The analytical approach requires a large volume of data, detailed mathematical equations and the understanding of the dynamics of the system. Due to the unavailability of accurate mathematical equations for most dynamic systems, and given the large volume of data required, the analytical method is inadequate and time consuming. Moreover, it requires long simulation time to assess the stability limits of the system. Therefore, the analytical approach is inadequate to handle real time operation of power system.

In order to carry out real time transient stability assessment under an increasing non-linear and time varying dynamics, fast scalable and dynamic algorithms are required.

These algorithms must be able to perform advanced monitoring, decision making, forecasting, control and optimization. Computational Intelligence (CI) based algorithm such as neural networks coupled with Wide Area Monitoring System (WAMS) such as Phasor Measurement Unit (PMUs) have been shown to successfully model non-linear dynamics and predict stability limits in real time.

To cope with the shortcoming of the analytical approach, a computational intelligence method based on Artificial Neural Networks (ANNs) was developed in this thesis to assess transient stability in real time. Appropriate data related to the hybrid generation (i.e., Solar PV, wind generator, small hydropower) were generated using the analytical approach for the training and testing of the ANN models. In addition, PMUs integrated in Real Time Digital Simulator (RTDS) were used to gather data for the real time training of the ANNs and the prediction of the Critical Clearing Time (CCT).

Five artificial neural network approaches were used in this thesis to monitor the state of the system in real time and predict the critical clearing time. These are: Multilayer Feed Forward Neural Networks (MLFNNs), Recurrent Neural Networks (RNNs), Radial Basis Function Neural Networks (RBF), Generalised Regression Neural Networks (GRNNs) and Self-Organising Feature Map Neural Networks (SOFM).

Comparison of the developed artificial neural network methods and the analytical approach shows that artificial neural network techniques provide faster real time monitoring and prediction of the critical clearing time compared to the analytical method.

The performances of the five ANNs in predicting the critical clearing time were also compared. It is shown that Radial Basis Function Neural Networks (RBF) give the best accurate prediction of the CCT compared to the rest of the ANNs. On the other hand, Self-Organising Feature Map Neural Networks (SOFM) gives the worst performance in terms of both accuracy and speed of prediction of the CCT. Multilayer Feed Forward Neural Networks (MLFNN) gives the fastest prediction of the CCT followed by Radial Basis Function Neural Networks (RBF).

This research work shows the advantages (i.e., overall improved transient stability) of using Hybrid distributed generation over a single DG source, but also the vulnerability of the system to instabilities when HDG is used. In particular HDG made of three or more renewable energy sources under high penetration level (export mode). It is also shown

that computational intelligence approaches coupled with PMU are an effective tool for online and real time transient stability assessment.

Table of Contents

List of Figures

List of Tables

Nomenclature

Abbreviations

AC	Alternating Current
AIS	Artificial Immune System
ANNs	Artificial Neural Networks
ART	Adaptive Resonance Theory
AI	Angle Index
AVR	Automatic Voltage Regulator
BGA	Breeder Genetic Algorithm
CCA	Critical Clearing Angle
CCT	Critical clearing time
CDSG	Converter Driven Synchronous Generator
CG	Centralized Generator
CHP	Combined Heat and Power
CI	Computational Intelligence
CIM	Common Information Model
COI	Centre of Inertia
DG	Distributed Generation
DFIG	Doubly Fed Induction Generator
DC	Direct Current
DDSG	Direct Drive Synchronous Generator
DDPMSG	Direct Drive Permanent Magnet Synchronous Generator
DMS	Distribution Management Software
DPCA	Distributed Power Coalition of America
DSA	Dynamic Security Assessment
DVI	Dynamic Voltage Index
EC	Evolutionary Computing

EAC	Equal Area Criterion
EMS	Energy Management System
FS	Fuzzy System
GHG	Green House Gas
GPC	Giga Processor Card
GA	Genetic Algorithm
GIS	Global Integrated System
GRNN	Generalised Regression Neural Networks
GTNET	Giga-Transceiver Network Communication Card
GTWIF	Giga Transceiver Workstation Interface Card
GPS	Global Positioning System
GTSYNC	Global Time Synchronization
HDG	Hybrid Distributed Generation
HDG	Hybrid Distributed Generation
HDGS	Hybrid Distributed Generation System
HIS	Historical Information System
HPS	Hybrid Power System
IED	Intelligent Electronic Device
IGBT	Insulated Gate Bipolar Transistor
IRC	Inter-Rack Communication
LSI	Load Sheading Index
MFDI	Maximum Frequency Deviation Index
MLFNN	Multilayer Feed-Forward Neural Network
MLP	Multilayer Percetron
MSE	Mean Square Error
MSEREG	Mean Square Error with Regularization
NIST	National Institute of Standards and Technology
IC	Internal Combustion
IES	Integrated Energy System
ICT	Internet and Communication Technology
IGBT	Insulated Gate Bipolar Transistor
OMIB	One Machine Infinite Bus

ULTC	Under-Load Transformer Tap Changers
PFI	Power Flow Index
PWM	Pulse Width Modulation
PSS	Power System Stabilizer
PSS/E	Power System Simulation for Engineering
PI	Proportional Integrator
PMSG	Permanent Magnet Synchronous Generator
PMU	Phasor Measurement Unit
PV	Photovoltaic
PBIL	Population Based Incremental Learning
PSO	Particle Swarm Optimization
RBF	Radial Basis Function
RTU	Remote Terminal Unit
RNN	Recurrent Neural Networks
rpm	revolution per minute
RSCAD	Real System Computer Aided Design
RTDS	Real Time Digital Simulator
SOFM	Self Organising Feature Map
SCADA	Supervisory Control and Data Acquisition
SHP	Small HydroPower
SI	Swarm Intelligence
SMIB	Single Machine Infinite Bus
SRN	Simultaneous Recurrent Neural Network
TDS	Time Domain Simulation
TSCPG	Transient Stability Constrained Power Generation
T&D	Transmission and Distribution
TEF	Transient Energy Function
UHF	Ultra High Frequency
ULTC	Under-Load Transformer tap Changers
VPP	Virtual Power Plants
VFC	Variable Frequency Converter
WECS	Wind Energy Conversion System

VHF	Very High Frequency
VSC	Voltage Source Converter

Roman Symbols

A_p	Pipe area
A	Exposed Area
b	Bias
C_{PV}	Overall heat capacity per unit area of the PV cell/module
C_p	Power coefficient
e_{gap}	Band gap of the material
E	Voltage behind transient reactance
f	Frequency
h_w	Effective pressure head of water across the turbine (m)
H	Inertia constant
G	Gate position
g	Acceleration due to gravity
i_{dr}	Rotor d-axis current
i_{qr}	Rotor q-axis current
i_{ds}	Stator d-axis current
i_{qs}	Stator q-axis current
i_{xr},i_{yr}	x and y components of the rotor current
i_{fd}	Field current
I_p	Photocurrent of the PV
$i(x)$	Discriminant function
I_o	Saturation current
I_{pv}	Load current
I_D	Diode current
$I_{mp,ref}$	Maximum power point current at the reference condition
$I_{SC,ref}$	Short circuit current at the reference condition
$I_{o,ref}$	Saturation current at the reference condition
I_p	Photocurrent of the PV cell
$I_{pv,ref}$	Light current at the reference condition

I	Current
$k_{in,PV}$	Transmittance-absorption product of PV cells
k_{loss}	Overall heat loss coefficient
K_u	Constant of proportionality
K	Boltzmann's constant
L_{dm}	Mutual inductance in d-axis
L_{qm}	Mutual inductance in q-axis
$L_{\sigma s}$	Stator leakage inductance
L_{fd}	Field inductance
L	Length of conduit
m_d	Modulation depth for d-component of the rotor side converter
m_q	Modulation depth for q-component of the rotor side converter
m	Diode quality constant
N_s	Number of cells in series of a PV module
P_m	Mechanical power
P	Accelerating power
P_e	Electrical power
P_{pv}	Power output
P_s	Stator active power
P_r	Rotor active power
P_{hyd}	Hydraulic power produced at the turbine shaft
P_w	Total wind power
Q_w	Water flow rate passing through the turbine
Q_p	Number of input pattern
q	Charge of an electron
Q_s	Stator reactive power
Q_r	Rotor reactive power
R_{fd}	Field resistance
Rss	Series resistance of the PV cell
R_s	Stator resistance
R	Resistance; blade length; wind turbine radius; specific gas constant for air; radius of a cylinder

s	slip
t_c	Critical clearing time
T_a	Ambient temperature
Tt	Turbine aerodynamic torque
T	Net Torque
T	Acceleration Torque
$T_{c,ref}$	Reference temperature
T_e	Electrical Torque
T_m	Mechanical Torque
T_s	Synchronizing torque
t	Time in second
Tc	PV cell Temperature
$t(k)$	Target of the neural network
T_D	Damping Torque
u_{ds}	stator voltage for
u_j	Centre of the radial basis function
V_{Wind}	Wind speed
u_{rd}	Rotor voltage for d-component
u_{rq}	Rotor voltage for q-component
u_{rd}	Generator AC voltage output for d-component on the rotor side
u_{rq}	Generator AC voltage output for q-component on the rotor side
u_{qs}	Stator q-axis voltage
u_{ds}	Stator d-axis voltage
u_s	Stator voltage
u_{qr}	Rotor q-axis voltage
u_{dr}	Rotor d-axis voltage
$V_{mp,ref}$	Maximum power point voltage at the reference condition
v	Water velocity in m/s
V_{pv}	PV output voltage (in volts)
V_{DC}	Voltage of the DC-Link
$V_{oc,ref}$	The open circuit voltage of the PV module at reference condition
WR^2	Moment of Inertia

w	Neural network weight
X_m	Mutual reactance
x	Input vector for neural network
X_s	Stator reactance
$y(k)$	Output of the neural network
Z_{n-1}	Context unit of the recurrent neural network

Greek Symbols

$\mu_{I,sc}$	Temperature coefficient of the short-circuit current
ρ_w	Density of water
p	Pressure of the water
σ_x , σ_y	Standard deviations
δ	Rotor angle
ω_m	Angular velocity of the rotor in p.u
ω	Rated synchronous speed in p.u
ω_0	Rated synchronous speed in rad/sec
ω_s	Angular velocity of the stator field in electrical rad/sec
θ_e	Electrical angle
θ_m	Mechanical angle
α	Mechanical angular acceleration
δ_c	Critical clearing angle
δ_0	Initial rotor angle
$\Delta\omega$	Speed deviation
δ_{cimax}	Maximum deviation of the load angle
$\delta_{cimaxadm}$	Maximum admissible load angle
$\Delta f_{i,max}$	Maximum deviation of frequency
$\Delta f_{i,max,adm}$	Maximum admissible of frequency
ρ	Air density
λ	Tip-speed ratio
λ_{opt}	Optimal Tip-speed ratio
β	Pitch angle

ω_{turb}	Rotational speed of the wind turbine shaft
ψ_{dqs}	Flux linkages
ψ_{ds}	Total fluxes of stator d-axis
ψ_{qs}	Total fluxes of stator q-axis
ψ_{dr}	Total fluxes of rotor d-axis
ψ_{qr}	Total fluxes of rotor q-axis
ψ_{fd}	Excitation winding flux
α_{th}	Thermal voltage timing completion factor
α_{ref}	The value of α_{th} at the reference condition
η_t	Turbine simplified efficiency
ω_m	Electrical angular frequency
η	Efficiency of the solar PV
ϕ	Irradiance
ϕ_{ref}	Reference irradiance
γ	Performance ratio
σ	width of the radial basis function
Φ	Radial function

Chapter 1

Introduction

Transient stability analysis and monitoring is becoming increasingly important due to the vulnerability of modern grids to blackouts and instabilities. The modern grids accommodate new technologies such as power electronic devices, distribution generation with single and mixed sources, electric vehicles etc., resulting in complex dynamic systems. As a result, stability margins are compromised leading to frequent blackouts and load shedding. The August 14, 2003 and the September 12, 2005 blackouts in North America show that new technologies in the area of monitoring, control and management are needed in order to avert further occurrences of blackouts [1], [2].

The interest in distributed generation (DG) and hybrid distributed generation (HDG) across the globe is due to the steep rise in load demand and the growing concern about environmental pollution, global warming and climate change [3]. Other drivers towards DG/HDG are application of combined heat and power (CHP) systems, premium power with improved power quality and reliability and ancillary services such as reactive power support and voltage control, black start power for utilities etc., [3].

It is not sustainable in the long term to depend solely on fossil fuel such as coal. However, because of the advantages that coal is cheap and abundant, some countries like South Africa, the United States of America and other parts of the world considered it as major option for meeting their load demands. Coal which is one of the dirtiest sources of energy was the fastest growing fossil fuel [4]. From 1965 to 2008 the use of fossil fuels continued to grow and their share of the energy supply has increased by 80-90 percent from 2003 to 2008 [4]. The growth in the use of coal continued to increase because of continued increase in oil price [4]. It is estimated that Eskom in South Africa (with a population of 50 million) generates approximately 208 million tons of CO_2 over the past years [5]. This is the highest emission rate on the African continent and the 15th largest emission rate in the world [6]. The countries where coal is used to supply the largest electricity are facing serious global warming and rising concern for sustainable energy delivery to customers [7].

In order to achieve sustainable renewable energy that will offer a sustainable alternative to fossil fuel dependence in future years, a hybrid mini grid has been developed that will give citizens universal access to energy and electricity. A local small scale grid also known as a hybrid mini grid or stand-alone system possesses the capabilities to reduce energy shortage, load shedding and transmission losses. This will enable an affordable, secure and modern energy system for low-income households. The role of renewable energy sources in this regard has led to South Africa setting a target of 10,000 GWh of energy, to be generated from renewable sources (wind generator, Solar PV, small hydropower and biomass) by 2013 [8]. The first step towards this commitment was demonstrated in 2008 by the commissioning of the first phase of the 5.2MW Darling wind farm comprising of 4 wind turbines (1.3MW each). In addition, the constructions of a 30MW wind farm near Jeffrey's Bay, in Eastern Cape and a 50MW Helena St. Bay wind farms are underway. An estimated 25-40GW of new generating capacity is anticipated by the year 2025 to meet the increasing power demand in South Africa. A sizable part of this is expected to come from renewable energy [8], which includes solar PV, wind generator, small hydropower, fuel cell and biomass.

In the United States of America, 12.1 percent of the domestically produced electricity in 2012 comes from the renewable energy. Renewable energy in USA provides 14% of electrical generation during the first half of 2013 [9]. Hydropower is growing and at the moment, USA is the fourth largest producer of hydropower in the world [10]. It is projected that 3000 GW of new generation capacity would be needed worldwide by 2020 to meet the growing electricity demand. It is expected that 1500GW would be contributed by DG [11]. The Distributed Power Coalition of America (DPCA) indicated that 20% of all new generating capacity in the USA over the next two decades will be from DG [12].

The easiest way to achieve the objective of sustainable energy is by integrating renewable energy sources such as wind turbines, solar PV etc. Such small scale renewable energy sources need to be connected close to consumers either as standalone or grid integrated ranging from a few kilowatts to over 100MW- operated either by utilities, utilities customers or third parties. Whenever several DGs are combined to provide power to the customers, this is called hybrid distributed generation (HDG). When HDGs (in mini grids) are grid-connected they begin to offer more advantages such as voltage support to electric grid, lower system losses, deferred capital investments in transmission and

distribution systems, reduced security risk [13],[14],[15]. In the future, there will be an explosive increase in grid integration of DG/HDG, where issues regarding real time stability assessment will be critical.

With the advent of distributed generation (DG) and hybrid distributed generation (HDG), the grids will further experience increasing stress and risks. This is due to intermittent behaviour of most renewable energies especially wind generator and solar PV. Distributed generation and hybrid distributed generation integrated into the transmission grid or distribution grid introduce additional dynamics and produce increasing complexity. Hence the security margin of the system is affected.

In this thesis, where the term DG is used, it represents single source while HDG represents mixed sources.

1.1 Definition of Distributed Generation and Hybrid Distributed Generation

The definition of distribution generation (DG) in the literature can be stated as follows: A small capacity power plant based on either combustion-based technologies, such as reciprocating engines and turbines, or non-combustion based technologies such as fuel cells, photovoltaic, wind turbines, located on or near end-users and are characterized as renewables or cogeneration non-dispatched sources [3], [16],[17].

The definition addresses decentralization of an energy system where small generators are connected to a distribution network to service the local loads. Generators connected to the transmission lines rather than the distribution lines to service industrial loads are also termed distributed generation. A distribution system with DG is active rather than passive with power flowing in bi-directional ways.

Hybrid Distributed Generation (HDG) system can be defined as a small set of co-operating units generating electricity and heat, with diversified primary energy carriers (renewable and non-renewable), while the coordination of their operations takes place by utilization of advanced power electronics and are located close to the consumers end [18],[19]. Hybrid Distributed Generation Systems (HDGS), a form of DG, are located close to the end-users and can run as a sustainable backup power solution with the grid. These new systems harness energy from multiple sources and also provide storage

capabilities. Not only does this solution prove to be a cost-effective and an efficient alternative but also improves the entire system capacity, security and reliability [18],[20].

1.2 Hybrid Distributed Generation Concept

HDG is expected to form an active part of future power system network in order to meet the future increasing demand for energy. The inherent potential to provide higher quality power, minimize power loss and produce more reliable power to consumers than a system based on a single source is the motivation behind the use of hybrid power generation. The objective of the integration is to capitalize on the strengths of both conventional and renewable energy sources, both cogeneration and non-cogeneration types. HDG can either be grid-connected or standalone system, renewable or non-renewable system. HDG with one or more renewable (stochastic) or non-stochastic energy sources interact with the existing grid during import and export of power generation. This interaction contributes different level of fault current, reactive power, different inertia, therefore making the system vulnerable to different instabilities compare to single energy source. Presently, the promising sources of hybrid distributed generation are wind generator, solar PV, fuel cell, micro-hydro, small hydro, biomass, geothermal, tides, wave generator. Wind generator and solar PV are the most commonly used.

1.3 Benefits of Hybrid Distributed Generation

The basis for hybrid systems is the need to have a more reliable supply of energy. So many benefits can be derived from the implementation of DG/HDG in the distribution network [21],[22],[23],[24],[25],[26]. The benefits can be categorised into two modes namely; standalone mode and grid connection mode.

During the standalone operating mode, DG/HDG:

- Provides electricity more cheaply than grid extension.
- Provides more reliable electricity compared to grid power.
- Allows better use of local natural resources.
- Operates more effectively than diesel-only systems.
- Is modular and relatively easily assembled from standardized packages.

During the grid connected mode, DG/HDG provides:

- Voltage profile and power improvement.
- Voltage stability support, supply the spinning reserve and regulation.
- Reduction in power loss and increased overall energy efficiency.
- Reduction in security risk.
- Relieved transmission and distribution (T&D) congestion.
- Better customer control over their energy
- Helps in peak load shaving and load management programs.
- Improved competitiveness and market opportunities. [16],[21]-[24].

1.4 Technical Issues

Despite the numerous benefits and the growing application of DG/HDG, there are also technical challenges. Some technical problems associated with DG/HDG are discussed below:

- **Real Time Stability Challenges**

Some of the renewables are stochastic in nature fluctuating with changes in weather. Examples of such are solar PVs and wind turbines. The fluctuation poses serious stability challenges to the grid even at low penetration levels. As the penetration increases, the network will be stressed because it was not designed to transmit power in a bi-directional way. Hence, the integration of DG/HDG transforms the distribution network into an active system involved in generation as well as bi-directional transportation of power to the grid. As a result, the distribution system is further stressed. At present, stability is not yet an issue in the distribution system. This is because the penetration is still low. However, when more DG/HDG will be integrated into the grid, the problem of large rotor excursion, small signal stability, low frequency oscillation and voltage collapse will be a serious concern [5], [13], [25]. The increasing integration of DG/HDG will increase the complexity of the system thereby making system stability cumbersome for analytical approach to solve in real time. The concern of system operators is now shifting toward delivering the results of stability assessment in real time or near real time.

1.5 Offline/Online/Real Time Stability Issues

There are two basic modes in which security assessment can be conducted. They are offline and online modes. Offline is used in most cases to [1]:

- Plan for present and future extension.
- Perform post-mortem analysis
- Verify real time data
- Troubleshoot the stability problems shown in the online operation
- Assess the present operating conditions

Before the advancement of technology, electricity industries across the globe compute stability limits several times every day so as to take the necessary control actions in case of critical contingencies. This is done offline. Offline stability assessment with the use of conventional approaches involves a rigorous exercise in which the operator performs a detailed transient stability calculation on an extended collection of contingencies for the purpose of determining whether the post contingencies states are stable or not. The approach to offline stability assessment is based on analytical methods such as dynamic simulation and load flow algorithm available in commercial simulation tools such as DIgSILENT, Eurostag, PSS/E, etc., It is based on routine exhaustive time domain simulations and direct energy methods [1],[2]. The complexities of the time domain algorithms, coupled with the extent of the modelling details render their online implementation difficult but not impossible [5]. Apart from this, the time to compute stability going through vast number of non-linear equations is longer. For instance, linearizing wind turbine state equations that involve additional power electronic interface and different controllers such as automatic voltage regulator (AVR), pitch angle controller in wind turbine, power system stabilizer (PSS) takes more time than expected. To detect the risk of blackout this way in real time is not a trivial exercise. With the advancement in technology, stability assessment can be performed online and in real time using for example Phasor Measurement Unit-PMUs. Online and real time is not the same. Online means the data are available to the operator in the PMU itself and hence also being available to some other separate systems while real time means the operation is performed in actual time (i.e., 1 second in the field is also 1 second on the system). Real

Time Digital Simulator (RTDS) is used today for real time simulation. It means 1 second in the field is also 1 second on RTDS.

Real time stability assessment involves the use of real data that reflect the conditions of the system at a particular point in time. It also involves processing the data in a short period of time with the results made known to the operator in a fraction of second.

In order to avoid the risk of blackout due to instability, the state of the system must be predicted ahead of time so that corrective measures can be deployed to quickly avert the unforeseen contingencies. The ability to predict the state of the system lies on the capability to quantify and compute the distance to the stability limit or to monitor the current operating state and the state when it is stressed. Monitoring in real time points to the need to perform stability calculations within continuously running real time network analysis sequences, and make the results available within a short period of time or before the next state estimation [1].

1.6 Analytical Versus Computational Intelligence Approach in Real Time Application

One of the most challenging problems facing the power system operators is how to assess the system dynamic security in real time [27],[28]. Analytical approach involves a rigorous exercise through the deterministic and exhaustive method to provide stability assessment in real time. The analytical methods have the following limitations [1]:

- Computation of large power system offline gives room for errors.
- Smaller time intervals are needed to ensure numerical stability. Even with small time interval, the negative impact on the performance of the simulation is significant.
- Each contingency must be treated separately i.e., it is a deterministic approach.
- Require long simulation time because of exhaustive non-linear simulation to perform.

In order to carry out real time transient stability assessment under increasing non-linear and time varying dynamics, fast scalable and dynamic algorithms are required. These algorithms must be able to perform advanced monitoring, decision making, forecasting, control and optimization. A computational intelligence (CI) based algorithm such as artificial neural networks have been shown to successfully model the non-linear dynamics of power system offline or online and in real time. Computational intelligence is the study of adaptive mechanism to enable or facilitate intelligent behaviour in complex, uncertain and challenging environment [29].

1.7 Research Motivation

The analytical approach to stability assessment is based on exhaustive offline step by step time domain simulation methods and direct energy method [1],[30]. However, the analytical (or classical) approach is computationally too demanding for a real time implementation. This is because many calculations that involve a set of algebraic-differential equations are computed using time domain simulations under large disturbances such as short circuits, transmission lines disconnections and loss of large load or generation blocks. The time domain is a fixed time-step approach that could affect the simulation results when fast –acting control devices such as static VAr compensators or DC links are to be represented.

To maintain stability in such a power system network requires the use of high speed circuit breakers, quick response excitation systems with automatic voltage regulators. The use of a high speed circuit breaker will reduce the fault duration time and hence the accelerating power. However, with a fast acting circuit breaker, the critical clearing time (CCT) is set ahead of time (i.e., the CCT is fixed for all system operating conditions) in a conventional power system. The critical clearing time is the maximum allowable time for the system to maintain synchronism. It measures the robustness of the system to various contingencies. If the fault is cleared within this time, the power system remains stable. But if the fault is cleared after this time, the power system is most likely to lose synchronism [31],[32].

In time domain simulations, appropriate models and fault information (pre-fault and post fault information) are needed to make accurate decision. However, it is difficult to get these data and make such a decision in real time.

Another method of calculating the CCT in power system is the transient energy function or Liapunov method. In transient energy function, if all the kinetic energy injected into the system during fault can be converted into potential energy when the fault is cleared then the system is stable, otherwise the kinetic energy will increase causing the system to loose synchronism.

However, the transient energy function has limitation. Finding Liapunov's function for the power system requires the calculation of the potential energy at the controlling equilibrium point with respect to the stable equilibrium point of the post fault system. Accurate critical energy functions are obtained through an extensive process that makes it cumbersome and time consuming for application in real time operation [33],[34].

Moreover, for a single machine or two machines system, the equal area criterion (EAC) is an effective method to assess power system stability. The calculation of CCT in a multi machine is not a trivial task. One way of addressing the problem of CCT calculation in a multi machine system is to reduce the system into an equivalent two-machine aggregate system under the assumption that the system is separated into two clusters and later reduce the two machines (clusters) into one machine infinite bus (OMIB) system [1],[35]. In this case, the dynamics of the system cannot be adequately represented by one single machine. Therefore the results give scope for errors. The author in [30] first identified the critical generator and applied equal-area criterion on the machine [34]. The CCT for the critical generator is then taken as the CCT for the system. However it is difficult to calculate the equilibrium points [34]. Identifying a severely disturbed machine and performing Equal-Area Criterion (EAC) on the machine also proves effective when only one generator is disturbed. When two or more generators are disturbed then the approach fails. An approach where the critical clearing time is obtained from two generators of most forward angle and most large angle named generator pair for assessing power system stability is presented in [36]. Combining relative power angle characteristic curves of the generator pair, EAC is directly applied to the generator pair to assess stability quickly. This is quite easy when it is applied to single machine infinite bus (SMIB) but it is time consuming when it comes to its application in multi-machines.

However, apart from these methods mentioned above, another method used in electric industry is to increase the fault duration until there is instability in the system. This method seems to be accurate and it is used in this thesis [37]. Due to the limitations of this approach, a computational intelligence (CI) approach to transient stability has been proposed.

Computational Intelligence (CI) approach based on Artificial Neural Networks (ANNs) is proposed in this thesis to provide real time transient stability assessment. The approach is based on critical clearing time prediction ahead of time so that appropriate control action can be taken in other to prevent unfortunate events that can lead to blackouts or catastrophe situations. CI can be tested with a small number or large volume of data if that is what is available to make a decision. Five CIs are used in this thesis to predict CCT and monitor the state of the system in real time. These are Multilayer Feed Forward Neural Networks (MLFNNs), Recurrent Neural Networks (RNNs), Radial Basis Function Neural Networks (RBF), Generalized Regression Neural Networks (GRNNs) and Self-Organizing Map Neural Networks (SOFM).

1.8 Computational Intelligence Methods

1.8.1 Multilayer Feed- Forward Networks (MLFNNs)

Multilayer Feed- Forward Networks (MLFNNs) are the most common type of neural networks. They consist of an input layer, an output layer and generally, one or more hidden layers in-between. The input signal propagates through the network in a forward direction, on a layer by layer basis. MLFNNs have been applied to solve different kind of problems by training them in a supervised manner using back propagation algorithm. They are the commonly used ANNs for pattern classification which is trained to produce spatial output pattern in response to an input spatial pattern. The mapping is static and is not at all suitable for a temporal pattern [38], [39].

1.8.2 Recurrent Neural Networks (RNNs)

Recurrent neural networks on the other hand are a brain-like model. The recurrent neural networks have feedback connections which add the ability to also learn the temporal characteristics of the data set. RNNs make use of memory to encode past history and have been shown to be effective modelling tool in recent applications to stability issues [40]. RNNs are used as computational models to solve computationally intensive problems. Unlike the widely used MLFNNs that can only establish static mapping relationships between input and outputs, RNNs contain internal feedback loops and states and can perform highly non-linear dynamic mappings and thus have temporally extended applications [41],[42]. There are two types of RNNs: Jordan recurrent neural network and Elman recurrent neural network. In this thesis Elman recurrent neural network is used.

1.8.3 Radial Basis Function (RBF)

Radial basis function neural networks are feed-forward neural networks where hidden units do not implement an activation function, but represents a radial basis function [43]. This is a type of neural network that approximates desired functions by superposition of non-orthogonal, radially symmetric functions [44]. The architecture resembles that of MLFNN but it uses distance of the input vectors from the weights as the input vector to the network, unlike MLFNN that uses the input vector directly. It has an input layer, a hidden layer of radial units and linear output units. It maps the input to a desired output by approximation of a desired function and superposition of non-orthogonal symmetric function [44].

1.8.4 Generalized Regression Neural Networks (GRNNs)

Generalized regression neural networks are supervised learning neural networks that implements Bayesian decision strategy for classification. They have four layers namely: input layer, pattern layer, summation layer and the output layer. They actually have the same structure as radial basis function except the summation layer. The GRNNs have a

special property that enables the users to flexibly configure the network suitable for real hardware implementation, by adjusting only two parameters: the centre and width [43],[44].

1.8.5 Self-Organising Feature Map (SOFM)

Self-Organising feature map was motivated by the self-organization characteristics of the human cerebral cortex. Self-Organising Feature Map adopts an unsupervised learning algorithm for clustering [44]. These networks are based on competitive learning in such a way that the output neurons of the networks competes among themselves to be activated or fired so that only one output neuron (winning neuron) is on at any time. SOFM effectively clusters the input vectors through a competitive learning process [43], [45].
The application of these CIs can be found in stability assessment, load forecasting, protection, modelling and power flow computation.

1.9 Objectives of the Research

The objectives of this research are to:

(1) Investigate the impact of hybrid distributed generation (HDG) on transient stability of power systems using dynamic models of wind turbine, solar PV and small hydropower.

(2) Investigate the impact of HDG on transient stability of power system in real time using Artificial Neural Networks such as Multilayer Feed-Forward neural networks, Recurrent neural networks, Radial basis function neural networks, Generalised regression neural networks and Self-organising Map neural networks.

(3) Assess the impact of HDG on transient stability using RTDS integrated with phasor measurement Units for wide area monitoring (and the prediction) of critical clearing time using data collected from PMU. These data are then trained using recurrent neural networks.

1.10 Methodology

A literature review was conducted. The areas covered in the literature review are basically on hybrid distributed generation and future networks, modelling of hybrid

distributed generation (HDG) with analytical method, computational intelligence methods and lastly real time transient stability assessment using critical clearing time.

To measure the stability margin, critical clearing time is used as the stability index. In this thesis, single machine infinite bus system and multi-machine power system models (i.e., Modified IEEE 39-Bus New England system and 68-Bus system) are used. The single machine infinite bus system (SMIB) was used to investigate the impact of hybrid distributed generation (HDG) on transient stability of a power system. For this network, only three single source DGs were considered in order to form the HDG. They are solar PV, small hydropower system (SHP), and wind generator (Doubly fed induction generator (DFIG)). The following hybrid DGs were derived from the single source DG:

- HYBRID SOLAR PV+ SHP
- HYBRID DFIG+ SHP
- HYBRID DFIG+SOLAR PV
- HYBRID DFIG+ SOLAR PV+ SHP

To investigate the impact of HDG on transient stability of power system, DIgSILENT power factory 14.1 is used for the modelling of SMIB with HDG. The impact of HDG on transient stability is measured by considering the followings:

1. Penetration levels (i.e., import mode (40%), balanced mode (50%) and export mode (80%)), and different types of HDG (the combination of solar PV, SHP and DFIG)
2. Load conditions (Annual increase in load for 30years at 24 MW increase interval)
3. Location of the HDG (Dispersed or concentrated HDG)
4. Transmission line length (The length is varied from 100km - 500km).

The modified IEEE 39-Bus New England system network consists of grid integrated HDG which was modeled in DIgSILENT power factory. The purpose of this study was to investigate the impact of HDG on transient stability using artificial neural networks. In order to investigate this impact, five types of neural networks were used as discussed earlier. Using five neural networks enable us to investigate the relative strength and weakness of each of these neural networks in providing accurate and quick prediction of the critical clearing time.

The data for the training of the neural network models was gathered from the DIgSILENT model of the modified IEEE 39-Bus system. In order to generalize the neural network models, data that covered relatively large operating conditions were collected by applying various faults such as three-phase fault, double-line- to- ground fault, line-to-line fault and single line-to-ground fault.

Finally, real time transient stability assessment was conducted on the modified 68-Bus system using RTDS. The disturbances that were considered are a three-phase fault and a loss of generations. The 68-bus system was integrated with phasor measurement unit (PMU) for data measurement. There are four outputs from the PMU, which are: voltage, current, voltage angle and current angle. The impact of HDG on transient stability is investigated by integrating HYBRID SOLAR PV+SHP to replace the existing generator 4 only. This is done in order to investigate the impact of HDG on transient stability if the conventional generators were to be replaced.
The data from the PMUs are used to obtain the rotor angle as well as the active power of the 16 generators. This data is also used to train the recurrent neural network for the determination of critical clearing time in real time.

1.11 Contribution and Scope of the Research

The contributions of this work are

1.11.1 Impact of hybrid distributed generation on transient stability.

The integration of HDG into the existing grid is increasing and at the moment research on the impact of HDG on transient stability is very limited.
This thesis investigated the impact of HDG on transient stability. The HDG are obtained by combining wind generator, solar PV and a small hydropower system. Accurate dynamic modelling of HDG will bring out clearly the impact of HDG on the existing grid. DIgSILENT power factory which was believed to contain the modelling detail necessary to carry out the investigation was used. Comparison between HDG and the

single source DG was carried out. New results were obtained in terms of the effect of HDG on the first swing rotor angle of generators as well the impact on the critical clearing time.

1.11.2 Real time stability assessment using Computational Intelligence Approaches and Real Time Digital Simulator

Dynamic simulation software performs analysis 24hrs in advance. Such analysis is not a simple task and it might not give a detailed assessment of the network. Network operators used preventive approach rather than corrective operating practices. The preventive approach ensures that the stability status is known ahead of time. In order to devise a corrective approach one must be able to predict the risk of instability in real time or near real time. To successfully handle this, a computational intelligence approach to transient stability assessment is used in this thesis. The computational intelligence approach works hand in hand with a conventional simulation tool (such as DIgSILENT power factory) for data training and prediction of the CCT. Novel results were obtained in terms of the performance of the five ANNs used in predicting the critical clearing time.
Furthermore, real time digital simulator (RTDS) with integrated phasor measurement units (PMUs) was used to provide a platform for performing wide area real time transient stability assessment.

1.12 Thesis Outline

The thesis is organized as follows:
Chapter 1 gives the detail background of the work. It covers basic definitions and benefits of distributed generation and hybrid distributed generation. Computational intelligence approaches applied to transient stability are also presented. The research motivation and objectives, contributions and scope of the research are described in this chapter.

In chapter 2, an overview of future network architectures and modelling of hybrid distributed generation is presented. The architectures that are presented include, vertically integrated network, horizontal integrated network, and smart grid. The basic form of

integrating hybrid distributed generation is discussed. It includes virtual power plant, micro-grids, integrated energy system, energy hubs, and intelligent power grid. The analytical modelling of a wind turbine, solar PV and small hydropower are presented. This chapter also includes the HDG configurations and operations.

In chapter 3, the review of computational intelligence techniques used in this thesis is presented. The CI techniques (i.e., neural networks) used include Multilayer Feed forward Neural Networks (MLFNNs), Recurrent Neural Networks (RNNs), Radial basis function Neural Networks (RBF), Generalized Regression Neural Networks (GRNNs) and Self-Organizing Feature Map Neural Networks (SOFM). Comparisons of various artificial neural networks were discussed. This chapter also contains a description on hybrid systems, performance evaluation, modelling of dynamic system using artificial neural networks and general overview of artificial neural network applications.

In chapter 4, the detail on real time transient stability assessment using critical clearing time is presented. The mathematical equation guiding toward the calculation of critical clearing time is discussed. Analysis of the real time modelling with the real time digital simulator (RTDS) and other stability indices such as Angle index, maximum frequency deviation index are discussed. Real time stability issues and the concept behind the phasor measurement unit (PMU) are presented. The chapter is concluded by presenting the role of computational intelligence in dynamic security assessment as well as an overview of the simulation tools used.

In chapter 5, the impact of hybrid distributed generation on transient stability of a power system is discussed. This chapter gives the detail of the modified single machine infinite bus system used. Different scenarios describing the different forms of HDG and penetration levels are discussed. The impacts of different HDG types, load condition, HDG location and transmission line length on both the critical clearing time and rotor angle are investigated.

Chapter 6 describes the ANN-based dynamic modelling and monitoring of hybrid distributed generation using the modified IEEE 39-bus system. Simulations conducted

using MLFNN, RNN, RBF, GRNN and SOFM are analysed and discussed in detail. The simulations cover the real time monitoring of rotor angle and the critical clearing time.

Chapter 7 gives the detail of real time modelling and estimation of CCT using RTDS integrated with PMUs. In this chapter, the real time critical clearing time calculated analytically is discussed. The results of real time transient stability assessment using RNN are also discussed.

Conclusion is presented in chapter 8 together with recommendations for future work.

Chapter 2

Overview of Future Network Architectures and Modelling of Hybrid Distributed Generation

Power system structure consists of generation, transmission and distribution systems. The power generated is transmitted at high voltage over long distances to distribution level. At the distribution level, the voltage is step down through the transformer to a safer voltage level. This structure has existed for a long time and is termed a vertically integrated structure [46]. However, due to electricity market liberalization and the possibility of integration of large quantity of DGs and HDGs into the distribution system to meet load demand, there is a transition from a vertically integrated structure into a horizontal integrated structure. In the horizontal integrated structure, power flows from the large power plants into the distribution network and also from the distribution network into the grid. In this structure, DG/HDG plays an active role where customers who are supposed to consume power, can also generate from their private owned DGs/HDGs into the grid. There is an active participation of distribution system in generation resulting in bi-directional flow of power. The effect is that transmission line limits can be violated and additional dynamics are introduced into the system thereby increasing power system complexity.

As the electric grid become more market driven and more technologies are being integrated into the grid to become large interconnected system with numerous regulatory bodies [47], the interconnected grid is now prone to failure as a result of increasing complexities. Recently, intelligent grid or future-Grid has been proposed to address the problem of increasing complexity and others that occurs at all levels- horizontally and vertically. When intelligent grid is fully implemented, the grid will be seen as a digital upgrade of the existing electricity infrastructure in order to allow for dynamic optimization of current operation as well as to incorporate dynamic gateways for alternative sources of energy production [29]. The core brain of intelligent grid is

computational intelligence (CI). The CI techniques consist of artificial or bio-inspired intelligence paradigm that exhibit an ability to generalize, associate, learn and adapt to new situations [29], [48]. Hence, the grid is undergoing transformation from the vertically integrated structure to a horizontally integrated system and sometime in the future into smart grid. In the next section, the power system structures are reviewed.

2.1 Vertically Integrated Structure

This structure is as old as power system itself. It consists of large power plants that are used to generate power at low voltage and transformed into high voltage before transmitting into the distribution level (at low voltage) where it is made available to end users. Hence, the structure is a vertically integrated structure. Besides, electro-mechanical conversion takes place at the generating centre and long transmission lines are used for the transmission. Examples of the generating stations that are associated with vertically integrated structure are the large hydropower station, nuclear power station, coal or gas power station, etc.,. Fig 2.1 shows the three levels of the power system network structure. In practice, these three levels are linked by transformers (not shown in the figure) which introduce different in voltage levels [46]. The structure is managed by single utility and the control methodology is centralized.

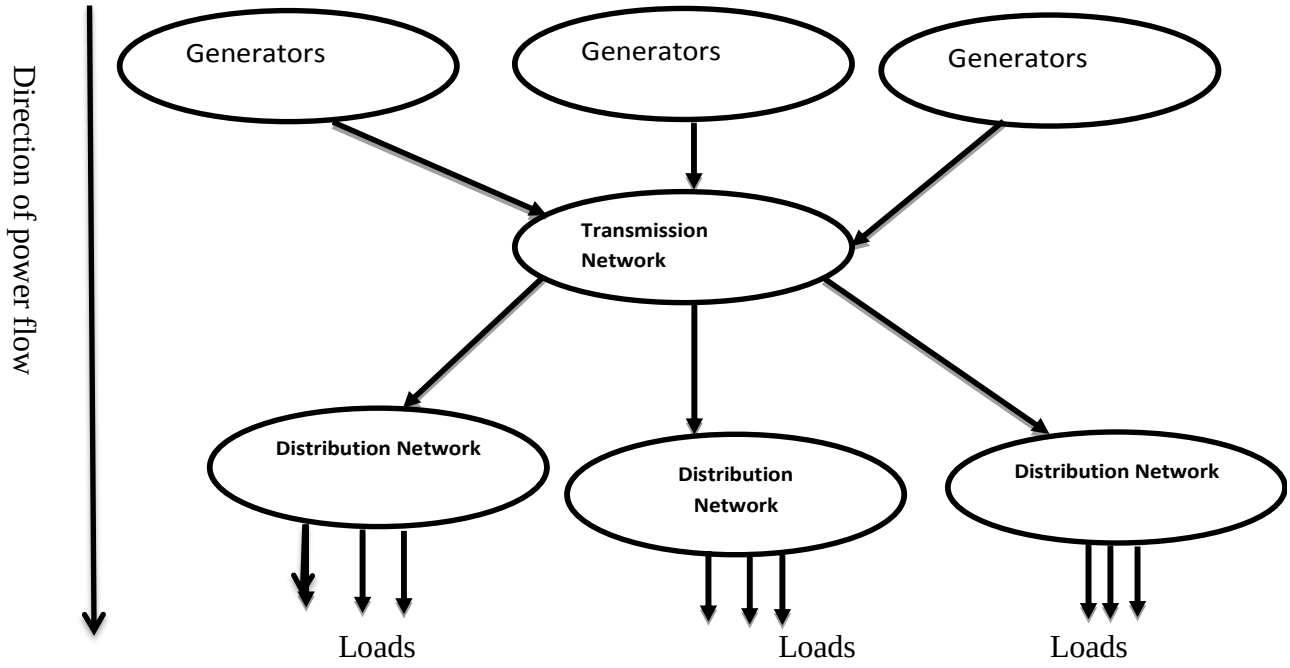

Fig 2.1: Vertically Integrated Structure.

This figure assumes that there are three generators and 3 distribution networks. However, there could be more than three.

2.2 Horizontally Integrated Structure

The transition from vertically integrated structure to horizontally integrated structure involves active participation of distribution system in generation due to the integration of DGs/HDGs. In this structure, power flow from the distribution system to service load at the same level or higher level in term of voltage. The horizontally integrated structure permits bi-directional power flow and it is a decentralized system where the energy produced by DGs/HDGs is consumed directly in the place where it is produced with the view of reducing power loss and to enhance power system security and reliability [46], [49]. When the concept is fully implemented, certain numbers of centralized generators will be displaced by the grid integration of DG/HDG [46]. Basically, DG/HDG is powered through renewable or non-renewable energy system, using both modern and conventional technologies. The different DG technologies including storage systems can be divided according to the primary resources used as described below [14]:

- Fossil- Fuel based DG such as: gas engine, gas turbine, stirling engine, fuel cell, etc.
- Non Fossil-Fuel based DG such as: wind turbine, photovoltaic, biomass, etc.
- Storage system such as battery, flywheel, super-capacitor, superconducting coil, etc.

Many sizes of DGs/HDGs are available in the market today and can be connected to a number of voltage levels from high voltage to medium voltage and low voltage. Only small generators may be connected to the lowest voltage network. The conventional distribution systems are very passive with centralized control. They are designed to accommodate all combinations of loads. Fig 2.2 is used to explain the flow of power from the centralized generators to the loads and from DG to the loads and the grid. It is assumed that the number of centralized generators in this case has reduced compared to Fig 2.1 because the dependence on centralized generator is shifting to DG/HDG in some countries. On the other hand, the entire network can also allow the integration of DG/HDG without reduction in the number of centralized generators. In this case, the DG/HDG is made to service the increasing load demands. In any of the case, the power flow is bi-directional compared to power flow in Fig 2.1. The dotted lines in Fig 2.2 shows the direction of the power flow when DG/HDGs are connected. It also shows that, if the dotted lines that connect distributed generators in Fig 2.2 to distribution networks are removed, the DGs/HDGs fall into standalone. Standalone system produces power independently of the utility grid [50]. In standalone, the DG/HDG can begin to supply power to villages without input from the grid [50].

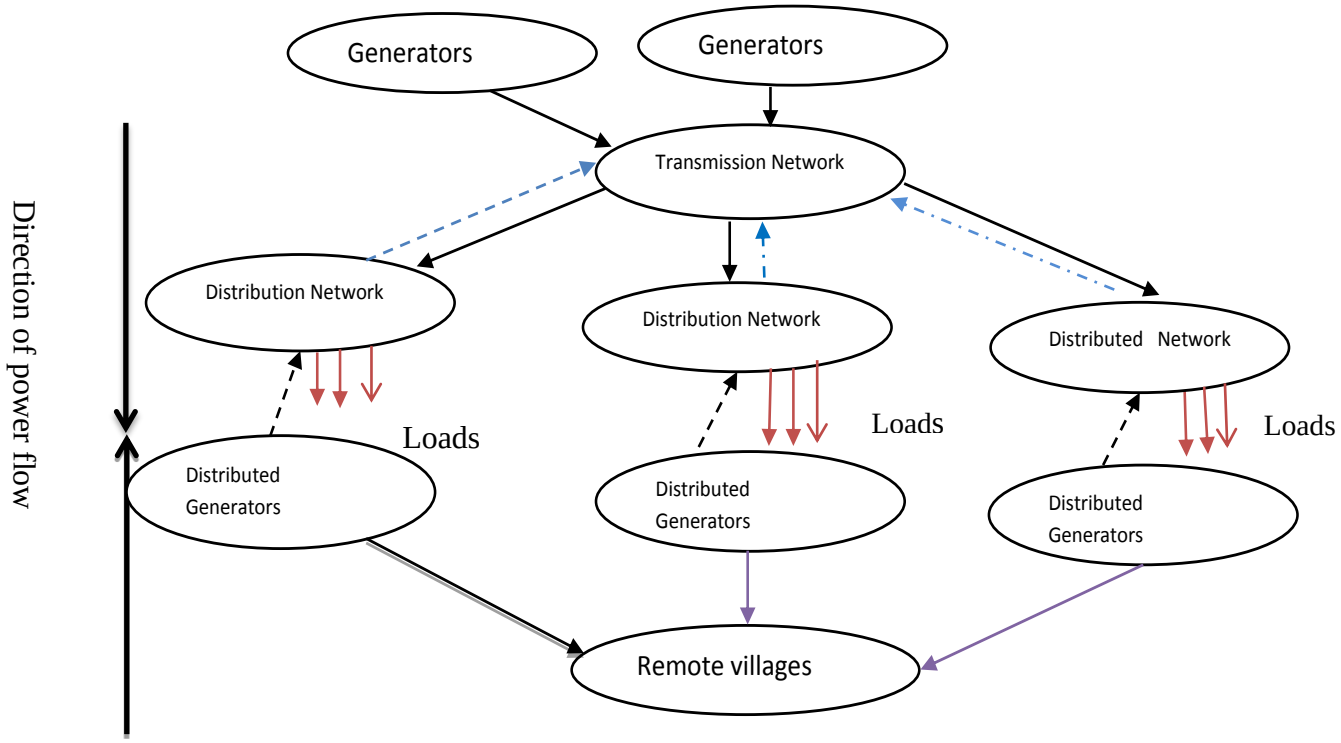

Fig 2.2: Horizontally Integrated Structure

Power generation nearer to the demand centres is focusing on meeting loads and reducing losses [50]. The implementation of distribution generation can handle the rural electrification by providing energy which is reliable, sustainable, and affordable. However, the deployment of DGs in the active distribution network could pose stability problems to network operators as well as end users. This is due to the fact that the distribution system network was not originally designed to accommodate distributed generators [47],[51]. As a result, there is an increase in complexity, uncertainties, and difficulties in modelling the power system leading to challenges at all levels of power grid. To overcome the challenges of complexity, the power system needs intelligence in all structures- horizontally and vertically [29] that will process information accurately and timely in order to make critical decisions locally or globally.

2.3 Smart Grid or Intelligent grid

Recently, the electric industries and academia began to investigate the possibility of building a modernized distribution network by introducing technologies that can help with demand-side management, revenue protection, control, stability monitoring and assessment [52],[53]. This is motivated by the rapid increase in the cost of fossil fuels, coupled with the inability of utility companies to expand their generation capacity in line with the rising demand for electricity. The basic objectives of smart grid are minimization of cost of energy and reduction in emission [52].

The European Smart Grids defines the future/smart grids as "electricity networks that can intelligently integrate the behaviour and actions of all users connected to it - generators, consumers and those that do both – in order to efficiently deliver sustainable, economic and secure electricity supplies"[28],[54]. We will adopt the definition from [55] because it is explicit enough to cover the area of our focus in this thesis.

"A Smart grid is basically the embedding of intelligence to enable bi-directional power flows between sources of electric power generation (traditional and renewable sources), and smart devices (traditional loads, energy storage, etc.), within some specified constraints and performance requirements**"** [29],[55].

If this definition is combined with the one in [52], it will give a clear understanding of what smart grid is.

In [52], smart grid is defined as "the collection of all technologies, concepts, topologies, and approaches that allow the hierarchies of generation, transmission, and distribution to be replaced with an end-to-end, organically intelligent, fully integrated environment where the business processes, objectives, and needs of all stakeholders are supported by the efficient exchange of data services, and transactions" [52].

In summary, smart grids are intelligently controlled active networks that facilitate the integration of a wide variety of generation options such as distributed generation, plug in electric vehicles and hybrid distributed generation into the power system in a well-structured topologies [29]. It allows energy management system where customers are allowed to adjust their energy consumption and cost. Also a smart grid/intelligent grid is a self-healing system and that allows the prediction of imminent failure, real time/online

stability assessment, dynamic optimization of current operations, etc. [29]. A smart grid structure as shown in Fig 2.3 incorporates:

- The use of digital information and controls technology to improve reliability, security and efficiency of the electric grid.
- Dynamic optimization of grid operations and resources, with full cyber-security.
- Integration of distributed resources and generation, including renewable resources.
- Development and incorporation of demand response, demand-side resources, and energy-efficiency resources [1].
- Deployment of "smart" technologies involving real-time, automated, interactive technologies that optimize the physical operation of appliances and consumer devices for metering, communications concerning grid operations and status, and distribution automation.
- Integration of "smart" appliances and consumer devices.
- Deployment and integration of advanced electricity storage and peak-shaving technologies, including plug-in electric and hybrid electric vehicles, and thermal-storage air conditioning.
- Provision to consumers of timely information and control options.
- Development of standards for communication and inter-operability of appliances and equipment connected to the electric grid, including the infrastructure serving the grid.
- Capability of self-healing.
- Fault-tolerant by resisting attacks [29].

The components of smart grid in comparison with present exciting grid are shown in Table 2.1.

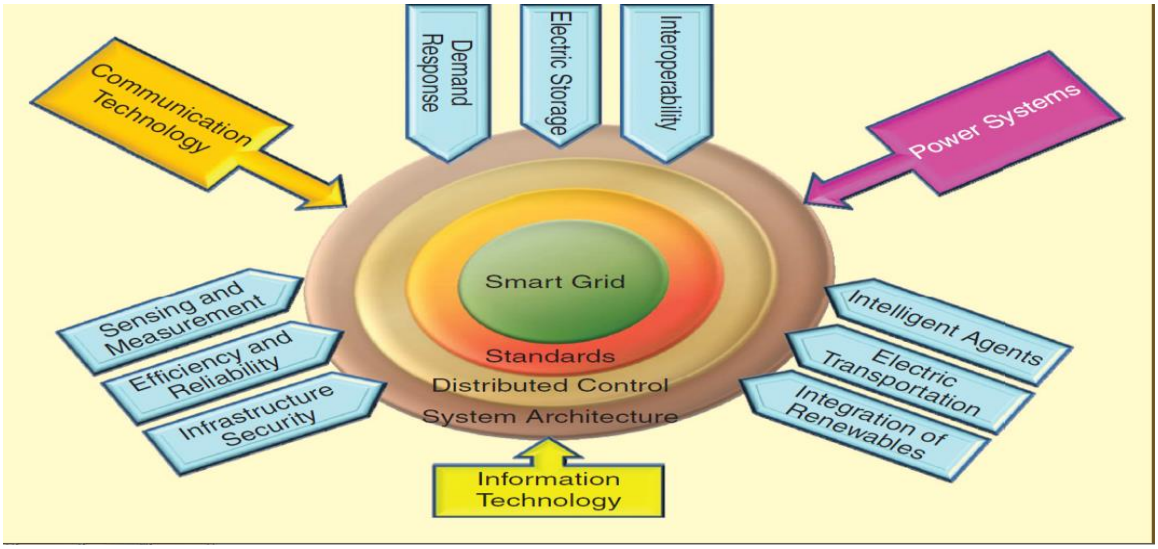

Fig 2.3: Basic Smart Grid Ingredients [52]

In view of these smart grid capabilities, communication, information technology and data management system are seen as an indispensable part for the implementation of smart grid concept. This will allow utilities to integrate intelligence into the present power system network in order to enhance accessibility, stability monitoring and assessment, management and the control of demand-side response [52]. Generally, the integration of communication technology and information technology with power system engineering will be assisted with array of new approaches, technologies and applications to transform the present existing grid to smart grid as can be seen in Table 2.2.

Table 2.1: Comparison of Smart Grid With The Existing Grid.[52]

Serial number	**Existing Grid**	**Smart Grid (Intelligent Grid)**
1	Electromechanical	Digital
2	One-Way Communication	Two-Way Communication
3	Centralized Generation	Distributed Generation
4	Hierarchical	Network
5	Few Sensors	Sensors Throughout
6	Blind	Self-Monitoring
7	Manual Restoration	Self-Healing
8	Failures and Blackouts	Adaptive and Islanding
9	Manual Check/Test	Remote Check/Test
10	Limited Control	Pervasive Control
11	Few Customer Choices	Many Customer Choices

Essentially, there are smart grid technologies for every corner of the traditional electric power infrastructure which are based on advanced sensing and communication system such as advanced metering infrastructure and Phasor measurement units (PMUs) [56]. It is true that advanced sensing and communication systems are indispensable parts of a smart grid, since they provide channels for monitoring critical data and sending back control commands. However, they do not provide the smartness for data analysis and decision making. Intelligent use of information will be the core of a smart grid [28],[29].

For smart grid to be smarter, computational intelligence (CI) techniques have been suggested [27],[28]. Intelligent techniques will help to monitor and report any instability timely and accurately in other to prevent blackouts [30]. These techniques accurately and timely compute stability limits to check whether the transmission loading progresses or is projected to progress beyond the operating stability limits [1]. These algorithms must be fast, scalable and dynamic in order to overcome the challenges of complexity, sheer size of the network [28].

The implementation of intelligent grid will be assisted with infrastructure and technology that will enhance the future vision of intelligent grid (see Table2.2). As a result of this,

dynamic assessment and monitoring will involves look-ahead concept, stochastic approach; dynamic models update and real time validation. Online stability assessment problems can be solved with the use of intelligent techniques [57]**.**

.

Table 2.2: Infrastructure and Technologies needed for Future Assessment Functions [57]

Present	**Infrastructure and Technology Needed**	**Future**
Online contingency analysis	Tools to perform online comprehensive stability analysis	Online voltage stability Online transient stability Online Small Signal Stability
Alarming without prioritization	Alarm management tools	Prioritization of alarming messages by identifying root causes
Pre-defined generation and transmission model	Tools to perform real-time load modelling and generator dynamic model update and validation	Dynamic models updated and validated in real-time
Network modelling fixed and predefined	Online algorithms for model validation	Real-time network modelling validation and adjustment
Analysis is based on real-time state estimation	Implement look-ahead function into existing analysis tool	Look-ahead to near future
Deterministic contingency analysis	Tools to perform online risk assessment	Consider probability of outages in contingency analysis
N-1 Contingency Analysis	Fast simulation Methods to enable N-k analysis	Investigate cascading failures

Looking at the definition and advantages of smart grid or intelligent grid, one can say that the intelligent grid will only materialised through intelligent control and monitoring alongside with the existing grid. This necessitates a topology or architecture that allows its growth and that will enhance the increasing penetration of DG/HDG.

The next section shows the basic topologies that enhance HDG penetration and allows the mixed energy source to be accumulated together before integration into the grid

2.4 Hybrid Distributed Generation Architectures

An emphasis has been placed on the need to move away from fit and forget rule of DG integration [47] in order to enhance active management of mixed energy sources at distribution level. If fit and forget rule is allowed, it might be difficult for HDG to provide voltage support. There are emerging topologies to HDG integration in the future intelligent grid. In other word, intelligent grid will be made up of the following topologies/architectures:

- Virtual power plant
- Micro-grids
- Integrated energy system
- Energy hubs

With the above architectures, the HDG will be able to support the grid, increased overall energy efficiency and enhance system reliability and security [58],[59].

2.4.1 Virtual Power Plants

In the Virtual Power Plants (VPP) model, an energy aggregator gathers a portfolio of smaller generators and operates them as a unified and flexible resource on the energy market or sells their power as a system reserve.

The purpose of Virtual Power Plants (VPP) as shown in Fig 2.4 is to enhance the visibility of HDG and to provide proper interaction among local components and the grid. Besides, it allows the use of distributed control mechanism and permits an optimal use of

available capacity. By this, HDG will be able to participate in energy marketing. Besides, VPP allows the integration of many DGs in clusters form into the grid in order to minimize the impact of variability of the DG and to increase the capacity of the DGs that participate in the market (see Fig 2.4) [58].

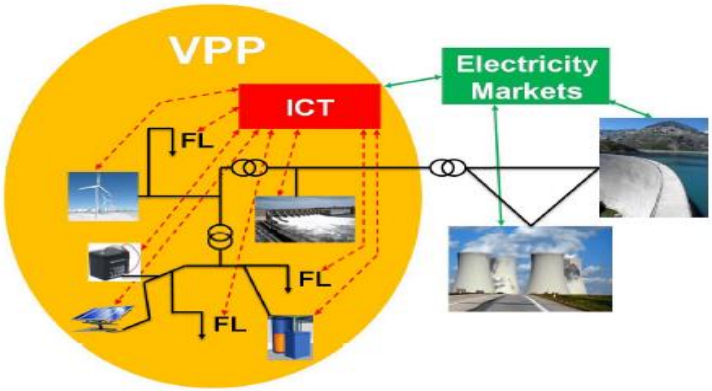

Fig 2.4: Virtual power plants [58]

2.4.2 Micro-Grids

The micro-grid is a clustering combination of DGs in order to service local loads. A typical diagram of micro-grid is shown in Fig 2.5. The figure shows the clustering of solar PV, fuel cell, micro turbine and wind turbine to form an entity integrated into the grid. It can operate in an autonomous mode (Islanded mode) or non-autonomous mode (Grid-connected). The purpose of micro-grids is to increase the availability of DG, allow modular operation planning, optimisation and management of energy mix and increase efficiency and reliability. Islanded mode requires frequency and voltage control. In a case of energy balancing, energy storage is required to provide supply-demand balancing. The grid-connected mode requires adequate knowledge of grid synchronisation in case of difference in frequency and voltage. During small and large disturbances, this type of integration is helpful and enhances stability and service restoration [60], [61], [62], [63].

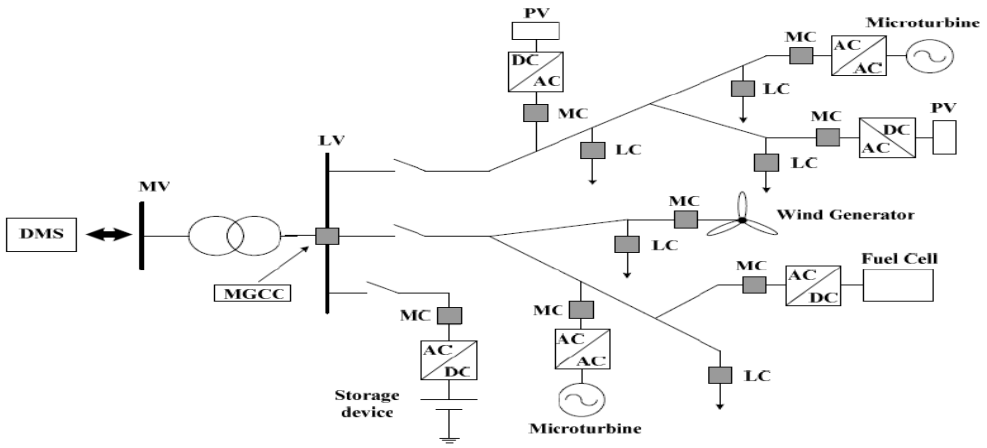

Fig 2.5: Micro Grid [61]

In micro grid, the generators inertia is very small compared to the centralized generator. Some even have no inertia at all (e.g., solar PV and fuel cell). The influence of inertia on the transient stability varies depending on the type of generator.

2.4.3 Integrated Energy Systems

Integrated Energy Systems (IES) use the combination of on-site power or distributed generation technologies and thermally activated technologies to provide cooling, heating, humidity control, energy storage and/or other process functions using thermal energy which is normally wasted in the production of electricity/power [64]. The purpose of the integrated energy system (IES) is to maximize the efficiency of energy use, reduce harmful emissions to the environment, improve power quality and reliability and provide flexibility for meeting electric power peak load demands as compared with large central power plants. IES combines DG equipment with thermally activated technologies such as micro turbine, heat recovery, and desiccant and absorption chiller units. Micro-turbine generates power for the local loads and the exhaust gas is recycled for heating, drying and cooling [65].

2.4.4 Hybrid Energy Hub

An energy hub is considered as a unit where multiple energy carriers can be converted, conditioned, and stored [66]. It represents the interface between different energy infrastructures and loads. It provides easy combination of different energy carriers so as to achieve the desired services such as electricity, heating and cooling. In Fig 2.6, the inputs are electricity natural gas, etc. The outputs can be electricity, heating or cooling at the output port. Within the hub, energy is converted and conditioned using transformer or combined heat and power technology. Energy hub allows grid optimisation and storage [66] and increase availability and reliability of the system. There are three basic elements of energy hub namely: direct connection, converter and storage devices. The direct connection delivers the input into output without any conversion. Examples of direct connections are pipeline, overhead lines etc. The converter converts power into other forms. Examples of converters are steam and gas turbines, combustion engines, electric machines, fuel cells etc.

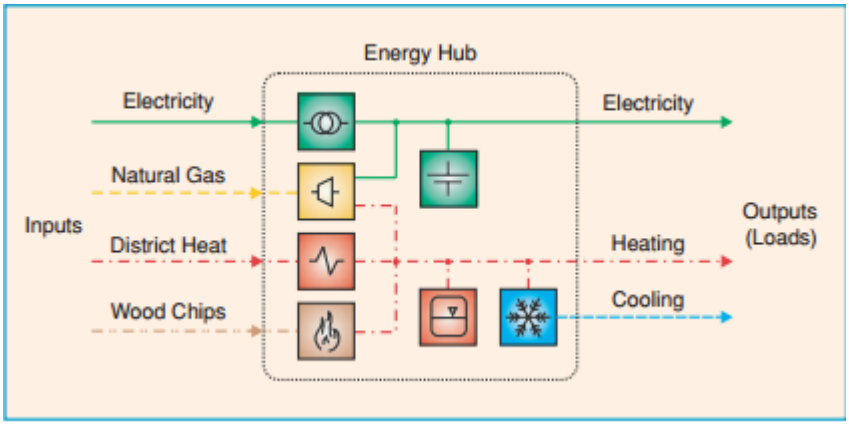

Fig 2.6: Example of an energy hub [66]

However, despite the use of well-structured architectures or topologies methods of HDG integration as described above, there are still some challenges operators faced in the operation of DG/HDG. They are discussed in the next section.

2.5 Power Quality

The challenge of maintaining appropriate frequency and voltage level is increasing due to increasing interest in HDG [24]. At present, the concern of the consumers is to have access to quality electricity without any effect on their loads. To achieve this, power quality such as voltage flickers and harmonics must be appropriately checked in the new active distribution network.

The main power issues affected by DG/HDG are: sustained interruption, voltage regulation, harmonics, voltage sag and voltage flickers [67].

In order to maintain good power quality, there must be [23],[24]:

- Fast response from energy storage to protect the load from momentary voltage variations
- Conversion of the stored energy into clean power
- Control for synchronization and paralleling between systems
- Seamless transfer (also called soft transfer) to the alternate power source and back again
- Immediate isolation from any grid disturbances
- Sufficient quantity of stored energy to ride through until primary or secondary power is restored
- Ability of the HDG system to provide clean power to the critical loads
- Dispatch-able varying local load.

2.5.1 Voltage Flicker

Voltage flickers are impressions of unsteadiness of visual sensation induced by a light stimulus whose luminance or spectral distribution fluctuates with time [15]. A voltage flicker is caused by a variation of the load current. Since DGs/HDGs are modelled as negative load [15],[68], integration of DGs/HDGs can also cause flickers especially when

a large DG/HDG unit is started or when a DG/HDG characterised with variable output such as wind turbine is connected to the grid. To mitigate this problem, the unit with variable energy source is integrated with converter or well-designed controller to extract the maximum output from the intermittent sources.

2.5.2 Harmonics

Harmonics create a distortion of the normal electrical current waveform, generally transmitted by non-linear loads. Non-linear loads, rotating synchronous generator, power electronic loads, rectifiers and inverters in electric drives are some of the major sources of harmonics in power system [15],[69],[70]. Most of the DGs/HDGs such as fuel cell, solar PV today are decoupled from the grid using power electronic interface. As a result, it contributes more harmonics due to additive effect of harmonics from individual HDG. The effect can be devastating resulting in overheating, equipment failure, false tripping of protective units and nuisance tripping of sensitive load with interference with communication circuit [70]. Today, the effect of harmonics is reduced because of the use of an insulated gate bipolar transistor (IGBT) which uses pulse width modulation (PWM) to generate quasi-sine waves. Other solutions include:

- Use non-resonant switching frequencies
- Use reactors in the neutral, or generators with a 2/3 coil winding pitch.

2.6 Islanding Challenges

Islanding occurs when a certain portion of power system network that contains the loads and the generators such as DGs disengage from the electric grid intentionally or unintentionally and remain energized. There are many concerns in operating islanding system such as violation of acceptable voltage and frequency limits, etc., The current industry practice is to disconnect all distributed generators immediately after the occurrence of islands. This is done to prevent equipment damage or to avoid unnecessary hazards [71],[72]. There are provisions in the grid code now to avoid disconnection of generators during disturbances. The affected generators should be equipped with reactive power capability to ride through fault.

2.7 Protection Systems

The conventional system (i.e., passive distribution network) is designed to incorporate a protection scheme different from active distribution network. The vertical flow of protection signal is to coordinate an essential operational method toward ensuring proper tripping in case of fault. However, the dynamic change in the current network has allowed the horizontal flow of fault currents thereby making the existing protection scheme inadequate for the present system. Some protection challenges generated by integrating DG/HDG are [72],[73]:

- False tripping of feeders
- Nuisance tripping of production units
- Blinding of protection
- Increased or decreased fault levels
- Unwanted islanding
- Prohibition of automatic reclosing
- Unsynchronized reclosing

Some of the solutions provided could include

- Adding recloser to incorporate another protection zone.
- Equipping the recloser with directional and microprocessor unit.

2.8 Short Circuit Current

When several generators containing different inertia are aggregated in the distribution networks, more fault current is introduced into the systems which interfere with protection scheme that was designed for passive distribution system. It also results in false tripping of the protective scheme. The fault current depends on so many factors among which are the strength of the grid, the type of generator (induction or synchronous generators) etc. The contribution of inverter based energy source is also an important factor that contributes to large fault current [15],[74].

2.9 Modelling of Hybrid Distributed Generation

There are two methods described in literature for modelling renewable energy. They are time-step simulation methods [75] and probabilistic methods [76]. The time-step simulation is based on analytical method or deterministic approach of modelling. It goes through a simulation period step by step and the conditions are assumed to be known ahead of time. Generally, time-step simulation is deterministic approach where the fault application or other disturbances are fixed or set ahead of time. Probabilistic approach on the other hand is based on a stochastic method. It is good at processing stochastic uncertainties such as uncertainties about training data, type of fault and location of fault coupled with the conditions of the system [77], [78]. Probabilistic approach can be used with time-step simulation. Recently, computational intelligence (CI) techniques are gaining recognition in modelling and assessment of dynamic stability. This research is proposing the use of computational intelligence method in modelling and assessment of hybrid DG (HDG). This is relatively a new idea proposed in this thesis to determine transient stability margin of grid integrated HDG instead of using the time-step simulation or probabilistic method. CI techniques involve the use of data gathering and training. CI techniques can be combined with time-step simulation and also used with probabilistic method [76], [78].

This section describes the modelling of wind generator, solar PV, and small hydropower system using analytical modelling approach. The reason for choosing the above three renewable generators is because they are available in abundance and environmentally friendly [79], [80], [81], [82]. Rather than standalone type distributed generators (DG), the utility interactive HDG [138] is considered which at the moment is gaining popularity.

.

There are two types of models in hybrid power generation [83],[84].

1. Logistical models
2. Dynamic models

Logistical models are used primarily for studying long time performance, economic analysis, component sizing and prediction whereas dynamic models are used mainly for component design, assessment of system stability and power quality.

Wind generator, solar PV and small hydropower for distributed generation applications are explained in the following sections**.**

2.10 Hybrid Distributed Generation Combination

The combination of hybrid power generation was represented in matrix form in [18]. Fig 2.7 covers almost all the possible hybrid combinations that are commercially available or ongoing research and development. It also shows the hybrid power generation that are not available or plausible. For example in the first row of IC engine, natural gas and water purification cannot be combined together while natural gas and CHP are already commercially available. In the same row (IC engine) combining natural gas and wind is a subject of ongoing research and development but natural gas and hydro is not yet possible. The same explanation can be given for other. However, this diagram does not explain the hybrid combination of three energy sources which is considered in this thesis. From Fig 2.7, wind generator and hydropower is possible but hydro and solar PV is recorded under 'not applicable' while wind generator and solar PV are already in the market.

The commercially available hybrid systems are solar PV-Battery, solar PV-diesel, wind-battery, wind-diesel, solar PV-wind-battery and solar PV-wind-diesel-battery [18], [85]. This research work focused on the possible combination of wind generators, solar PV and small hydropower system for hybrid distributed generation.

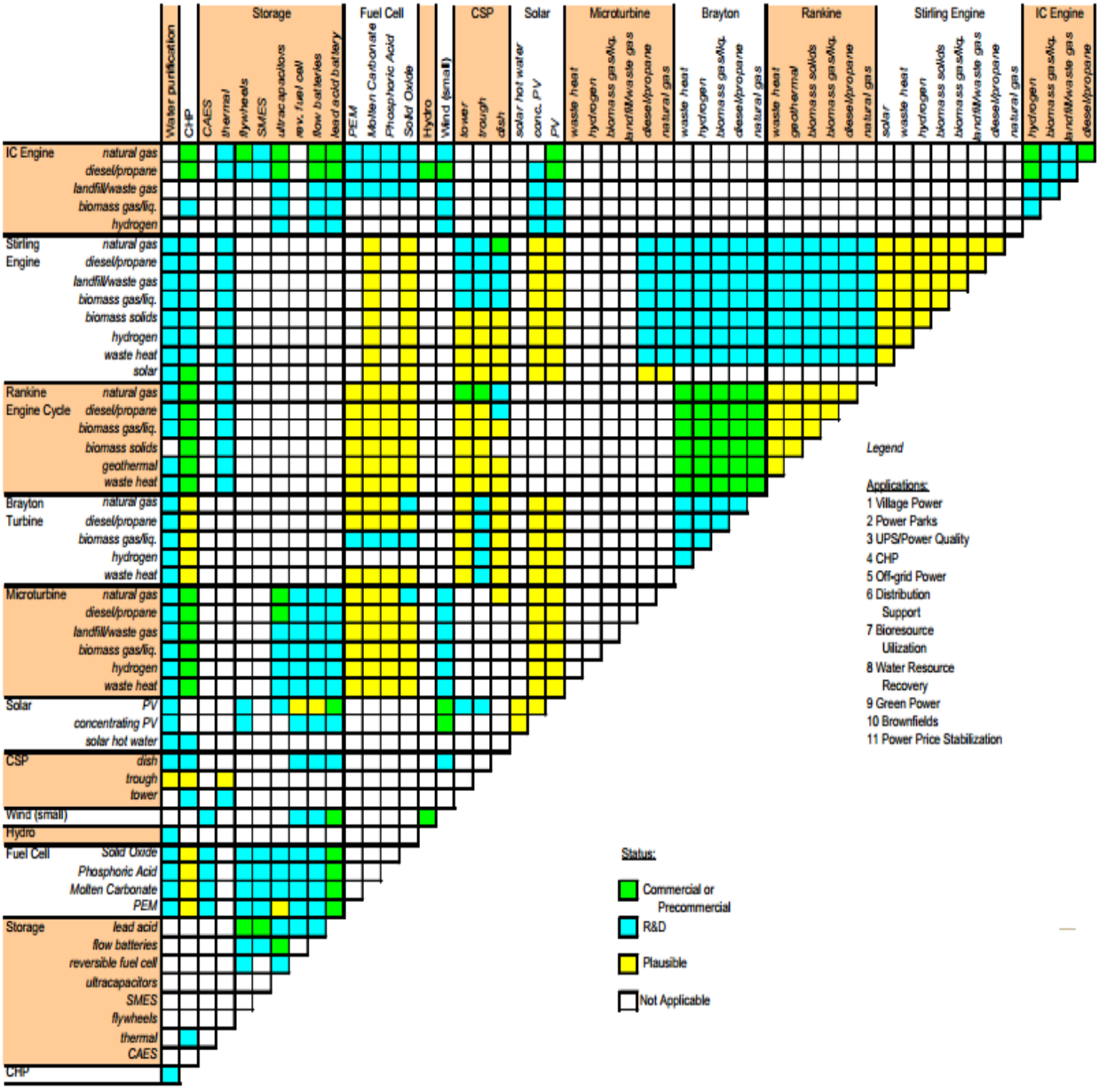

Fig 2.7: Hybrid combinations overview [18]

2.11 Dynamic Integration/Operation of Hybrid Distributed Generation

In most cases, HDG is designed to supply electricity to isolated area. HDG operates independently of the grid (standalone) as shown in Fig 2.8. It consists of HDG supplying

electricity to the local customers. On the other hand, HDG can also be integrated into the grid (grid-connected) as shown in Fig 2.9. The former is typically referred to as emergency and standby power. Many remotes villages have been powered with a standalone system [50]. In grid-connected type, the power generated can directly be used to feed local loads and the excess is exported to the grid. Power electronic devices are viable components that will enhance proper interface.

Besides, several other issues are of concern when HDG is integrated to the grid. For example, the reactive power supply by the DG/HDG into the grid is different depending on the DG/HDG types and as a result, it introduces different dynamic interaction compared to single energy source. The internal dynamics of the mixed energy system are also different, producing a large transient stability impact compared to single source energy system [46].

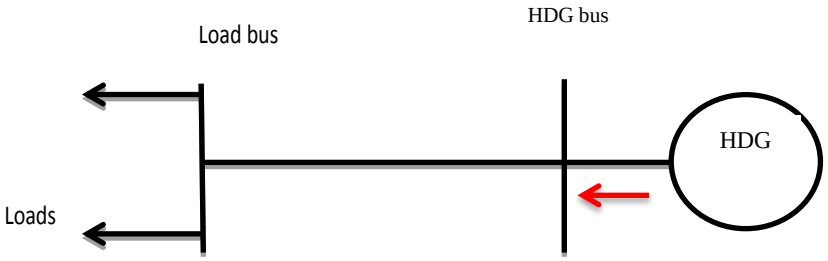

Fig 2.8: Standalone System

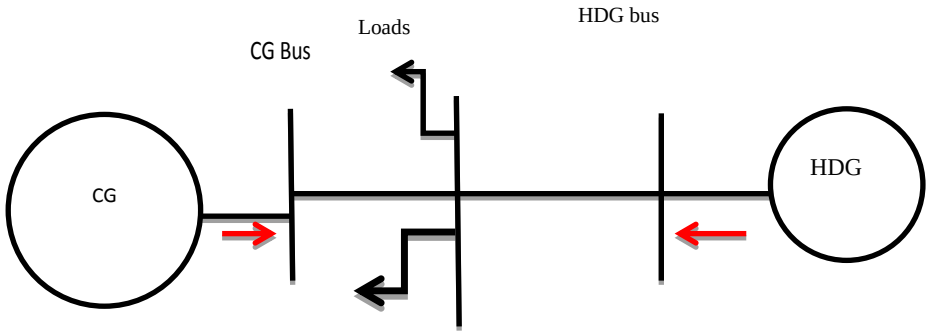

Fig 2.9: Grid-Connected Modes with Centralized Generator (CG)

2.12 Criteria for Hybrid Distributed Generation System Selection

Many components can be combined together to form hybrid system [18]. Few of them that are used in this research are explained in the next sections. They are wind turbine, solar PV and small hydropower

In literature, various indices have been used to evaluate HDG such as load ratio, battery to load, non-availability of energy, etc., [85]. These indices are used in order to select an optimal combination of HDG to meet the load demand. However, evaluation of transient stability may be carried out by using critical clearing time as stability index rather than using the common method of economic index. This will help in choosing the appropriate hybrid option from stability point of view and at the same time compliment the economic index.

2.13 Overview of Wind Generator

Amongst new renewable resources (excluding large hydropower), wind power contributes the largest megawatt to the total renewable energy capacity in the world. The capacity growth rate of wind power over the past 10 years is just over 25% per annum, which implies a doubling of capacity every three years. Wind power now generates 437 TWh of electricity which is around 2% of total electricity generated. At the moment, the leading countries in wind generation are Germany, USA, Denmark, India, China and Spain. More than 83% of worldwide wind energy capacity is utilized in these countries [86].

In 2008, existing wind power capacity grew by 29% to reach 121 GW which is more than double of the 48 GW capacities that existed in 2004. The 2008 increase was led by high growth in the strongest markets of the United States (8.4 GW added), China (6.3 GW), India (1.8 GW) and Germany (1.7 GW) [87]. In 2012, 45GW of wind power capacity was introduced into the power market which increases the global wind capacity of 19% to almost 283GW [88]. Small scale wind power is also growing because of the advantages it offers in providing power to remote communities that has no access to utility power. Individuals may purchase these systems to reduce or eliminate dependence on the grid electricity for economic or other reasons, or to reduce their carbon footprints.

They may also be hybrid with battery storage to reduce the effect of intermittence of wind. Other resources that might be added to wind-battery hybrid are solar PV, diesel generators, micro turbines or small hydropower. With the advent of power-electronic interface technologies, small wind turbines may be integrated to the grid that would back up the grid supply to provide uninterrupted power to the consumers.

In general, wind energy can be classified according to speed control and power control ability.

The speed control criterion leads to two types of wind turbines:

- Fixed-speed
- Variable speed.

While the power control ability criterion, on the other hand, classifies wind energy conversion systems (WECS) into three categories [89]:

- Stall-controlled
- Pitch-controlled
- Active-controlled wind turbines.

2.14 Modelling Of Wind Generator

• Generic Model of Wind Generator

There is a generic wind generator model which illustrates the general structure of wind model. It incorporates six blocks as described in Fig 2.10. Each of these six blocks is available in any wind model irrespective of the wind technologies. They are:

- Aerodynamic system
- Mechanical system (turbine rotor, shafts, gear box and the generator rotor)
- Generator drive (generator and power electronic converters, if any)
- Pitch control system
- Wind turbine control system
- Protection system of the wind turbine

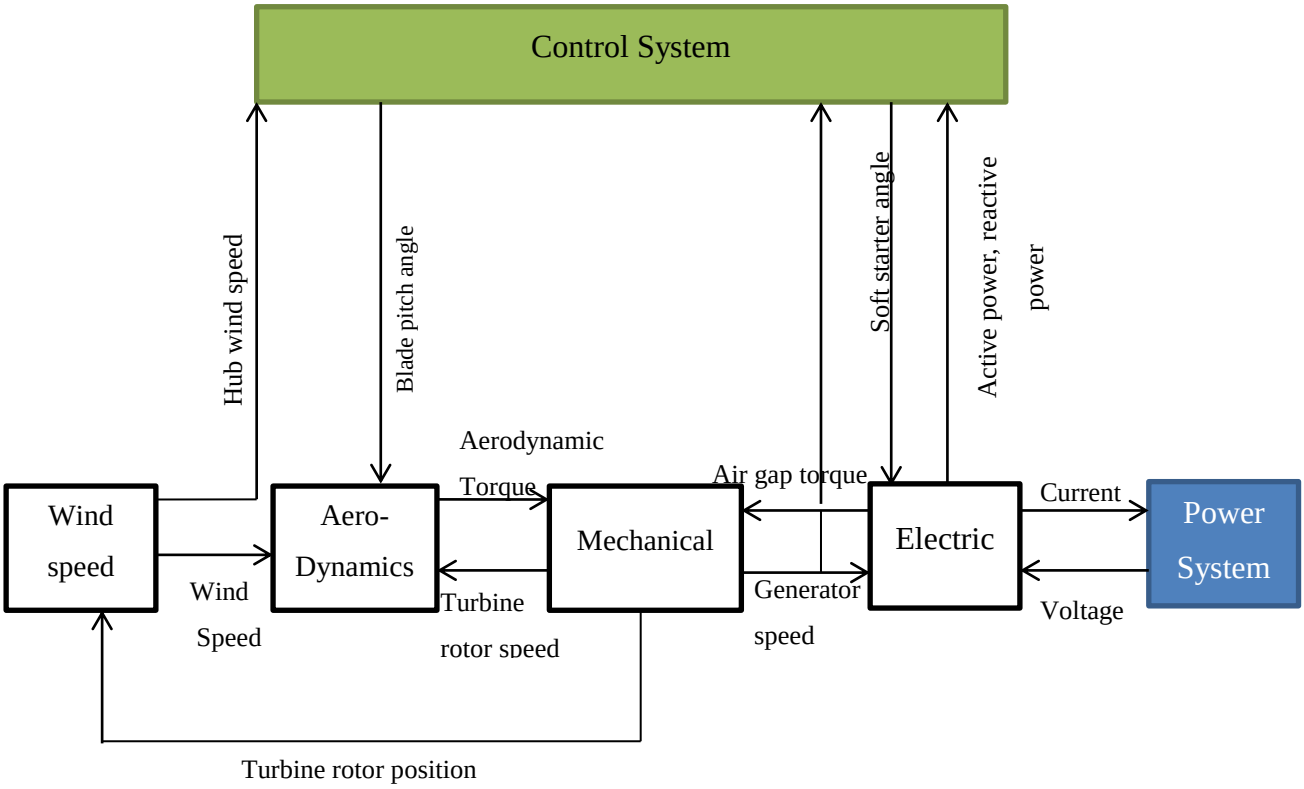

Fig 2.10: Generic wind model [90]

The aerodynamic model interfaces the wind and the mechanical model while the electrical model interfaces the mechanical model with the grid as shown in Fig 2.10. The aerodynamic model provides the torque for the mechanical drive train and uses the turbine rotor speed, blade pitch angle and equivalent wind speed as inputs. The aerodynamics drives the turbine rotor which transforms absorbed kinetic energy to mechanical power. The mechanical system of a wind turbine consists of the drive train. The drive train consists of the rotating masses and the connecting shafts, including a possible gear system. For a fixed speed, squirrel cage induction generator, the drive is just the induction generator because it is directly coupled into the grid. For wind turbine like variable speed generator, it consists of a decoupled system in addition to the masses and the generator.

The electrical model consists mainly of electrical generator interfacing with the power system via the voltages and current. It also provides the generator air gap torque and uses the generator speed as input. At the same time, electrical model output the active and the reactive power which is also used as control parameters.

2.15 Variable Speed Wind Turbine

In the near future it is expected that the interest in fixed speed wind turbines will gradually decrease because the striker rule of grid connection requirements. Variable-speed wind turbines are now dominant in the market due to its improved technology that incorporates power electronics converters interface. The other advantages of variable-speed wind turbines are an increased energy capture, improved power quality and reduced mechanical stress on the wind turbine [86]. The challenges in the use of this turbine are increased losses and cost [91], [92], [93], [94]. The increasing interest is based on the development of power electronics that made it easy for dynamic integration. With variable-speed operation it is possible to either accelerate or decelerate the rotational speed of the turbine with the wind speed. This decoupling of the wind generators from the grid by the power converter makes the electrical system more complicated than the fixed-speed wind turbine. Examples of variable speed wind turbines are doubly-fed induction generators (DFIG) or direct drive permanent magnet synchronous generator (DDPMSG) or gear box permanent magnet synchronous generators also known as converter driven synchronous generator. The variable speed concept allows the wind turbine to operate at optimum tip-speed ratio and optimum power coefficient for a wind speed range.

Dynamic simulation is guided by accurate modelling of the generator and is tailored towards the phenomenon of interest. Some guiding equations are analysed below:

The total wind power P_w available per unit for any turbine is given by:

$$P_w = (\frac{1}{2}\rho A V_{Wind}^3) \tag{2.1}$$

Where ρ is the density of the air in kg/m^3, *A i*s the exposed area in m^2, and V_{Wind} is the wind velocity in m/s. The theoretical maximum power that can be extracted from the wind is based on the discovery made by Berz in 1926. According to Berz only 59% of the power of the wind can be extracted assuming there is no loss [86]. The amount of power that can be extracted is denoted by the power coefficient C_p. The mechanical power of the turbine is also obtained from the power of the wind and is transmitted to the generator

through an electromechanical operation. The mechanical power output (the maximum power that can be extracted) is:

$$P_m = C_p P_w \tag{2.2}$$

where C_P= 0.59 and is the coefficient of power conversion

The electrical power output depends on the wind speed. The wind turbine operates at the speed of the available wind and increase until it reaches a maximum of 12-16m/s depending on the design of the turbine (see Fig 2.11). The power stays at 1500kW regardless of further increases in speed. The turbine continues to produce maximum power until the cut-out speed is achieved. The cut-out wind speed is the wind speed where the wind turbine stops production of power. Typically, the cut-out wind speed is in the range of 20 to 25 m/s. The power can be regulated either passively (e.g., by stall control), by designing the blades to go into an aerodynamic stall above a certain wind speed or actively (e.g., pitch control) by designing the blades as feathered in order to spill the unwanted power. The first method is called stall-regulation; the second method is called pitch-control [95],[96].

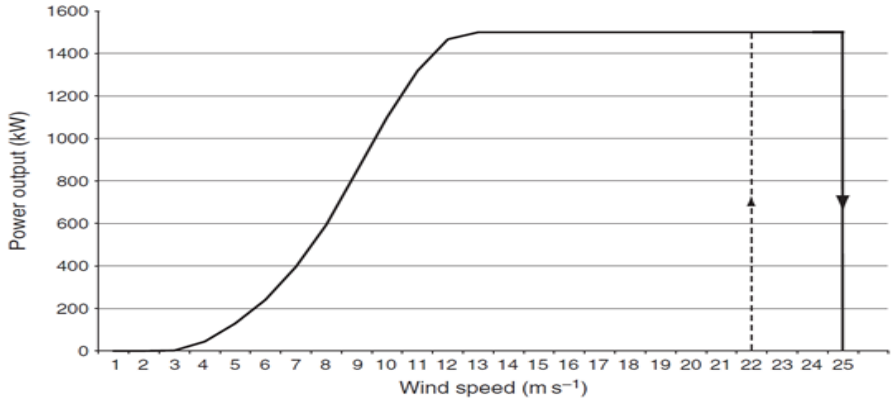

Fig 2.11: Typical power curve with cut-out of 25m/s [86]

If the torque T_m is to be applied instead of the power P_m, it is conveniently calculated from the power P_m by using the turbine rotational speed ω_{turb}.

$$T_m = \frac{P_m}{\omega_{turb}} \tag{2.3}$$

Another commonly used term in the aerodynamics of wind turbines is the tip-speed ratio λ, which is defined by:

$$\lambda = \frac{\omega_{turb} R}{V_{Wind}} \tag{2.4}$$

where ω_{turb} is the rotational speed of the wind turbine shaft.

R=radius of the turbine blade, V_{Wind} = wind speed (m/s) λ is the tip-speed ratio, β is blade angle.

For an optimal operating point, the relationship between the power efficiency and the tip-speed ratio can be used. The optimal rotational speed for a specific wind speed depends on the turbine radius, R, which increases with the rated power of the turbine [96].

It follows from this that C_P can be expressed as a function of β and λ:

$$C_p = \mathrm{f}_{\mathrm{C_p}}(\lambda, \beta) \tag{2.5}$$

The general relations between wind speed and mechanical torque holds. This is derived from a simplified aerodynamic model. This simplified aerodynamic model is typically based on the aerodynamic power coefficient C_p (β, λ) provided by a standard aerodynamic program. Equation 2.3 can be rewritten as: [86]

$$T_m = \frac{1}{2} \frac{C_p(\lambda,\beta)}{\lambda} \rho \pi R^3 V_{wind}^2 \tag{2.6}$$

The mechanical power is calculated as

$$P_m = \frac{\rho}{2} C_p(\boldsymbol{\lambda}, \beta) A V_{wind}^3 \tag{2.7}$$

T_m is the mechanical torque of the turbine (Nm), P_m is the mechanical power which represent the power extracted from the airflow (W).

The power coefficient C_p of the wind turbine in equation 2.5 is a function of tip-speed ratio λ which is given by equation 2.4. If the C_P- λ curve is known, it is easy to find the rotational speed of the wind turbine for any wind speed because the tip-speed will vary

proportional to the rotational speed assuming the wind speed is constant and the blade angle is fixed. For fixed speed wind turbine, the design is done is such a way as to make the rotational speed of the wind turbine to match the wind speed in that area of installation. In other word, it is not possible for a fixed speed to maintain operation with optimized power efficiency at any other wind.

In case of variable wind turbines, rotational speed of the wind turbine is adjusted over a wide range of wind speed in such a way as to maintain tip-speed ratio at λ_{opt} (see Fig 2.12). Therefore the optimal operational point is as indicated in Fig 2.12 which is at point λ_{opt} . The optimal location is known by tracking the rotor speed to the point λ_{opt} . At this point, power efficiency is maximum and the mechanical power output of a variable speed turbine is higher than that of a similar fixed-speed turbine over a wide range of speed [86]. The curve of C_p against the rotational speed in Fig 2.13 shows that the C_p depends on the rotational speed, which can be known at a given wind speed [78],[98],[91].

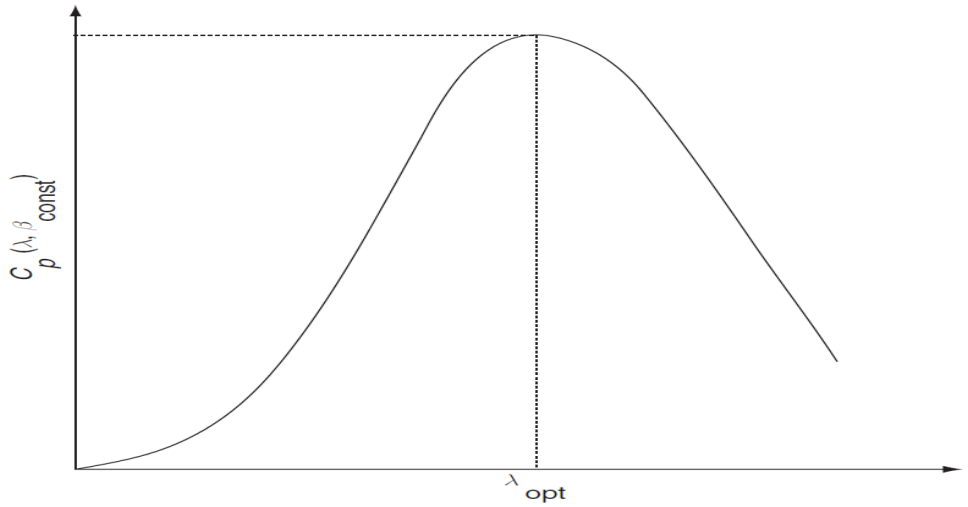

Fig 2.12: Power efficiency coefficient, C_P, for a fixed blade angle C_P as a function of tip-speed ratio, λ [86],[89]

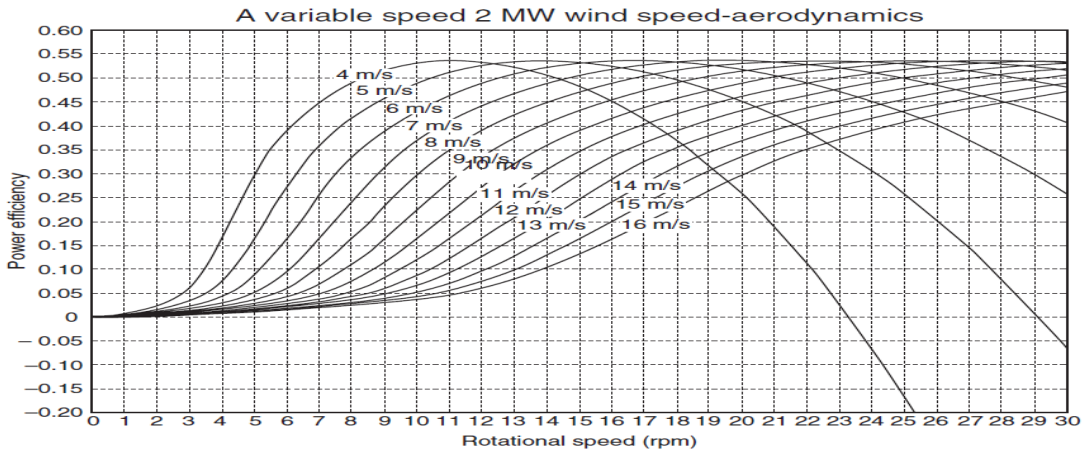

Fig 2.13: C_P as a function of rotational speed for various wind speeds (4-16m/s) [86],[91]

These two graphs (Fig 2.12, Fig 2.13) show clearly that the C_p depends on the tip-speed ratio and the rotational speed. The optimal rotational speed is a function of the tip-speed ratio and on the radius of the turbine blade. Fixed speed wind turbine has to be designed specially to suit the wind speed of the site, unlike variable speed wind turbine that has a varying rotational speed. In other word, variable speed wind turbine produces higher mechanical power output than the fixed speed wind turbine.

2.15.1 Modelling Doubly-Fed Induction Generator (DFIG) For Stability Studies

DFIG is widely preferred as the electrical generator for a wind turbine because of easy control and robustness. DFIG is a wound rotor induction generator with voltage source converter connected to the slip-rings of the rotor. DFIG interact with the grid through the rotor and stator terminal. The induction generator is connected to the grid through the stator terminals, but the rotor terminals are connected to the grid via a partial-load variable frequency AC/DC/AC converter (VFC) [89] as shown in Fig 2.14.

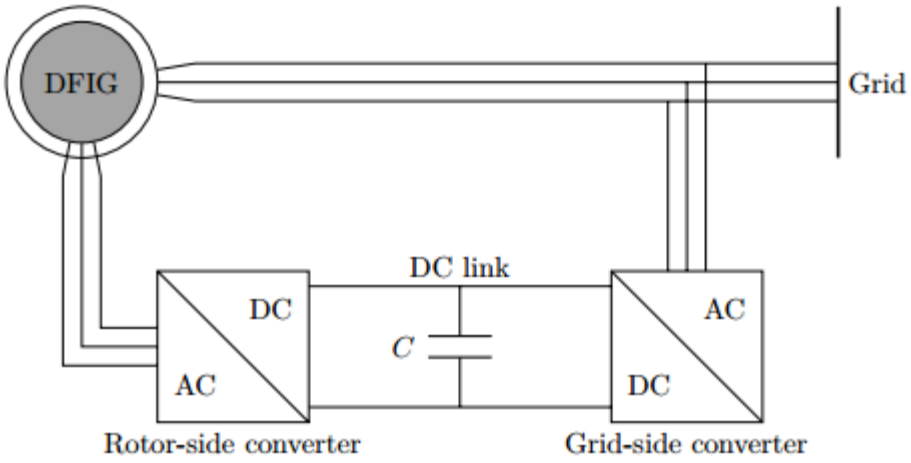

Fig 2.14: DFIG with its converter

Their control methodologies have been stall control or pitch control so as to limit the speed. Stall control is not an active control but pitch control and provides good power control performance, assisted start-up and emergency-stop power reduction. The focus is to develop very large wind turbine so as to reduce the dependence on conventional generators to a reasonable extent. It is also expected that the production of the low–power wind turbine will increase because of its application in distributed energy production in both grid-connected and stand-alone system wind plants, as well as in hybrid power system along with other types of generators. Active power of a variable-speed generator is controlled electronically by fast power electronics converters, which reduces the impact of wind-fluctuations to the grid. Additionally, frequency converters that are in use today (self-commutated PWM-converters) allow for reactive power control, where no additional reactive power compensation is required. To represent induction machine under system disturbance, it is desirable to use a double-cage model which represents transient and sub transient behaviour of the machine accurately [91],[92]. For modelling the DFIG converters it is assumed that the converters are ideal and the DC link voltage between the converters is constant. The rotor side converter is connected to the rotor of DFIG via brushes while the grid-side converter is connected to the grid. A capacitor is connected between the converters that act as DC voltage source. The DC voltage source decouples the rotor side converter from the grid-side converter. The rotor side converter is modelled as a voltage source whereas the grid-side converter is modelled as a current

source [94],[99]. The torque and the speed are controlled by the rotor side converter. The rotor speed is controlled by q-component of the injected voltage, through rotor side converter. The d-component of the rotor side converter voltage is used for compensation for the generator magnetizing reactive power. The main objective for the grid-side converter is to keep the dc-link voltage constant. In DFIG, the rotor side converter is controlled by using different control techniques such as scalar and vector controls. In scalar control, the torque and flux have a coupling effect while in vector control, the torque and flux has a decoupling effect.

The DFIG equipped with four-quadrant ac-to-ac converter increases the transient stability margin of the electric grids compared to the fixed-speed wind systems based squirrel-cage generators [100].

The stator and the rotor modelling of DFIG are given below:

$$u_{ds} = -R_s i_{ds} - \omega_s \psi_{qs} + \frac{d\psi_{ds}}{dt} \quad (2.8)$$

$$u_{qs} = -R_s i_{qs} + \omega_s \psi_{ds} + \frac{d\psi_{qs}}{dt} \quad (2.9)$$

$$u_{dr} = -R_r i_{dr} - s\omega_s \psi_{qr} + \frac{d\psi_{dr}}{dt} \quad (2.10)$$

$$u_{qs} = -R_r i_{qr} + s\omega_s \psi_{dr} + \frac{d\psi_{qr}}{dt} \quad (2.11)$$

where *s* is the slip, *u* is the voltage, *i* is the current, *R* is the resistance, and ψ is the flux, ω_s is the synchronous speed of the stator field. All quantities are measured in per unit. The subscripts d and q stand for direct and quadrature component, respectively while subscripts r and s stand for rotor and stator respectively.

The real and reactive power at the rotor and the stator can be calculated by:

$$P_s = u_{ds} i_{ds} + u_{qs} i_{qs} \quad (2.12)$$

$$Q_S = u_{qs} i_{ds} - u_{ds} i_{qs} \quad (2.13)$$

$$P_r = (u_{dr} i_{dr} + u_{qr} i_{qr}) \quad (2.14)$$

$$Q_r = (u_{qr} i_{dr} - u_{dr} i_{qr}) \quad (2.15)$$

For DFIG

$$P = P_s + P_r = u_{ds}i_{ds} + u_{qs}i_{qs} + u_{dr}i_{dr} + u_{qr}i_{qr} \quad (2.16)$$

$$Q = Q_s + Q_r = u_{qs}i_{ds} - u_{ds}i_{qs} + u_{qr}i_{dr} - u_{dr}i_{dr} \quad (2.17)$$

2.15.2 Modelling Synchronous Generator Wind Turbine

The two common types of synchronous generator wind turbines are the direct drive synchronous generator (DDSG) and the converter driven synchronous generator (CDSG). Direct drive synchronous generator is a high pole generator designed for low speed. The DDSG is shown in Fig 2.15.

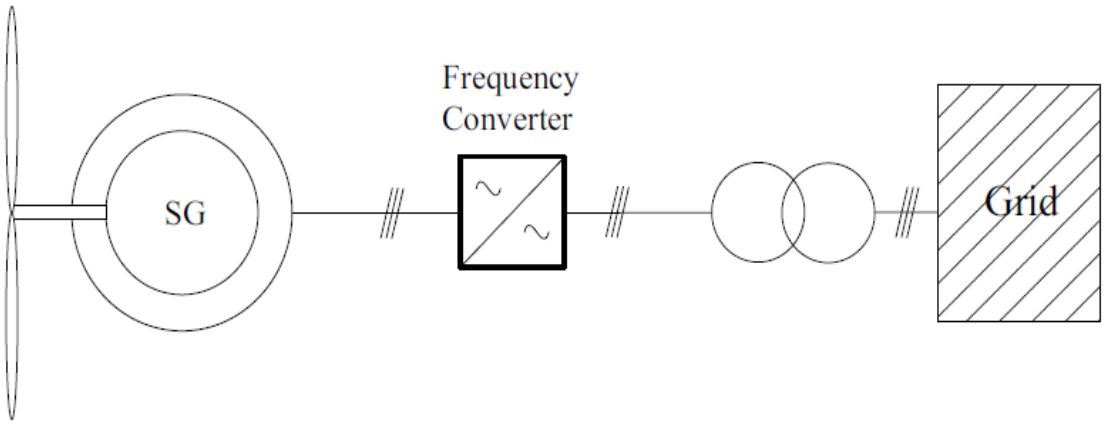

Fig 2.15: Direct- drive synchronous generator

Due to its large number of poles, it has a large size. The main advantages are:

- Wind turbines are gearless
- Excitation system is replaced by permanent magnets.
- Higher efficiency of permanent magnet synchronous generator (PMSG)
- Wide range of speed control in the PMSG.

Direct drive synchronous machine can be achieved either with a permanent magnet synchronous generator (PMSG) or a wound rotor synchronous generator (SG) with full scale power converters. The power converters allow easy control of the generator during grid integration. For these machines, the rotor model and the pitch angle controller are similar to that of DFIG. Only the converter and protection features are different [101], [102].

Fig 2.16 shows, the converter driven synchronous generator which incorporates a gear box and has a reduced number of poles. The gear box with low ratio is used in order to allow for lower number of poles and a smaller generator than in a pure direct drive wind generator. The converter driven synchronous performs almost in the same way as the DDSG from the electrical point of view. Some of the largest units currently available are built on the direct drive synchronous machine concept [101].

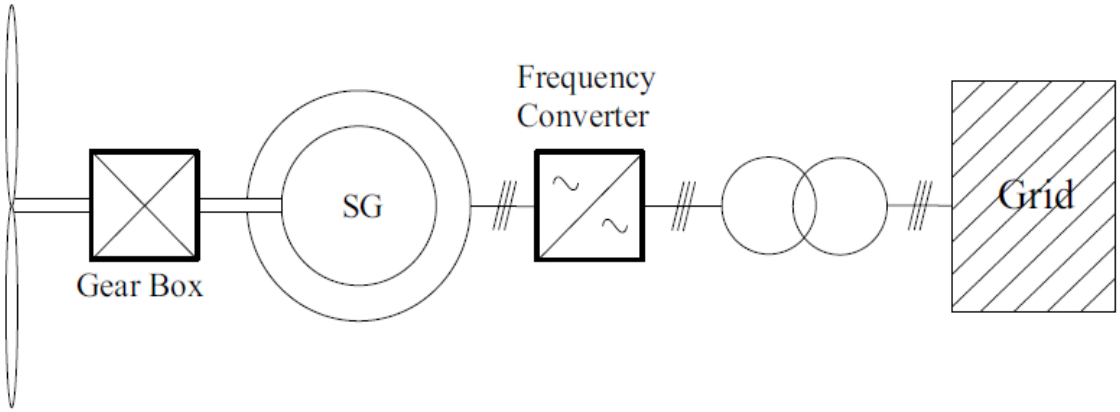

Fig 2.16: Converter- driven synchronous generator

The general structure of converter driven synchronous generator contains the pitch controlled wind turbine, the synchronous generator with full- scale power converters. The power converter comprises of two back-to-back pulse width modulated (PWM) voltage source converters (VSC) interconnected by a common DC bus. The converter is built on the concept of self-commutated pulse width modulation converters. An L-C filter is used to connect the converter to the grid [102].

The generator is made of a wound rotor synchronous generator and the voltage equations follow the general equations reported in [101],[96] as described in equations 2.18- 2.20. The assumption is that the magnetic flux distribution in the rotor is sinusoidal in order to allow vector modelling [103].

$$u_{ds} = -R_s i_{ds} - \omega_m \psi_{qs} + \frac{d\psi_{ds}}{dt} \quad (2.18)$$

$$u_{qs} = -R_s i_{qs} + \omega_m \psi_{ds} + \frac{d\psi_{qs}}{dt} \quad (2.19)$$

$$u_{fd} = R_{fd} i_{fd} + \frac{d\psi_{fd}}{dt} \quad (2.20)$$

The flux equations are:

$$\psi_{ds} = -(L_{dm} + L_{\sigma s}) i_{ds} + L_{dm} i_{fd} \quad (2.21)$$

$$\psi_{qs} = -\left(L_{qm} + L_{\sigma s}\right) i_{qs} \quad (2.22)$$

$$\psi_{fd} = L_{fd} i_{fd} \quad (2.23)$$

Where *fd* indicates the field quantities. For the 3rd order modelling, the quantities dψ /dt are neglected because the associated time constants are small and to avoid detailed representation of phenomenon that are not of interest thereby simplifying the equations [86].

In case of permanent magnet rotor the quantities u_{fd} and ψ_{fd} in equation 2.20 and equation 2.23 disappear because they refer to field quantities. Hence the equations 2.18- equation 2.20 are reduced when dψ /dt in the stator voltage equation is neglected. The reduced equations are:

$$u_{ds} = -R_s i_{ds} + \omega_m (L_{\sigma s} + L_{qm}) i_{qs} \quad (2.24)$$

$$u_{qs} = -R_s i_{qs} - \omega_m (L_{\sigma s} + L_{dm}) i_{ds} \quad (2.25)$$

$$u_{fd} = \quad R_{fd} i_{fd} + \frac{d\psi_{fd}}{dt} \quad (2.26)$$

R_{fd} is the field resistance, L_{dm} is the mutual inductance in d-axis, L_{qm} is the mutual inductance in q-axis, $L_{\sigma s}$ is the stator leakage inductance, L_{fd} is the field inductance and i_{fd} is the field current, ω_m is the angular synchronous speed of the rotor.

The electromagnetic torque can be calculated from this equation as well as the active and reactive power by:

$$T_e = \psi_{ds} i_{qs} - \psi_{qs} i_{ds} \quad (2.27)$$

where T_e is the electrical power.
The active and the reactive power released to the grid are calculated as:

$$P_s = u_{ds} i_{ds} + u_{qs} i_{qs} \quad (2.28)$$

$$Q_s = u_{qs} i_{ds} - u_{ds} i_{qs} \quad (2.29)$$

The integration through the power converters follows the same procedure with DFIG. It is integrated through vector control decoupled means. In the same way, the rotor side control the active and reactive power while the grid-side converter controls the voltage and the reactive power [104], [105]. In CDSG the generator is fully decoupled from the grid. The power factor of the generator does not affect the reactive power of the grid connection. The reactive power of the grid is affected by the converter.
The system is entirely built in order to extract the maximum power from the wind at a constant tip-speed.

The presence of the power converter allows DFIG a more versatile and flexible operation compared with a squirrel-cage induction machine. The power converter compensates for the difference between the mechanical and electrical frequency by injecting a rotor current with a variable frequency according to the shaft speed.
Two control levels which have different bandwidths and are strongly connected to each other, can be distinguished in the overall control system [99]:

- Doubly-fed induction generator control (control of active and reactive power)

- Wind turbine control

The DFIG control encompasses the electrical control of the power converters and of the doubly-fed induction generator. Since this controller is an electric one, it works very fast. The DFIG control level has as goal to control the active and reactive power of the wind turbine independently. The DFIG control contains two decoupled control channels: one for the rotor side converter and one for the grid side converter.

- **Rotor side converter and its control**

The rotor of DFIG is decoupled from the main grid through power converter. The rotor side converter allows the control of slip ring voltage of the generator in magnitude and phase angle. Thereby controls independently the active and reactive power in the measurement grid point, and therefore the stator flux oriented rotor current control approach is used. The rotor side converter control consists of two PI-control loops in cascade:

- A slower (outer) power control loop
- A very fast (inner) rotor current control loop

The power control loop controls the active and reactive power, while the fast current control loop regulates the machine's rotor currents to the reference values that are specified by the slower power controller [89].

The output of the PI controller are pulse-width modulation factor m_x and m_y defined in stator flux reference frame which are rotated back to the dq-reference frame to get m_d and m_q.

Let V_{DC} be the voltage of the DC –link.

m_d and m_q be the modulation depths set by the rotor side converter for d- and q components respectively.

The rotor voltage components are therefore set as [99]:

$$u_{rd} = m_d \frac{\sqrt{3}V_{DC}}{2\sqrt{2}} \tag{2.30}$$

$$u_{rq} = m_q \frac{\sqrt{3}V_{DC}}{2\sqrt{2}} \quad (2.31)$$

- **Controlling active power and reactive power**

From equation 2.28, the active power can be controlled by acting upon stator power but to control the active power by means of rotor currents, the stator active power can be rewritten as:

$$P_s = -\frac{X_m}{X_s}(u_{ds}i_{dr+}u_{qs}i_{qr}) \quad (2.32)$$

Where X_m is the mutual reactance and X_s is stator reactance, u_{ds} is the stator d-axis voltage, i_{dr} is the rotor d-axis current, u_{qs} is stator q-axis voltage, i_{qr} is the rotor q-axis current.

If the stator reactive power can be controlled, then the total reactive power is also controlled. However, the grid-side converter is controlled so as to maintain a constant voltage or controlled reactive power.

Using equation 2.29, the stator current can be transformed to the rotor current. The stator reactive power is then expressed as:

$$Q_s = -\frac{X_m}{X_s}(u_{ds}i_{qr} - u_{qs}i_{dr}) - \frac{1}{X_s}u_s^2 \quad (2.33)$$

The expression shows how stator voltage and the reactive power are tightly coupled. Either of these two values can be controlled.

The grid-side converter is controlled to prevent any flow of reactive power between the rotor and the grid. This expression (equation 2.34) is a simplification of equation 2.32 expressed in the stator flux reference frame. The two expressions above for reactive and active power can be simplified if the relation between stator voltage and stator flux is used. To simplify the relations between stator reactive and active powers, a new change of reference frame is generally applied. The new reference frame, called the xy-reference frame, has its x-axis aligned with the stator flux vector and its y-axis leading by 90 degree. In the new reference frame, equations 2.32 -2.33 become:

$$P_s = -\frac{X_m}{X_s} u_s i_{yr} \tag{2.34}$$

Stator reactive power is

$$Q_s = -\frac{X_m}{X_s} u_s i_{xr} - \frac{1}{X_s} u_s^2 \tag{2.35}$$

where i_{yr} and i_{xr} are x and y component of the rotor current.

In the stator flux reference frame, active power is controlled by using the y component of the rotor current and reactive power by acting on the x-component of the rotor current [106].

- **Grid-Side Converter and its control**

The grid-side converter of DFIG usually regulates DC-voltage and reactive power. The aim of the control of the grid side converter is to maintain the dc-link capacitor voltage in a set value regardless of the magnitude and the direction of the rotor power and to guarantee a converter operation with unity power factor (zero reactive power). This means that the grid side converter exchanges only active power with the grid, and therefore the transmission of reactive power from DFIG to the grid is done only through the stator [99].

The stator-side controller operates in a stator-voltage oriented reference frame, in which the d-axis represents the active component and q-axis the reactive component. The dc-voltage and the reactive power are controlled indirectly by controlling the grid-side converter current.

However, the PI control loops is cascaded and can be used to explain the operation of grid-side converter. PI comprises of:

• A slower (outer) DC-voltage control loop

• A very fast (inner) converter current control.

As usual, the reference voltage is regulated by the DC- voltage control loop and the reference current is regulated by the fast converter current control. As a result of this decoupling, the d-axis converter current component is used to control the DC voltage while the q-axis converter current is used to control the reactive power [99].

2.16 Solar Photovoltaic (PV)

2.16.1 Overview of Solar Photovoltaic (PV)

Solar photovoltaic (PV) arrays convert solar radiation into direct current electricity. Solar PV is increasing across the globe with total global operating capacity reaching 100GW in 2012. The installed capacity varies from country to country but the leading countries in number of solar PV capacity are Germany, Italy, China, USA, and Japan. Germany has a total capacity of 32.4GW as at 2012 [88]. Across the globe, solar PV projects continue to increase and in USA, a total of eight states have already established policies to encourage community solar PV project by 2012. Off-grid projects represent a large number of this solar PV project in most developing countries but the focus has been shifted to grid-connected [88].

Presently material used for photovoltaic includes monocrystalline silicon, polycrystalline silicon, micro crystalline silicon, cadmium telluride, and copper indium selenide /sulphide [96], [107]. Solar PV can operate over several years with little maintenance or intervention after their initial set-up. A grid-connected solar PV system can be used locally thereby reducing transmission and distribution losses. Though solar power is attractive, its deployment is more expensive and its energy generation needs to be backed up by some form of storage due to the stochastic nature of solar energy. If properly designed and implemented, grid-connected solar PV systems can be immensely helpful in solving the problem of load shedding during peak load hours. Due to the numerous advantages eight countries in Europe, three in Asia, the USA and Australia had at least 1GW of total capacity. However, integrating solar PV could create transient stability problems because of its stochastic nature and the behaviour of power electronic interface devices. Due to this, current research interest is also diverted toward solar PV so as to

investigate its inherent characteristics and possible stability problems when large and small disturbances are applied. Some of the major advantages of solar PV are as follows:

- Short lead time to design, install, and start up a new plant.
- Highly modular, hence, the plant economy is not a strong function of size.
- Power output matches very well with peak load demands.
- Static structure, no moving parts, hence, no noise.
- High power capability per unit of weight.
- Longer life span with little maintenance.
- Highly mobile and portable because of light weight.

The disadvantage is the high cost of production and installation. However, over two decades now the production cost has dramatically reduced. It is clear that the cost of solar PV will continue to reduce in the near future. Continuing development has resulted in many solar PV technologies in the market today. These include [96],[107]:

- Single-Crystalline Silicon
- Polycrystalline and Semi crystalline
- Thin Films
- Amorphous Silicon
- Spheral
- Concentrated Cells

Generally solar resources are better correlated to the load than wind. This has two important consequences that will be discussed below.

- Solar generation is easier to integrate into the system than wind generation because of its lesser impact on the incremental variability of net load compared to the variability of load alone.
- Solar generation has higher value to the system than wind because of its availability during periods of higher load demand. Compared to wind, solar PV displaces more expensive generation [96],[107].

2.16.2 Modelling of Solar PV

Generally the modelling of solar PV systems has been based on series and parallel connection of cells. The cells are initially connected in series to generate appropriate 12V encapsulated into modules. The modules can be joined together in parallel to generate voltage that will be sufficient for various applications. Solar cells are basically a p-n junction fabricated in a thin wafer or layer of a semiconductor. The physics of solar cell is based on the semi-conductor PN junction [96]. However, the non-linear complex solar PV module is represented by an equivalent electrical circuit [107]. There are many equivalent circuits of solar PV in literature such as single diode equivalent circuit; the double diode equivalent circuit etc.

The double diode equivalent circuit is shown in Fig 2.17. The equivalent circuit comprises of two diodes. The first one represents the recombination in the base and the emitter region while the second one represents the recombination in the space charge region [107]. In a conductive, doped semiconductor, the space region represents a region of empty mobile charges or an area where the mobile charge carriers have been diffused away by an electric field. The only elements left in the depletion region are ionized donor or acceptor impurities. The two-diode allows detailed description of the recombination process of charge carrier both on the surface and in the bulk material.

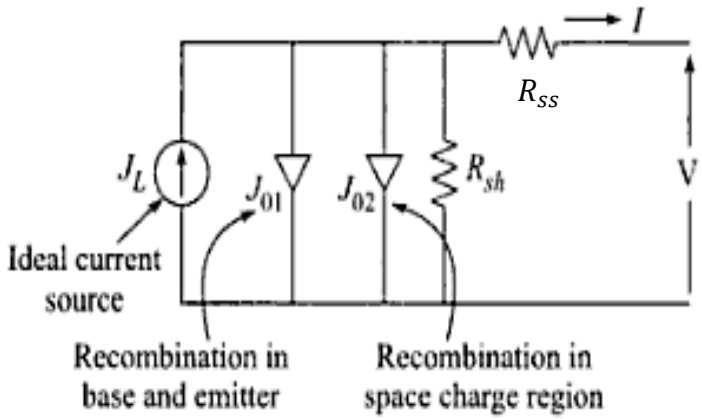

Fig 2.17: Equivalent circuit of a P-N junction solar cell

However, the most commonly used equivalent circuit is the single diode equivalent circuit as shown in Fig 2.18. A single-diode model presents a good compromise between

simplicity and accuracy [108]. The simplicity of the single-diode offers an easy way of adjusting the basic parameters such as I_p I_o R_{ss} R_{sh} and α_{th} (shown in equations 2.36 and equation 2.38).

This is the most common used model when predicting the energy production of solar PV [109]. For simplicity, the shunt resistance is generally neglected and the series resistance is used in the calculation. In the single diode model, there is a current source parallel to a diode. The current source represents light-generated current I_P that varies linearly with solar irradiation. The equivalent circuit in Fig 2.18 is used in this thesis.

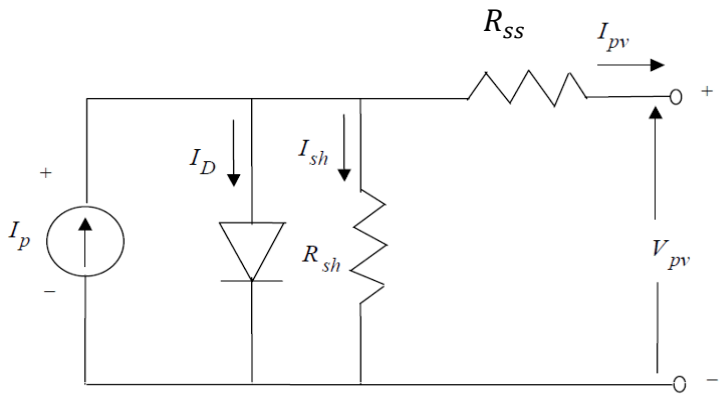

Fig 2.18: Equivalent circuit of a single lumped circuit solar cell

Fig 2.18 comprises of solar cells represented by an ideal current source, even though, in practice, the ideal situation is not attainable. There are two resistances: a series resistance R_{ss} and the shunt resistance R_{sh} connected into the equivalent circuit and they are responsible for the ohmic losses. The series resistance is the resistance of the cell material to current flow while the shunt resistance is referred to as the leakage path of the current in the solar cell. Series and parallel resistance reduce the fill factor. The efficiency can be increased when the value of the series resistance is decreased and the shunt resistance is increased [107], [110]. .

In Fig 2.18, the output terminal of the circuits is connected to the load. The output current source is the different between the photocurrent I_p and the normal diode current I_D. The voltage (V) and current output (I) have a non-linear relationship. For an ideal solar cell the mathematical equations describing the V-I characteristic are:

$$I_{pv} = I_p - I_D = I_p - I_o[\exp\left(\frac{V_{pv}+iR_{ss}}{mKT_c}\right) - 1] \quad (2.36)$$

where I_{pv} is the load current (in amperes),

I_p is the photocurrent of the solar PV cell (in amperes),

I_o is the saturation current, and

I_D is the diode current

V_{pv} is the solar PV output voltage (in volts),

R_{ss} is the series resistance of the solar PV cell (in ohms)

and *m*, *K* and *Tc* represent the diode quality constant, Boltzmann's constant and temperature respectively.

The power output of a solar cell is given by [110].

$$P_{pv} = V_{pv}\, I_{pv} \quad (2.37)$$

where P_{pv} is the output power of solar cell (W).

The output power depends on the temperature and the irradiance. The dependence of power generated by a solar PV array can readily be seen in the current-voltage (I-V) and the power-voltage (P-V) characteristics of solar PV arrays.

The value of the thermal voltage timing completion factor depends on the ambient temperature and can be defined from this relation.

$$\alpha_{th} = \mathrm{mkT_c} \quad (2.38)$$

where α_{th} = thermal voltage timing completion factor (V).

α_{th} is given as:

$$\alpha_{th} = \frac{\mathrm{T_c}+273}{\mathrm{T_{c,ref}}+273}\,\alpha_{\mathrm{ref}} \quad (2.39)$$

However,

α_{ref} can be calculated as:

$$\alpha_{ref} = \frac{2V_{mp,ref} - V_{oc,ref}}{\frac{I_{SC,ref}}{I_{SC,ref} - I_{mp,ref}} + \ln\left(\frac{1 - I_{mp,ref}}{I_{SC,ref}}\right)} \quad (2.40)$$

where $V_{mp,ref}$= maximum power point voltage at the reference condition (V);

$I_{mp,ref}$ = maximum power point current at the reference condition (A);

$I_{SC,ref}$= short circuit current at the reference condition (A).

The value of series resistance can be derived from the equation if it was not provided by the manufacturer.

$$R_{ss} = \frac{\alpha_{ref}\ln\left(1-\frac{I_{mp,ref}}{I_{SC,ref}}\right)+V_{oc,ref}-V_{mp,ref}}{I_{SC,ref}} \quad (2.41)$$

The saturation current I_o is also derived from the equation:

$$I_o = I_{o,ref}\left(\frac{T_{c,ref}+273}{T_c+273}\right)^3 \exp\left[\frac{e_{gap}N_s}{q\alpha_{ref}}\left(1 - \frac{T_{c.ref}+273}{T_c+273}\right)\right] \quad (2.42)$$

where $I_{o,ref}$ = saturation current at the reference condition (A);

e_{gap} = band gap of the material (1.17 eV for Si materials);

N_s= number of cells in series of a solar PV module;

q = charge of an electron (1.60217733×10-19 C);

α_{ref}= the value of α at the reference condition.[111]

$I_{o,ref}$ is given by:

$$I_{o,ref} = I_{pv,ref}\exp\left(-\frac{V_{oc,ref}}{\alpha_{ref}}\right) \quad (2.43)$$

Where $V_{oc,ref}$= the open circuit voltage of the solar PV module at reference condition (V) and this can be read from the data sheet.

The load current also known as the I_{pv} is

$$I_{pv} = \frac{\phi}{\phi_{\mathrm{ref}}}\left[\mathrm{I_{pv,ref}} + \mu_{\mathrm{I,sc}}\left(\mathrm{T_c} - \mathrm{T_{c,ref}}\right)\right] \quad (2.44)$$

where ϕ = irradiance (W/m2);

ϕ_{ref}= reference irradiance (1000 W/m2 is used in this study);

$I_{pv,ref}$ = light current at the reference condition (1000W/m^2 and 25 °C);

T_c= solar PV cell temperature (°C)

$T_{c,ref}$ = reference temperature (25 ° .0.C is used in this study);

$\mu_{I,sc}$ = temperature coefficient of the short-circuit current (A/°C).

Both $I_{pv,ref}$ and $\mu_{\mathrm{I,sc}}$ can be obtained from manufacturer data sheet.

Solar cell temperature increases with temperature and irradiance. Thermal temperature can be calculated as:

$$C_{PV}\frac{dT_c}{dt} = k_{in,PV}\phi - \eta\phi - k_{loss}(T_c - T_a) \quad (2.45)$$

where C_{PV} = the overall heat capacity per unit area of the solar PV cell/module [J/(°C·m^2)];

$k_{in,PV}$= transmittance-absorption product of solar PV cells;

k_{loss}= overall heat loss coefficient [W/(°C·m^2)];

T_a = ambient temperature (°C)

η = Efficiency of the solar PV

It is essential therefore to track the power of the system since the maximum power output of the solar PV array varies with solar radiation or load current [112].

2.17 Overview of Small Hydropower System

A hydropower system utilizes the natural or artificial fall of water to produce electricity. It is the oldest energy source but it has received a renewed interest because of the numerous benefits it offers. The renewed interest is because it is a clean energy, renewable and friendly to the environment. The main disadvantage of the hydropower system is ecosystem damage. The total global installed capacity was 990 GW as at 2012.

China, Brazil, USA, Canada, and Russia are the leading countries for hydro. China has an installed capacity of 229 GW and despite this large installed capacity; their projected vision by 2015 is to reach 290GW. In Africa, the Grand Renaissance Dam in Ethiopia will be the largest hydropower in Africa with the capacity of 6,000 MW [88]. At present, hydropower contributes the largest portion (about 85%) of the total power generated from renewable [113].

There are different sizes of hydropower namely: pico, micro, mini and small scale hydropower. The rating of the different sizes of hydropower stations is given below:

- Pico hydro from few hundred Watts up to 5kW
- Micro hydro from 5kW to up to 100kW
- Mini hydro above 100kW but below 1MW
- Small scale hydro: 1-15 MW.
- Medium scale hydro: 15-100 MW
- Large scale hydro more than 100MW.

The small hydropower system is preferred for distributed generation compared with other non-renewable sources because:

- It does not contribute to environmental damages by resettlement
- It can be used as a decentralized, low-cost and reliable form of energy.
- It saves the consumption of fossil fuel, and firewood.
- It is self-sufficient without the need of fossil fuel importation.

Small scale hydropower is cost effective and it provides reliable energy and clean electricity generation. It is based on 'run-of river' where there is only a small dam and little or no storage. Therefore, it has a reduced adverse effect on the environment compared to large scale hydropower.

2.17.1 The Concept of Small Hydropower (SHP)

The water is first fed into a forebay tank or storage. An enlarged forebay tank is called a reservoir. The pressurized water in the forebay tank flows through a penstock and comes out from the nozzle of a high pressure jet. The water from the nozzle through the pressure falls on the runner. The runner rotates and converts the power from the nozzle. This

process is the conversion of hydropower to mechanical power as shown in Fig 2.19. The runner spins 1500 times per minute and is responsible to drive the generator. The generator converts the mechanical power to electrical power.

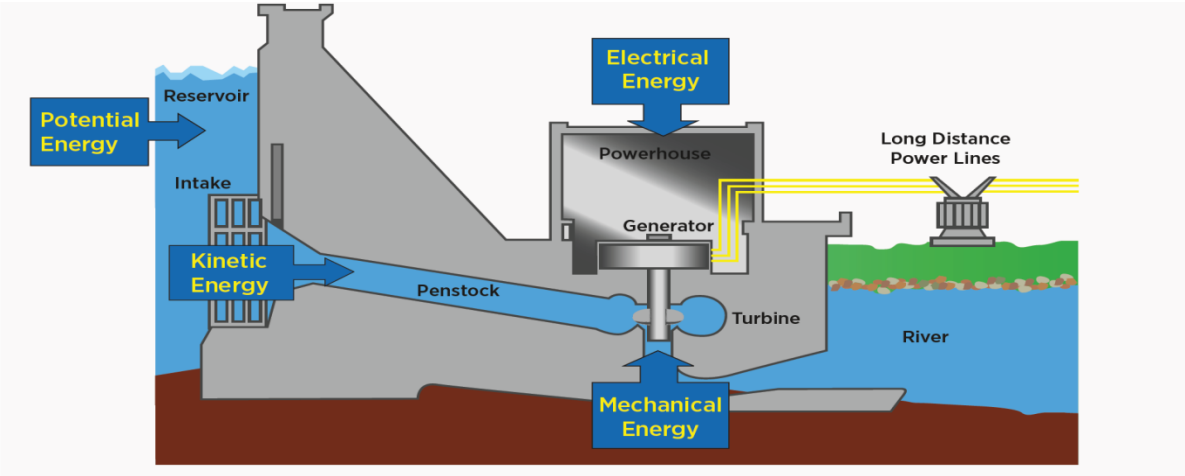

Fig 2.19: Typical "low head" hydropower plant with storage [114]

(Picture adapted from hydropower news and information (hTTp://www.alTernaTive-energy-news.info/Technology/hydro/

In a river, the available potential energy or gross head will be converted in a system through the following components:

Reservoir: It constitutes a storage form of the available potential energy and creates the conditions for water diversion through the intake.

Conveyance system: It includes the intake, conveyance canal, penstock, galleries and tailrace or outlet where part of the available energy is converted into kinetic energy, another part is transformed into reversible flow work capacity (pressure head) and another part is dissipated as heat (by fluid viscosity) resulting in the net or useful head.

Hydraulic turbine: This is where the net head is converted into rotor speed of the turbo-machine [115].

Generator rotor: The mechanical energy on the shaft maintains the speed of the rotor and it is transformed into electric energy according to electromagnetic laws [115].

2.17.2 The Small Hydro Turbine

A hydro turbine converts the energy in falling water into shaft power. Turbines are mainly divided into two basic types: impulse turbines and reaction turbines. The impulse turbines are mainly used in high head plants. In this type of turbine, the entire pressure of water is converter into kinetic energy in a nozzle. They rely on the velocity of water to move the turbine wheel. Examples are Pelton and Turgo etc,. [116]. The reaction turbines are mainly for low and medium head plants. Reaction turbines depend on pressure rather than velocity to produce energy. The entire blade maintains constant contact with water.

Reaction turbines are mainly used in large- scale hydropower sites except propellers and Kaplan turbines which can be used for micro hydro sites [116].
Based on the head pressure, the turbine runner can be categorised into high, medium and low. Table 2.3 gives the summary of the two turbines.
Table 2.3: Categorization of turbine runner [117]

	High	**Medium**	**Low**
Impulse Turbines	Pelton, Turgo, multi-jet pelton	Cross flow, Turgo, Multi-jet Pelton	cross flow
Reaction Turbines	-	Francis	Propeller, Kaplan

The Francis turbine is for head up to 360m and can be used for a wide range of head and flow rates while the propeller is for head pressure up to 45m. The Francis turbine is common while the Keplan turbine that was derived from the Francis turbine is also efficient and can operate at head pressure between 10m and 70m. In the categories of impulse turbine, Pelton is also widely used with high head pressure [114].

Generally for a short penstock, the representation of the hydraulic turbine and water column in stability studies is based on the following assumptions.

- The hydraulic resistance is negligible.
- The penstock pipe is inelastic and the water is incompressible.

- The velocity of the water varies directly with the gate opening and with the square root of the net head.
- The turbine output power is proportional to the product of head and volume flow.

The velocity of the water in the penstock is given by:

$$v = K_u G \sqrt{h_w} \tag{2.46}$$

where,

v= water velocity in m/s

G= gate position

h_w= effective pressure head of water across the turbine (m).

K_u= a constant of proportionality

The acceleration of water column can be calculated from

$$\left(\rho_w L A_p\right) \frac{d\Delta v}{dt} = -A_p(\rho_w g)\Delta h_w \tag{2.47}$$

where,

ρ_w= density of water (1000 kg/m^3)

L=length of conduit (m)

A_p= pipe area (m^2)

$\rho_w L A_p$=mass of water in the conduit (kg)

g = acceleration due to gravity (9.81 m/s^2),

$(\rho_w g)\Delta h_w$= incremental change in pressure at turbine gate

$\frac{d}{dt}$ is the per unit time derivative

The general formula for calculating the mechanical power of the turbine is:

$$\mathrm{P_{hyd}} = \rho\, g Q_w h_w \tag{2.48}$$

$$Q_w = A_w v_w \tag{2.49}$$

where, $\mathrm{P_{hyd}}$ is the hydraulic power produced at the turbine shaft (Watts),

ρ is the density of water

$Q_w$is the water flow rate passing through the turbine (m^3/s).

The relation between the mechanical and the hydraulic powers can be obtained by using hydraulic turbine efficiency η_t, as expressed by the following equation:

$$P_m = \eta_t \, P_{hyd} \tag{2.50}$$

where,

P_m is the turbine mechanical power

The whole equation is derived from Bernoulli's theorem given in equation 2.51 [118]

$$\frac{v^2}{2g} + h_w + \frac{p}{\rho g} = \frac{P_{hyd}}{\rho g Q} \tag{2.51}$$

p is the pressure of water (N/m^2)

2.18 Structural Configuration and Operation of Hybrid Distributed Generation

There are two major ways of configuring hybrid energy sources into the grid: AC couplings and DC couplings as shown in Fig 2.20 and Fig 2.21, respectively. Solar PV generates a DC voltage which can only drive DC loads. There is a need to convert the DC voltage to AC voltage to power the AC loads as shown in Fig 2.20. In this case an inverter is used to connect to an AC and connect to AC bus. In case of wind generator and small hydropower, they are connected directly to the AC bus while conversion into DC voltage through a rectifier is needed to connect it to a DC bus as shown in Fig 2.21.

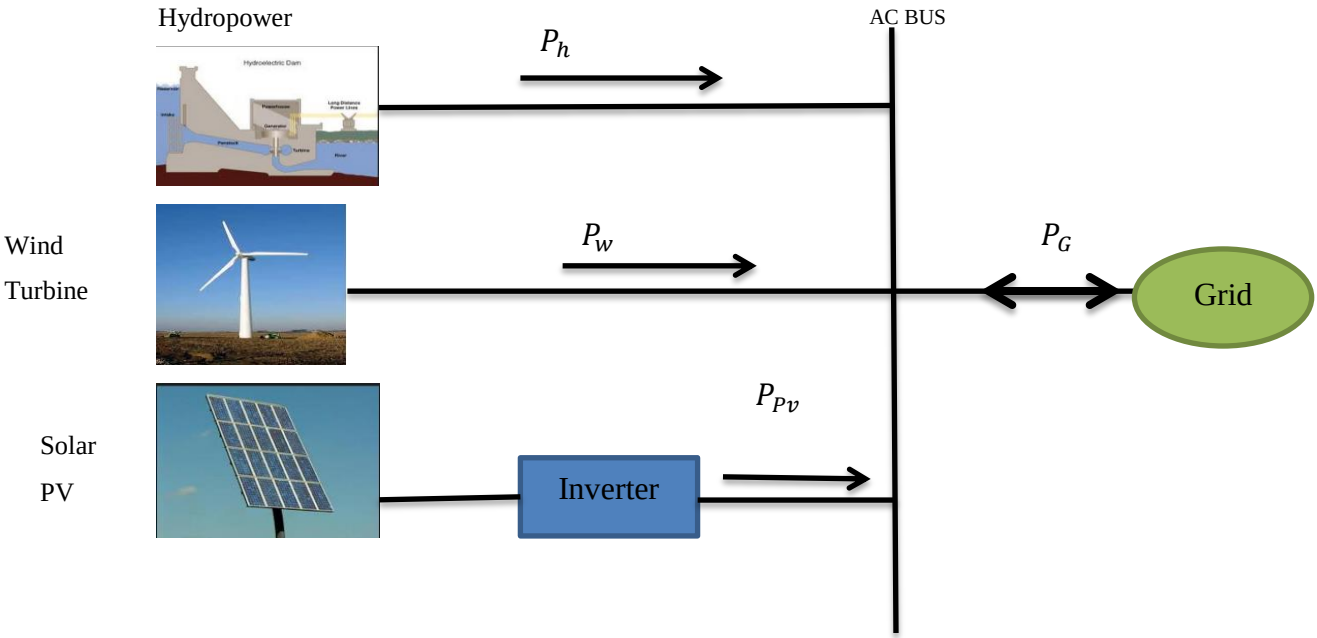

Fig 2.20: Hybrid distributed generation integration: AC Coupling

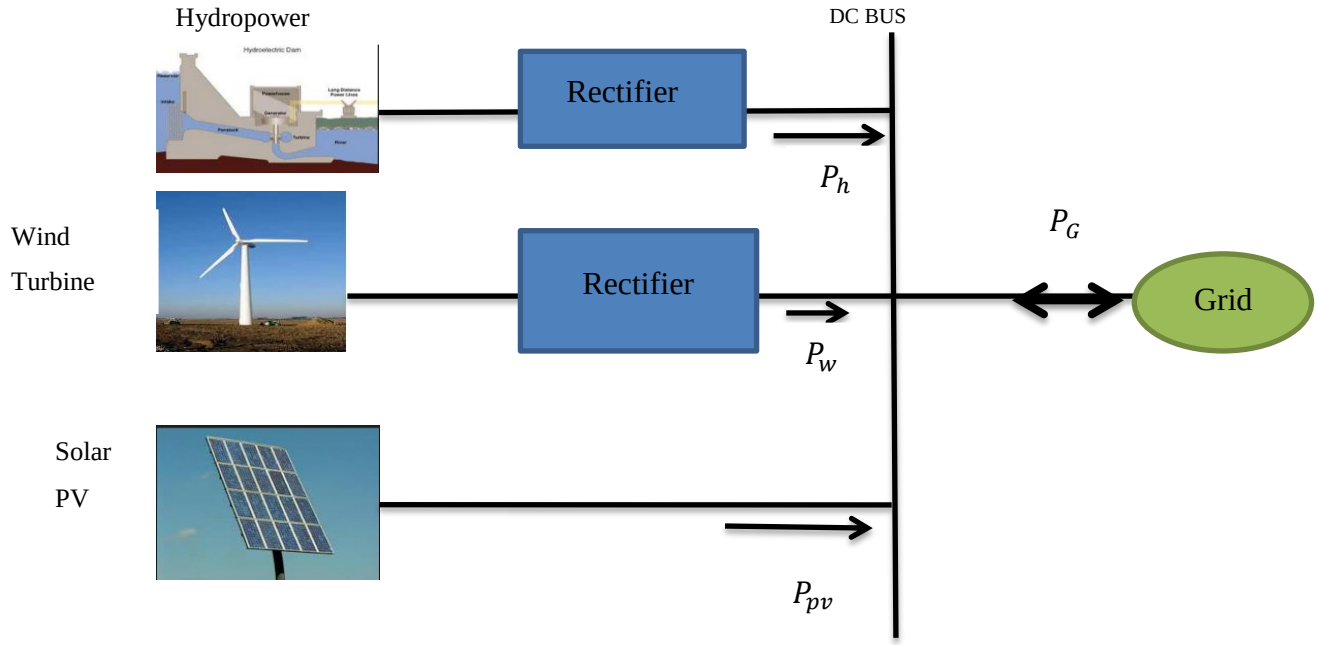

Fig 2.21: Hybrid distributed generation integration: DC Coupling

In the above Figs 2.20 and 2.21, P_h is power from hydropower, P_w is power from the wind and P_{pv} is power from solar PV.

In DC coupling configuration the DC load can be connected directly. DC coupling seems to be the oldest type of integration and it enhances easy integration but is expensive to maintain or install due to additional power electronic devices. The most cost-effective configuration with high reliability and easy grid integration is the AC coupling. The AC coupling configuration is used in this work.

Chapter 3

Overview of Computational Intelligence Approaches

Computational intelligence (CI) approaches can be used in modelling to solve complex problems that cannot be modelled by analytical approach. The main purpose of using CI in modelling (or system identification) is to identify a model of unknown plant so as to predict the behaviour of the plant [119]. Besides, mathematical model is not accurate enough to define most dynamic processes or the inherent non-linearity of most dynamics system is difficult to be represented by mathematical model such as transfer function. The importance of CI techniques over the analytical mathematical modelling is that they can model any events using data even if there is no established mathematical equations and give the result of prediction timely [119]. In most case, modelling reductions or assumptions are made in order to solve real time transient stability problems analytically [120]. Such assumptions or reductions can lead to decision making that negatively affects the operation of power system or lead to false alarm during power system operation. Besides, CI techniques can handle large volume of data without any prior knowledge of the mathematical equations and perform step-ahead prediction timely and accurately. This section explains the computational intelligence paradigms, modelling capability and their applications in stability studies. Application of CI techniques can be found in pattern recognition, identification, classification, optimisation and control systems [28],[29],[43] etc. They also facilitates intelligent behaviour in complex adaptive system, under semi-autonomous distributed control and handle a lot of uncertainties [53]. These adaptive mechanisms include intelligence paradigms that can learn, generalize and adapt into a changing environment.

3.1 Computational Intelligence Methods for Dynamic Modelling

Computational intelligence (CI) is the study of adaptive mechanism to enable or facilitate intelligent behaviour in complex, uncertain and changing environments. These adaptive mechanisms include artificial intelligence paradigms that exhibit the ability to learn or adapt to new situations, to generalize, abstract, discover and associate [29], [44],[53],[122]. The various types of CI paradigms are:

- Artificial Neural Networks (ANN)
- Swarm Intelligence (SI)
- Evolutionary Computing (EC)
- Fuzzy System (FS)
- Artificial Immune System (AIS).

Each of these CI paradigms has its origins in biological systems. Artificial Neural Networks (ANNs) model the biological network, SI models the social behaviour of organism living in swarms or colonies, EC model natural evolution (including genetic and behavioral evolution), FS originates from studies of how organisms interact with their environment and AIS models the human immune system [123], [124]. The typical CI paradigms and their possible hybrid systems are illustrated in Fig 3.1. These paradigms can be combined to form hybrids such as Neuro-Fuzzy systems, Neuro-Swarm systems, Fuzzy-PSO systems, Fuzzy-GA systems, Neuro-Genetic systems, etc. CI can be used to solve real- life problems e.g., real time transient stability assessment. Some of the advantages of CI techniques are:

- CI techniques have the potential to stimulate transient stability assessment faster than analytical methods.
- CI techniques take advantages of exhaustive offline studies to uncover the inherent system attributes related to the objective and provide accurate and fast prediction models for online application using real time measurements.

The CI methods used in this research are Artificial Neural Networks such as Multilayer Neural Networks, Recurrent Neural Networks, Generalized Regression Neural Networks, Radial basis function Neural Networks and Self Organizing feature map.

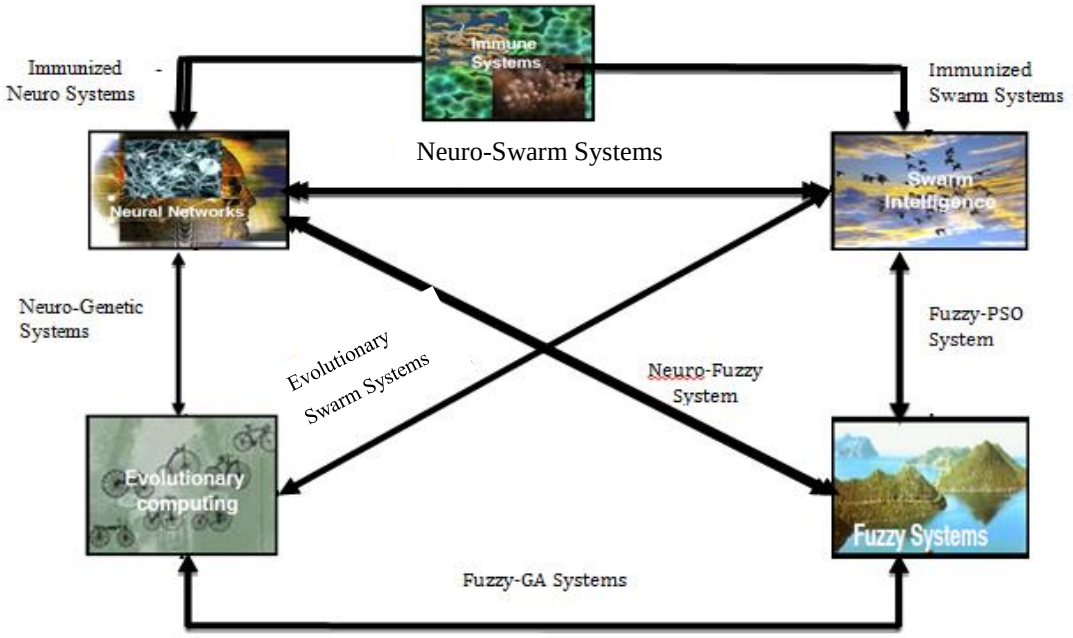

Fig 3.1: Five main CI paradigms and typical hybrids [44]

3.1.1 Artificial Neural Networks (ANNs)

Artificial Neural networks are composed of massively connected simple neurons with similar structures to their biological counterparts. Just as power system networks are made up of thousands of components interconnected together, the brain also is made of 10- 500 billion neurons connected together with 60 trillion synapses [44]. The nerve cell is the basic building block of the biological neural system comprising of dendrites, axon and cell body as shown in Fig 3.2. The interconnection of one neuron to another is through the synapse while axon transfers the signal to all other dendrites. The axon receives a transmitted signal only when the neurons have been fired. ANN is modelled in

the form of biological neuron receiving signal from the environment and transmit it to all connected ANNs. Fig 3.2 represents an artificial neural network or artificial neuron [44].

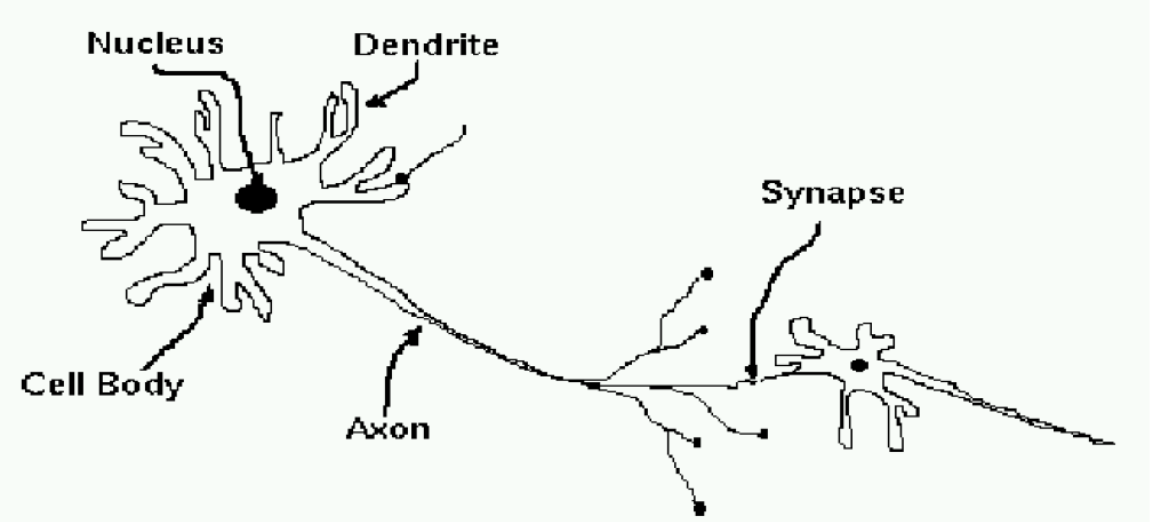

Fig 3.2: Biological Neuron [44]

The brain has the ability to perform pattern recognition, matching and associative etc. Artificial Neural Networks (ANNs) are the artificial modelling of the brain. ANN is modelled to perform the same task as the brain. In other word, ANNs are computational modelling tools used in science and engineering for modeling complex-world problems. They simulate human intuition in making decisions and drawing conclusions in even when presented with complex, noisy, irrelevant and partial information. In some applications, such as in power system stability studies, they are trained using input data to classify system stability into a stable or unstable state. The elementary processing unit in a neural network is a neuron. All neural networks which have been proposed over the years share this common building block [125]. The basic structure of ANN is shown in Fig 3.3 [35],[44]. It consists of input vector (X_1, X_2, X_3, X_4), hidden neurons, weights (w), transfer function and the outputs. The product of the input and the weight forms the weighted input. The transfer net uses the weighted input to produce the output. The output of the unit is a function of the sum value as shown in equations 3.1. The transfer function could be linear sigmoid, bipolar sigmoid, hyperbolic tangent, etc. [53]. The weight and the bias are not constant but vary and can be modified or adjusted to follow the desired behaviour. But in most cases the bias *(b)* used is assumed to be 1.

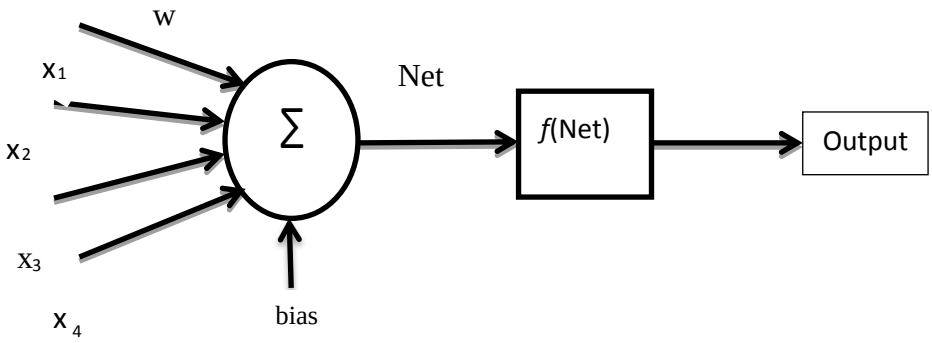

Fig 3.3: Single neuron structure [35]

Mathematically,

$$wx + b = output \tag{3.1}$$

where *x* is the input data and the output can be any signal or quantity of interest. In this thesis, rotor angle, or Critical Clearing Time (CCT) are used as outputs.

ANNs are trained with specific data sets until they learn pattern used as inputs to perform a specific task.

Learning in Artificial Neural Networks can be implemented in two ways, i.e. batch mode and online mode. Batch mode means to train the model on the entire sequence adapting the parameters only once while online learning means that learning can be performed at the same time as the normal operation of the system, adapting the model at each step i.e., the weights and biases are updated each time an input is presented to it [44],[126]. Specific characteristics of ANNs are [125] :

- They can automatically learn to recognize patterns in data from real systems or from physical models, computer programs, or other sources.
- They can handle many inputs to produce answers that are suitable for designers.
- They can also work with numerical or analogue data that would be difficult to deal with by other means.

- They are robust even in the presence of noise in the input data. This makes them appropriate for online assessment and control system.
- Their high parallelism implies fast processing and hardware failure- tolerance.
- They can learn and adaptively allow the system to modify its internal structure in response to changing environment.

In addition to the above characteristics, neural networks have the following properties:

Non-linearity- Neural networks are made up of interconnected non-linear neurons that are distributed across the network. Most real systems are non-linear such as power system networks. This property enhances its usefulness in real time application**.**

Adaptivity: When Artificial Neural Networks are properly trained in a specific environment they can work in another environment and also adapt to changes in environment especially when the changes are minor**.** Adaptivity of the neuron is based on the synaptic weight adaptation using the training algorithm**.**

Fault-tolerance: Artificial Neural networks are inherently fault tolerant. Information in neural network is distributed and this makes it to build resistance to fault as result of missing data or erroneous data. The error must be enormous before catastrophic failure occurs [44].

3.1.2 Basis Categories of Artificial Neural Networks

Based on their structures, artificial neural networks can generally be grouped into two categories, namely

- Feed-forward neural networks.
- Recurrent Neural networks

Feed-forward neural networks are static because they produce only one set of output values rather than a sequence of values from a given points. They include single layer perceptron, multilayer perceptron and radial basis function nets, Kohonen's self-organized Map, etc.

Recurrent networks on the other hand are dynamic networks because their outputs doesn't only depend on the present inputs but also on the past inputs. They consist of Hopfield network, adaptive resonance theory (ART) models, Discrete-time recurrent neural

network, Elman recurrent neural networks and simultaneous recurrent neural networks (SRNs). They all have their strengths and weaknesses [118].

3.2 Learning Paradigm

An important issue worth mentioning is the training or learning process. Learning involves weights and bias update in order to find a point of minimum error at which the network output will be closer to the target. However, there are three basic classifications of learning, namely: Supervised learning, Unsupervised and Reinforcement learning. The taxonomy of the learning process is shown in Fig 3.4.

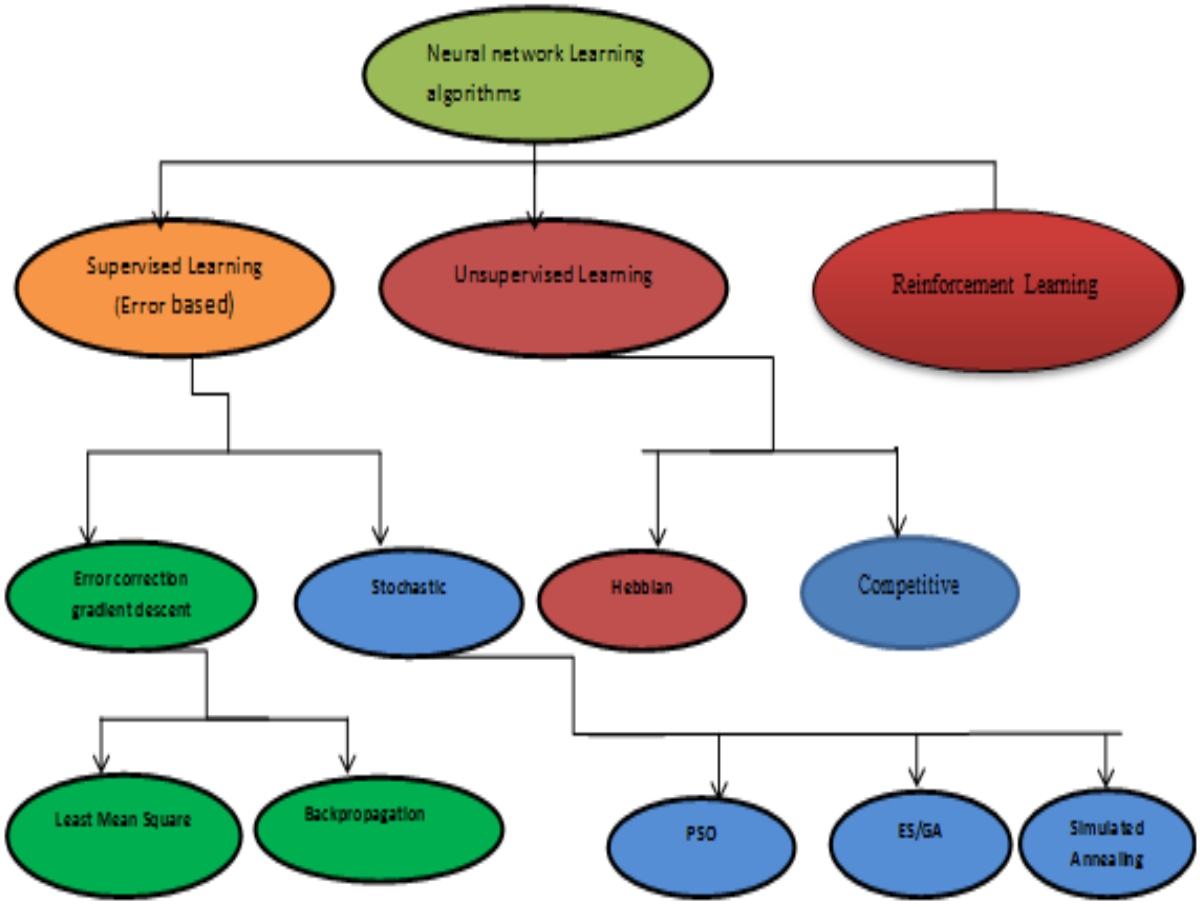

Fig 3.4: Taxonomy of learning process [44]

3.2.1 Supervised Learning

In supervised learning, the input is mapped into the desired target. This is called training with a teacher. In Fig 3.5, the ANNs output is compare with the actual target and the error is fed back to the system for training. This goes on step by step and the error reduces in succession.

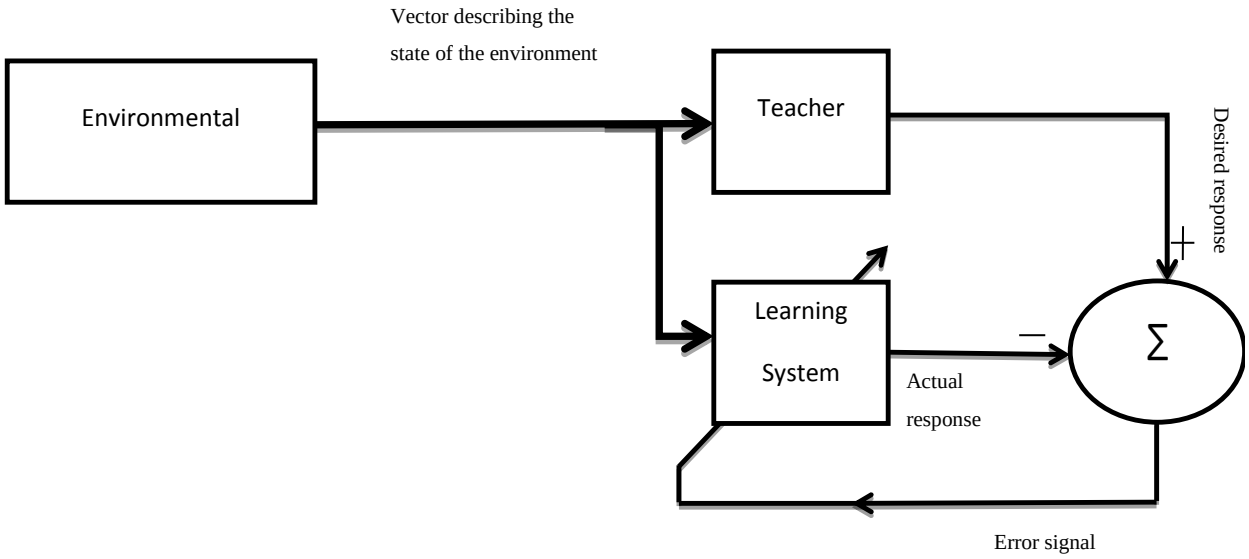

Fig 3.5: Diagram of supervised learning [42]

3.2.2 Unsupervised learning

In contrast to supervised learning, unsupervised learning involves training of the inputs to respond to cluster of patterns in the inputs. In this learning algorithm, there is no desire target, rather the system develop its own representation of the input stimuli [127] .

In unsupervised learning, there is no teacher. The objective is to discover patterns or features in the input data with no help from a teacher, basically performing a clustering of input space.

3.2.3 Reinforcement Learning

In this method, a teacher indicates whether the output is correct or incorrect. A reward is awarded to neurons with good performance and a penalty is giving to neurons with poor performance. Reinforcement learning (RL) is defined as learning by trial-and error with performance feedback from the environment or an external evaluator [44].

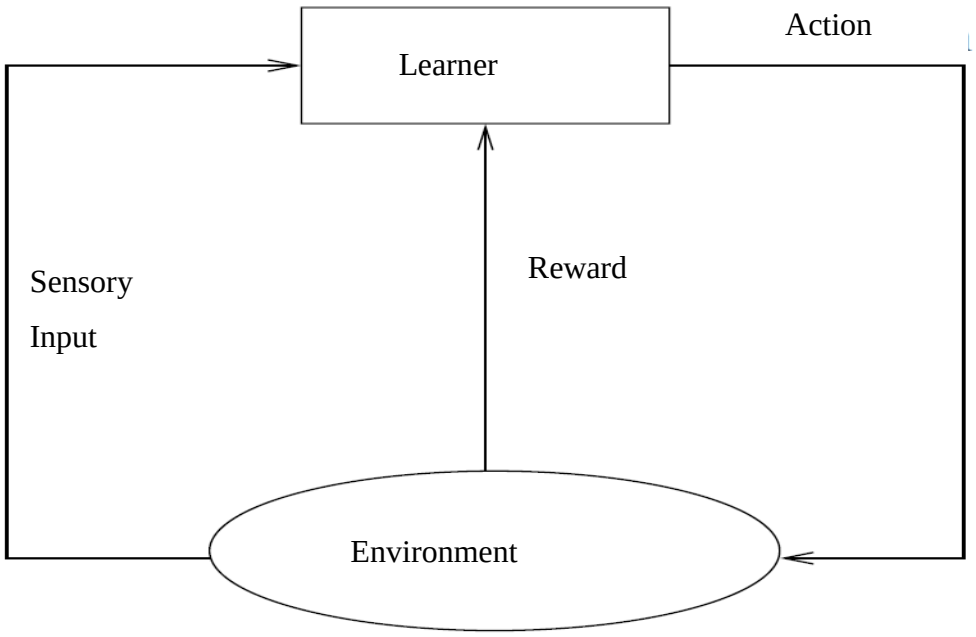

Fig 3.6: Diagram of Reinforcement learning [44]

Fig 3.6 shows reinforcement learning with a typical RL problem. In the diagram, the learner receives sensory input from the environment. Action is taken based on this. Then reward is given based on this action. This reward can be a positive or negative signal, depending on the correctness of the action. A negative reward has the effect of punishing the agent for a bad action. The action may cause a change in the agent's environment, thereby affecting the future options and actions of the agent. The effects of actions on the environment and future cannot be predicted [44].

3.3 Learning Algorithms

Learning forms the major aspect of the formation of artificial neural network machine. Learning is done based on an optimisation algorithm called gradient descent. The gradient descent back-propagation algorithm moves the weight along the negative of the gradient. This algorithm has problem such as; operating with fixed learning rate and convergence problem [43]. Over time an improvement has been made by researchers that are based on advanced optimisation methods in order to improve the training time and reduce the memory space. The faster algorithms fall into two categories.

The first category is the heuristic optimisation which was developed from an analysis of performance of steepest gradient descent algorithm such as variable learning rate back propagation.

The second one is the numerical optimisation such as quasi-Newton, conjugate-descent algorithm and Levenberg-Marquardt. The heuristic optimisation (variable learning rate back propagation) changes the constant learning rate to adaptive, while the numerical optimisation provides a faster convergence by performing a search along a conjugate direction to find the step size that minimizes the performance function. The quasi-Newton type of numerical algorithm requires calculation of the second derivative. The Levenberg-Marquardt algorithm does not have to calculate the second derivative which is the Hessian matrix. Hessian matrix is the second derivatives of the performance index at the current values of the weights and biases [43].The Levenberg-Marquardt algorithm is popular because of its speed and accuracy. It is used here in this research [43],[44],[128].

3.4 Multilayer Feed-Forward Neural Networks

Multilayer Feed-Forward Neural Networks (MLFNNs) are the common type of artificial neural networks. Multilayer feed-forward neural networks are used for approximation of a non-linear relationship between input and output. It is the commonly used ANNs for pattern classification which is trained to produce a spatial output pattern in response to an input spatial pattern. The mapping is static and is not at all suitable for a temporal pattern [38],[39]. MLFNN consists of an input layer, an output layer and generally, one or more hidden layers in-between and passes information in one way only as shown in Fig 3.7. The output is produced when each unit sums it inputs, add the bias to the sum and non-

linearly transforms the sum. The behaviour of the network is determined by the activation function. Various activations functions have been used in literatures to train MLFNN such as: threshold, piece-wise linear, sigmoid, tangent hyperbolic, and the Gaussian function [53]. Linear and sigmoid activation functions are used in this thesis.

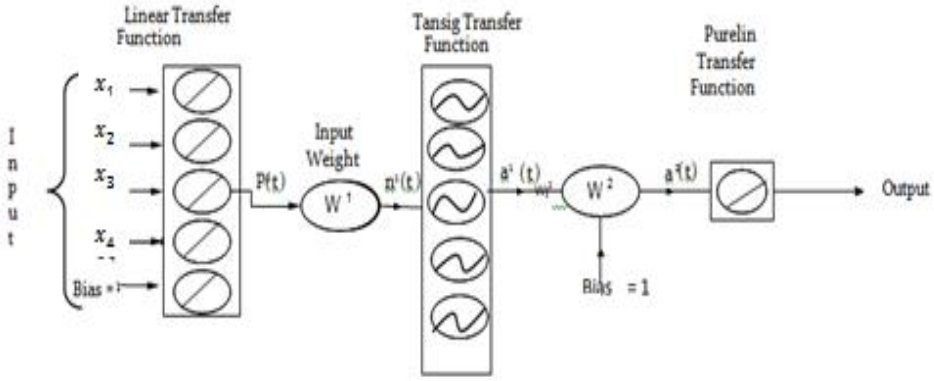

Fig 3.7: Multilayer Feed-Forward Neural Networks

3.5 Recurrent Neural Networks (RNNs)

To convert static ANNs into dynamic recurrent ANNs, a feedback integrator is used in a recursive mode to model the dynamic of the system. The recurrent neural networks on the other hand are a brain-like model. The Recurrent Neural Networks (RNN) makes use of memory to encode past history and has been shown to be an effective modelling tool in recent applications to stability issues [40]. Fig 3.8 shows a simple Recurrent Neural Network architecture which consists of context layer in addition to what is found in MLFNN. RNNs are used as computational models to solve computationally intensive problems. Unlike the widely used MLFNN that can only establish static mapping relationships between inputs and outputs, RNNs contain internal feedback loops and states and can perform highly non-linear dynamic mappings and thus have temporally extended applications [41], [42]. There are basically two types of RNN namely: ELMAN recurrent neural networks and Jordan recurrent neural networks. Elman RNN makes a

copy of the hidden layer as shown in Fig 3.8, which is referred to as a context layer. The function of the context layer is to store the previous state of the hidden layer. Jordan recurrent neural networks make a copy of the output layer referred to as state layer. The diagram of the Jordan neural network is not shown in this thesis but can be found in [44]. Applications of recurrent neural networks can be found in wind speed prediction, power forecasting [129] and impedance measurement techniques for power electronic systems [125], and management of distributed generation [40].

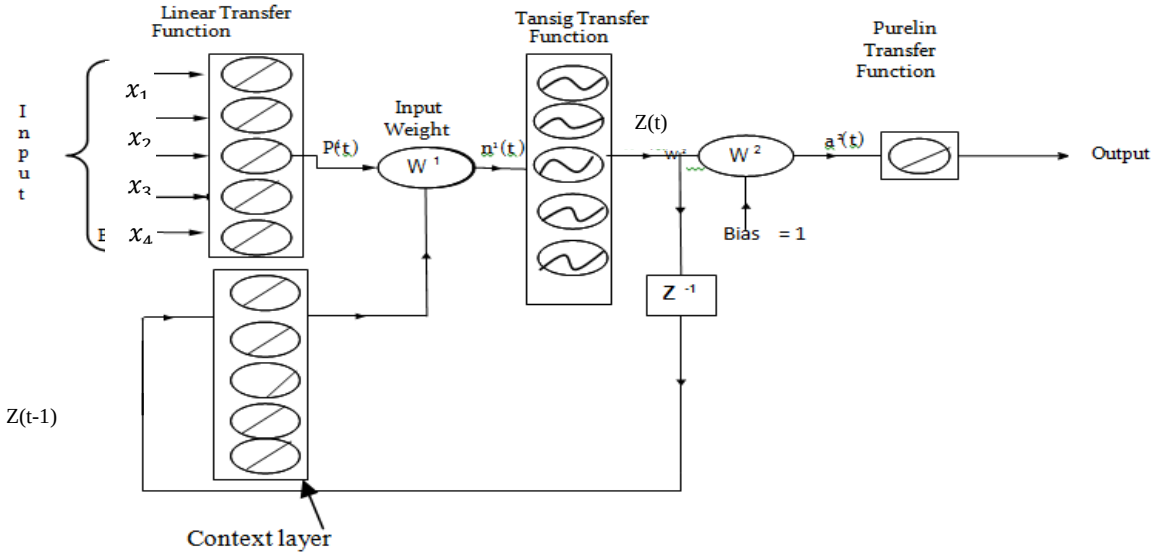

Fig 3.8: ELMAN Recurrent neural network Architecture

The input vector for Elman recurrent neural networks is therefore

$$\mathbf{Z(t)}= \underbrace{\boldsymbol{x_1}, \ldots\ldots\ldots \boldsymbol{x(t+1)}}_{\text{Actual Inputs}}, \underbrace{\boldsymbol{Z(t-1)} \ldots\ldots\ldots\ldots \boldsymbol{Z(t-j+1)}}_{\text{Context Units}}, \tag{3.2}$$

The context unit in Fig 3.8 is denoted by Z(t-1). This unit is interconnected with the hidden units with a weight that is equivalent to 1. It is also possible to have weight that is not equal to 1. In that case the complexity of the neural network increases [130]. The output equation is described as a function of weight, bias and the input vector. Equation 3.3 shows the output of the network.

$$y_{k,x} = f_{ok}\left(\sum_{j=1}^{J+1} w_{kj} f_{yj}\left(\sum_{i=1}^{I+1+J} v_{ji} z_{i,x}\right)\right) \quad (3.3)$$

where $(Z_{I+2,p,}\ldots\ldots\ldots,Z_{I+1+j,p}) = \left(z_{t-1,p}(t-1), \ldots\ldots, z_{t,p}(t-1)\right)$.

The ELMAN recurrent neural network is used in this thesis because of its simplicity.

3.6 Radial Basis Function (RBF)

Another type of artificial neural network is radial basis function. This is a type of artificial neural networks that form the input set based on distance of the input vectors from the weights. The architecture resembles that of MLFNN but its performance is quite different from MLFNN. It has an input layer, hidden layer of radial units and linear output units as shown in Fig 3.9. The input set is the vector distance between the weight and the input vector multiplied by the bias. It maps the input to a desired output by approximation of desired function and superposition of non-orthogonal symmetric function [126]. The hidden neurons do not implement an activation function but represents a radial basis function. In the same way the biological receptor works, the neural network also employs a local receptor to perform function mapping. In RBF neural networks, a radial unit (i.e., local receptor field) is defined by its centre point and a radius. The linear radial basis function of the i-th radial unit is:

$$h_i = \Phi\left(\left\|x - u_j\right\|_2\right) \quad (3.4)$$

where x is the input vector, u_j denote the centre of the radial basis function, Φ is the i-th radial basis function.

$\|.\|_2$ represent the Euclidean norm. Weights from the input units to hidden units represent the centre of the radial basis function of hidden unit j. The common radial basis function adopted the Gaussian function and is defined as:

$$\Phi\left(\left\|x - u_j\right\|_2, \sigma\right) = \exp\left(\frac{\left\|x - u_j\right\|_2^2}{2\sigma_j^2}\right) \quad (3.5)$$

where σ is the width or the spread (the distance an input vector must be from a neuron's weight vector) and some radial basis function neural networks normally use the width. For such basis function, the weight from the basis unit in the input layer to each hidden unit represent the basis width of the basis function [44]. For such radial basis function, the weight from the input vector to the hidden layer is the width of the function. However, the output of the function is:

$$y = purelin(u_i * a^1 + b_2) \tag{3.6}$$

where a^1 is the output of the first layer and u_i is the weight vector in the second layer. b_2 is the bias in the first layer and b_2 is the bias in the second layer.

Radial basis function performs better than MLFNN in terms of time at the same time radial basis function can accommodates more data during training [38].

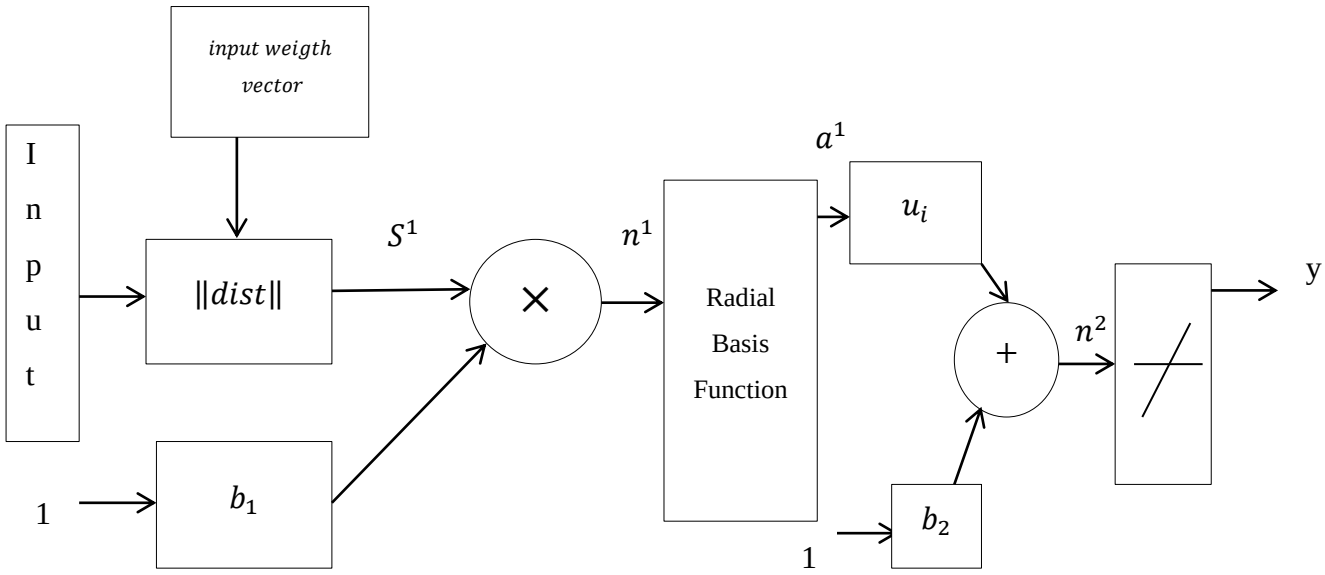

Fig 3.9: Radial Basis Function Architecture

In addition radial basis function displays some unique characteristics. At the centre, the function is at a maximum and reduces gradually to zero away from the centre. The output of the hidden units indicates the closeness of the input vector to the centre of the basis function. 1 indicates that the input is close or identical to the weight. As the distance

between weight and input vector decreases, the output increases. There are many types of radial basis functions such as: Linear function, Cubic function, Thin-plate-spline function, Inverse multi-quadratic function, Gaussian function and Logistic function.
Above all, the accuracy of the prediction depends on the number of the basic function used, the width of the receptor field and the centre of the function.

3.7 Generalized Regression Neural Networks

A generalized regression neural network is a supervised learning neural network that implements Bayesian decision strategy for classification. It actually has the same structure with radial basis function except in the second layer. The first layer is made up of input and pattern layer, while the second layer comprises of the summation layer and the output layer as can be seen in Fig 3.10.

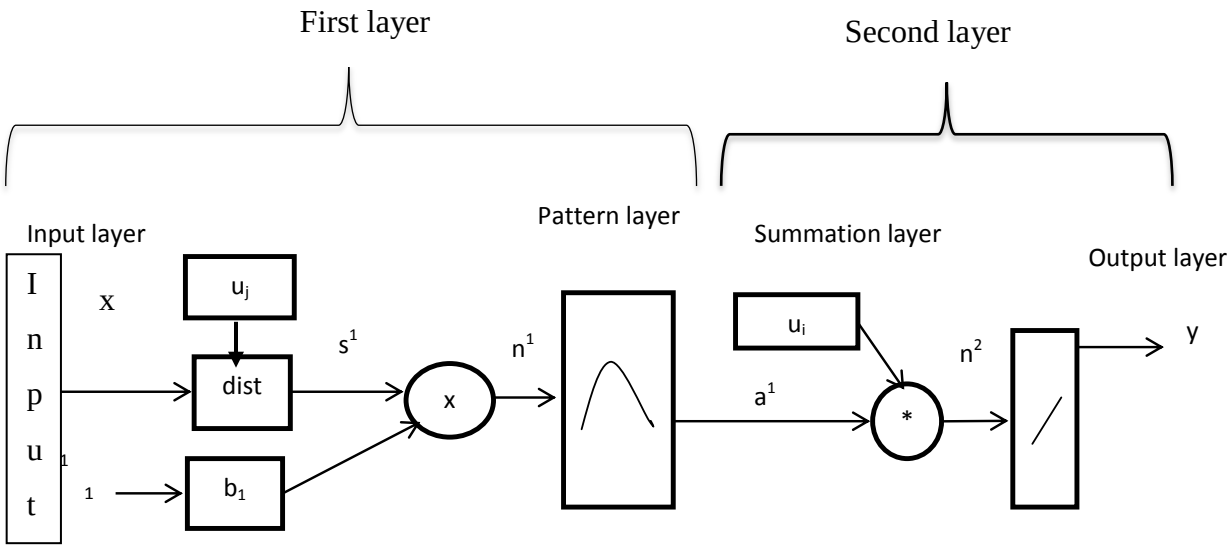

Fig 3.10: Generalized regression neural networks

The number of input units in the first layer is equal to the independent factors, *x*. The pattern layer contains the biases. The Euclidean distance between the input set and the weight set is used as the input to the pattern layer. The only bias in the network is connected to the pattern layer. Each pattern layer unit is connected to the neurons in the

summation layer. The summation computes the dot product of the weight u_i and the input a^1 and normalised it by the sum of input vector a^1 [131].
The output y is

$$y = \ purelin\ (n^2) \tag{3.7}$$

The output of the hidden layer is

$$a^1 = \Phi\left(\left\|x - u_j\right\|\right) \tag{3.8}$$

where a^1 , Φ, $\left\|x - u_j\right\|$ have already been defined.

3.8 Self-Organizing Feature Map (SOFM)

This is an unsupervised learning algorithm that is used for clustering. The self-organizing map or Kohonen network is an array of processing neurons arranged in a certain dimension or topology. Various dimensions exist to tackle different kind of problems depending on the complexities of the problems. For example, one dimension neuron topology can map the shape and the topology of higher dimension input vectors. It does this without a target or a teacher. There are two types of the self-organizing map models [45] [128]:

- Wilshaw Von-Der-Malsburg
- Kohonen self-organizing map

In the Willshaw Von-Der-Malsburg model, the input dimension is the same as the output dimension; whereas in the Kohonen model, mapping is done from high-dimensional signal spaces to a lower dimensional topological structure as shown in Fig 3.11.

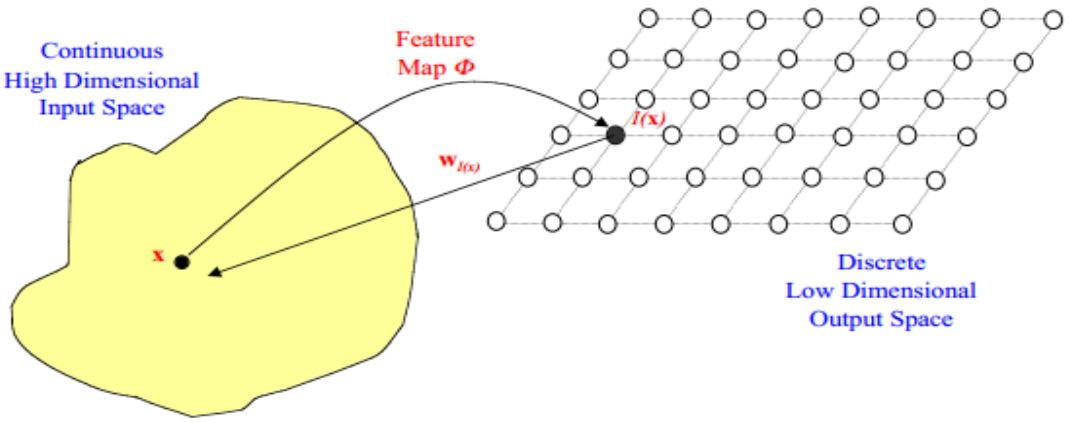

Fig 3.11: Organization of the mapping [132]

Each point in the input space (point x) is mapped to the corresponding point in the output space *I(x).*

These mappings are performed adaptively in a topologically ordered fashion. The mappings make topological neighborhood relationship geometrically explicit in a low-dimensional feature map.

The Kohonen neural network used in this research is modelled in the same pattern as shown Fig 3.12. The only difference is the number of neurons. Instead of 6x6, we used 10x10.Fig 3.12 shows the structure of 6x6 dimensions SOFM. This type of self-organizing map has a feed-forward structure with single computational layers arranged in a rows and columns. A self-organizing map classifies input according to how they are organized. The neuron can take any shape as specified by the programmer. The specific shape depends on the nature of the problems. The neuron organizes itself in such a way that it will resemble the shape of the input vectors. The winning neuron is identified based on some discriminant function. The neuron with the largest discriminant function is dominant.

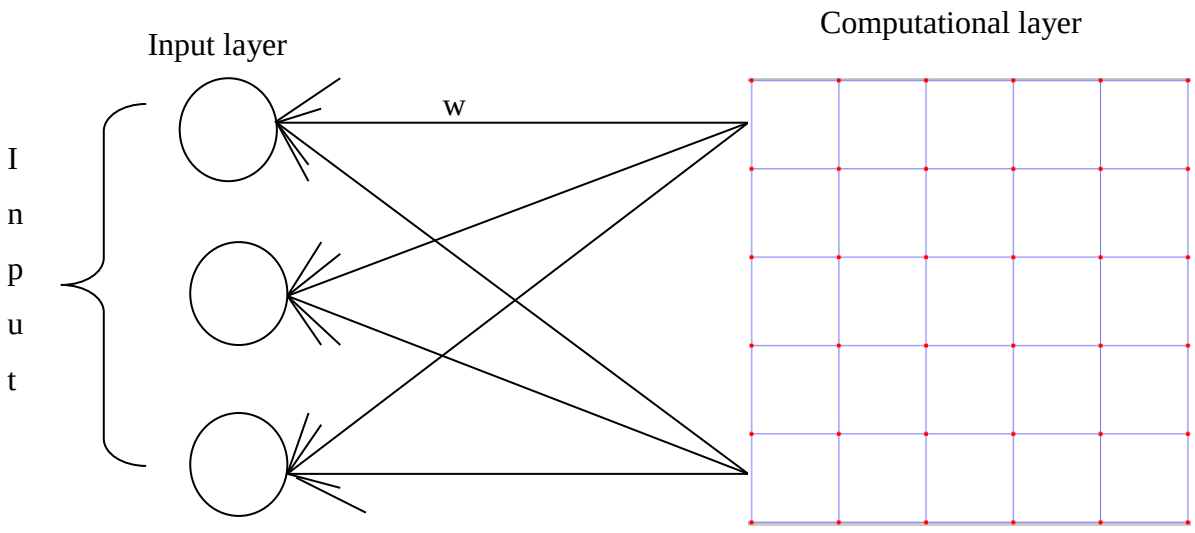

Fig 3.12: Self-Organising Feature Map

Depending on the topology of the input vector, the neuron takes the shape of the input after a certain number of iterations. If *N* dimensions of input are presented to *M* dimension of neurons to be trained, the *M* dimension of neurons arrange itself in a grid-like structure to mimic the input structure. Actually, the structure can take different shape. The neurons in the layer of an SOFM are arranged originally in physical positions according to a topology function. These topology and distance between neurons are described in topologies pattern such as gridtop, hextop, randtop.

The winning neuron is identified based on some defined functions known as discriminant function and both the wining neuron and the neighborhood neurons are updated. Each weight is connected to the neuron to form a bundle of weights. There are four steps into the SOFM algorithm [43].

- Initialization
- Competition
- Co-operation
- Weight adaptation

- **Initialization**

The weights are initialized randomly

- **Competition**

Competition computes the discriminant function for each neuron. The neuron with the smallest value of the discriminant function is declared the winner. The winning neuron is determined by calculating the discriminant function in equation 3.9.

$$i(x) = \sum_{i=1}^{D}(x_i - w_j)^2 \quad (3.9)$$

where the minimum index *i(x)* is selected as the winning neuron.
where *x* is the input vector and w_j is the weight vector. The corresponding weight vector is also updated during the training process.

- **Cooperation**

At this stage, the winning neuron determines the spatial location of topological neighbourhood of excited neuron. The winning neuron selects the neighbourhood based on the pre-defined neighbourhood functions [133].

- **Weight adaptation**

In order to enhance the response of the winning neuron to subsequent application of a similar input pattern, the discriminant function of the excited neurons is decreased in relation to the input pattern by adjusting the associated weight.

3.9 Comparison of Various Neural Networks

Most of the publication on stability analysis and prediction make use of multi-layer perceptron in classifying stability of power system network. The main drawback of multi-layer perceptron networks is that the weights updating do not utilize any information on the local data structure and the function approximation is sensitive to the training data. Since recurrent neural networks incorporate feedback, they have powerful representation capability and can successfully overcome the disadvantages of feed-forward neural

networks. For computational intensive problems, the use of recurrent neural network is recommended [134]. The general idea behind RNNs is that the input data is mapped into the output. This is achieved by using a training algorithm designed with the transfer function. Table 3.1 gives the general comparison of the five neural networks in this chapter.

Table 3.1: Comparison of neural networks

MODEL	**ADVANTAGES**	**LIMITATIONS**
Multilayer neural networks	Proven effective for classification Fast during recalling.	Not suitable for temporal pattern
Recurrent neural networks	Suitable for time series prediction, temporal classification and system identification	A longer training time, vanishing gradient problem leading to difficulty in learning of long term dependencies.
Radial Basis Function Neural Networks	Less computer time consuming	Require more neurons than standard feed forward back propagation networks
Generalized Regression Neural Networks	It has good performance of local approximation and doesn't sink into the local minimum. The computation speed is relatively very fast.. It is good at solving the problems of approximation, prediction and classification	Depend heavily on the spread factors. The larger that spread is, the smoother the function approximation. Too large a spread means a lot of neurons will be required to fit a fast changing function. Too small a spread means many neurons will be required to fit a smooth function, and the network may not generalize well.
Kohonen neural networks	Easy to implement	• Training process time consuming. • Manual labeling to represent different data classes at the end of training, • Suffer from stability and plasticity Dilemma.

3.10 Hybrid Systems

A single technique may not be adequate enough to effectively solve the real world problems. One method of dealing with this problem is to combine two or more CI techniques to generate hybrid solutions in order to combine their strengths and overcome the individual weaknesses.

Hybrid system techniques can be formed through combination, integration, fusion and association.

3.11 Improving the Training Algorithm

Gradient-descent learning algorithms, i.e., learning algorithms that modify the network parameters following the gradient of an error function, have difficulties in learning the topology (number of nodes and their connections) of the net. Modifications have been suggested in literature to fast track the training process through variable learning rate and standard optimisation techniques such as conjugate gradient, Quasi-Newton and Levenberg Marquardt [126]. For large power system networks with several machines, coherent machines can also be replaced by equivalent machine to reduce the training time. The feasibility of using heuristic methods such as population Based Incremental Learning (PBIL), Genetic Algorithm (GA), Breeder Genetic Algorithm (BGA) etc., for training the neural networks should be explored in order to make it applicable to real time scenario. Heuristic methods provide a faster rate and reduced memory. Reference [135] presents an approach to solve the online transient stability constrained power generation (TSCPG) by a mixture of a modified particle swarm optimization (PSO) and artificial neural networks (ANNs). This mixture (PSO-ANN) is used as an optimization tool to guarantee searching of the optimal solution within the hyperspace thereby reducing the time used in the computations and at the same time keeping the quality of the selected solution. Comparison made between PSO and GA in training ANNs shows the superiority of PSO over GA [136]. PSO can achieve faster result when heuristic programming is used in training. There is a possibility of using PBIL and BGA for training ANN, this will bring good improvement to the training process.

3.12 Features Selection

Feature selection is essential in order to reduce the dimensionality of the input data by selecting the subset of the features. This is achieved by selecting a set of features from a large number of features. The selected feature must be able to give detail information that will be able to build appropriate neural network model. Feature selection enhances the accuracy of the classification process. There are many methods in feature selection[44].

- Engineering Judgment
- Sequential forward selection
- Filter method

3.13 Performance Evaluation

The performance of artificial neural networks can be measured based on accuracy, convergence and complexity. One important point to note is that neural networks must be trained very well with minimum generalisation.

Accuracy: The most common measure of accuracy is the Mean Squared Error (MSE). The performance of ANN can also be evaluated based on Mean Square Error with Regularization (MSEREG). MSEREG is better and can easily overcome the problem of over-fitting. The mean square error is given as:

$$mse = \frac{1}{Q_p}\sum_{k=1}^{Q_p}\{(t(k) - y(k)\}^2 \tag{3.10}$$

where Q_p is the number of input pattern, *t(k)* is the target, and y*(k)* is the output of the neural networks. In order to improve generalization, the performance function is modified by adding the mean sum of the square of the weights and biases.

$$MSEREG = \gamma * mse\ (1-\gamma) * (\frac{1}{n}\sum_{j=1}^{n} w_j^2\ ) \tag{3.11}$$

where $MSEREG$ is the mean square error with regularization, γ is the performance ratio, wj is the weight.

In case of classification problem, correctly and incorrectly classification is used as another measure of accuracy.

Correlation analysis is another factor for measuring the accuracy. Correlation coefficient calculates the correlation between the output and target values for all patterns. The correlation coefficient is given as:

$$r = \frac{\sum_{i=1}^{n}(x_i - \bar{x})\sum_{i=1}^{n}(y_i - \bar{y})}{\sigma_x \sigma_y} \quad (3.12)$$

where x_i and y_i are observations, $\bar{x}$ and $\bar{y}$ are respectively the averages over all observations x_i and y_i and σ_x and σ_y are the standard deviations of the x_i and y_i observations respectively.

The correlation coefficient quantifies the linear relationship between the approximated (Learned) function and the true function. A correlation value close to 1 indicates a good approximation to the true function.

3.14 Application of Artificial Neural Network in Transient Stability Assessment (TSA)

The potential inherent in computational intelligence such as artificial neural networks among others CI techniques have been identified as a promising contributor for reaching the goal of on line TSA [31], [137],[138]. Several versions of ANN that are said to be promising have already been described in the previous sections. These ANN types have been explored in recent years to classify, predict and model the dynamics of power system under large disturbances (transient stability). ANN can provide the following functions at the control centre.

- Stability margins determination
- Current operating point qualitative evaluation
- Visualization of security regions
- Available transfer capability [138].

In order to be quantifiable, these functions must be expressed in practical terms such as:

- Critical clearing time
- Oscillation time (damping)
- Generator out of step and machine load angle (instability)
- Line loading
- Critical under/over voltages
- Critical under/over frequency, and
- Angle differences between system parts [1].

Critical clearing time is used in transient stability evaluation but in transient stability prediction the focus is to monitor the status of power system and find out if the swing is divergent or convergent. The first stage in either prediction or evaluation is system identification or modelling. The stages involves in modelling are described in the next sub-section.

3.14.1 Neural Networks For Modelling Dynamics Systems

The universal function approximation capabilities of most ANNs have made then suitable for modelling dynamic systems. The common ANN use for modelling dynamic systems is the Recurrent Neural Networks (RNNs). The main purpose of modelling (or system identification) is to identify a model of unknown plant so as to predict the behaviour of the plant. Since the mathematical model is not accurate enough to define most dynamic processes or the inherent non-linearity of most dynamics system is difficult to be represented by mathematical model such as transfer function, RNN is now used to offer remedy by providing input-output capabilities and can identify the transfer function from input-output data.

3.14.2 Neural networks identification model

Fig 3.13 shows the general block diagram for artificial neural networks modelling procedure or identification procedure. In the model the plant output and ANNs output are compared and the error is fed back to a learning algorithm. The model is modified using the training algorithm to produce the new model that is so close to the actual plant output. The prediction error must be very small and this is used as neural network training signal.

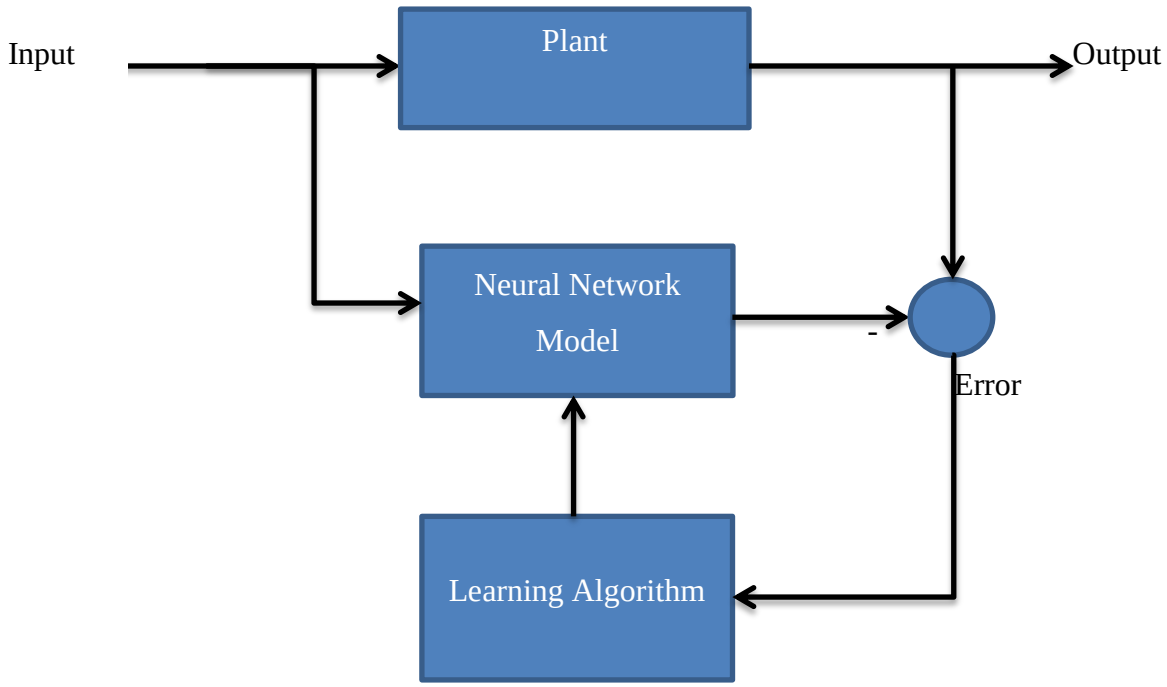

Fig 3.13: System identification/modelling block diagram

3.15 General Overview of Neural Network Applications

The application of artificial neural networks in power system has been reported widely in literatures. Sobajic and Pao in 1989 [139] reported the possibility of using ANN to assess the transient stability of power system by determining the CCT. The work applied adaptive pattern recognition approach based on feed-forward neural networks with back propagation learning algorithm to identify the critical clearing time. The work done by [140] is an improvement on the work reported in [139] by using the same input features but also used variable learning algorithm. The common multi-layered perceptron networks was built composing of 3 inputs, one hidden layer and one output. It was discovered that for a larger power system network, more input feature is probably be needed in order to enhance high accuracy. It was suggested that time delay must be introduced to achieve a better training accuracy.

The work reported in [141] is based on recurrent radial basis function to predict the rotor angle and angular velocities for multi-machine power systems. In the scheme, power system is assessed based on monitoring generators' angles and angular velocities with time and check whether it exceeds the limit specified for system stability or not. The proposed method used radial basis function to model system's dynamics and a feed-back integrator is then used to solve the state variables trajectories. This study was conducted without the use of PMU.

However, the author in [142] use multilayer to estimate the rotor angle of synchronous generator using data from the PMU. Many other literatures have also used PMU data to predict instability [143],[144].

Combined use of supervised and unsupervised learning for transient stability assessment based on concept of stability margin is reported in [145]. The author developed a new adaptive pattern recognition method for estimating critical clearing time, based on highly parallel information processing using artificial neural networks. Prediction and generalization capabilities of these networks provide a basis for the robust, flexible mapping of input attributes into the single valued space of the CCT. A new unsupervised learning algorithm is developed for clustering large bodies of data on the basis of discovered similarities. Convergence to stable cluster formation is very fast usually within ten iterations. It can be used to screen power system contingencies quickly in

transient stability analysis. A supervised learning paradigm then uses the clustered data to synthesize accurately the CCT.

The authors in [146] used ANN to predict the best configuration of hybrid power system. The hybrid combinations considered are micro-hydropower system, grid and wind. ANN improves the time compared to economic software (i.e., economical base simulator) used. The consideration was based on economic function. However, other indices are neglected such as stability index. This thesis based its approach on the stability index only in real time.

The thesis also uses the combination of recurrent neural networks and other artificial neural networks for prediction of critical clearing time. The recurrent neural networks are used to predict the active power of the renewables since they are not constant but depends on the varying energy source.

Chapter 4

Real Time Transient Stability Assessment using Critical Clearing Time

Since the 1920s when the power system stability was identified as a problem, the need to maintain stability has become a focus of concern to the power industry [147],[148]. The importance of stability assessment is identified in the recent blackouts recorded in the USA (August, 2003), UK and Mainland Europe utilities (September 2003) [1],[149]. The importance is again stressed in a deregulated market where there is vast integration of new technologies such as distributed generation, hybrid electric vehicles, power electronics interfacing, advanced controllers, intelligent controllers etc. into the electric grid. Power system stability can be defined as the property of a power system that enables the system to remain in a stable equilibrium state under normal operating conditions and to regain an acceptable equilibrium state after being subjected to a disturbance [1],[148]. The system's instability can be classified into:

- Rotor angle instability
- Frequency instability
- Voltage instability

When disturbance occurs that lead to instability, there is a need to restore and maintain system stability requirements in keeping the synchronous generator operational with adequate dispatch capacity to meet electricity demand and changes in system topology.
The three basic classes of stabilities are shown in Fig 4.1 [148].
Instability in any system can be as a result of small disturbances or large disturbances depending on the size of the disturbance. The small disturbance stability can be analysed by linearization over a certain operating point [150]. Whereas a large disturbance can be

analysed by using a non-linear approach such as time domain simulation, etc. These phenomena can be short or long term depending on the time span [148].

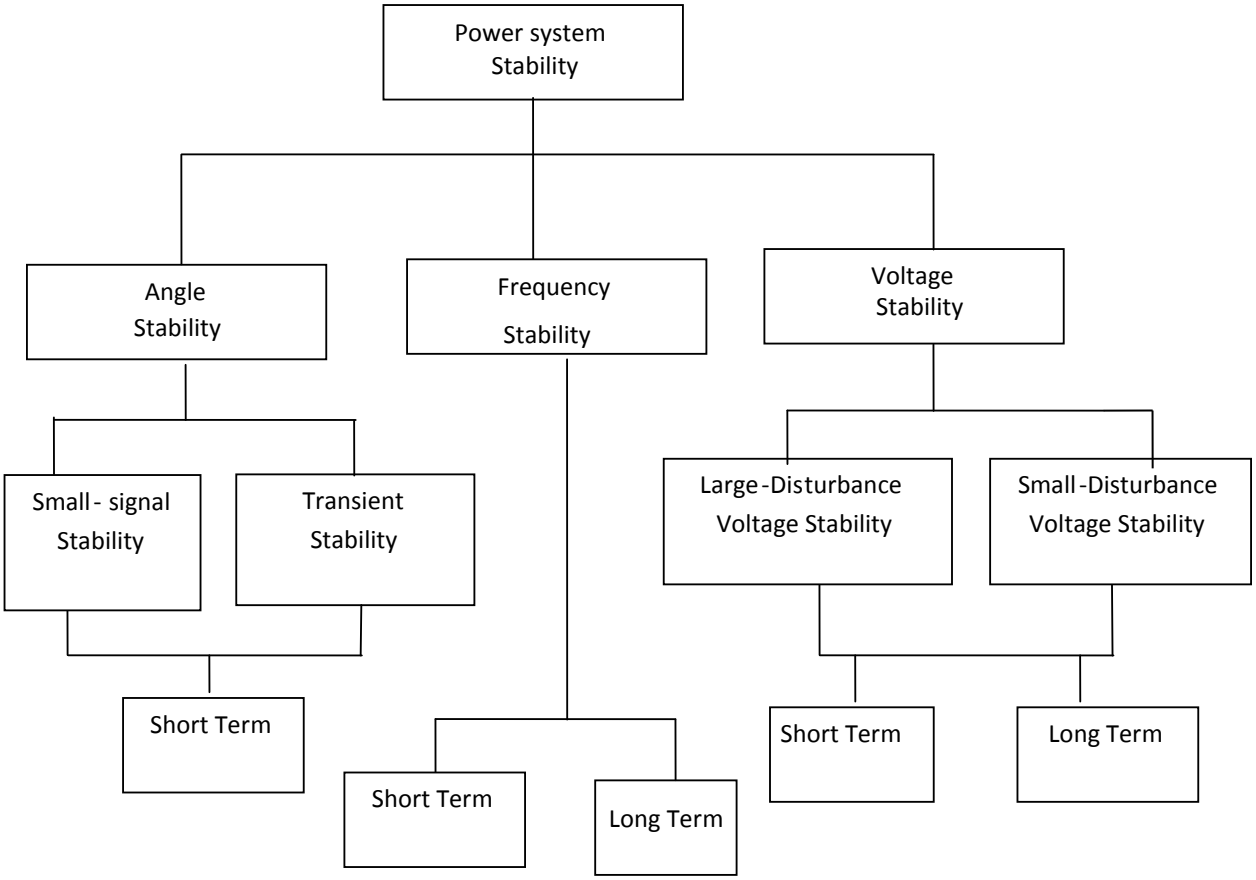

Fig 4.1: Classification of Power system [148]

4.1 Rotor Angle Stability

Rotor angle stability is the ability of interconnected synchronous machines in a power system to remain in synchronism under normal operating conditions and after being subjected to a disturbance [147]. In an interconnected power system, if the system is stable, all the machines swing together under the law of equilibrium which is established between the input mechanical torque and the output electrical torque of each machine where speed is constant. A disturbance may lead to the loss in stability due to loss of equilibrium between the opposing forces. During this stage, the synchronous machine falls out of step, resulting in the following behaviours:

- The rotor runs at a higher or lower speed than the synchronous speed,
- The terminal voltage is generated at a lower value than the one generated at the system frequency.
- The slip between the rotating stator field and the rotor field results in large fluctuations in the machine power output, current and voltage resulting in isolation of certain faulted parts by the protection system.

A stable or unstable system therefore can be explained from equation 4.1 based on synchronising torque and the damping torque. Lack of sufficient synchronizing torque results in instability through an aperiodic drift in rotor angle (i.e., T_s is negative and T_D is positive) and other hand, lack of sufficient damping torque results in oscillatory instability (i.e., T_D is negative and T_s is positive) [148].

$$\Delta T_e = T_s \Delta\delta + T_D \Delta\omega \tag{4.1}$$

where $T_s \Delta\delta$ is the component of torque change in phase with the rotor angle perturbation $\Delta\delta$ and it is referred to as the synchronising torque component. T_s is the synchronising torque coefficient. $T_D \Delta\omega$ is the component of torque in phase with the speed deviation $\Delta\omega$ and it is referred to as the damping torque component; T_D is the damping torque coefficient. There are two categories of rotor angle stability namely:

- Transient stability
- Small signal stability

The ability of a power system to maintain synchronism after being subjected to large or severe transient disturbances such as three-phase fault or loss of generation is called transient stability [151]. The first swing instability is of importance and is caused by insufficient synchronising torque. Sometimes instability also occurs after the first swing which is always due to superposition of several modes of oscillation causing large excursions of rotor angle beyond the first swing. The study period of interest is between 3-5 seconds after disturbance and sometimes 10 seconds when considering a large system with dominant inter-area mode of oscillation [148]. When the disturbance is relatively small, small signal instability occurs as a result of insufficient synchronising or damping

torques resulting in a steady increase in rotor angle or increasing amplitude resulting into oscillatory instability.

The ability of the power system to maintain synchronism under small disturbances is known as small signal stability. This type of stability is usually analysed by using a linearized set of system equations over an operating point [148].

4.2 Frequency Stability

Frequency stability refers to the ability of a power system to maintain steady frequency following a severe system upset resulting in a significant imbalance between generation and load. The causes of frequency instability are linked with inadequacies in equipment responses, poor coordination of control and protection equipment or insufficient generation reserve. To maintain frequency during load increment or generation changes is vital to system operator and it all depends on the ability to maintain/restore equilibrium between system generation and load, with minimum unintentional loss of load [152]. Instability may result in the tripping of generating units, load shedding, and under-generated island with insufficient under-frequency load shedding such that frequency decays rapidly causing blackout of the island within a few seconds [57],[147]. Over the last decade, blackout incidents have increased in some parts of the world such as North America [67],[153]. Several causes of this have been suggested, including changes in [148]:

- An interconnection's moment of inertia
- Load types
- Generation control practices
- Frequency control (monitoring and regulating) practices.

4.3 Voltage Stability

Voltage stability is the ability of a power system to maintain steady acceptable voltage at all buses in the system under normal operating conditions after being subjected to a disturbance [147]. With sufficient reactive power, rotor angle swings in power system network can be maintained within the required limit of 120 degree. However, the main contributor to sustained voltage instability is the load and may not be the rotor angle

swing. The situation is even worst when the local impact is wide spread resulting into cascaded voltage collapse. Cascaded voltage collapse results in a run-down situation that will cause voltage instability when load dynamics attempts to restore power consumption beyond the capability of the transmission system and the connected generation.

During the occurrence of large disturbances such as system faults, loss of generation or circuit contingencies, voltage instability occurs if the system is not able to provide required reactive power. The inherent ability of the system network to withstand this is called large disturbance voltage stability. This problem can be resolved by understanding the existing dynamic load characteristics and the interaction of both continuous and discrete controls and protections. One can also measure or determine the stability of the system by capturing non-linear dynamic performance of under-load transformer tap changers (ULTC) and the generator field-current limiters. On the other hand, small disturbances such as incremental load changes can result into small signal voltage instability if the continuous and the discrete control are not well implemented. With appropriate assumptions, system equations can be linearized for analysis purposes, thereby allowing computation of valuable sensitivity information useful in identifying the main factors influencing stability. This linearization, however, cannot account for non-linear effects such as tap changer controls (dead bands, discrete tap steps, and time delays). Therefore, a combination of linear and non-linear analyses is used in a complementary manner [154] [155], [156], [157] in order to achieve optimised system stability.

Apart from the above classification, power system phenomena can further be explained with time scale. Fig 4.2 shows an approximate time-scale structure of power system phenomena of interest. A, B, C, and D denote fast transients, generator dynamics, quasi steady state, and steady state, respectively. From Fig 4.2, it can be seen that the entire time scale can be grouped into two large groups namely: Fast and slow dynamics, depending on the time scale of the underlying physical processes triggering the mechanisms of power system instability [26]. The understanding of the time scale of various phenomena will enhance the choice of appropriate modelling detail to use. For efficiency and easy analysis, complete modelling incorporating the entire phenomena is avoided.

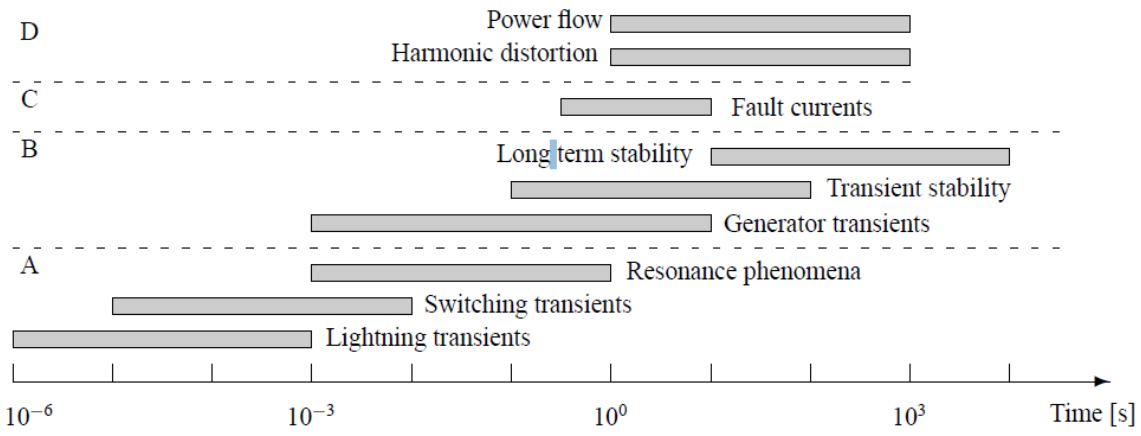

Fig 4.2: Simplified chart of dynamic phenomena in power systems [26]

4.4 Overview of Transient Stability Assessment

The ability of power system to maintain synchronism after being subjected to large or severe transient disturbances such as three-phase fault or loss of generation is called transient stability [151]. Power system during the swinging operation goes through pre-fault, fault and post fault periods. The transient stability problem is the study of the asymptotic stability of the post fault system, with initial condition given by the faulted system response. The post fault period actually reveals the state of the system after the fault has occurred. Power system transient stability problems can be categorized into two, namely [31],[158]:

- Evaluation
- Prediction.

4.4.1 Transient Stability Evaluation

Transient stability evaluation usually focuses on the critical clearing time (CCT) of the power system in response to a fault, which is defined as the maximum time after

occurrence of disturbance, during which if the fault is cleared, the power system can regain its transient stability.

4.4.2 Transient Stability Prediction

In transient stability prediction, the state of system is monitored to show the progress of power system transient. Prediction is usually concerns with transient swings convergent or divergent after a large disturbance. The key point here is that, the state of the system is monitored a step or multi-step ahead of time. The problem of transient stability prediction, considered in this thesis, usually involves the pre-fault and post fault stages in order to evaluate and predict the state of the system in real time.

4.4.3 Mathematical Formulations of Transient Stability

When unbalance between mechanical torque and electrical torque acting on the rotor occurs, the net torque causing acceleration or deceleration is given by:

$$T = T_m - T_e \tag{4.2}$$

where T is the acceleration torque (net torque) and T_m is the mechanical torque and T_e is the electrical torque.

The electrical angle is related to the mechanical angle as follows:

$$\theta_e = \frac{60f}{rpm}\theta_m \tag{4.3}$$

where f is the frequency and θ_m is the mechanical angle in radian and *rpm* is revolution per minute.

The electrical angular position with respect to the rotatory synchronous reference axis is given by:

$$\delta = \theta_e - \omega_0 t \tag{4.4}$$

where ω_0 = rated synchronous speed in rad./sec

t = time in seconds

θ_e= electrical angle in radian

δ= rotor angle in electrical radians with respect to synchronously rotating reference

The angular acceleration in derived by taking the second derivative of equation 4.4:

$$\frac{d^2\delta}{dt^2} = \frac{d^2\theta_e}{dt^2} \tag{4.5}$$

The net torque acting on the rotor of a synchronous machine can also be given as:

$$T = \frac{WR^2}{g}\alpha \tag{4.6}$$

where α is the mechanical angular acceleration in rad/s^2

WR^2 = is the moment of inertia in kg-m^2, W is the weight of rotating parts, R is radius of gyration.

The mechanical angular acceleration can be defined as:

$$\alpha = \frac{d^2\theta_m}{dt^2} = \frac{rpm}{60f}\frac{d^2\theta_e}{dt^2} \tag{4.7}$$

Differentiating equation 4.3 twice and combining it with the net torque equation (equation 4.6) and equation 4.7, we arrive at equation 4.8.

$$T= \frac{WR^2}{g}\frac{rpm}{60f}\frac{d^2\theta_e}{dt^2} \tag{4.8}$$

However,

Define the kinetic energy as

$$\text{K.E} = \frac{1}{2}\frac{WR^2}{g}\omega_0^2 \tag{4.9}$$

where $\omega_0 = 2\pi\frac{rpm}{60} = 2\pi f$

The inertia constant *H* is given as:

$$H = \frac{kinetic\ energy\ at\ rated\ speed}{Base\ KVA} \tag{4.10}$$

$$H = \frac{1}{2}\frac{WR^2}{g}\left(2\pi\frac{rpm}{60}\right)^2\frac{1}{Base\ KVA} \tag{4.11}$$

Converting to p.u, equation 4.12 is used.

Let the base torque be defined as $T_{Base} = \frac{Base\ KVA}{2\pi\left(\frac{rpm}{60}\right)}$ (4.12)

Combining equation 4.11 with equation 4.12 and substitute that into equation 4.8, torque in per unit is obtained

$$\frac{T}{T_{Base}} = \bar{T} = \frac{H}{\pi f}.\frac{d^2\delta}{dt^2} \tag{4.13}$$

Where $\bar{T}$ is the torque in p.u

Equation 4.13 can be rewritten as

$$\bar{T}_m - \bar{T}_e = \frac{H}{\pi f}.\frac{d^2\delta}{dt^2} \tag{4.14}$$

Or stated differently using power instead of torque noting that $and\ \bar{P}_m = \omega\bar{T}_m$ and $and\ \bar{P}_e = \omega\bar{T}_e$, where ω is the rated synchronous speed in p.u.

$$(\bar{P}_m - \bar{P}_e) = \frac{H}{\pi f} . \frac{d^2\delta}{dt^2} \quad (4.15)$$

$\bar{P}_m$ and $\bar{P}_e$ are mechanical power and electrical power, respectively**.** The torque per unit is equal to power in per unit if speed deviation is neglected.

Equation 4.14 and equation 4.15 are called swing equations.

4.5 Critical Clearing Time

The most common transient stability criterion is critical clearing time (CCT). CCT measures the robustness of the system to any disturbance. Apart from measuring the robustness of the system, it can also be used to screen a set of contingencies and rank those one of interest i.e., the one that is close enough to operating time of system protection [137]. For computational intelligence (CI) training, data indicating stable and unstable conditions can be gathered by first calculating the CCT. When the fault is cleared after the CCT value, the system is stable otherwise it is unstable. With a circuit breaker, the critical clearing time (CCT) is set ahead of time possibly with the use of offline load flow simulation. The CCT value is therefore assumed constant throughout the system operating points. However, CCT is not a constant stability index but changes with time and the location of the fault. The use of fixed value to represent CCT will possibly give false alarm to system operators. The CCT used in this thesis is calculated from the analytical method and monitored by using CI techniques. By using CI techniques, the state of the system can be monitored and also predicted.

4.6 Calculating Critical Clearing Time from Swing Equation Using Equal Area Criterion

Equal Area Criterion (EAC) is commonly used when stability analysis is the major focus. EAC helps in the determination of the maximum swing of δ and the stability of the system [148]. Actually, EAC is applied to Single Machine Infinite Bus (SMIB) and cannot be directly applied to multi-machines power system. Information concerning the

maximum angle excursion and the stability may be obtained from the power-angle diagram. The mathematical analysis is described below.

Equation 4.15 which represents the swing equation can be used and modified to obtain:

$$\frac{2H}{\omega_s}.\frac{d^2\delta}{dt^2} = \bar{P}_m - \bar{P}_e = \bar{P} \qquad (4.16)$$

$\bar{P}_e$ is a non-linear function of δ and therefore equation 4.16 cannot be solved directly. For simplicity, the "- "on top of *P* or *T* will be omitted in the rest of the discussion. It is assumed that *P* and *T* are in p.u.

The diagram in Fig 4.3(a) shows the P-δ curve for a single machine infinite bus system (for a lossless system). Note that in the steady state P_m=P_e. Whenever a three-phase fault occurs near the generator bus on the radial transmission line, the electrical power transmitted through the line to the infinite bus becomes zero but the mechanical power remains constant. It is assumed that when the fault is cleared, the system returned to its initial condition. The mechanical energy represented by area abcd accelerates the machine and the rotor angle position moves from δ_0 (which is the initial rotor angle) to δ_1 assuming the fault is cleared at δ_1.Then the operating point moves from c to e. At point f, the area defg is formed. The rotor comes back from f and settle at a, where $P_m = P_e$. If area A is equal to area B, then stability is maintained.
δ_1 is the clearing angle and the corresponding time *t* is the fault clearing time. This form the basis of equal area criterion

When the fault clearing time is increased from *t* to t_c such that $\delta_1 = \delta_c$, t=t_c and area A = area B, then any further increase in *t* will not keep area A to be equal to area B. This is shown in Fig 4.3 (b). The value of t_c at this point is the critical clearing time (CCT) and δ_c is the critical clearing angle.

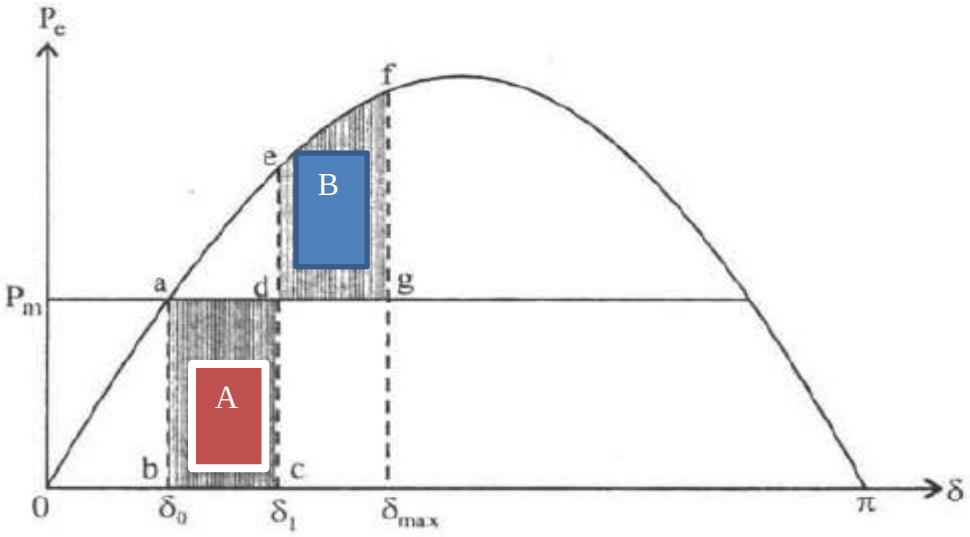

a

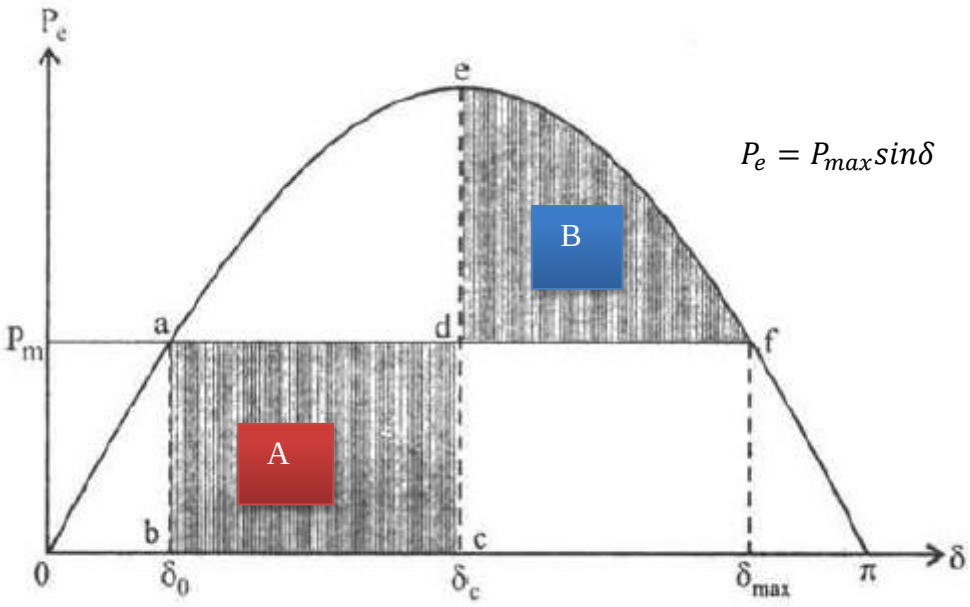

b

Fig 4.3: Calculating CCT using Equal Area Criterion (a&b)

The critical clearing time is a mechanical variable and varies with changing operating condition.

The decrease in critical clearing time (CCT) indicates an increase in instability. It also shows that the CCT depends on the fault location. As the fault location moves toward the

reference bus, the power flow direction is altered and thus the CCT changes with progressive reduction.

For equal area criterion, area A= area B, in that case, area A and Area B can be calculated from Fig 4.3 (b) as follows:

$$A= \int_{\delta_0}^{\delta_c}(P_m - 0)d\delta = P_m(\delta_c - \delta_0) \tag{4.17}$$

$$B = \int_{\delta_c}^{\delta_{max}}(P_{max}sin\delta - P_m)\, d\delta \qquad \text{since } P_e = P_{max}sin\delta \tag{4.18}$$

$$=P_{max}(cos\delta_c - cos\delta_{max}) - P_m(\delta_{max} - \delta_c) \tag{4.19}$$

For area A= area B and knowing that $\delta_{max} = \pi - \delta_0$

$$\delta_C = cos^{-1}[\frac{P_m}{P_{max}}(\pi - 2\delta_0) - (cos\delta_0)] \tag{4.20}$$

During the period of the fault, the swing equation from equation 4.15 is also written as

$$\frac{H}{\pi f}.\frac{d^2\delta}{dt^2} = P_m \quad \text{when } P_e=0 \tag{4.21}$$

Integrating both sides twice

$$\delta_c = \frac{\pi f}{2H}P_m t^2 + k \tag{4.22}$$

At t=0; $\delta_0 = \delta$, hence k=δ_0 (4.23)

Hence

$$\delta_c= \frac{\pi f}{2H}P_m t^2 + \delta_0 \tag{4.24}$$

δ_c is the critical clearing angle.

The critical clearing time for a Single Machine Infinite Bus (SMIB) is therefore obtained as follows:

$$CCT = t_c = \sqrt{\frac{2H(\delta_c - \delta_0)}{\pi f P_m}} \quad (4.25)$$

$$\delta_c = cos^{-1}\ ((\pi - 2\delta_0)sin\delta_0 - cos\delta_0) \quad (4.26)$$

where CCT is the critical clearing time, *H* is the inertia, δ_c is the critical clearing angle.

For multi-machine, the critical clearing time is calculated by increasing the fault clearing time until the system is at the point of losing synchronism, where further increase will make the system goes out of step. For each machine, the CCT is obtained and the minimum is assumed to be the critical clearing time of the system. This is because each machine has the potential of losing synchronism especially when the location of the fault is close to the generator. This method avoids the stress of going through the critically disturbed generator and therefore save enormous time.

A three-phase fault on the reference generator bus will have a significant impact than when the fault is away from the reference generator bus. Generally, the critical clearing time increases with increasing transfer admittance i.e., from 0-0.5 p.u of the distance as shown in Fig 4.4. The CCT will decrease from this point (i.e., 0.5 p.u) until it reaches minimum point at 1 p.u of distance. The maximum transfer admittance occurs at the midpoint of the transmission line. The curve between transfer admittance and the distance of fault will be symmetrical at about 0.5 p.u length where maximum transfer admittance occurs if the circuit is symmetrical about the middle of the line as shown in Fig 4.4 [159].

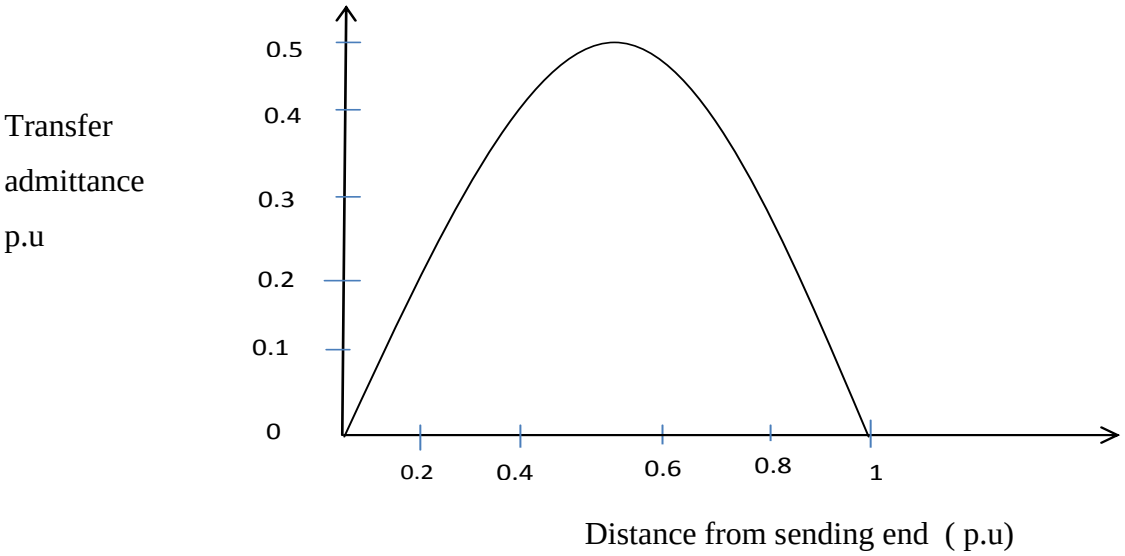

Fig 4.4: Influence of transfer admittance on critical clearing time [152]

4.7 Modelling Of Generators for Real Time Transient Stability Assessment

In real time digital simulator, the common reference approach is used. The centre of inertia can also be used. The approach is based on settling one generator as the reference generator and relates the other generators to this reference generator. The modelling of the multi-machine power system (68-bus system) is conducted in RTDS and the results will be discussed in chapter 7.

4.7.1 Time Frame for Real Time Dynamic Simulation

Timing is important for real time prediction. In order to predict the state of the system, the following must be taken into consideration.

Communication delay, controller decision time, data manipulation and transfer time and data arrival time. The time of prediction should be less than all this time listed above so as to allow time for control action [160].

For example, let us assume that the fault is applied at t_{FT} and cleared at t_c, as shown in Fig 4.5. There is always a communication delay as a result of communication device used such as communication lines. The communication delay time is represented by T_D and T_{SI}

is the simulation time for first swing while T_{SN} is the simulation time for multiple swings and the RTDS speed ratio is ρs as shown in Fig 4.5.

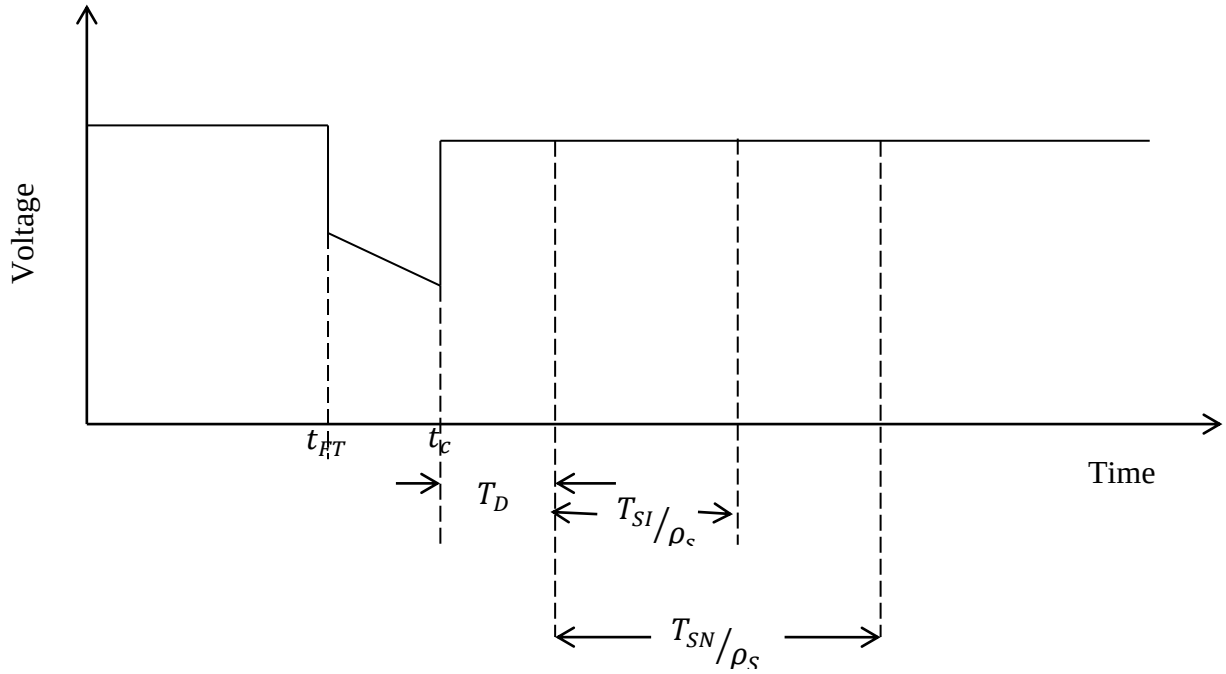

Fig 4.5: Timing sequence for the Estimation

Considering the simulation time for first swing stability and the multi swing stability used in practice which is 1s and 3-10s respectively [161]. We set T_{SI}=1s and T_{SN}=10s, and ρs=10s and T_D=0.02s. The estimation for first swing and multi-swing should be obtained at 0.12 seconds and 1.02 seconds after fault clearing [161].

The time for the first swing and the multi-swing are not fixed for all power system networks but the time for assessment depends on the size of the network. For moderately sized network, the response time for stability assessment is less than one second [162].

Data arrive at the data base (data concentrator) every one cycle of frequency. For a 60Hz frequency, the data comes in at every 16.7ms [162]. That is, the sampling interval of PMU is 16.7ms or 0.0167s for 60Hz and the reporting rate for 60Hz frequency is 60 frames per second [163] (see detail of PMU in section 4.10). Prediction of the stability condition of the system is carried out with this data at every 16.7 ms in order to know the stability condition of the system. This is known as one-step-ahead prediction and is used in this thesis. There is also multi-step ahead prediction which is based on time more than one cycle.

4.8 Supplementary Indices

There are some stability indices that are recorded in literature which can also be used to measure or quantify the transient stability margin apart from using the CCT. Sometimes rather than using a single index a combination of dynamic stability indices can be used. This section is used to explain few of the indices that can be used.

4.8.1 Angle Index (AI)

Generally, generators are to be protected to prevent damages and asynchronous operation. To do this, the system is designed with protection-based relay. The purpose is to monitor the impedance observed in the transformer high voltage bars. The protection adjusts the load angle of the generator and ensures it does not exceed 120^0. In case of loss of synchronism, the relay acts to separate the generator from the entire system. The maximum slip of the load angle offers a suitable security margin, since in case this is not exceeded, the generator may regain its synchronism [164]. The angle index (AI) is defined as

$$AI = min\left\{1, max_{i=1.....n}\left(\frac{\delta_{ci,max}}{\delta_{c,\max adm}}\right)\right\} \tag{4.27}$$

Where $\delta_{ci,max}$ is the maximum deviation of the load angle of the ith generators during the simulation time, $\delta_{c,\max adm}$ is the maximum admissible load angle given by the protection relay and *n* is the number of generators operating in the system. The higher this value is the higher the instability.

4.8.2 Maximum Frequency Deviation Index (MFDI)

The maximum frequency deviation from its rated value after contingency is applied and can be used to measure the impact of the contingency on the state of the system. The higher this value, the higher the negative impact it has on the system. The index ranges

from 0 for a case in which there is no frequency deviation to 1 when the frequency reaches its maximum admissible value [164].

$$\omega_k = \min\{1, max_{i=1....n}\left(\frac{|\Delta f_{i,max}|}{\Delta f_{max,adm}}\right)\} \quad (4.28)$$

where n is the number of generators operating on the system, $\Delta f_{i,max}$ is the maximum frequency deviation and $\Delta f_{max,adm}$ is the maximum admissible frequency deviation The maximum admissible value is related to the under and over frequency protection of generators. These protections are set about $\pm 5\%$ of rated frequency.

Other indices are Load Shedding Index (LSI), Power Flow Index (PFI), Dynamic Voltage Index (DVI) etc., and it can be found in [164].

4.9 Real Time Stability Issues

In order to avoid the risk of blackout due to instability, the state of the system must be predicted ahead of time so that corrective measures can be deployed to quickly avert the unforeseen contingencies. The ability to predict the state of the system lies on the capability to quantify and compute the distance to the stability margin or to monitor the current operating state and the state when it is stressed.[1].

In real time mode, supervisory control and data acquisition or energy management system (SCADA/EMS) plays a major role. In order to ensure that the control action being taken is safe and correct they are often supervised by SCADA. Basically, the field is interfaced with the remote terminal unit (RTU) and devices located within the substation. Data collected from the field through RTU can be processed in the central location, transferred to the center through communication networks, which include a mix of leased telephone lines, a power-line carrier, microwave radio, copper and fiber optic cable as well as VHF and UHF radio. Processing is done by powerful computer systems at a central location or for the hierarchical control system. Processing and analyzing this information at the SCADA center and displaying it to the operator with appropriate control action to be taken either automatically or by an operator. This is followed by transmitting the request for control to the field equipment. It then monitors the completion of the control request

and builds a real time database and periodically saves real time information in historical information system (HIS) for archival purpose. An alarm is triggered when necessary. Moreover, the availability of relatively inexpensive GPS receivers and more powerful electric utility and telecommunication networks have enabled the synchronization of the phasor measurements over large geographical areas. This allows direct measurement of the voltage and current phasor throughout the entire network and allows monitoring of dynamic behavior of power systems. Phasor measurement unit (PMU) can be used to detect possible system separation and system oscillations in close to real time. The installation of a phasor measurement unit is core in real time simulation.

The key components in real time transient stability assessment and control are shown in Fig.4.6. There are five main blocks in Fig 4.6 which can be used to describe a procedure towards real time stability analysis. The first step in operating the real time is data modelling which include power flow data from the state estimation function in energy management system (EMS), auxiliary data and dynamic data. After this, security assessment is obtained. If any risk is observed in the system, control action will be instigated to restore the system back to normal. The control actions include preventive measures such as generator rescheduling, or corrective actions such as load shedding. In conventional methods of real time assessment, the simulation is often terminated as soon as the stability can be clearly determined or the contingencies screening is done to filter out stable ones. The last one is the display unit. However, as can be seen in the diagram, computational intelligence was incorporated. CI is capable of performing security assessment and control.

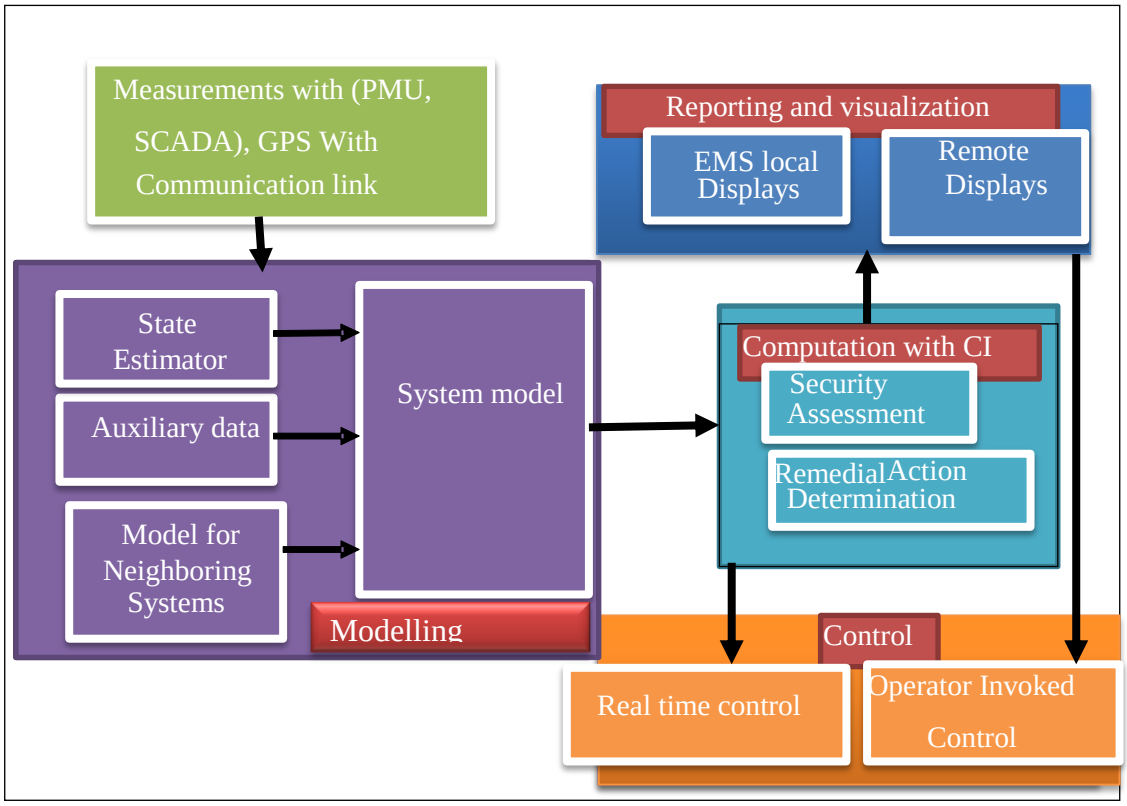

Fig 4.6: Key Components in Real Time Stability Assessment [165]

The structure that will enhance full integration of conventional stability assessment tools in real time should shows a transition from steady state to dynamic security assessment, from deterministic approach to probabilistic approach or computational intelligence approach, from offline model validation to on line model validation, from analysis of the next operational interval to look-ahead analysis, from N-1 contingency to N-k contingencies [57].

The function of future control centres can be classified as monitoring functions, assessment functions and controllability. While the present monitoring focuses on output from state estimation which is subject to a delay, security assessment based on contingency screening by using steady state power flow analysis and protection and control system based on local information, the future power system is expected to accommodate more of PMU for state measurement, online voltage, transient and small signal stability analysis with real time controlled separation and restoration.[57].

4.10 Phasor Measurement Units (PMUs) Concept

One of the main components in real time digital simulator (RTDS) is phasor measurement units (PMUs). The phasor measurement unit (PMU) is a power system intelligent electronic device (IED) that can provide synchronized and more accurate measurements in real time [166],[167]. Phasor measurement units (PMUs) measure the dynamic state of power system in real time and allow a timely response to be made to an event in progress. Before the advent of PMU, state estimator has been extensively used to collect unsynchronized data of line flows, both real and reactive power in order to estimate the voltage angles and magnitude. The complex bus voltages are the state of the system and are used in state estimation and transient stability analysis. Unfortunately, prior to PMU, the state could not be measured directly but only infer from unsynchronized data. But due to the advent of a global positioning system (GPS), it has become possible to synchronize data by providing geographical coordinates and time synchronization. By synchronized sampling of microprocessor-based systems, phasor calculation can be placed on a common reference [168] in order to achieve synchronized phasor measurement units. This emerging technology of PMU and GPS will output the synchrophasor such as phasor voltage and current, as well as their angles. Direct measurement of the voltage and current phasor throughout the entire network essentially eliminates the need for state estimators. However, because of measurement error and bad and missing data, state estimation will be necessary.

Usually PMUs are located at substations to measure phasor voltages and currents on a power grid and can output accurately time-stamped voltage and current phasor. Because these phasors are synchronized, by using global position system (GPS) synchronized comparison of two quantities is possible, in real time. These comparisons can be used to assess system conditions. Other than locating PMUs at substations, they can be located at optimal points in the power system. In one second, 60 samples of PMU measurements are provided. That is, the sampling interval of PMU is 0.017s for a 60Hz system (60 frames per second) [168]. Another important fact is that PMUs at the present time are not fully integrated with standard supervisory control and data acquisition systems (SCADA), instead a separate phasor data concentrator is used to receive and process phasors [1]. The data is archived and can be sent to the SCADA database. In the future, SCADA systems are expected to be fully integrated for control and supervision of data. In that case, when

fault occurs on the system, the sudden changes in the system data are collected with PMUs and are transmitted through the communication network to the control centre SCADA for processing and analysing (stability assessment is performed) and later display the result to the operator. The dynamic system update is carried out based on the data from the PMU and the state estimator (see Fig 4.7).

Rotor angle and speeds are the most important variables for transient stability studies. Speed deviation can be used in case of growing instability, but to estimate the dynamic status requires the knowledge of the first swing. This can only be determined using rotor angle. However, rotor angle estimation cannot be measured directly. Estimating it from the PMU output data is a challenging task. This is because most of the PMU measurements today are designed for steady state. This thesis also considers the use of output of the PMU to estimate the rotor angle of each generator under large disturbance and the results are presented in chapter 7. It is noted that PMUs are another mechanism for monitoring the power system stability status but they do not have predictive capability. This thesis also includes the prediction at one step-ahead of time.

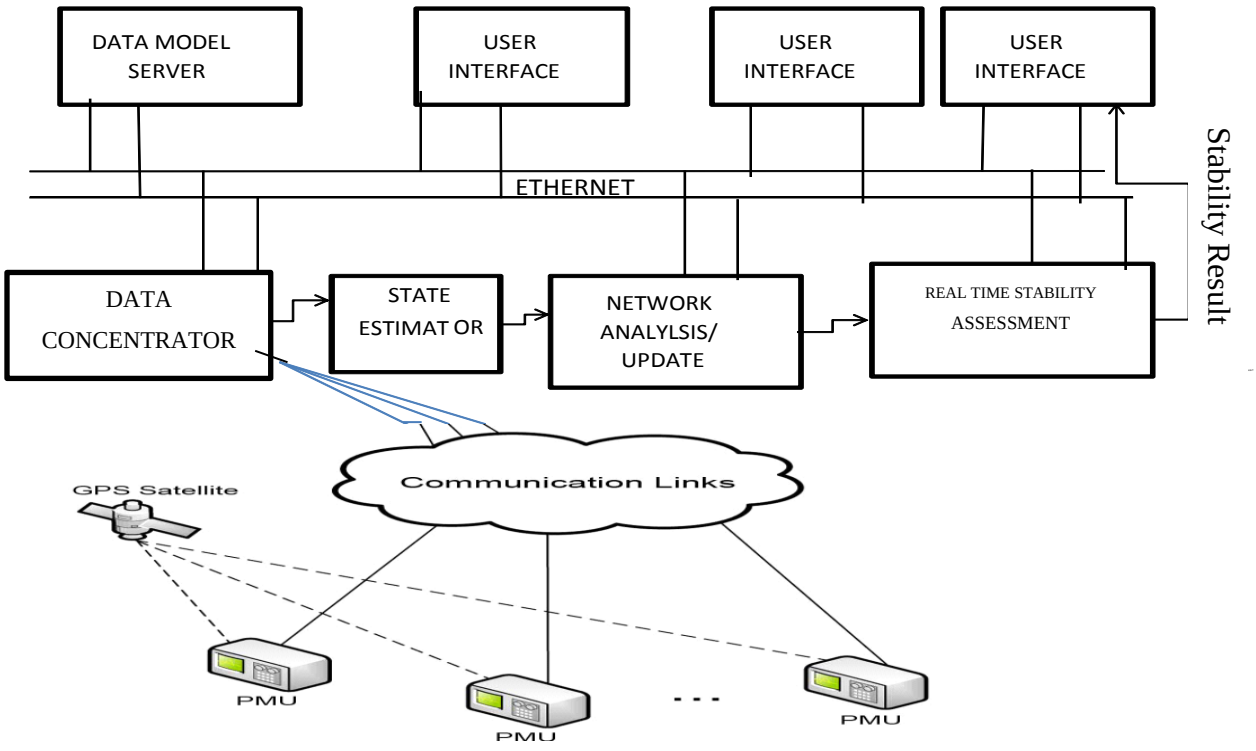

Fig 4.7: Data Measurement Concept

Now PMU is considered to be one of the most important measurement technologies in power systems due to its unique ability to sample voltage and current waveforms data in synchronism with a GPS-clock and compute the corresponding 50/60 Hz phasor component from widely dispersed location [143]. The sinusoidal representation of phasor is shown in Fig 4.8. Assuming a single frequency constant sinusoid of frequency which is extracted from a group of corrupted frequency by using Fourier Transform is observed at t=0 as shown in Fig 4.8. the sinusoid can be represented by [169]:

$$x(t) = X_m \cos(2\pi f t + \emptyset) \tag{4.29}$$

f is the frequency of the signal in Hz, and $\emptyset$ is the phase angle in radian, X_m is the peak amplitude of the signal.

The phasor has a magnitude which is the root mean square of the sinusoid and whose angle is the angle between the peak of the sinusoid and the t=0.

To extract the single frequency from corrupted frequency, Fourier transform called Discrete Fourier Transform (DFT) is commonly used.

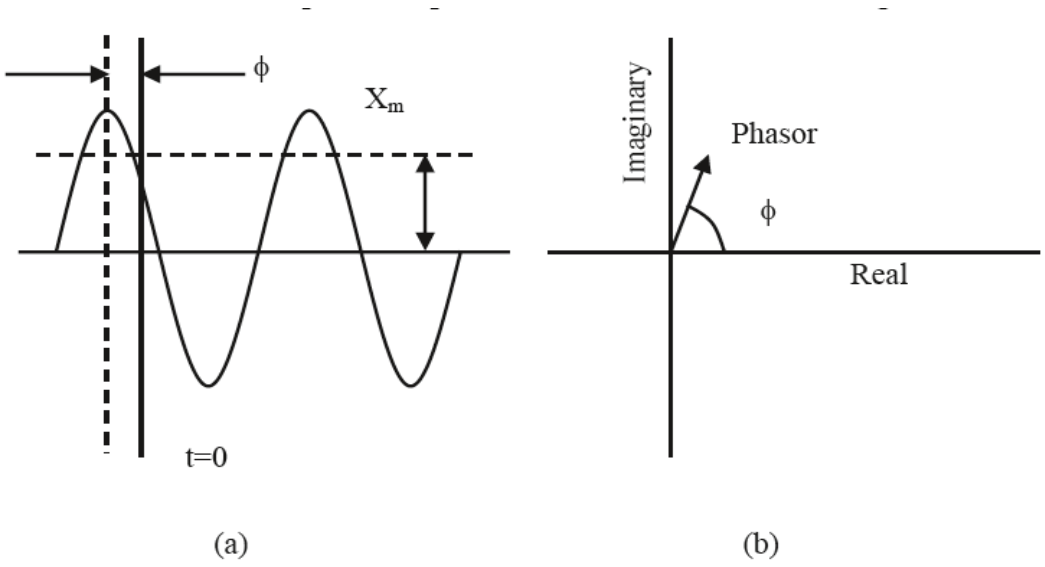

Fig 4.8: A sinusoid (a) and its representation as a phasor (b) [169]

The sinusoid in equation 4.29 can be transformed into complex number known as its phasor representation:

$$x(t) \leftrightarrow X = \left(\frac{X_m}{\sqrt{2}}\right) e^{j\emptyset} = \left(\frac{X_m}{\sqrt{2}}\right) [cos\emptyset + jsin\emptyset] \quad (4.30)$$

The principal interest of phasor measurement is to calculate the fundamental frequency component which can be obtained from equation 4.30. However, the phasor calculation is a continuous process, it is necessary to update the phasor estimate as newer data samples are acquired. The best algorithm to use is recursive algorithm. This algorithm estimates the phasor recursively by adding the contribution made by the new sample and subtracting the contribution made by the older samples. In contrast to the non-recursive algorithm, the recursive algorithm is computationally efficient though very numerically unstable. Recursive algorithm is preferred and is used in most application today due to its computational efficiency.

Generally, phasors of phase voltages and current collected at each data window (which is the phase angle$\emptyset$) are recursively updated. The modern PMU uses one pulse per second provided by the GPS satellite receivers. This make the positive sequence phasor to be time-tagged with timing information provided in the GPS. The important of the time tagged is to provide an indexing tool for PMU data that arrives at different time. This will help in creating a coherent picture of the power system out of such data [169].

4.10.1 Phasor Measurement Unit (PMU) Placement and Rotor Angle Measurement

In this thesis, PMUs are placed at the extra high voltage side of the transformer [142] because the direct measurement of the state is faster than extracting the same states from the system state estimator. Data collected from the PMUs are transformed using equation 4.31. However, the simplest way to compute rotor angles from phasor measurements is to rely on the classical generator model and relate phasor to reactance (step-up transformer, generator) to get rotor angles. The internal voltage from the classical model of a generator can be computed from the terminal voltage and current phasor measurement.

$$E'\angle\delta = V\angle\theta_v + jX'I\angle\theta_I \quad (4.31)$$

where E' is the constant voltage, V is generator terminal voltage, X' is transient reactance, and I is the generator terminal current and δ is the generator rotor angle. θ_v and θ_I are the angle of the voltage and current, respectively.

4.10.2 Role of Computational Intelligence in Dynamic Security Assessment (DSA)

A successful online dynamic security assessment (DSA) can be implemented in an integrated environment where computational techniques can work alongside conventional software. The intelligence techniques must be accurate, fast and robust with the capability to provide stability assessment, determine critical contingencies, security limit for all scenarios. The diagram of DSA incorporating the CI component for system stability assessment, optimization problem is shown in Fig 4.9. In Fig 4.9, the information gathering units obtain the information of various variables and communicate it to the control centre. One-step or multistep prediction is conducted to cater for the short mid-term variation of system condition while the dynamic model update and validation of generator and transmission lines model is based on real time and not offline. Due to the fact that transmission lines are more stressed than ever, deterministic approaches that are applicable to n-1 contingencies cannot be applied to N-x contingencies. A better approach like probabilistic or CI approach should be considered that would cater for the probability of occurrence of critical contingencies. Time domain simulations are used to complement the CI techniques in the determination of the status of the system. In case of overshoot of stability margin, overloading etc., the control action is triggered to mitigate the action [1],[57]. The alarm is prioritized in order to distinguish severe contingencies from the un-severe one. The advantage of CI approaches over other methods of real time simulation is the ability to predict ahead of time.

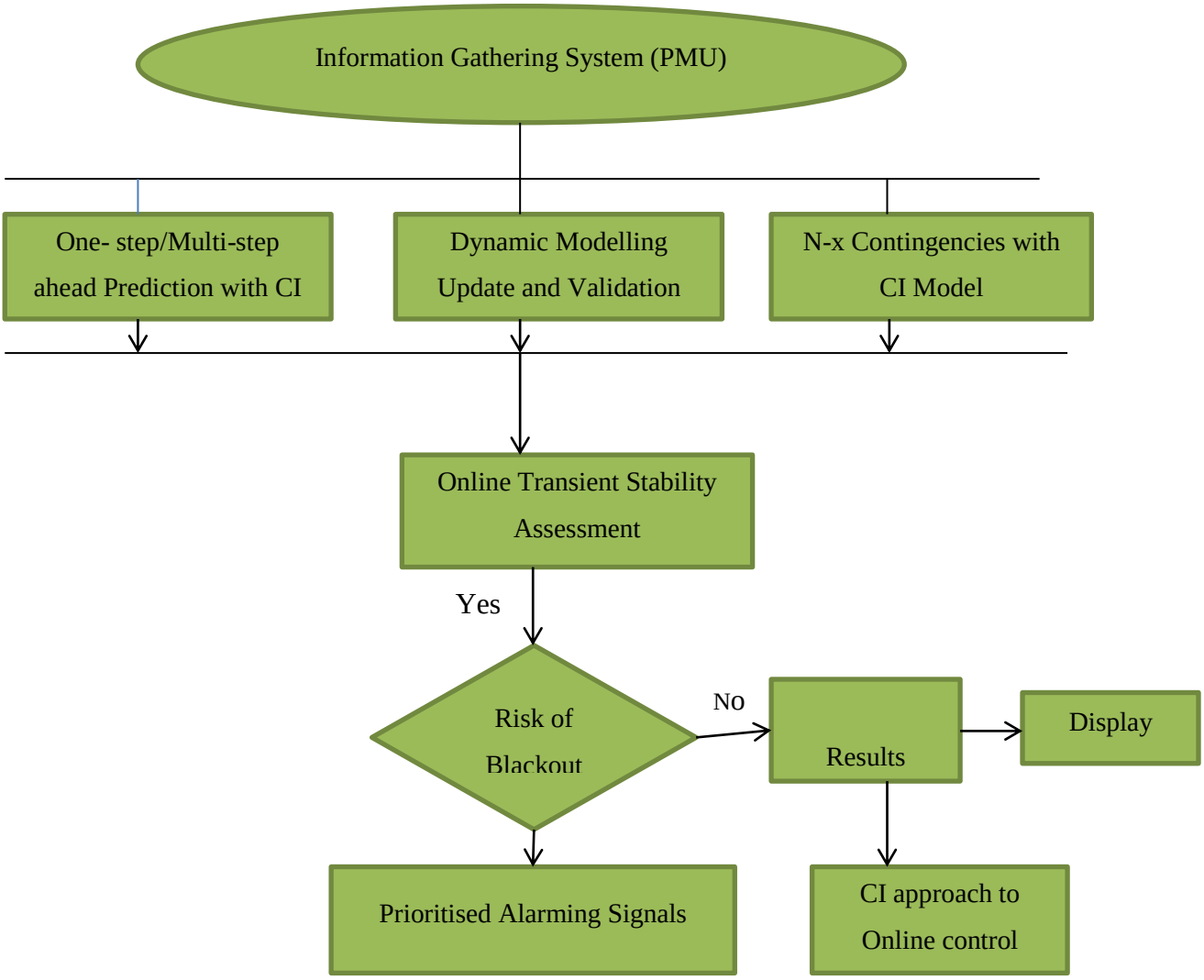

Fig 4.9: Vision of future assessment functions incorporating computational intelligence techniques

4.11 Challenges Faced By Implementing Real Time Stability Assessment.

There are various challenges faced with an attempt to implement real time stability assessment. They are listed below:

- Unavailability of real time data.
- Availability of real time application software that can monitor event and deliver results timely.
- Power system models deployed to integrate real time transient stability assessment application software with a SCADA/EMS system are quite different from the offline planning mode. The difference can be seen in bus numbering and naming convention and the level of detailed modelling used for power system components.
- Common information model (CIM) needs to allow the integration of different models from a variety of vendors.

4.12 Overview of Simulation Tools Used

4.12.1 DIgSILENT Power Factory

DIgSILENT power factory like any other software is used in modelling, simulations and analysis of various models which are seamlessly integrated into the grid. DIgSILENT has proven advantages in its functional integrations and applicability to modelling of various circuits such as distributed network integrated with distributed generation, transmission and generating system. The all-in-one power factory software caters for all new technologies such as wind power and solar PV, DG/HDG and the handling of very large power systems. In addition to the stand-alone solution, the power factory engine can be smoothly integrated into the global integrated system (GIS), distribution management software (DMS) and energy management system (EMS). It has a well-defined pre–programming library model ranging from simple models to complex models such as

generators, inverters and solar system. The software has been improved to cater for many things among which are generating adequacy so as to investigate the impact of external factors such as temperature and humidity have on stability [170]. It is user friendly, with an easy to use graphical display unit.

4.12.2 Real Time Digital Simulator (RTDS)

Real System Computer Aided Design (RSCAD) software is the main interface with the RTDS hardware and is a user friendly graphical display unit. It is designed to allow the users to perform all the necessary steps to prepare and run simulations, and to analyze the simulation results.

It consists of various library models that can enhance complete network modelling. The modelling detail is processed by a faster processing machine called Real Time Digital Simulator (RTDS). RTDS is made up of processing card such as giga processor card (GPC), 3PC, PB5, etc. When there are more than 7 racks, the racks are linked together by inter-rack communication (IRC) otherwise they can be directly connected. The Giga Transceiver Workstation Interface card (GTWIF), is a PPC405 based processor card whose primary function is to handle communication between the RTDS power system simulator and the host computer while the Giga Transceiver Synchronization (GTSYNC) synchronizes RTDS simulation time-step with the external time-step. The Giga-Transceiver Network Communication Card (GTNET) provides a real time communication link to and from the simulator via Ethernet. Lastly, the system entirely operates at 50 micro-second time-step which is an added advantage over offline simulation tools such as DIgSILENT. RTDS therefore addresses most of the limitations emanated from other offline software packages such as the slow rate of stimulation due to reduce simulation time-step. The software has the following advantages [171]:

- It allows small time–step during simulation.
- It allows user defined models
- It allows complete modelling to be implemented
- It allows real time and online simulation to be conducted.
- There are no problems of numerical error due to modelling reduction.

4.12.3 Matlab Version 7.12 (R2011a)

MATLAB comprises of a high-performance language for technical computing integrated with numeric computation, data visualization, programming, and data analysis. Using the MATLAB product, one can solve technical computing problems faster than with traditional programming languages, such as C, C++, and Fortran [43]. It has easy-to-use graphical display.

Application of Matlab includes signal and image processing, communications, control design, test and measurement, modelling and analysis. It contains some toolboxes where collections of special-purpose MATLAB functions, available separately are used to solve particular problem areas. Example is neural network toolboxes. Neural networks toolbox contains special functions that can aid fast implementation of training and testing. It allows code generation and subsequently modification to fit into the required purpose. It also aids result preparation and has user friendly graphical display [43].

Chapter 5

Impact of Hybrid Distributed Generation on Transient Stability (SMIB)

This chapter describes the impact of hybrid distributed generation (HDG) on transient stability of a power system using critical clearing time (CCT) and rotor angle swinging (first swing and the settling time). CCT is the maximum time after occurrence of disturbance, during which, if the fault is cleared, the power system can regain its stability. This occurs at the maximum rotor angle excursion also known as critical clearing angle (CCA). A power system is stable when the rotor angle deviation is less than the critical clearing angle, otherwise it is unstable. When the CCT is exceeded, the synchronism of the generators can no longer be maintained. The generators will go out of step leading to an increase in rotor angle separation. The impact of penetration level of HDG is investigated based on the following:

1. Different types of HDG (Solar PV, Small Hydropower (SHP), Doubly-Fed Induction Generator (DFIG))
2. Load conditions (Annual increase in load)
3. Location of the HDG (Dispersed or concentrated HDG)
4. Transmission line length (100km - 500km)

5.1 Modified Single Machine Infinite Bus System

Fig 5.1 shows the modified single machine infinite bus system model. Used in this chapter. This power system model consists of an infinite bus system (Grid) represented by GEN1, one centralized generator (GEN2), a hybrid distributed generation (HDG) and two equal loads (LOAD1 and LOAD2). GEN1 is connected to bus 2 via line 3. The transmission lines (line 1, line2 and line3) are modelled as equivalent $\boldsymbol{\pi}$ transmission

lines. Line 1 and line 2 are 100km long each, while line 3 is 40km long. GEN 2 is connected to bus 3 via a 100MVA transformer (transformer 1) and has a capacity of 80MW and 60MVAr. The DG/HDG consisting of wind generator (DFIG), SOLAR PV and small hydropower system (SHP) is connected to bus 3 via another 100MVA transformer (Transformer 2). Each DFIG is rated 8MW, 0.89 power factor lagging. The SOLAR PV is rated 8MW real power at unity power factor. When SOLAR PV alone is connected to the HDG bus, a capacitor bank is used at that bus to compensate for reactive power. The hydropower is rated 8MW and 4MVAr. LOAD1 and LOAD2 are connected to bus 2 and bus 3, respectively, and are rated 80MW and 40MVAr each.

DIgSILENT power factor 14.1 was used to model this test system. To investigate the effect of a large disturbance, a three-phase fault was applied in the middle of line 2 and cleared after 200ms by removing the line. The data for GEN 2 and DG/HDG are given in Tables A1-A3 in Appendix A. The transformed data are listed in Table A4 in Appendix A.

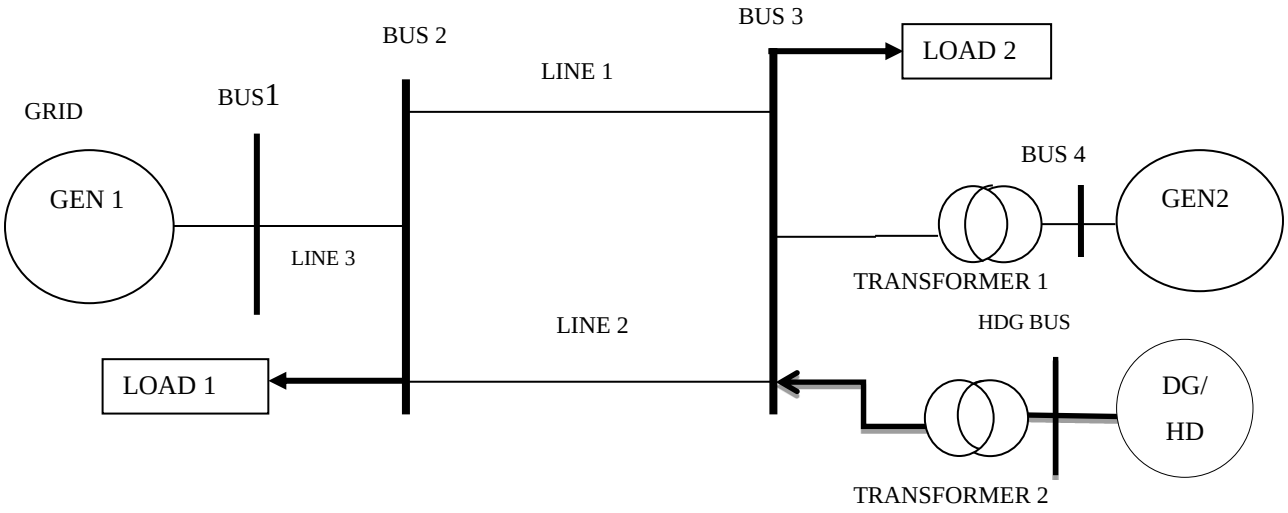

Fig 5.1: Modified Single Machine Infinite Bus System

This power system model was used to investigate the impact of HDG on transient stability.

The focus is to investigate the impact of Hybrid solar PV, wind turbine (Doubly-Fed Induction Generator- DFIG) and small hydropower systems (SHP) on transient stability. In order to obtain all possible combinations, a truth table is formed as shown in Table 5.1. The truth table shows how the three generators can be combined to form HDG. The first column shows various scenarios. There are 8 scenarios. For example, scenario 1 shows the case where there is no integration of DG/HDG. Scenario 2 shows the case where only SHP is integrated and so on. Zero (0) means no generator is connected while one (1) means a generator is connected. The base cases are single source DGs (Scenarios 2, 3 and 5). These base cases were chosen in order to draw out comparisons between HDG and single source DG.

\

Table 5.1: Truth table describing the combination of different DG

SCENARIOS	**WIND TURBINE (DFIG)**	**SOLAR PV**	**SMALL HYDROPOWER (SHP)**	**INFERENCE**
1	0	0	0	No DG Integration
2	0	0	1	Small Hydropower only **(Base case 1)**
3	0	1	0	SOLAR PV only **(Base case 2)**
4	0	1	1	SOLAR PV and Small Hydropower
5	1	0	0	Wind turbine only **(Base case 3)**
6	1	0	1	DFIG and Small Hydropower
7	1	1	0	DFIG and SOLAR PV
8	1	1	1	DFIG, SOLAR PV, Small Hydropower (SHP)

These scenarios will be discussed in detail in section 5.2.

5.2 Simulation Scenarios

The simulation scenarios are discussed in this section.

Case study 1 consists of scenarios 2 (Small Hydropower alone), 3 (SOLAR PV alone) and 5 (DFIG alone) which are the base cases.

Case study 2 consists of scenario 4 (Hybrid SOLAR PV and Small Hydropower)
Case study 3 consists of scenario 6 (Hybrid DFIG and Small Hydropower)
Case study 4 consists of scenario 7 (Hybrid DFIG and SOLAR PV)
Case study 5 consists of scenario 8 (Hybrid DFIG, SOLAR PV and Small hydropower)

Three penetration levels of HDG (PL_{HDG}) were considered:

(i) Import mode, PL_{HDG}=40%
(ii) Balanced mode, PL_{HDG}=50%
(iii) Export mode, PL_{HDG}=80%

The penetration level for HDG is defined as:

$$\%\ PL_{HDG} = \frac{P_{HDG}}{P_{HDG+P_{CG}}} \times 100 \qquad (5.1)$$

where $\%PL_{HDG}$ is the percentage penetration of the DG/HDG, P_{HDG} is the active power generated by HDG and P_{CG} is the active power from the centralized generators (GRID and GEN2).
Note that $P_{CG}+P_{HDG} = P_{LOAD}$
where P_{LOAD} is the power delivered to the load

In all the simulations, the active and the reactive power of GEN2 are kept constant. The descriptions of the penetration levels are as follows:

Import mode: In this mode, the load demands are supplied by GEN2 and HDG with additional supply from the GRID. This is shown in Fig 5.2.

Balanced mode: In this mode, the load demands are met by the combination of GEN2 and HDG without any extra supply from the GRID. This means that the power generated by HDG and GEN 2 is sufficient to meet the load demands. This is shown in Fig 5.3

Export mode: In this mode, HDG and GEN2 supply the loads and export the excess generation to the GRID. This is shown in Fig 5.4.

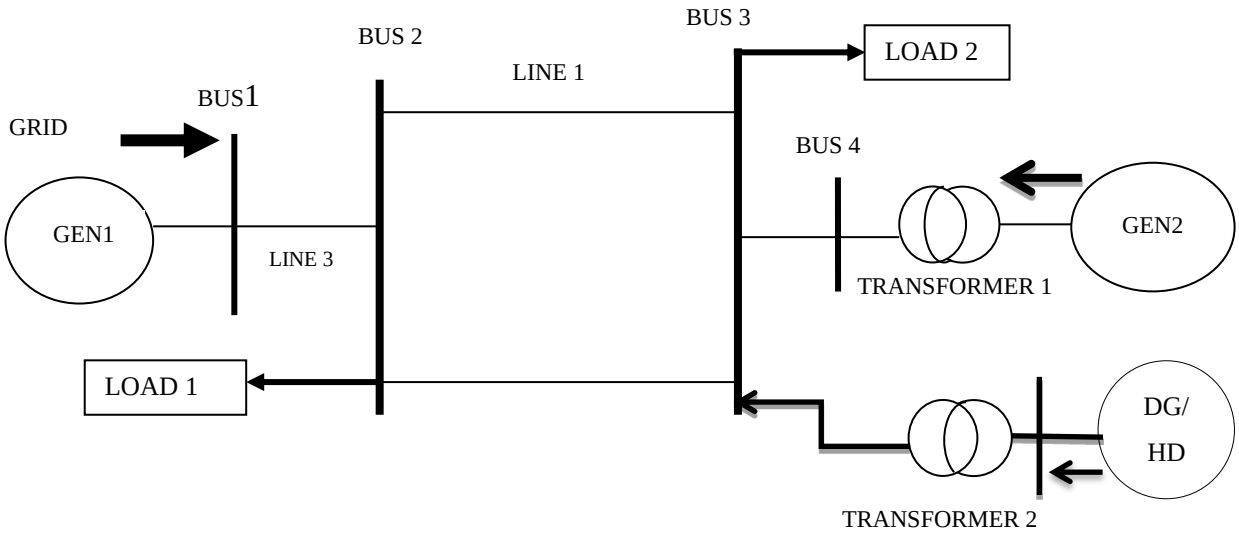

Fig 5.2: Modelling configuration for import mode

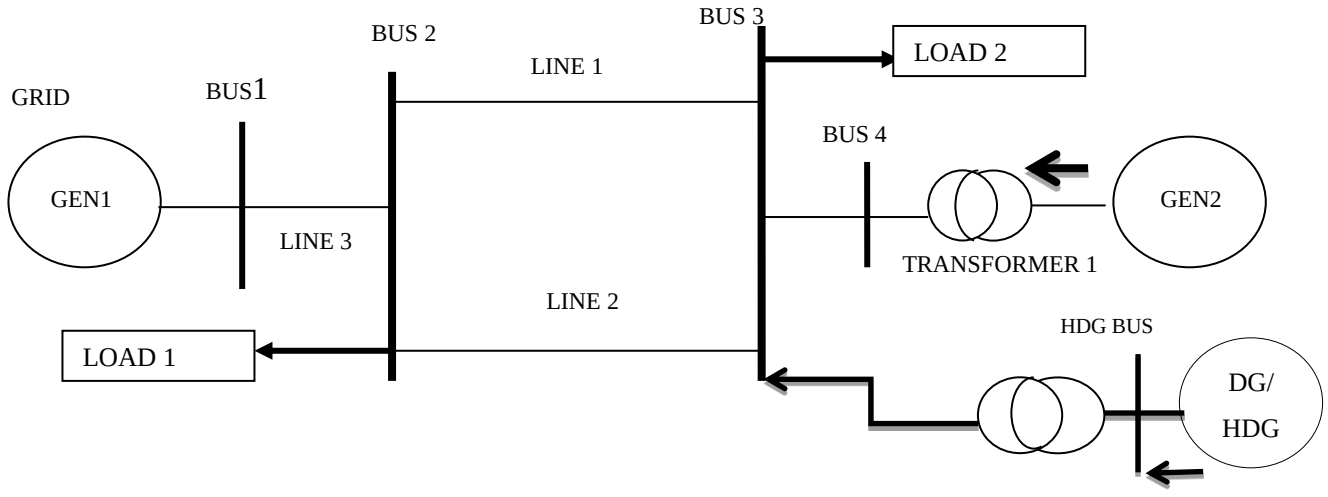

Fig 5.3: Modelling configuration for balanced mode

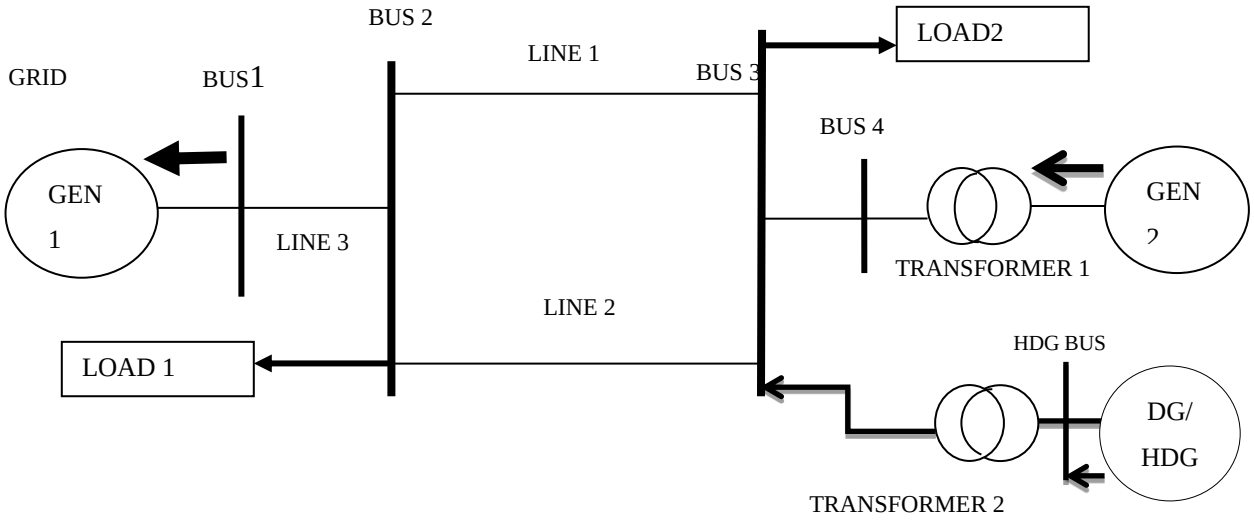

Fig 5.4: Modelling configuration for export mode

5.3 Impact of Hybrid Distributed Generation Using CCT

To measure the impact of HDG on transient stability, the critical clearing time (CCT) is used as the stability index. This index measures the stability margin and indicates the robustness of the system to disturbances. The longer the CCT, the longer the system can tolerate the fault, and the more robust is the system.

The impact of penetration level based on import mode, balanced mode and export mode on transient stability with HDG is investigated by monitoring the CCT. To assess the level of instability, the rotor angle is monitored when a temporary three-phase fault is applied in the middle of line 2 while the CCT is monitored by applying three-phase fault on line 2 at different locations from bus 3. The locations of the fault are 0%, 20%, 40%, 60%, 80% and 100% of the total length of the transmission line (bus 3-bus2). In other word, the fault distance is the distance from bus 3 to the fault location. For example, when the fault occurs at bus 3, the fault location will be 0% and when the fault occurs at bus 2, the fault location will be 100% and so on. The CCT is calculated by increasing the

fault clearing time (FCT) until the rotor angle of GEN 2 reaches its critical clearing angle where further increase will make the system unstable.

5.4 Transient Stability Simulation Results

For the simulation results in this section, the following factors have been taken into consideration: Penetration level, HGD type and load condition, location of HDG and transmission line length.

5.5 HDG Penetration Level and Different HDG Impact on Rotor Angle

The graphs in Figs 5.5-5.7 show the rotor angle swings of GEN 2 when SOLAR PV alone, DFIG alone and HYBRID DFIG +SOLAR PV are integrated into the system. The import mode, balanced mode and export mode are shown in Fig 5.5, Fig 5.6 and Fig 5.7, respectively. From Fig 5.5, it can be observed that when DFIG alone was integrated into the system, the first swing of GEN 2 rotor angle is the highest (i.e.,$-4.99°$) compared to when SOLAR PV and HYBRID DFIG+SOLAR PV were integrated. The second highest first swing occurs with HYBRID DFIG +SOLAR PV, (i.e.,$-8.36°$). The smallest first swing is shown when SOLAR PV alone is connected (i.e., $-15.13°$). It can be seen that when DFIG alone was connected the system has more oscillations compared with the cases with SOLAR PV alone and HYBRID DIFG+SOLAR PV. This suggests that when DFIG alone is integrated into the system, the system is prone to more instability compared to SOLAR PV alone and HYBRID DFIG+SOLAR PV. This is due to the crowbar which is triggered to block the rotor side converter and as a result, the voltage cannot recover completely immediately after the fault is cleared because the rotor side converter cannot provide the necessary reactive power to the generator for magnetization purpose. The generator then absorbs reactive power from the grid. When HYBRID DFIG+SOLAR PV is connected, the system is more transiently stable than when DFIG alone is connected. This can be seen at the settling time. The settling time when HYBRID DFIG+SOLAR PV is integrated into the grid is 8 seconds compared with 10 seconds for DFIG alone. The combination of DFIG and SOLAR PV has improved the first swing and

the subsequent swings. This is because of the good transient stability characteristics of SOLAR PV. When SOLAR PV alone is used, the system seems to have a better transient stability in terms of first swing compared with when HYBRID DFIG+SOLAR PV is used. However, for the subsequent oscillations, when SOLAR PV alone or when HYBRID DFIG+SOLAR PV is used, they have similar settling time. The same explanations can be applied to the balanced mode in Fig 5.6 and export mode in Fig 5.7. However, at the export mode, the GEN 2 rotor angle went out of step when DFIG alone was connected. This is because the penetration of DFIG is now high (80%). The HYBRID DFIG+SOLAR PV and SOLAR PV are transiently stable as shown in Fig 5.7 compared to when DFIG alone is used. The settling time when HYBRID DFIG+SOLAR PV is used is faster than when SOLAR PV alone or DFIG alone are used.

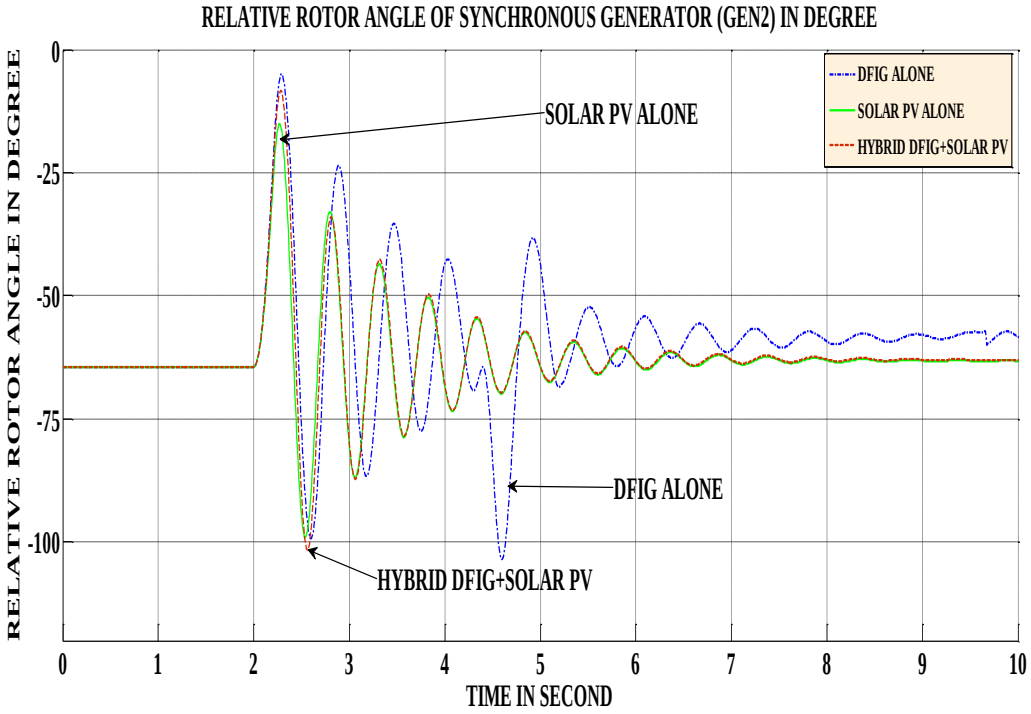

Fig 5.5: Comparison of the impact of SOLAR PV alone, DFIG alone and HYBRID DFIG+SOLAR PV on the rotor angle of GEN2 (Import mode)

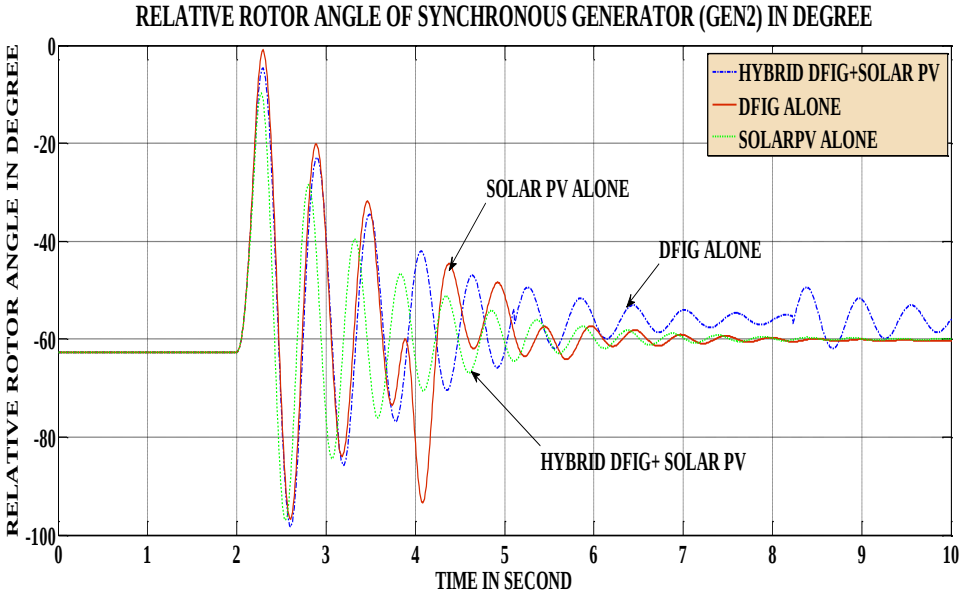

Fig 5.6: Comparison of the impact of SOLAR PV alone, DFIG alone and HYBRID DFIG +SOLAR PV on the rotor angle of GEN2 (Balanced mode)

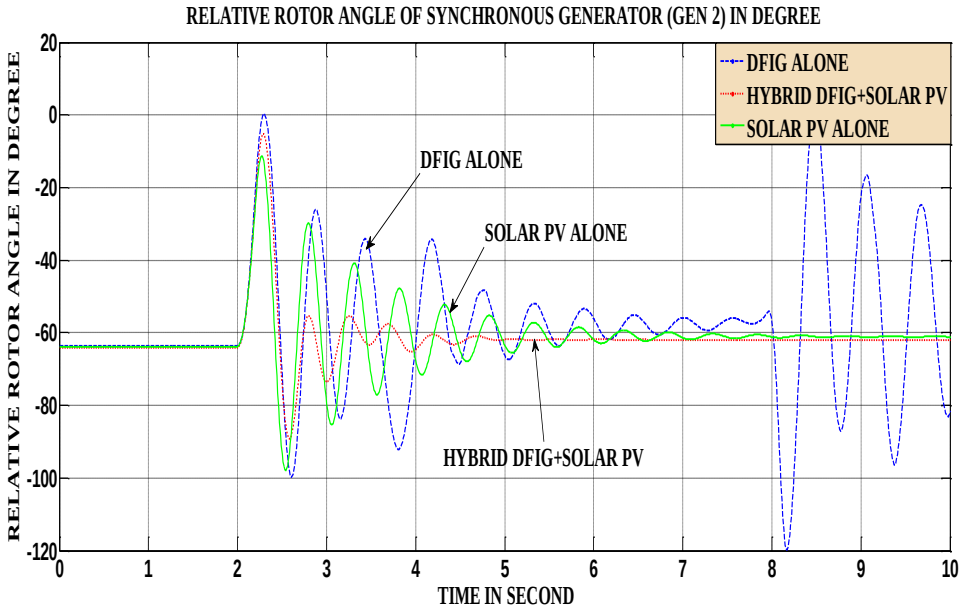

Fig 5.7: Comparison of the impact SOLAR PV alone, DFIG alone and HYBRID DFIG +SOLAR PV on the rotor angle of GEN2 (Export mode)

As it can be seen, the instability increases as the penetration level of the DG/HDG increases. If HYBRID DFIG+SOALR PV is used, the rotor angle shows a reduced first swing compared to DFIG alone.

Figs 5.8-5.10 show the simulation results when HYBRID DFIG+SOLAR PV, HYBRID DFIG+SHP, HYBRID SOLAR PV+SHP and DFIG alone were integrated into the grid, for import, balanced and export modes respectively. For import mode, (see Fig 5.8), there is not much difference in the first swing of rotor angle of all the curves though the highest first swing occurs when DFIG alone is integrated. The same happened in Fig 5.9, the rotor angle of GEN 2 when DFIG alone was integrated shows the highest instability. HYBRID SOLAR PV+SHP shows improved stability compared to DFIG alone. For the export mode (see Fig 5.10), the rotor angle of GEN2 when DFIG alone was integrated went out of step but when DFIG alone was combined with other energy sources (HYBRID DFIG+SOLAR PV, HYBRID DFIG+SHP), the transient stability is improved. When HYBRID SOLAR PV+SHP was used, the rotor angle of GEN 2 is more stable compared to the rest in Fig 5.10. The three hybrids (HYBRID DFIG+SOLAR PV, HYBRID DFIG+SHP, HYBRID SOLAR PV+SHP) settle down within 6 seconds while the DFIG alone is unstable even up till 10 seconds. HYBRID SOLAR PV+SHP shows the lowest first swing, followed by HYBRID DFIG+SHP, and then HYBRID DFIG+SOLAR PV.

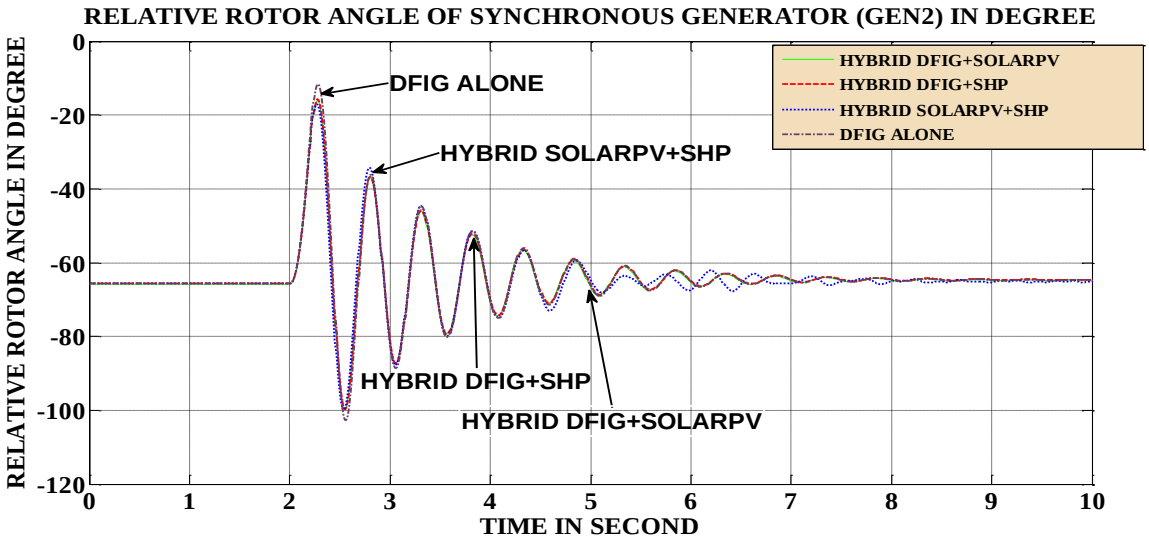

Fig 5.8: Comparison of the impact of HYBRID DFIG+ SOLAR PV, HYBRID DFIG+ SHP, HYBRID SOLAR PV +SHP, and DFIG alone system on the rotor angle of GEN2 (Import mode)

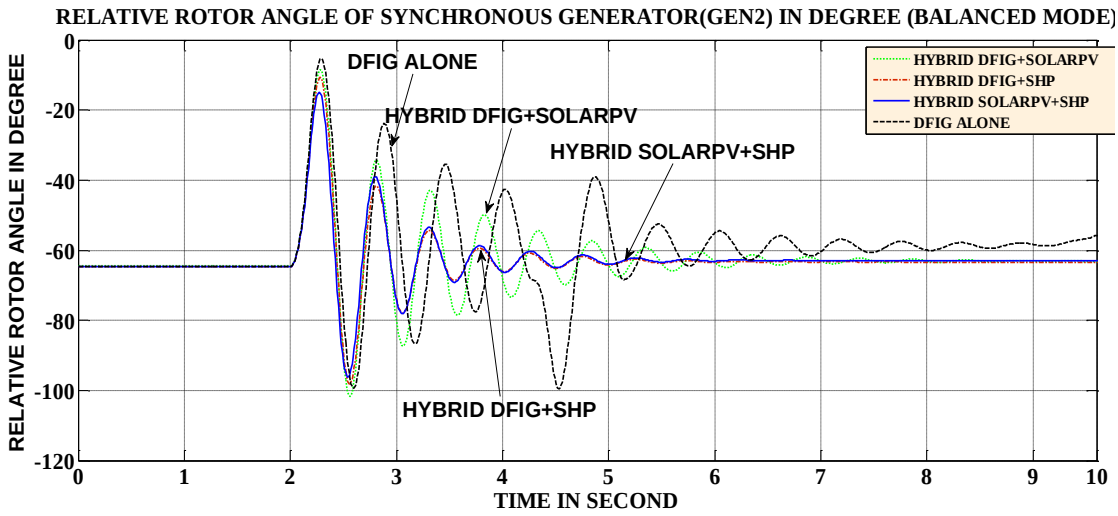

Fig 5.9: Comparison of the impact of HYBRID DFIG+ SOLAR PV, HYBRID DFIG+ SHP, HYBRID SOLAR PV +SHP, and DFIG alone system on the rotor angle of GEN2 (Balanced mode)

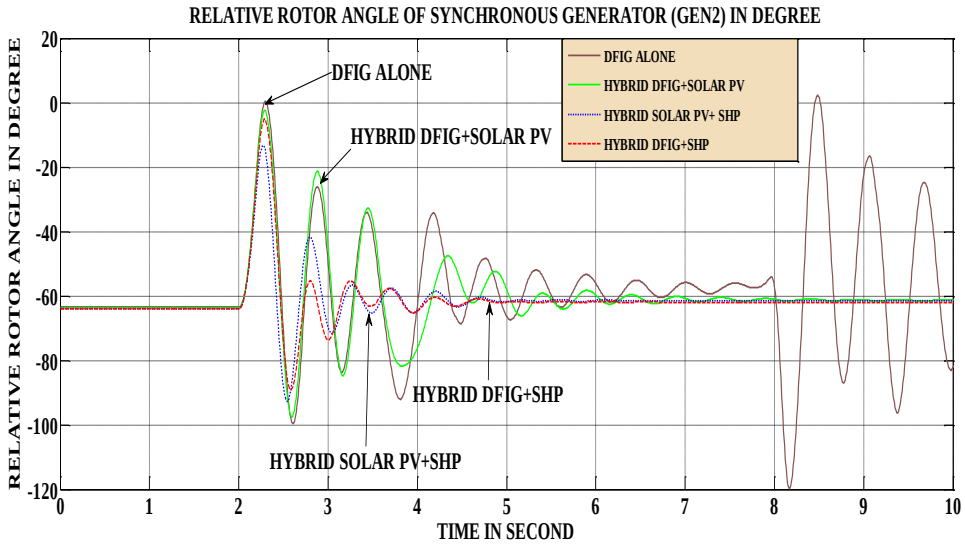

Fig 5.10: Comparison Of the impact of HYBRID DFIG+ SOLAR PV, HYBRID DFIG+ SHP, HYBRID SOLAR PV +SHP, and DFIG alone system on the rotor angle of GEN2 (Export mode).

It is already established from the simulations in Figs 5.5-5.10 that as the penetration level increases the instability also increases irrespective of the HDG type used. As a result of this, export mode alone will be considered in the rest of this section.

CASE STUDY 1

In this case study, comparison of single source DGs was made. The DG sources consist of SHP alone, SOLAR PV alone and DFIG alone.

Fig 5.11 shows the rotor angle of GEN2 when SHP alone, SOLAR PV alone and DFIG alone were integrated into the system. From Fig 5.11, it was observed that the highest first swing occurs when DFIG alone was integrated. With DFIG alone, the rotor angle of GEN2 went out of step within 8seconds while with SHP alone, the system settles down within 5.5 seconds and with SOLAR PV alone, it settles down within 7seconds. The least first swing is when SHP alone is used compared to when SOLAR PV alone is used. It can be seen that DFIG alone has more negative impact on the rotor angle than SHP alone and SOLAR PV alone. In other word, the transient stability improves when SHP alone and SOLAR PV alone are integrated into the system as compared to DFIG alone.

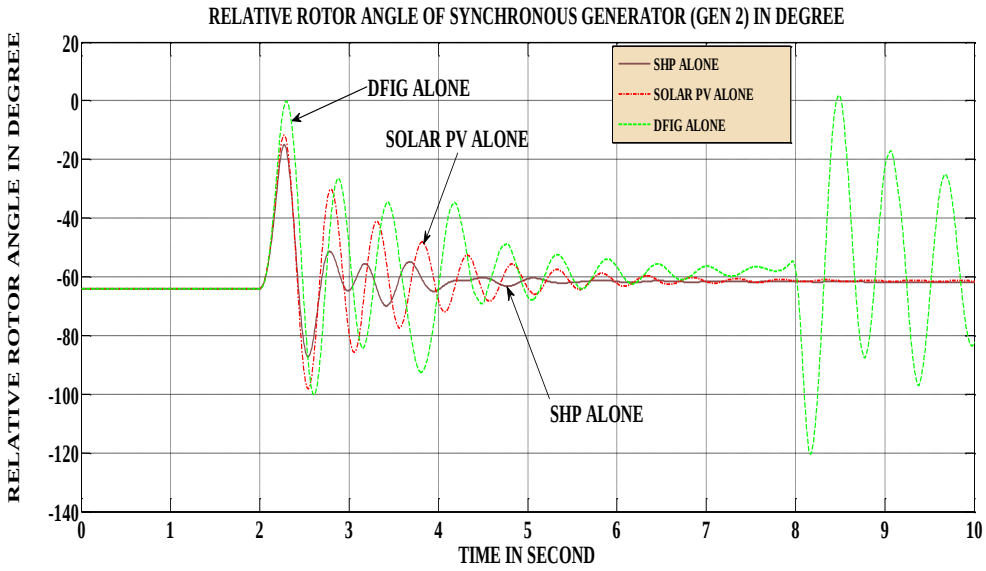

Fig 5.11: Comparison of the impact of SHP alone, DFIG alone and SOLAR PV alone on the rotor angle of GEN2 (Export mode).

CASE STUDY 2

In this case study, HYBRID SOLAR PV+SHP was compared with single source DGs in case study 1 (SHP alone, SOLAR PV alone, and DFIG alone).

The graph in Fig 5.12 shows the rotor angle of GEN 2 when HYBRID SOLAR PV+ SHP, SHP alone, SOLAR PV alone and DFIG alone were connected during export mode.

From the graph in Fig 5.12, it is observed that the highest first swing was when DFIG alone was connected. With DFIG alone, the rotor angle of GEN 2 went out of step. When HYBRID SOLAR PV+SHP was used, the first swing of the rotor angle of GEN 2 is almost the same as with the SHP alone. However, the rotor angle settles down within 5.5 seconds when HYBRID SOLAR PV+SHP and SHP alone were used compared to 7 seconds for SOLAR PV alone. It can be seen that, the impact of HDG on transient stability depends on the type of HDG involves. However, the stability is improved when HYBRID SOLAR PV+SHP is used compared to when SOLAR PV alone and DFIG alone were used. SHP alone and HYBRID SOLAR PV+SHP show almost the same degree of instability in term of the first swing. The worst transient stability characteristic is shown when DFIG alone is used.

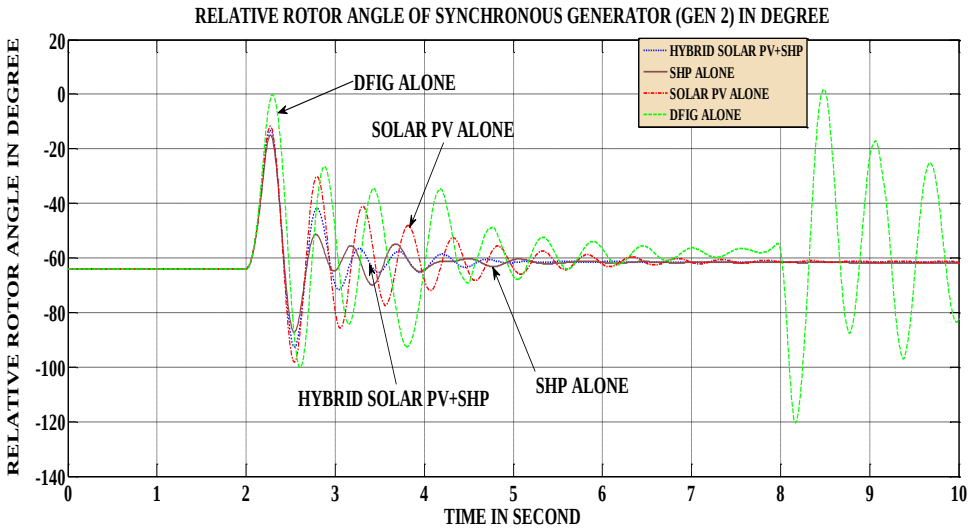

Fig 5.12: Comparison of the impact of HYBRID SOLAR PV + SHP and single source DGs (SHP alone, SOLAR PV alone, DFIG alone) on the rotor angle of GEN2 (Export mode).

CASE STUDY 3

In this case study, HYBRID DFIG+SHP was compared with single source DG in case study 1 (SHP alone, SOLAR PV alone, and DFIG alone).

The graph in Fig 5.13 shows the rotor angle of GEN 2 when HYBRID DFIG+SHP, SHP alone, SOLAR PV alone and DFIG alone were connected to the grid. When DFIG alone was used, GEN2 shows the worst first swing and went out of step within 8 seconds. The settling time when SHP alone was used is quicker (5.5 seconds) compared to the settling time when SOLAR PV alone was used (7 seconds). This is due to the fact that SHP supplies reactive power while SOLAR PV does not supply reactive power. When HYBRID DFIG+SHP is used, the stability is improved in term of first swing compared to when DFIG alone is used. At the same time, the stability is improved when HYBRID DFIG+SHP is used in term of the settling time compared with when SOLAR PV alone is used, but when HYBRID DFIG+SHP is used, the settling time is slightly faster than when SHP alone is used.

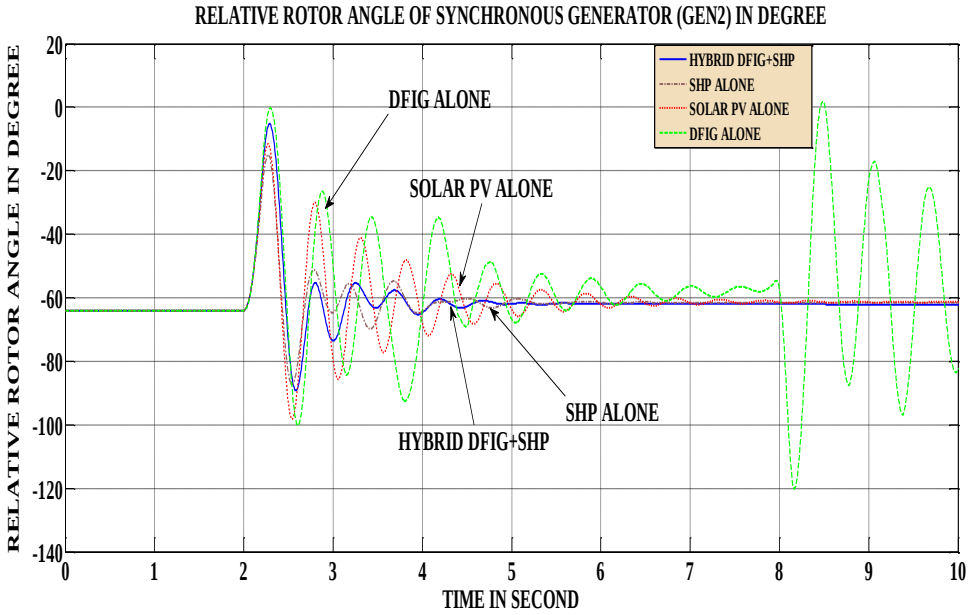

Fig 5.13: Comparison of the impact of HYBRID DFIG + SHP and single source DGs (SHP alone, SOLAR PV alone, DFIG alone) on the rotor angle of GEN2 (Export mode).

CASE STUDY 4

In this case study, HYBRID DFIG+SOLAR PV was compared with single source DGs in case study 1 (SHP alone, SOLAR PV alone, and DFIG alone).

The graph in Fig 5.14 shows the rotor angle of GEN 2 when HYBRID DFIG+SOLAR PV, SHP alone, SOLAR PV alone and DFIG alone were connected to the grid. The DFIG alone again shows the worst first swing and went out of step within 8 seconds, but when HYBRID DFIG+SOLAR PV was used, the first swing of the rotor angle of GEN 2 is reduced from (0°) to $(-1.24°)$ and settled in 5 seconds.

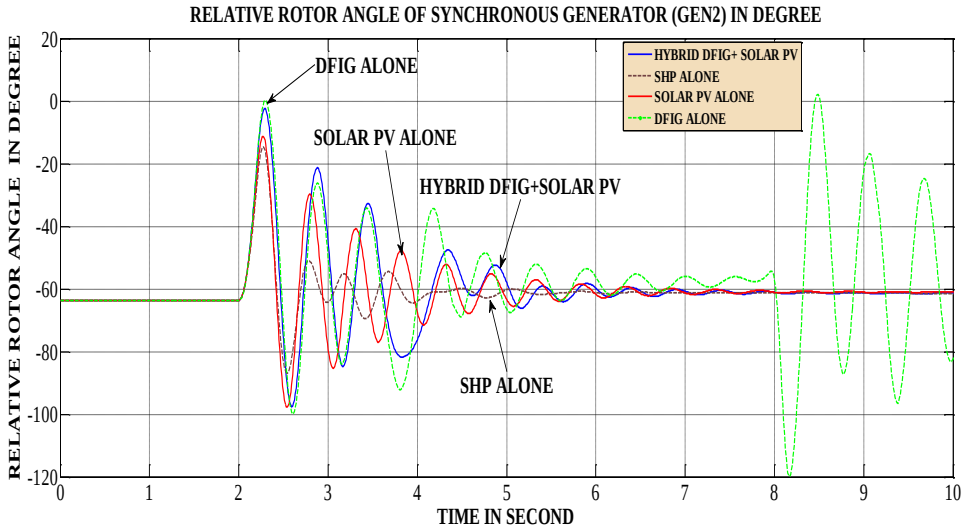

Fig 5.14: Comparison of the impact of HYBRID DFIG+ SOLAR PV and single source DGs (SHP alone, SOLAR PV alone, DFIG alone) on the rotor angle of GEN2 (Export mode).

CASE STUDY 5

In this case study, HYBRID DFIG + SOLAR PV+ SHP was compared with single source DGs in case study 1 (SHP alone, SOLAR PV alone, and DFIG alone).

The graph in Fig 5.15 shows the rotor angle of GEN 2 when HYBRID DFIG+SOLAR PV+ SHP, SHP alone, SOLAR PV alone and DFIG alone were connected to the grid.

The highest first swing oscillation was noticed when HYBRID DFIG+SOLAR PV+SHP was connected. The subsequent oscillations lasted until 10 seconds. When DFIG alone

was connected, the rotor angle of GEN 2 went out of step at 8 seconds compared to when HYBRID DFIG + SOLAR PV+ SHP was connected.

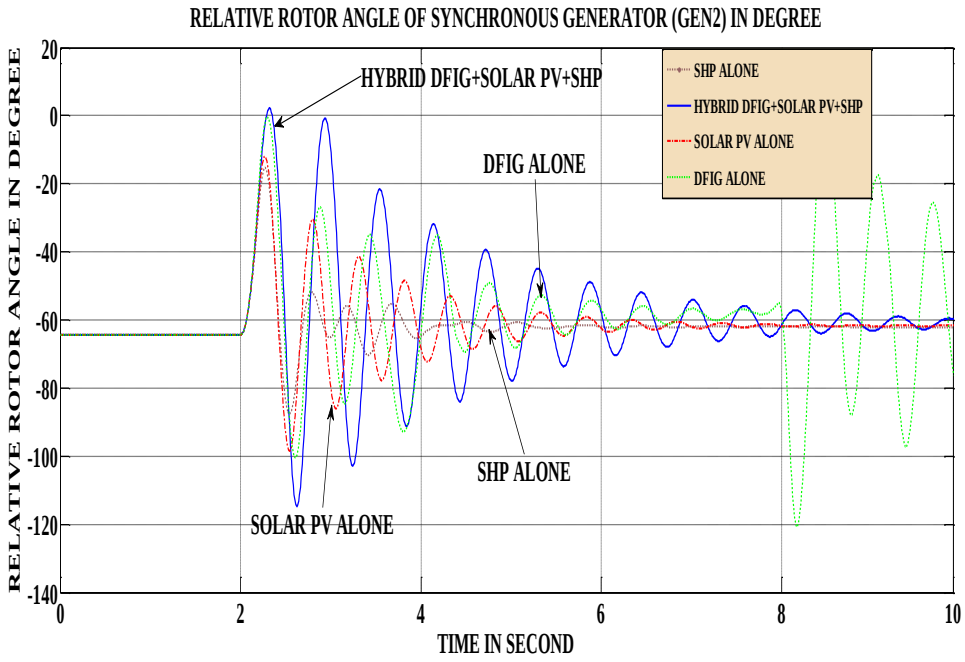

Fig 5.15: Comparison of the impact of HYBRID DFIG+SOLAR PV + SHP and single source DGs (SHP alone, SOLAR PV alone, DFIG alone) on the rotor angle of GEN2 (Export mode).

5.6 Summary

From all the simulations, it can be deduced that the highest first swing (i.e., (2.21°) occurs when HYBRID DFIG+SOLAR PV+SHP was integrated into the grid. HYBRID DFIG+SOLAR PV is the second highest (−1.24°), followed by HYBRID DFIG+SHP (−5.10°) and HYBRID SOLAR PV+SHP (−13.5°). It is observed that the system is closer to its stability margin if three DGs are combined together, compared to when two DGs are used. It can also be deduced that the first swing and settling time of GEN 2 improved whenever a hybrid type is used compared to when DFIG alone is used. On the average, the settling time is faster in all the hybrid types compared to when the single source DG is used, but the first swing of GEN 2 is better when single source DG is used compared to when hybrid type is used except for DFIG alone. The transient stability depends on the types of HDG used.

As the penetration increases, the instability also increases irrespective of the generators used or hybrid types used. SOLAR PV does not have a rotary part and it has zero reactive power. However, SOLAR PV operated in line with the grid codes (when operating at unity power factor) does not draw reactive power from the grid while DFIG does during fault. This is responsible for the instability noticeable in the system when DFIG is used. The crowbar in DFIG during operation triggers and blocks the rotor side converter and prevents voltage recovery completely after the fault. The rotor side converter cannot provide necessary reactive power to the generator for magnetization purpose. The generator then absorbs reactive power from the grid. However, SOLAR PV does not absorb reactive power from the grid and as a result the first swing oscillation is better than the DFIG.

For completeness, we have also investigated the case where another wind generator, namely, Converter Driven Synchronous Generator (CDSG) was used instead of DFIG. The results are included in Figs C1.1-C1.3 of Appendix C1. It is shown that, the transient stability margin when CDSG alone is connected is improved compared to when DFIG alone is used. When HYBRID CDSG+SOLAR PV+SHP is used, the transient stability is improved compared to when HYBRID DFIG+SOLAR PV+SHP is used.

For clarity sake, the comparison of single source DG (case study1) and other case studies in separate graphs are shown in Appendix C6.

5.7 HDG Penetration Level and Different Fault Locations on Critical Clearing Time (CCT)

In this section, the impact of HDG penetration level, different HDG types and fault locations on the critical clearing time (CCT) is investigated. The decrease in critical clearing time (CCT) indicates an increase in instability (decrease stability margin). Tables 5.2-5.4 show the CCT values and the average values of the CCT of the power system network for import, balanced and export modes when SHP alone, SOLAR PV alone and DFIG alone were integrated into the system, respectively. From Tables 5.2-5.3, it is observed that, as the fault location is increasing from 0% to 60%, the CCT values also increased from relatively smaller values to maximum values and then decreased again

from 80% fault location to 100%. This is fairly in agreement with the literature which state that the maximum transfer admittance occurs at the midpoint of the transmission line. The curve between transfer admittance and the distance of the fault will be symmetrical about 0.5 p.u. length, where maximum transfer admittance occurs if the circuit is symmetrical about the middle of the line. The CCT value will begin to decrease after the midpoint. Table 5.4 followed a similar pattern except for export mode where the maximum value of the CCT occurs at location 80% instead of 60%. However, the difference between the maximum CCT value of 80% and that at 60% is marginal (i.e., 0.0185%) which can be neglected.

Also from Tables 5.2-5.4, it can be seen that the transient stability margin decreases with increasing penetration level. For example, in Table 5.2, when the fault was applied at 100km from bus 3, i.e. exactly on bus 2, the CCT value decreases from 280ms in the import mode to 278ms in the balanced mode and later to 270ms in the export mode. The average value of the CCT at the import mode is 333.3ms, balanced mode is 329.7ms and the export mode is 318.5ms. This shows that, as the penetration level of the HDG increases, the CCT decreases (i.e., transient stability margin reduces). The same applied to Tables 5.3-5.4. As the penetration level increases, the decrease in the CCT values is very significant when DFIG alone is used compared to other DGs. This can be explained why the system with DFIG became unstable at export mode. This can be seen from the average values of the CCT reported in Tables 5.2-5.4.

Furthermore, the CCT value depends on the type of DG used. For example, the average values of the CCT when SHP alone is integrated into the grid (see Table 5.2) are higher at all the modes than the average values of the CCT when SOLAR PV alone is integrated into the grid (see Table 5.3). The average values of the CCT at all the modes when DFIG alone is connected to the grid are the smallest. This suggests that instabilities arising from integrating DFIG alone are higher compared to when SOLAR PV alone and SHP alone are connected. These CCT values agreed with the initial simulations when the rotor angle was monitored that the increase in penetration level increases the transient instability.

Table 5.2: The critical clearing time of synchronous generator (GEN2) with integrated SHP Alone

SHP Alone			
Fault location	**Import mode**	**Balanced mode**	**Export mode**
%	CCT (ms)	CCT (ms)	CCT (ms)
0	280	267	256
20	320	315	310
40	370	370	356
60	390	390	370
80	360	355	349
100	280	278	270
	Average (ms)		
	333.3	329.7	318.5

Table 5.3: The critical clearing time of synchronous generator (GEN2) with integrated SOLAR PV Alone

SOLAR PV Alone			
Fault location	**Import mode**	**Balanced mode**	**Export mode**
%	CCT (ms)	CCT (ms)	CCT (ms)
0	265	260	255
20	310	300	295
40	350	340	330
60	370	350	340
80	340	320	310
100	265	250	240
	Average (ms)		
	316.7	303.3	295

Table 5.4: The critical clearing time of synchronous generator (GEN2) with integrated DFIG Alone

DFIG Alone			
Fault location	**Import**	**Balanced mode**	**Export**
%	CCT (ms)	CCT (ms)	CCT (ms)
0	250	40	30
20	290	60	40
40	320	70	50
60	330	80	53
80	310	70	54
100	240	90	40
	Average (ms)		
	290	68.3	44.5

Tables 5.5–5.7 show the CCT values and the average values of the CCT when HYBRID SOLAR PV+SHP, HYBRID DFIG+SHP and HYBRID DFIG+SOLAR PV were integrated into the grid, respectively.

For example, at the export mode, the average values of the CCT for HYBRID SOLAR PV+SHP, HYBRID DFIG+SHP and HYBRID DFIG+SOLAR PV are 290ms, 256.7ms and 216.7ms, respectively.

This suggests that when HYBRID SOLAR PV+SHP is used, the system is more transiently stable (improved stability margin) compared to when HYBRID DFIG+SHP and HYBRID DFIG+SOLAR PV were used. This can be seen also from all the modes in Tables 5.5-5.7.

Comparing hybrid type with a single source, the average values of the CCT when HYBRID SOLAR PV+SHP is used indicates an improved stability compared to when DFIG alone and SOLAR PV alone are used except in the export mode of SOLAR PV. But in the case of SHP alone, the average values of the CCT are higher at the balanced and export modes alone compared to when HYBRID SOLAR PV+SHP is used.

The CCT values and the average values of the CCT when HYBRID DFIG+SOLAR PV+SHP is connected to the grid are shown in Table 5.8. It can be seen that for the

export mode, the average value of the CCT is smaller compared to other hybrids in Tables 5.5-5.7. The average values of the CCT for the import and the balanced modes in Fig 5.8 are generally smaller than the hybrid with two DGs such as HYBRID SOLAR PV +SHP and HYBRID DFIG+SHP except in the balanced mode when HYBRID DFIG+SHP is used. The difference between the average value of the CCT at a balanced mode when HYBRID DFIG+SOLAR PV+SHP and HYBRID DFIG+SHP is used is small (i.e., 0.0181%) and can be neglected. However, the average values of the CCT for HYBRID DFIG+SOLAR PV+SHP are higher at the import and balanced mode compared with when HYBRID DFIG+SOLAR PV is used. This suggests that the system with three DGs is more prone to instability than the system with two DGs and the stability worsen as the penetration increases compared to other hybrids.

For Completeness, we have also investigated the case where CDSG was used instead of DFIG. The results are given in Tables C2.1- C2.3 of Appendix C2. When HYBRID CDSG+SOLAR PV+SHP is connected to the grid, the stability is better compared to when HYBRID DFIG+SOLAR PV+SHP is integrated. It shows that hybridizing CDSG with other generators (SOLAR PV or SHP) up to three generators improves the stability more than when DFIG is hybridized with two other generators.

Table 5.5: The critical clearing time of synchronous generator (GEN2) with integrated HYBRID SOLAR PV+SHP

HYBRID SOLAR PV+SHP			
Fault location	**Import mode**	**Balanced mode**	**Export mode**
In %	CCT(ms)	CCT(ms)	CCT(ms)
0	270	267	260
20	330	310	300
40	390	360	320
60	420	370	330
80	390	340	300
100	290	260	230
	Average (ms)		
	348.3	317.8	290

Table 5.6: The critical clearing time of synchronous generator (GEN2) with integrated HYBRID DFIG+SHP

HYBRID DFIG+SHP			
Fault location	**Import mode**	**Balanced mode**	**Export mode**
In%	CCT(ms)	CCT(ms)	CCT(ms)
0	250	240	200
20	303	300	270
40	350	330	290
60	380	350	290
80	350	320	270
100	255	250	220
	Average (ms)		
	326.6	298.3	256.7

Table 5.7: The critical clearing time of synchronous generator (GEN2) with HYBRID DFIG +SOLAR PV

HYBRID DFIG +SOLAR PV			
Fault location	**Import mode**	**Balanced mode**	**Export mode**
In %	CCT(ms)	CCT(ms)	CCT(ms)
0	240	250	150
20	295	290	230
40	340	310	210
60	360	320	230
80	330	290	260
100	240	240	220
Average (ms)			
	300.8	283.3	216.7

Table 5.8: The critical clearing time of synchronous generator with integrated HYBRID DFIG+SOLAR PV+ SHP

HYBRID DFIG+SOLAR PV+ SHP			
Fault location	**Import mode**	**Balanced mode**	**Export mode**
In %	CCT(ms)	CCT(ms)	CCT(ms)
0	256	252	100
20	300	300	160
40	340	340	210
60	360	360	240
80	310	330	220
100	250	240	150
	Average (ms)		
	302.7	303.7	180

5.8 Summary

Comparing the export mode of Table 5.7 and Table 5.8, it shows that from a stability point of view and based on the simulation results, the stability is improved when DFIG is hybridized with other DG but worsen when hybridized with two DGs under a high penetration level. At import mode and balanced mode when the penetration is low and moderate, respectively, the average values of the CCT when HYBRID DFIG+SOLAR PV+SHP is used is better than when HYBRID DFIG+SOLAR PV is used. However, the average CCT when HYBRID DFIG+SOLAR PV+SHP is used is lower compared to when HYBRID SOLAR PV+SHP was used at all the modes.

The CCT value depends on the penetration level, fault location as well as the HDG types used. The CCT decreases with increase in penetration level irrespective of the HDG types used.

5.9 HDG Penetration Level and Load Condition Impact on Rotor Angle

Load demand is stochastic in nature. It changes with time. The impact of changing load on transient stability is presented in this section. It is assumed in this thesis that an additional load of 24MW and 12MVAr are added every 6 years. The load demand is estimated for a period of 30 years at 6 years step increase as shown in Table 5.9.

5.9.1 Simulation Results With Varying Load and Different types of HDG

In the simulation, the base load is 80MW and 40MVAr for each load (LOAD1 and LOAD2). Note that only the export mode is considered.

Table 5.9: The growth in demand for 30 years with 6 years interval

Years	**LOAD (MVA)**
0	80 +j40 (base load)
6	104+j52
12	128+j64
18	152+j76
24	176+j88
30	200+j100

The increase in load is covered by using one DG while the other DG covered half of the base load. In other word, after the first 6 years, the increase in load is estimated to be 24+j12MVA.One DG supplied 80+j40MVA (half of base load) while the other DG supplied 24+j12MVA. The choice of which DG to use to supply the step increase in load demand depends on the availability of the primary source and the location. When DG is used to supply the increasing load, it is assumed that the primary energy source is abundant in such location.

Three assumptions were made in this section.

1) Half of the base load was supplied by the SOLAR PV but the increasing load demand was supplied by SHP and vice versa. This is shown in Fig 5.16 with the label (SOLAR PV (base load) and SHP (Additional load).
2) Half of the base load was supplied by the SOLAR PV but the increasing load was supplied by the DFIG and vice versa. This is shown in Fig 5.17 with the label (SOLAR PV (base load) and DFIG (Additional load).
3) Half of the base load was supplied by the SHP but the increasing load was supplied by the DFIG and vice versa. This is shown in Fig 5.18 with the label (SHP (base load) and DFIG (Additional load).

The first assumption means that the steps increased in the load were supplied by SHP while SOLAR PV supplied half of the total base load and vice versa. Since there are

two loads (each 80+j40MVA), the total base load is 160+j80 MVA. While the first load increase is 24+j12MVA (reactive power has also increased).

Consider the year 30 where the total load is 200+j100MVA (see last row in Table 5.9). The total base load (LOAD1 & LOAD2) is 160+j80MVA. The load increase is 120+j60MVA for one load.

DG supplies the half of the base load (80+j40 MVA) and GEN2 supplies the other part of the base load (80+j40 MVA).

The graph depicted in Fig 5.16 shows that when SOLAR PV supplies the additional load increase (120+j60MVA) and SHP supplies half of the base load, the system has the larger first swing and more subsequent oscillations as compared to when SHP supplies the additional load increase. Also, when SOLAR PV supplies the load increase, which is higher than the base load, the impact of SOLAR PV will be higher or dominant. When SHP is used to supply additional load increase, the transient stability is improved because SHP can also supply reactive power to the grid.

From Fig 5.17 it can be seen that the transient stability margin is decreased when DFIG is used to supply the load increase compared to when SOLAR PV supplies the load increase. This is because in Fig 5.17, much of the load is supplied by DFIG which in this thesis shows the worst transient stability case. When SOLAR PV is used to supply the load increase in Fig 5.17, the stability is improved and the system settled down within 6 seconds.

Fig 5.18 shows that the transient stability margin is improved when SHP is used to supply the increasing load and DFIG is used for the base load compared to when DFIG is used to supply the additional load increase.

In all the three graphs (Figs 5.16-5.18), the stability is improved when SHP is used to supply the load increase but worsened when DFIG is used to supply the load increase.

The transient stability depends on the combination of different DGs. For example, the transient stability in Fig 5.16 worsened when SOLAR PV supplied the load increase, but in Fig 5.17 when SOLAR PV supplied the load increase and DFIG supplied the base load, the stability is improved.

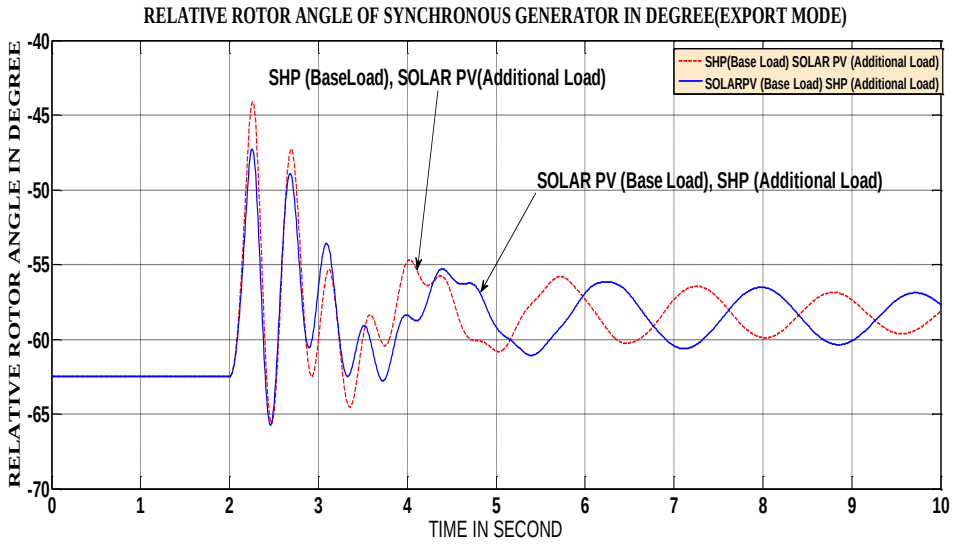

Fig 5.16: Rotor angle of (GEN2) indicating Load supply by SOLAR PV and SHP and vice versa

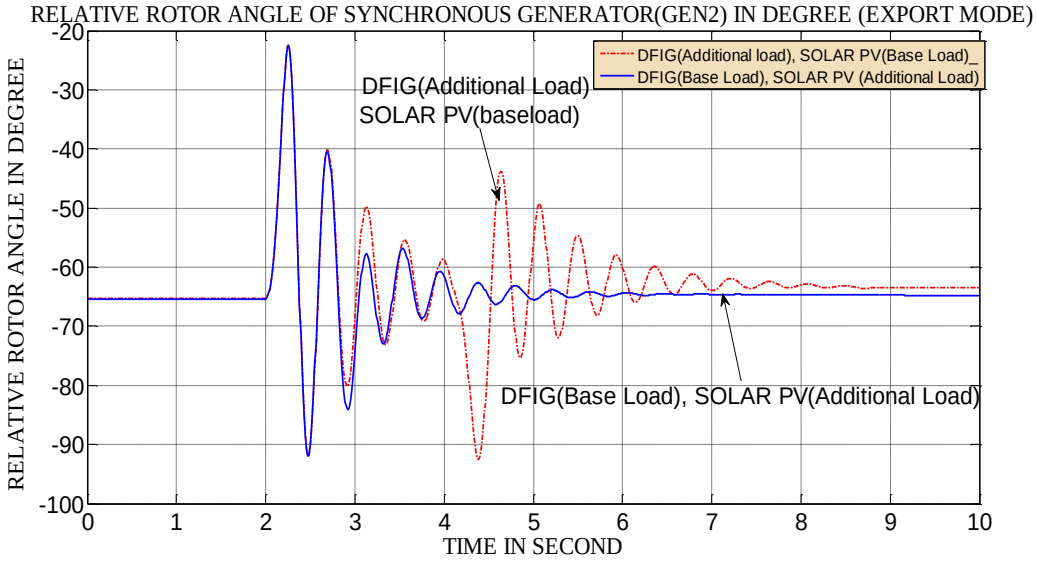

Fig 5.17: Rotor angle of (GEN2) indicating Load supply by SOLAR PV and DFIG and vice versa

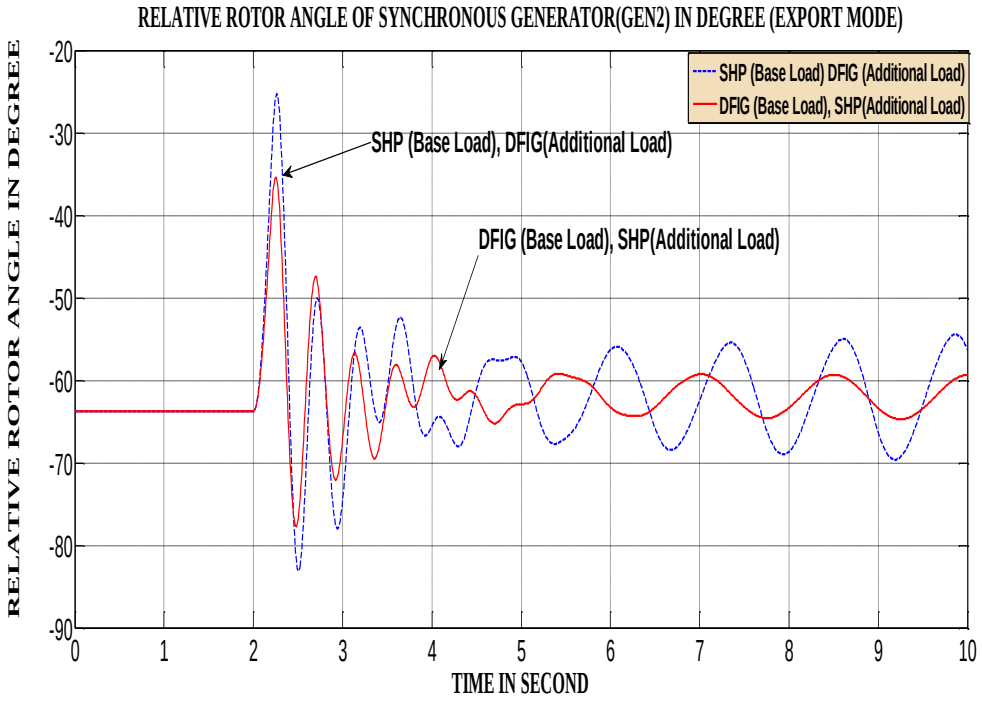

Fig 5.18: Rotor angle of GEN 2 indicating Load supply by SHP and DFIG and vice versa

5.9.2 HDG Penetration Level and Load Condition Impact on Critical Clearing Time (CCT)

Consider the last row of Table 5.10 (i.e., year 30) where the total load is 200+j100MVA. Since half of the base load (LOAD 1) is 80+j40, the load increase is 120+j60MVA. Table 5.11 shows the CCT values during step increase in load demand.

Table 5.10: CCT during Step Increase in Load Demand

LOADS (MVA)	**DFIG (Additional Load) and SOLAR PV (base load)**	**DFIG (base load) and SOLAR PV (Additional Load)**	**SOLAR PV (base load) and SHP (Additional Load)**	**SOLAR PV (Additional Load) and SHP(base load)**	**SHP (Additional Load) and DFIG (base load)**	**SHP (base load) and DFIG (Additional Load)**
	CCT (ms)					
104+j52	395	310	420	500	400	470
128+j64	380	300	450	490	390	450
152+j76	210	290	470	480	220	140
176+j88	70	130	480	460	120	100
200+j100	65	150	490	450	150	95
	Average (ms)					
	224	236	462	476	256	251

From Table 5.10, it is observed that the transient stability of the system depends on the DG that is used to supply the highest megawatt (i.e., dominant). For example, in column 2 of Table 5.10, DFIG is used to supply the additional load while SOLAR PV supplied the base load. When the load was 104+j52 MVA, DFIG only supplied 24+j12MVA, while SOLAR PV is used to supply 80+j40MVA. In this case, the impact of SOLAR PV on the transient stability dominates. As the additional load increases, the transient stability margin decreases because the DFIG now supplies the additional load increase and becomes dominant compared to SOLAR PV. Comparing column 2 with column 3, the transient stability is improved when SOLAR PV supplies the additional loads compared to when DFIG supplies the additional loads (see the average values of the CCT in Table 5.10).

It is therefore observed that whenever DFIG supplies the largest megawatt, the transient stability is worsened compared to other DGs.

However, the case of combination of SOLAR PV and SHP is different (column 4 and 5 in Table 5.10) when the load is 104+j52. Under this condition, when SOLAR PV supplies the additional load and SHP supplies the base load (column 5), the transient stability is improved compared to when SOLAR PV supplies the based load and SHP supplies the additional load (column 4). This is because SHP initially supplied the highest load (80+j40MVA). But when the load increases and SOLAR PV was used to supply the increasing load, the transient stability decreases, but when SHP supplies the increasing load in column 4, the stability improves.

However, when SHP supplies the additional load, the transient stability was lower initially compared to when SHP supplies the based load (column 5). As more additional loads are added, the transient stability continues to increase as can be seen by the increase in the CCT values which increases from 420ms to 490ms. But in column 5, the CCT values decreased. Column 6 shows the CCT when SHP supplies the additional load and DFIG supply the base load while column 7 shows the opposite. It can be seen that from the average values of the CCT, the average value of the CCT is lower when SHP is used to supply the base load and DFIG supply the additional load compared to when SHP supplies the additional loads and DFIG is used to supply the base load.

5.10 Summary

The stochastic nature of the load is investigated in this section. Based on the simulations transient stability is improved when the combination of HYBRID SOLAR PV+SHP is used compared to when HYBRID DFIG+SOLAR PV is used. However, the transient stability is worsened whenever DFIG is combined with other DGs to supply the additional load compared to when SHP and SOLAR PV are combined. As the additional load increases transient stability also decreases except in case of SOLAR PV (base load) and SHP (additional load).

5.11 HDG Penetration Level and Location of HDG Impact on Rotor Angle

The location of HDG is determined by the availability of primary energy source. HDG should be sited in a place where the primary energy source is abundantly available. HDG

can be sited at a single point (concentrated) or on several places in such a way that the generators are centrally coordinated (dispersed). Dispersed HDG is assumed to be close to the load (e.g., rooftop solar PV) while concentrated is located where the energy source could be found and possibly far from the load. This section explains the impact of HDG on the grid when the HDGs are dispersed, and when they are concentrated on a single point. Note that the simulation results presented in this section are for export mode only. The followings were investigated:

1) Dispersed and concentrated HYBRID SOLAR PV + SHP
2) Dispersed and concentrated HYBRID DFIG+ SHP
3) Dispersed and concentrated HYBRID DFIG+ SOLAR PV

5.11.1 Location of HDG Impact on Rotor Angle

Fig 5.19-Fig 5.21 shows the simulations that are used to investigate the impact of the location of HDG on transient stability. It is observed from the simulations that transient stability margin is improved (i.e., smaller first swing and quicker settling time) when dispersed HDG is used compared to concentrated HDG. The reason for this is probably due to the higher voltage drop in the concentrated compared to dispersed HDG since dispersed HDG is generally close to the load, therefore the voltage drop is small.

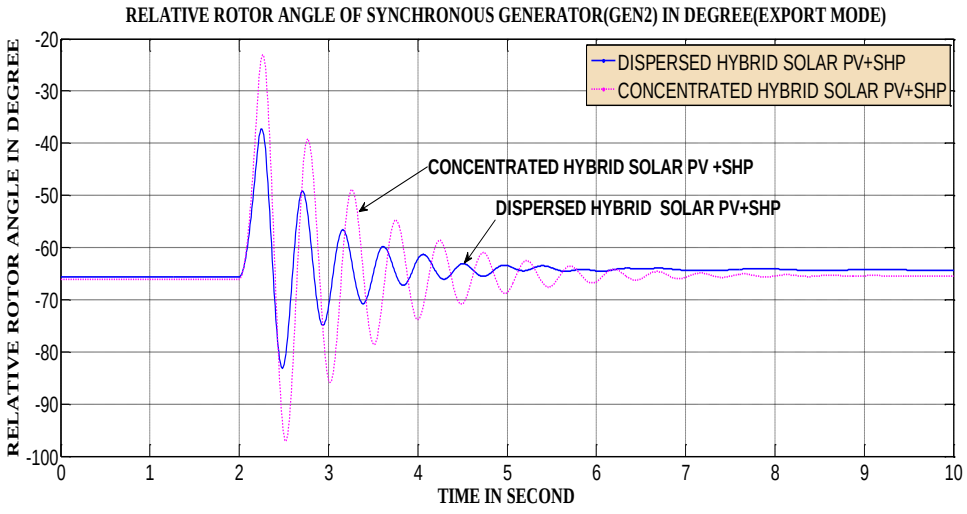

Fig 5.19: Rotor angle of GEN2 with concentrated and dispersed

HYBRID SOLAR PV+ SHP

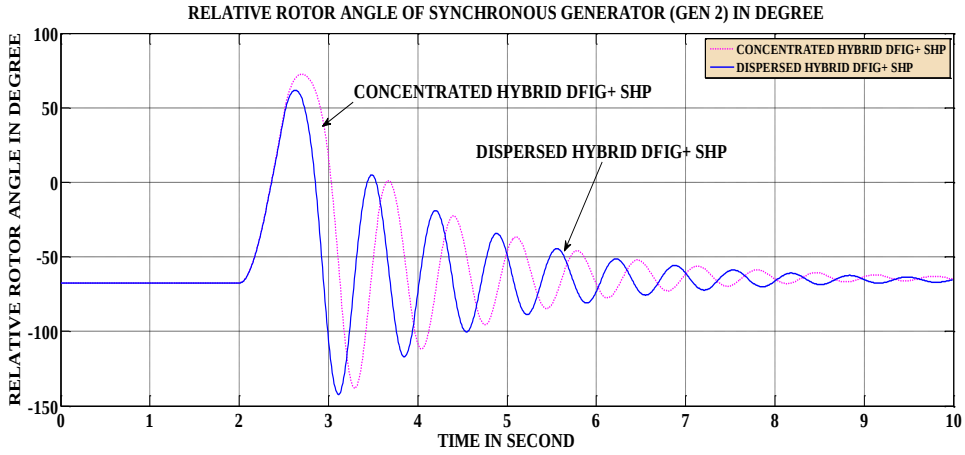

Fig 5.20: Rotor angle of GEN2 with concentrated and dispersed HYBRID DFIG+ SHP

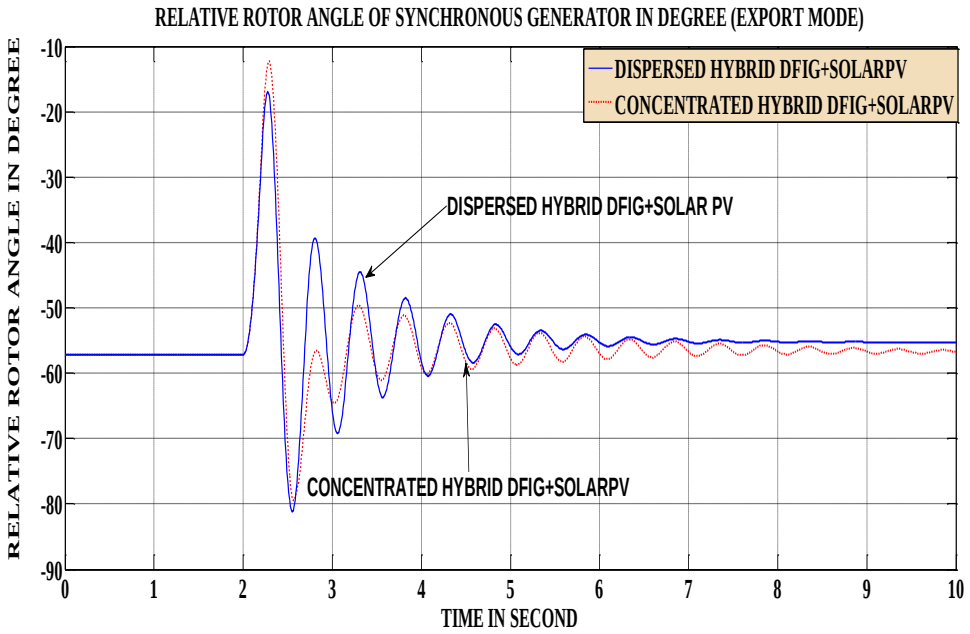

Fig 5.21: Rotor angle of GEN2 with concentrated and dispersed HYBRID DFIG+ SOLAR PV

In all the graphs, concentrated HDG shows higher first swing and longer settling time compared to dispersed HDG. It can also be seen that the impact of transient stability depends on the HDG type involved. For example, HDG using SOLAR PV and SHP is more stable than HYBRID DFIG+SHP or HYBRID DFIG+SOLAR PV. The less stable system is hybrid DFIG+SOLAR PV.

For completeness, we have also investigated the case where different type of wind generator, CDSG is used instead of DFIG. HYBRID CDSG+SHP and HYBRID CDSG+SOLAR PV are used instead of hybridizing DFIG with other sources. The results are given in Appendix C4. It is found that the dispersed HYBRID CDSG+SOLAR PV is more transiently stable compared to dispersed HYBRID DFIG+SOLAR PV as regard the settling time. However, the degree of impact of location of HDG on transient stability depends on the penetration level. For example, if the penetration level is increased, the transient instability will also increase.

5.11.2 Location of HDG Impact on Critical Clearing Time (CCT)

Again, in this section, only the results of export mode are shown. The CCTs for concentrated and dispersed HDG systems at export mode are shown in Table 5.11. For example, when HYBRID SOLAR PV+SHP is used, the CCT when dispersed HDG is used is 375ms compared to 330ms for concentrated HDG. The remaining values in the table also show that dispersed HDG has an improved stability compared to concentrated HDG. This further supports the results already established in the above simulations that the transient stability of a dispersed generation is better than concentrated HDG.

Table 5.11: Critical clearing time of a synchronous generator (GEN2) for concentrated and dispersed HDG scenarios

	CCT (ms) (Dispersed)	**CCT (ms) (Concentrated)**
HYBRID SOLAR PV + SHP	375	330
HYBRID DFIG+ SHP	380	265
HYBRID DFIG+ SOLAR PV	310	300
HYBRID DFIG+SOLAR PV+ SHP	250	230

For completeness, the CCTs for HYBRID CDSG+SHP+SOLAR PV have also been investigated and the results are given in Appendix C5. The CCTs when CDSG is used

with other DG is higher (i.e., improved stability margin) than when HYBRID DFIG+ SOLAR PV or HYBRID DFIG+ SOLAR PV+ SHP is used.

5.12 Summary

The two possible locations of HDG (dispersed and concentrated) are investigated. It is observed that transient stability depends on the location of the HDG and that the transient stability margin of dispersed HDG is generally better than that of the concentrated HDG irrespective of the HDG types used.

5.13 HDG Penetration Level and Transmission Line Length Impact on Critical Clearing Time

In this section, different line lengths such as short (less than 100km) medium (above 100km but below 300km) and long transmission lines (above 300km) were investigated to show the impact of HDG on the transmission line length. The transmission line between bus 5 and bus 3 in Fig 5.22 is varied between 100km-500km. It is assumed that appropriate voltage levels were used for medium and long lines.

Tables 5.12-5.15 show the critical clearing time (CCT) of HYBRID DFIG+SOLAR PV, HYBRID SOLAR PV+SHP, HYBRID DFIG+SHP, and HYBRID DFIG+SOLAR PV+SHP, respectively as the line increases. It can be observed that in general the CCT decreases with increase in line length. This is because the critical clearing time is a function of the power losses which in turn is a function of the line length. The longer the line, the greater the power losses and the lesser the critical clearing time. This means greater instabilities in the system. The simulation results show that the shorter the line, the better the transient stability of the system. Also, under an export mode, HYBRID DFIG+SOLARPV+SHP is less stable than when the hybrid is obtained by combining only 2DGs.

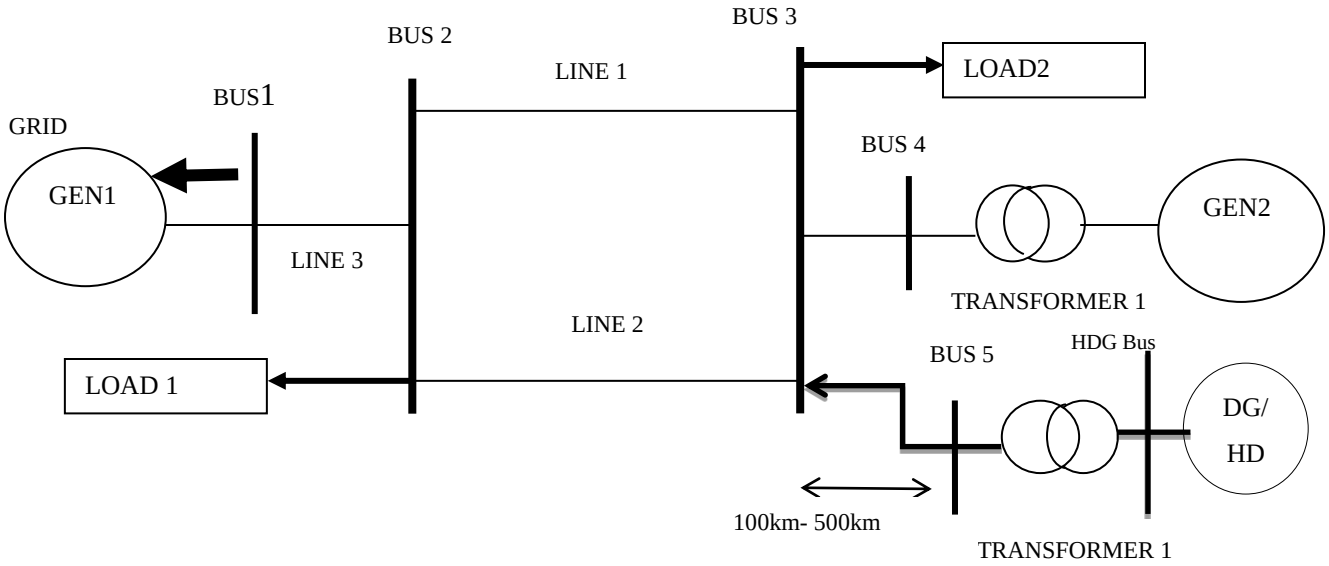

Fig 5.22: Modified One- Line Diagram of the Test System

From Tables 5.12-5.15, when HYBRID SOLAR PV+SHP is used, the system is more transiently stable compared to when HYBRID DFIG+SOLAR PV and HYBRID DFIG + SHP are used. The transient stability is worsened when DFIG is combined with SOLAR PV and SHP to form HYBRID DFIG+SOLAR PV+SHP (see Table 5.15).

Table 5.12: The critical clearing time of GEN2 with integrated HYBRID DFIG+SOLAR PV (Export mode)

HYBRID DFIG+SOLAR PV (Export mode)				
Fault location	**100km**	**200km**	**300km**	**500km**
%	CCT (ms)	CCT (ms)	CCT (ms)	CCT (ms)
0	230	220	219	218
20	260	250	245	230
40	310	300	290	280
60	320	320	310	310
80	290	280	280	278
100	220	210	210	200

Table 5.13: The critical clearing time of GEN2 with integrated HYBRID SOLAR PV+SHP (Export mode)

HYBRID SOLAR PV+SHP (Export mode)				
Fault location	**100km**	**200km**	**300km**	**500km**
%	CCT (ms)	CCT (ms)	CCT (ms)	CCT (ms)
0	351	351	343	335
20	351	351	344	330
40	360	352	345	335
60	372	360	360	340
80	340	330	330	320
100	310	267	267	265

Table 5.14: The critical clearing time of GEN2with integrated HYBRID DFIG+SHP (Export mode)

HYBRID DFIG+ SHP (Export mode)				
Fault location	**100km**	**200km**	**300km**	**500km**
%	CCT (ms)	CCT (ms)	CCT (ms)	CCT (ms)
0	245	243	241	235
20	249	280	270	250
40	320	310	305	300
60	340	330	320	310
80	310	300	290	280
100	240	235	230	228

Table 5.15: The critical clearing time of GEN2 with integrated HYBRID DFIG+SOLAR PV+ SHP (Export mode)

HYBRID DFIG+SOLAR PV +SHP (Export mode)				
Fault location	**100km**	**200km**	**300km**	**500km**
%	CCT (ms)	CCT (ms)	CCT (ms)	CCT (ms)
0	150	147	145	145
20	150	147	146	146
40	151	148	147	145
60	153	150	150	148
80	120	100	100	95
100	70	70	67	50

5.14 Summary

Transient stability of a power system is also influenced by the length of the transmission line. Transient stability decreases with increase in length irrespective of HDG used. Transient stability improves when HYBRID SOLAR PV+SHP is used compared to when HYBRID DFIG+SOLAR PV or HYBRID DFIG+SHP is used. The worst case is seen when HYBRID DFIG+ SOLAR PV+SHP is used.

Chapter 6

ANN-Based Dynamic Modelling and Simulations of Hybrid Distributed Generation

Chapter 5 describes the impact of penetration level of HDG on rotor angle and critical clearing time of a simple power system. The critical clearing time is not a static stability index. For example, it varies with time and location of the fault. The critical clearing time is a complex function of prefault system conditions (operating point, system structure, system parameters, etc.), fault structure (type and location) and the post fault conditions. Due to this involved dependence, it is quite a complicated task to estimate the critical clearing time analytically and offline as it can be seen in all the CCT values reported in the previous chapter. It is therefore important to monitor this stability index as the system parameters and operating conditions vary.

In this chapter, Artificial Neural Networks (ANNs) are used to monitor and predict the CCT and rotor angle in order to assess the status of the power system as its changes with time. Accurate monitoring of CCT and rotor angle will indicate the transient stability limits of the system as well as the impact of HDG on the grid. ANNs are preferred for modelling and monitoring because they are very fast and accurate [1], [122], [136], [137]. ANNs can map inputs into the expected outputs accurately and timely. There are four major functions of ANNs as recorded in literature. They perform classification, function approximation, pattern matching and optimisation [51], [55], [119]. When a mathematical relationship cannot be established between the inputs and the outputs, ANNs can be used to establish these relationships.

Generally, the simplest neural networks are the multilayer feed-forward neural networks (MLFNN). These artificial neural networks have proved to be effective in many applications dealing with steady and dynamic stability assessments. However, MLFNNs are not suitable for temporal pattern. Recurrent neural networks with one step-ahead prediction or multi-step prediction are currently being used in monitoring and control

[172] because they have the ability to perform higher non-linear dynamic mappings [41], [42].

The focus of this chapter is to model HDG using artificial neural networks with one step-ahead prediction. With one step-ahead prediction, the state of the system can be known ahead of time in order to prevent instability and blackouts. One step-ahead time used is 0.0167 seconds for a frequency of 60Hz (one cycle of the fundamental frequency). By standard design and from practical view point, PMU is designed to report data at control centre at 0.0167 seconds. This is reasonable considering the fact that every PMU is expected to provide data at every 1-5 cycles [142]. ANN proposed in this thesis used data collected at the interval of 0.0167 seconds for training and testing.

Modelling of HDG using RNN involves careful selection of data and features for the training. The selection of features is based on the parameters that have large impact on the transient stability. The first step is data collection followed by training which is done to capture the dynamics of the system. However, for generalization purpose, the data must be gathered from a wide range of operating conditions. Accurate prediction depends on the training and the algorithms used. Once the neurons have memorized the dynamics of the system during training, even the smallest data presented during testing will give the require prediction with minimum prediction error.

The dynamic behaviour of HDG is stochastic. For example, the power output of most renewable energy depends on the availability and the characteristic of the primary energy sources. Usually, solar PV is not available in the night and wind may not be available during the day. In addition, solar PV and wind are also stochastic in nature. Another challenge that needed to be solved when dealing with critical clearing time is that the location of the fault is not fixed or predictable. Different faults such as three-phase fault, single line-to-ground fault etc., can occur on the network. Customers load demands also changes with time. To capture the above stochastic nature and the dynamic behaviour of the grid integrated HDG, recurrent neural networks can be used. RNN as a simulation tool is used to monitor the behaviour of HDG during large disturbance. The RNN-based monitoring/prediction model is developed for Solar PV, SHP, DFIG and HYBRID SOLAR PV+SHP, HYBRID DFIG+SHP, HYBRID DFIG+SOLAR PV and HYBRID DFIG+SOLAR PV+SHP. The test system used in this chapter is the IEEE 39-Bus New

England system which was modified to include HDG. The modelling of the test system was conducted in DIgSILENT power factory software.

6.1 Modified IEEE 39-Bus New England system

The IEEE 39-bus New England system is a widely known test system used for dynamic simulations. For this thesis, this power system network was modified to include HDG. The parameters for the IEEE 39- bus test system are taken from reference [173] and are listed in Tables A5-A8 of Appendix A. Fig 6.1 shows the modified IEEE 39-bus New England system which consists of 10 centralized generators (CG) represented as (GEN1, GEN2-GEN10), 40 buses (39 buses and one additional bus from HDG), 46 transmission lines which are modelled as equivalent $\boldsymbol{\pi}$ circuits, and 19 loads. The DG used consists of SOLAR PV, DFIG and SHP. These DGs are combined to form HDG as discussed in the previous chapter. The DGs are rated 8MW, 4MVAr each, GEN10 is modelled as slack bus (i.e., infinite bus) and every other centralized generators (GEN1-GEN9) have their inertia. The centralized generators are modelled as a two-axis (dq) model of synchronous machine [170] and are equipped with a simplified excitation system models (IEEE T1 Exciter). The HDG is connected to bus 17 through a transformer. Table 6.1 shows the characteristics of the modified IEEE 39-bus New England test system. The data for the HDG are shown in TablesA1-A3 of Appendix A. The transformer data is shown in Table A4. The generator, excitation and line data are listed in Tables A5-A6, A7 and A8 respectively.

Table 6.1: Characteristics of the Modified IEEE 39-bus New England Test System

System Characteristics	**Value**
No of buses (including the HDG bus)	40
No of generators	10
No of loads	19
No of transmission lines	46
HDG (SHP, Solar PV, DFIG)	3 (8+j4MVA each)

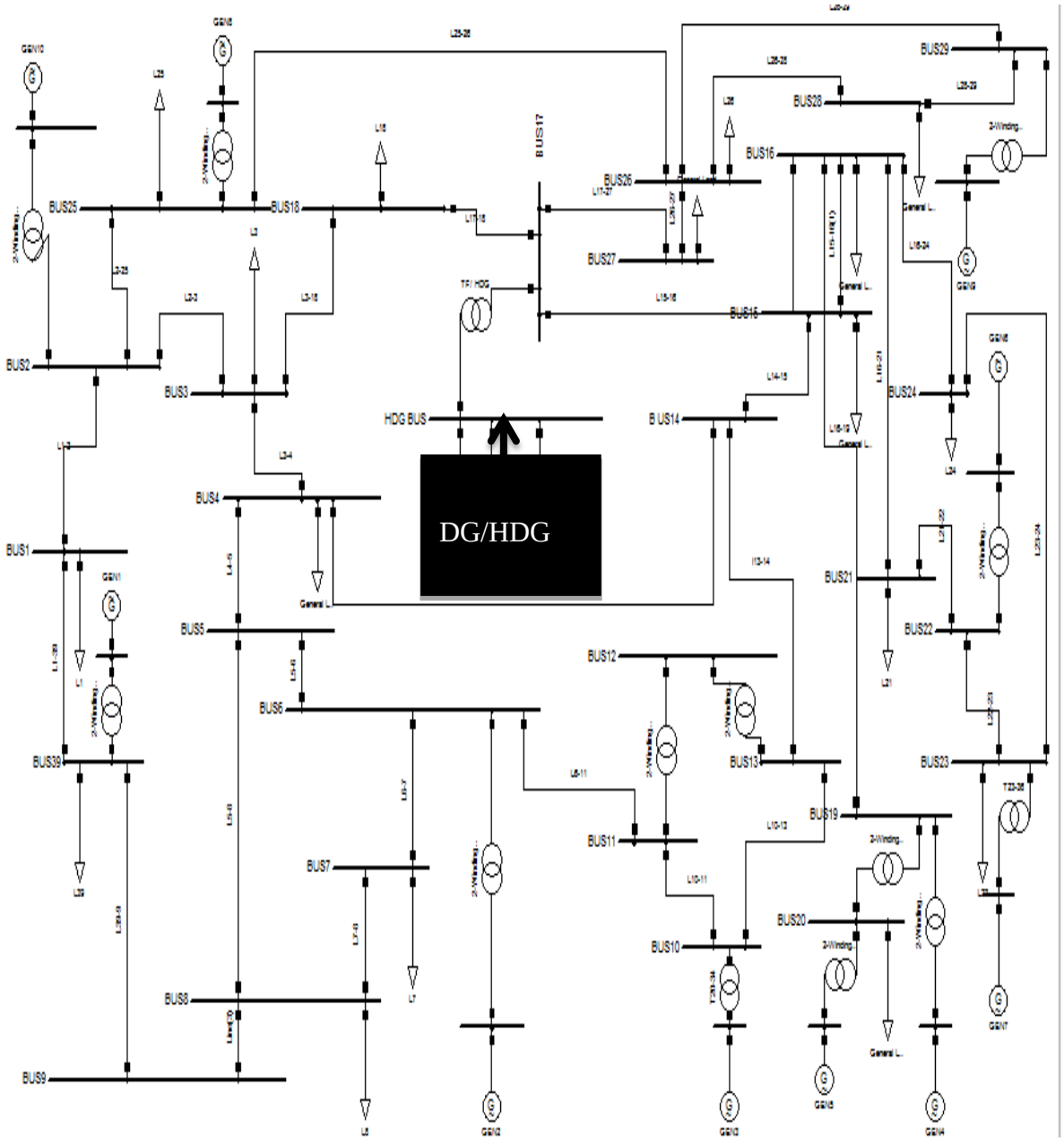

Fig 6.1: Single-line diagram of the Modified 39-bus New England test system in DIgSILENT

6.2 Artificial Neural Network Models

The artificial neural network models contain the detail of the basic design parameters. The parameters are: input features, outputs, bias, the number of neurons, numbers of

layers, etc. The entire neural network models used in this chapter consist of three stages of artificial neural networks (ANNs). In order word, the ANN models are made of three ANNs, i.e., ANN1-ANN3. The stages of the neural networks are arranged in block diagram and are described in the next section.

6.2.1 Flowchart for the Development of ANN Models

ANN1, ANN2 and ANN3 are the three proposed neural network models used. ANN1 and ANN2 are used to model the HDG while ANN3 is used for the CCT prediction. However, all the neural network arrangements used in this chapter go through the step by step algorithm described in the flowchart diagram of Fig 6.2. The flow chart shows the step by step modelling of HDG using ANN.

The first step is to determine the ANN1 and ANN2 architectures which include the inputs, outputs, the hidden layers, the transfer function and delay. The bias is assumed to be one.

The next step is to determine the number of hidden neurons. The number of hidden neurons is determined by trial by error.

The training of ANN1 and ANN2 is carried out with the input data and the target in case of supervised learning. After the training, the targets from ANN1 and ANN2 are obtained. Before the next training is carried out, the accuracy of the trained ANN1 and ANN2 is determined using MSEREG and the correlation coefficient. A good training will give a mean square error with regularization (MSEREG) value that is close to zero. The closer the MSEREG value to zero, the better is the training. Also, the closer the correlation coefficient to 1, the better is the training. After the training of ANN1 and ANN2, data are also exported to train and test ANN3. After ANN3 is trained, testing and validation are performed. After a successful testing and validation, the weights are frozen and the model can be used for prediction.

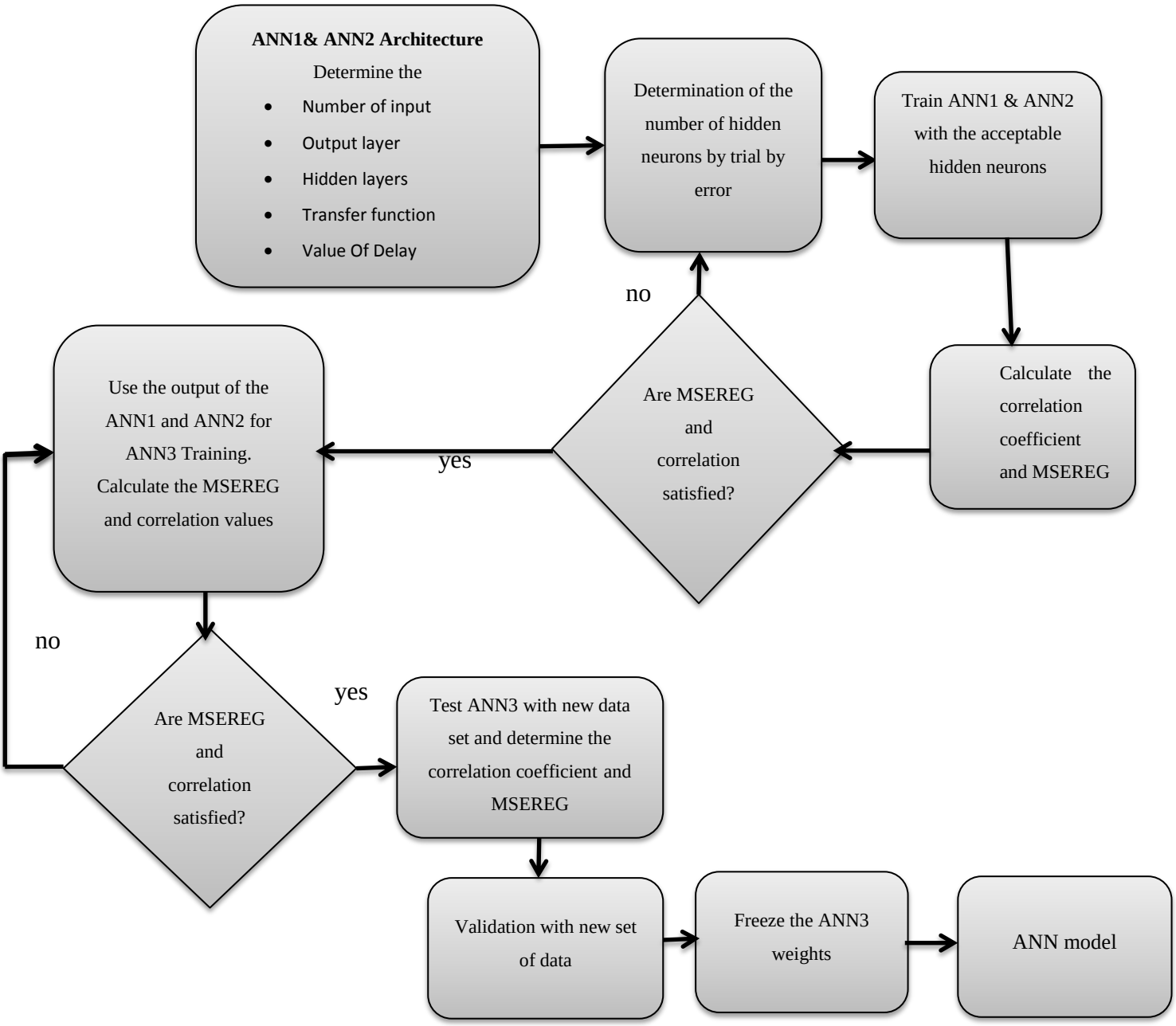

Fig 6.2: Flowchart for ANN models

6.2.2 Feature Selection and Design of the Artificial Neural Networks

Fig 6.3 shows the block diagram of ANN-HDG based model. It consists of 3 neural networks (ANN1, ANN2 and ANN3). The reason for using ANN1 and ANN2 is to be able to capture appropriately the various dynamics of the different DGs (DFIG, SHP and solar PV). In case of 3 DGs, the first two ANNs will have additional ANN. These neural networks are trained with different input data. For example, the input data for ANN 1 when solar PV is used does not include reactive power and the electrical torque because solar PV is not a rotary machine and it has a unity power factor, whereas the input data for DFIG and SHP include electrical torque and reactive power. The input features for ANN1 and ANN2 are as shown in Table 6.2. It can be seen that:

- 2 inputs are used when Solar PV alone is involved
- 4 inputs are used each when DFIG or SHP is involved

The output of the ANN1 and ANN2 are active power of SOLAR PV, DFIG or SHP. These active powers are fed into ANN3. ANN3 contains additional input data which are input from the centralized generators (in this case generator 8), and some of the inputs used for ANN1 and ANN2 (see Fig 6.3). The input features for ANN3 are shown in Table 6.3. It can be seen that:

- 8 inputs are used for HYBRID DFIG+SOLAR PV or HYBRID SOLAR PV+SHP.
- 10 inputs are used for HYBRID DIFG+SHP.
- 12 inputs are used for HYBRID DFIG+SOLAR PV+SHP

The output of ANN3 is either CCT or rotor angle. The advantage of ANN-HDG based model is to allow accurate prediction of CCT and rotor angle in order to obtain an accurate dynamic assessment of HDG.

Throughout the simulation in this chapter, an Elman recurrent neural networks (RNNs) were used for ANN1 and ANN2 which is represented as RNN. Recurrent neural networks are used because of their ability to model time series events and to learn accurately the

dynamic behaviour of power systems [43]. Fig 6.4 shows the modified block diagram of the neural networks. ANN3 is modified to contain five types of artificial neural networks. They are: Recurrent Neural Networks (RNNs), Multi-layer Feed forward Neural Networks (MLFNNs), Radial Basis Function (RBF), Generalised Regression Neural Networks (GRNNs) and Self Organised Feature Map (SOFM).

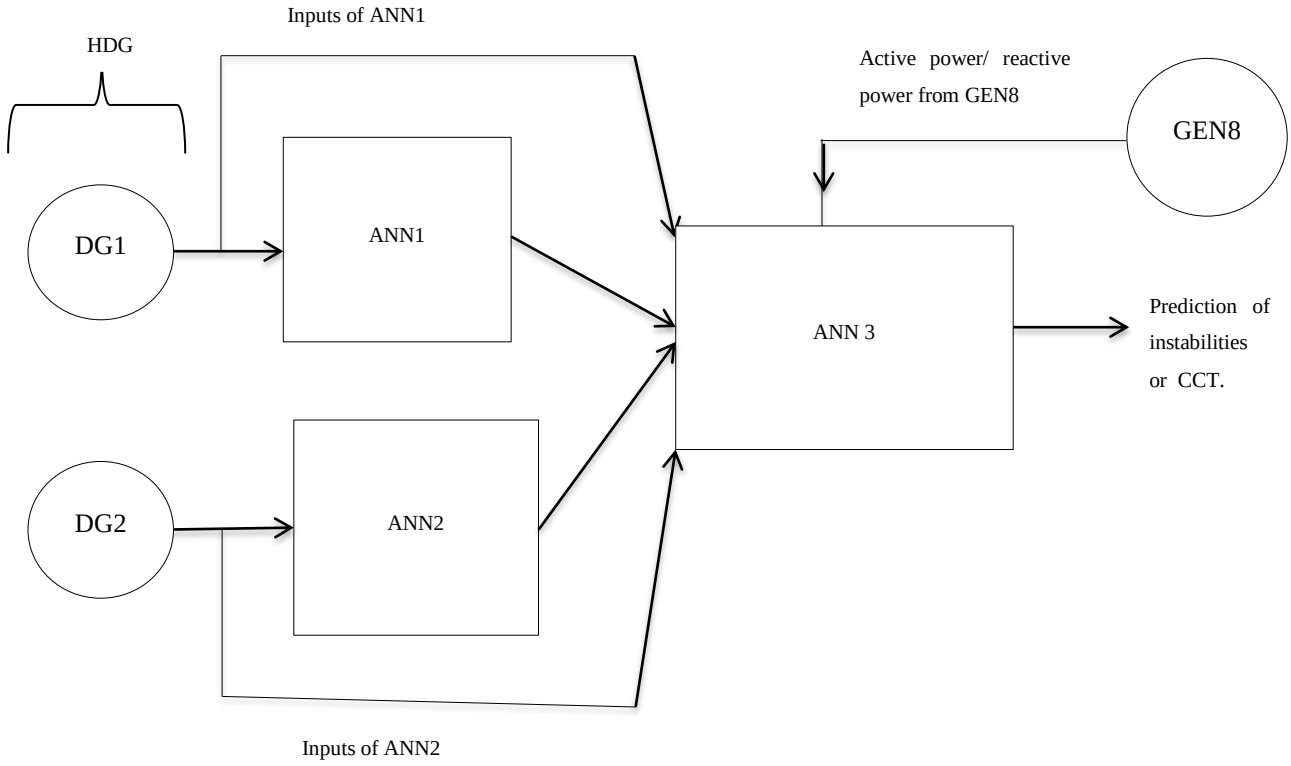

Fig 6.3: Block diagram of ANN Architecture

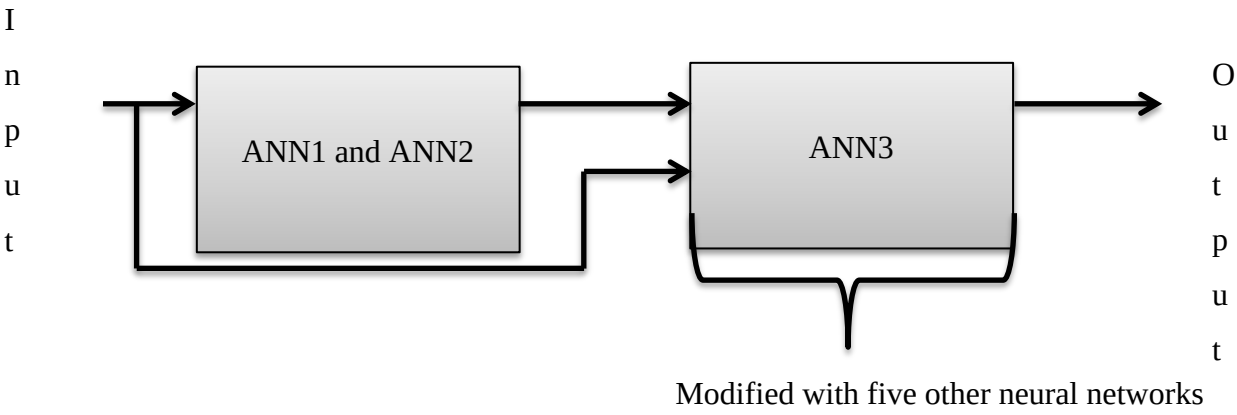

Fig 6.4: Modified Neural Network block diagram

Table 6.2 **:** Features selections for ANN1 and ANN2

	Input Features for ANN1 and ANN2	**SOLAR PV**	**DFIG or SHP**
1	Active power	1	1 each
2	Reactive power	Nil	1 each
3	Terminal voltage	1	1 each
4	Electrical Toque	Nil	1 each
	TOTAL	2	4 each (8 for both)

Table 6.3: Input Features for ANN3

No	**Input features for ANN3**	**SOLAR PV**	**DFIG OR SHP**
1	Active power (HDG) output of ANN1 and ANN2	1	1 each
2	Reactive power (For other generators except SOLAR PV), Electrical Toque (For other generators except SOLAR PV) and Terminal voltage of DG.	1	3 each
3	Active power and reactive power of generator 8 (generator 8 is used as an example of the grid)	2	

Table 6.4 contains the neural network data and structure used in the design of ANN1 and ANN2. RNN is used for ANN1 and ANN2 and it contains two-layer network. ANN1 contains 2 inputs if SOLAR PV is used, while ANN2 contains 4 inputs for either SHP or DFIG. ANN1 and ANN2 each contain 10 hidden neurons and 1 output, which is formed into a matrix 2x10x1(SOLAR PV) and 4x10x1(DFIG or SHP), etc. The training makes use of 4188 training data, 897 testing data and 897 validation data. They are trained with a Levenberg Marquardt algorithm for 1000 epochs. This epoch number is used and sometimes the maximum epoch is not reached. Levenberg Marquardt algorithm is used because it is very fast. Levenberg-Marquardt back propagation uses gradient descent method to adjust the weights in the steepest descent direction (negative of the gradient) which is the direction in which the performance function is decreasing most rapidly. RNN has a delay. The hidden layer used sigmoid function while the output layer used linear function.

Table 6.4: Neural Network Data and Structure of ANN1 and ANN2

No	**Features and structure of RNN**	
1	Number of inputs	(SOLAR PV) 4(SHP or DFIG)
2	Number of neurons in the hidden layer	10
3	Number of layers	2
4	Output	1
5	Training data	4188
6	Testing data	897
7	Validation data	897
8	Training algorithm	Levenberg Marquardt
9	Epoch	1000
10	Transfer function	Sigmoid, linear
11	Architecture	2x10x1(SOLAR PV),4x10x1 (DFIG or SHP)
12	Delay	1

The structure and features of other neural networks are the same as those of RNNs except for some minor differences. The features of ANN3 are shown in Table 6.5. ANN3 can be represented by MLFNN, RNN, RBF GRNN or SOFM. The structure for ANN3 is 8x10x1 when HYBRID DFIG+SOLAR PV or HYBRID SOLAR PV+SHP is used and 10x10x1 when HYBRID DFIG+ SHP is used and 12x10x1 when HYBRID DFIG+SOLAR PV+SHP is used. The first number (i.e., 8) in the matrix (8x10x1) represents the input features while the second number (i.e., 10) represents the number of hidden neurons and the third number (i.e., 1) represents the number of output. The

transfer function used for RNN is also used for other ANNs except for RBF and GRNN that used radial basis function because they are designed like that. Two layers exist in GRNN. The spread must be selected appropriately in order to avoid over-fitting. If the spread is very small, the radial basis function (the first layer) will steep. As the spread becomes larger, more neurons can respond to training with the result of the output becoming smoother. The distance between the data and the weight is used in this case.

The same feature selected for others ANNs was also used in the training of SOFM. The number of neurons in the Kohonen network depends on the application, but it must be formed in such a way as to make the Kohonen network capable of forming sufficient clusters of input vectors. It was found that 10x10 neurons in the Kohonen's layer give the best clustering for this particular system after rigorous training. The properties of the cluster can be analyzed from the weight associated with neurons in the clusters. The cluster with the same structure is grouped together.

Table 6.5: Parameters used for Neural Networks modelling (ANN3)

	PARAMETERS (RBF)	**RNN**	**MLFNN**	**RBF**	**GRNN**	**SOFM**
1	Number of inputs	8 for HYBRID DFIG+SOLAR PV or HYBRID SOLAR PV+SHP, 10 for HYBRID DFIG+SHP and 12 for HYBRID DFIG+SOLAR PV+SHP				
2	Number of neurons in the hidden layer	10	10	10	10	10x10
3	Number of layers	2	2	2	2	2
4	Output	1	1	1	1	100
5	Training data	4188	4188	4188	4188	4188
6	Testing data	897	897	897	897	897
7	Validation data	897	897	897	897	897
8	Training algorithm	Levenberg Marquardt	Levenberg Marquardt	Levenberg Marquardt	Levenberg Marquardt	Levenberg Marquardt
9	Epoch	1000	1000	1000	1000	1000
10	Transfer function	Sigmoid, linear	Sigmoid, linear	Radial basis, linear	Radial basis , linear	Sigmoid, linear
11	Architecture	8x10x1(SOLAR PV +DFIG or SOLAR PV+SHP), 10x10x1 DFIG+ SHP, 12x10x1(HYBRID DFIG+SOLAR PV+SHP)				
12	Delay	N/A	1	N/A	N/A	N/A

N/A means not applicable

6.3 Data Preparation

To collect and prepare the training data, a large number of input/output data patterns were generated from perturbing the system randomly over a wide range of operating conditions. In this thesis, the input / output pattern is generated by applying faults at the midpoint of selected transmission lines. The fault is applied and cleared after 200ms by removing the lines. The lines as shown in Table 6.6 were removed. In total, 16 lines were disconnected. Only shunt faults which are common are considered. The following faults were applied:

- Three-phase fault
- Double-line-to-ground fault
- Line-to-Line fault
- Single line-to-ground fault

Table 6.6: Disconnected lines

1	Line 1-2	5	Line 26-29	9	Line 5-6	13	Line 16-24
2	Line 16—19	6	Line 23-24	10	Line 7-8	14	Line 15-16
3	Line 4-5	7	Line 10-13	11	Line 13-14	15	Line 5-8
4	Line 2-3	8	Line 4-14	12	Line 16-21	16	Line 22-23

The data were gathered by increasing the penetration of HDG from the import mode (i.e., light penetration of HDG) to balanced mode (i.e., moderate penetration of HDG) and then to export mode (i.e., high penetration of HDG). The active power from HDG in import mode is 80MW whereas in balanced mode, the active power from HDG is 160MW. For the export mode, the active power from HDG is 240MW-400MW. The training and validation data consist of both pre-fault data and the post fault data. The pre-fault data and post fault data are used to train ANN1 and ANN2 while another pre-fault data and post fault data are used for training ANN3.

6.4 Training Of Recurrent Neural Network

Seventy percent (70%) of the data collected is used for training, 15% for testing (see Table 6.5) and 15% for validation. The total data is 5982.

The training is conducted with gradient descent back propagation algorithm. During the testing mode, the weight is kept constant, i.e. frozen. In the testing mode, different input data can be used. The result will show whether the network has generalized very well or not.

After the training, the impact of the HDG penetration on transient stability is investigated by using different data for testing. The accuracy of the training and testing is measured by the following performance indices.

- Mean square error with regularization (MSEREG)
- Correlation coefficient (R)

6.5 Simulations Results

The first result presented in this section shows the impact of HDG on transient stability by predicting the rotor angle and the critical clearing time.

6.5.1 Determining the Accuracy of Training and Testing Using RNN Model

- **Simulation results for the Training**

Figs 6.5-6.7 show the results of the training of ANN1 and ANN2. ANN1 (RNN) predicted the active power one-step ahead when SOLAR PV alone was used (see Fig 6.5). To measure the accuracy of the training, the MSEREG and the correlation coefficient were used. In Fig 6.5, it was observed that the training is very accurate. The MSEREG is 0.0321. The correlation coefficient, which is 0.9253 (92.53%) indicates that RNN predicted accurately. The time taken for training of RNN is 35ms while the Time Domain Simulation (TDS) in DIgSILENT took 4s.

Fig 6.6 shows the actual and the predicted active power of small hydropower (SHP). The MSEREG value is 0.0351 and the correlation coefficient is 0.9323(93.23%). The RNN simulation took 32ms whereas TDS took about 4s.

Fig 6.7 shows the actual and the predicted active power when DFIG alone is used. The MSEREG is 0.4562 and the correlation coefficient is 0.7847(78.47%). The RNN concluded the prediction/training at 40ms compared to 4s using TDS. This result is not as good as the previous results.

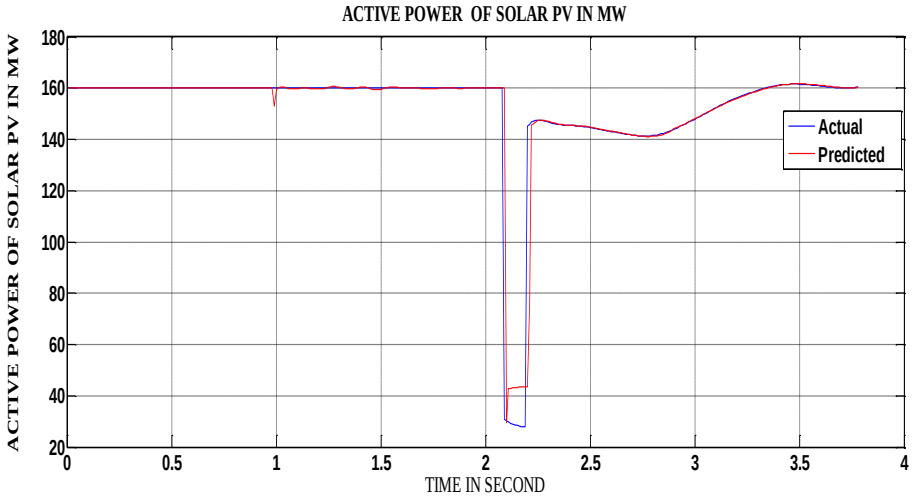

Fig 6.5: One step-ahead prediction of active power of Solar PV during training (ANN1)

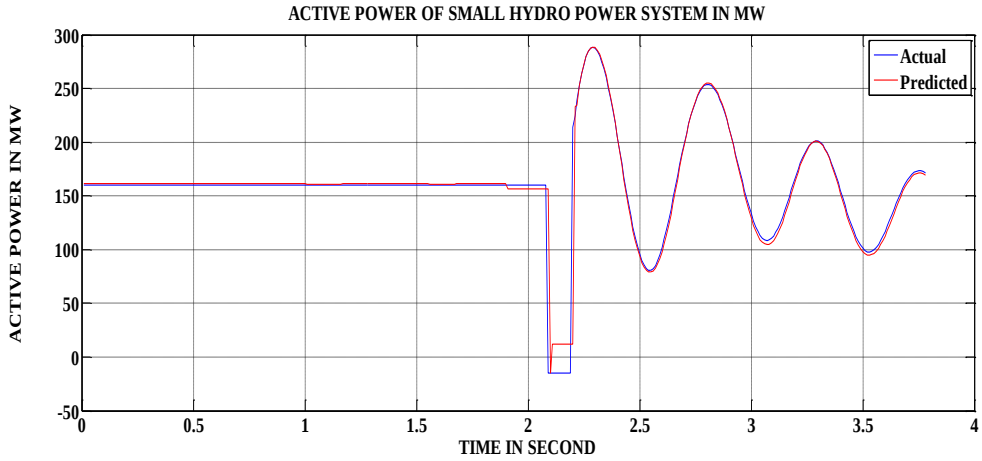

Fig 6.6**:** One step-ahead prediction of active power of SHP generator during training (ANN2).

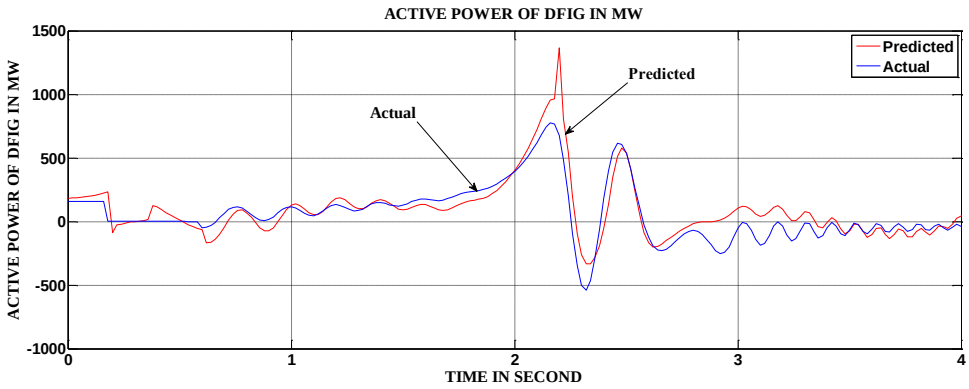

Fig 6.7: One step-ahead prediction of active power of DFIG generator during training (ANN2).

The training of ANN3 (RNN3) was also carried out. Fig 6.8 shows the rotor angle of the generator 8 during training of ANN3 when HYBRID SOLAR PV+SHP was used. The accuracy of the training is also measured by MSEREG and the correlation coefficient. The value of MSEREG is 0.0173 while that of the correlation coefficient is 0.9993. The ANN3 training took 70ms while TDS result was obtained in 12.5s. The testing of ANN3 was done with data different from the input data.

Fig 6.9 shows the graph of the testing carried out when new data that are different from the initial data were presented to ANN3. The MSEREG is 0.012 and the correlation coefficient is 0.9957. The testing time, which is 11ms is faster than the training time of 70ms and faster than the TDS (12.5s).

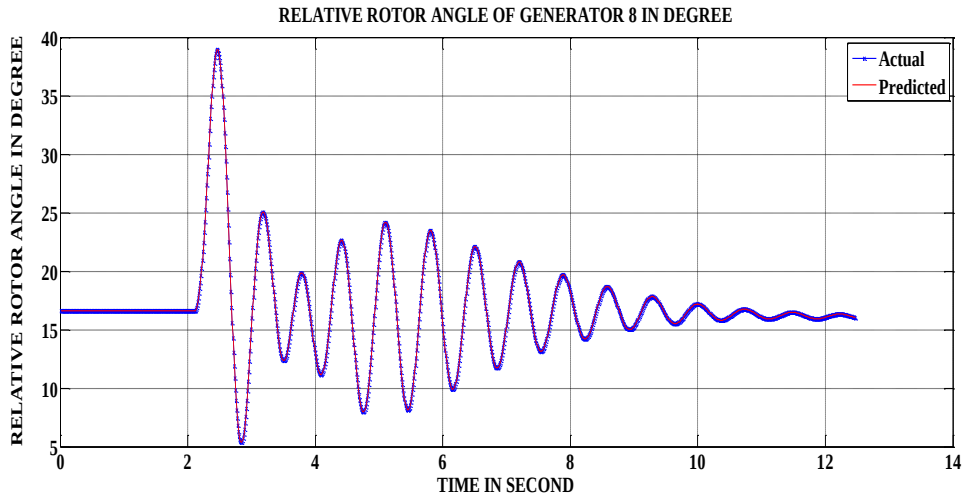

Fig 6.8: One step-ahead prediction of rotor angle of the generator 8 during training when HYBRID SOLAR PV+SHP is connected to the grid (ANN3).

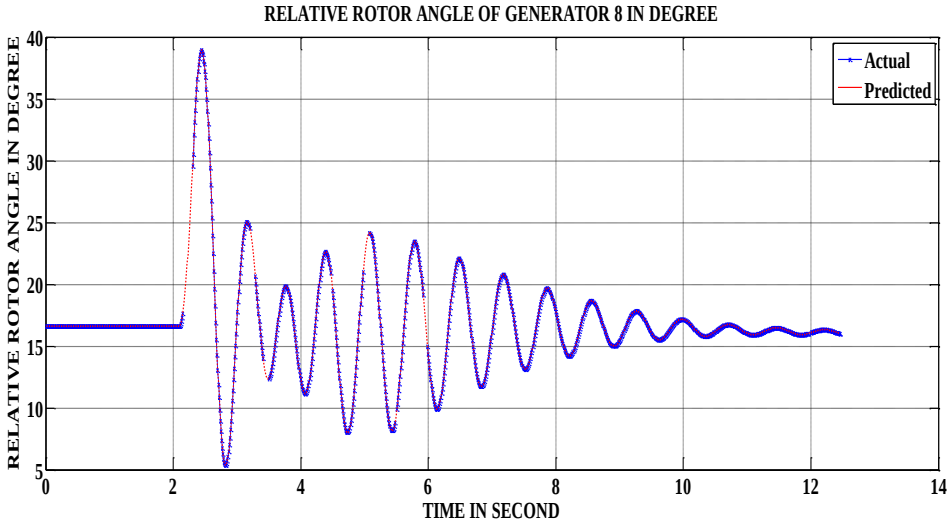

Fig 6.9: One step-ahead prediction of rotor angle of the generator 8 during testing when HYBRID SOLAR PV+SHP is connected to the grid (ANN3).

Figs 6.10-6.12 show the results of ANN3 during testing of HYBRID DFIG+SOLAR PV, HYBRID DFIG+SHP and HYBRID DFIG+SOLAR PV+SHP respectively. The results show that RNN has correctly learned the dynamics of the system by predicting accurately the results. The accuracy of the prediction was measured by MSEREG and the correlation coefficient. At the same time, the simulation time for ANN3 is also compared with the TDS in DIgSILENT. The results of the MSEREG, correlation coefficient and time taken for the prediction are given in Table 6.7.

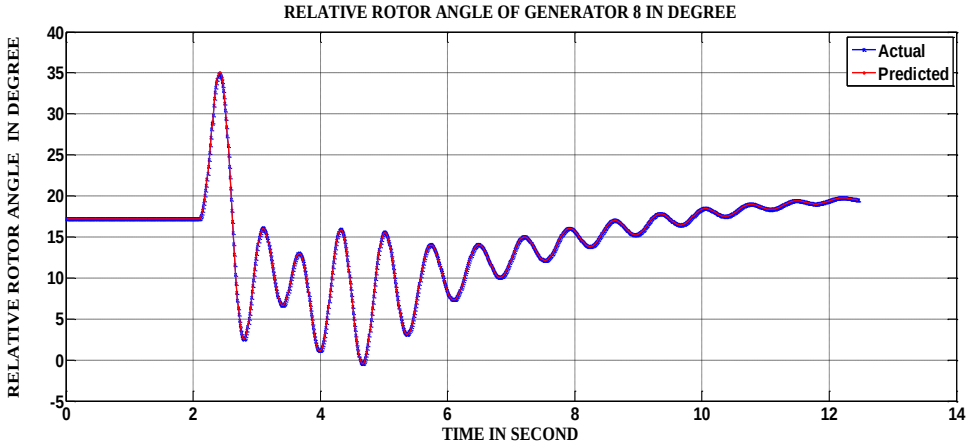

Fig 6.10**:** One step-ahead prediction of rotor angle of generator 8 during testing mode when HYBRID DFIG+SOLAR PV is connected to the grid (ANN3).

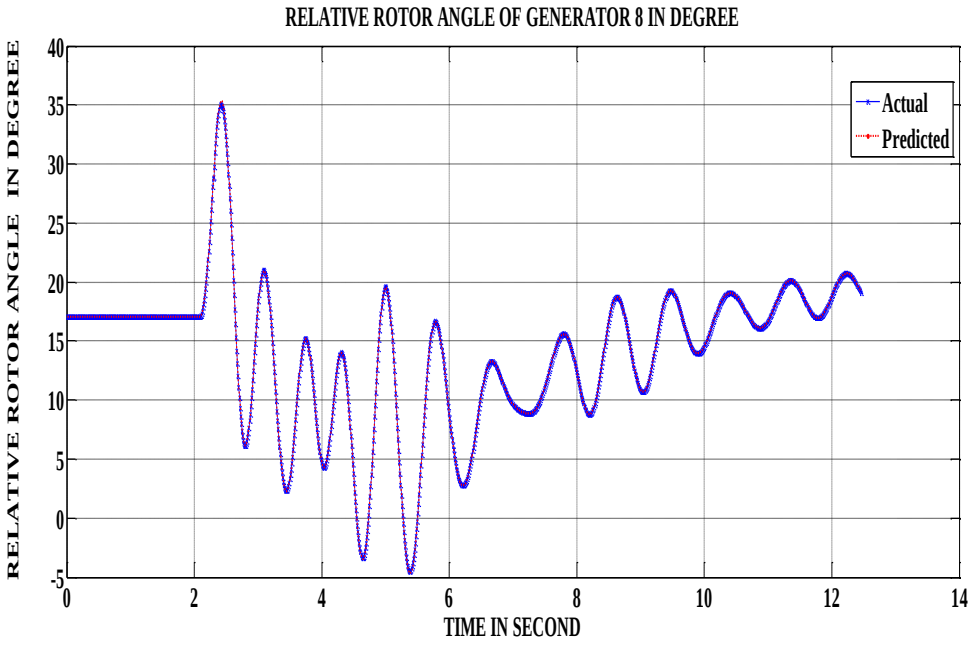

Fig 6.11: One step-ahead prediction of rotor angle of the generator 8 during testing mode when HYBRID DFIG+SHP is connected to the grid (ANN3)

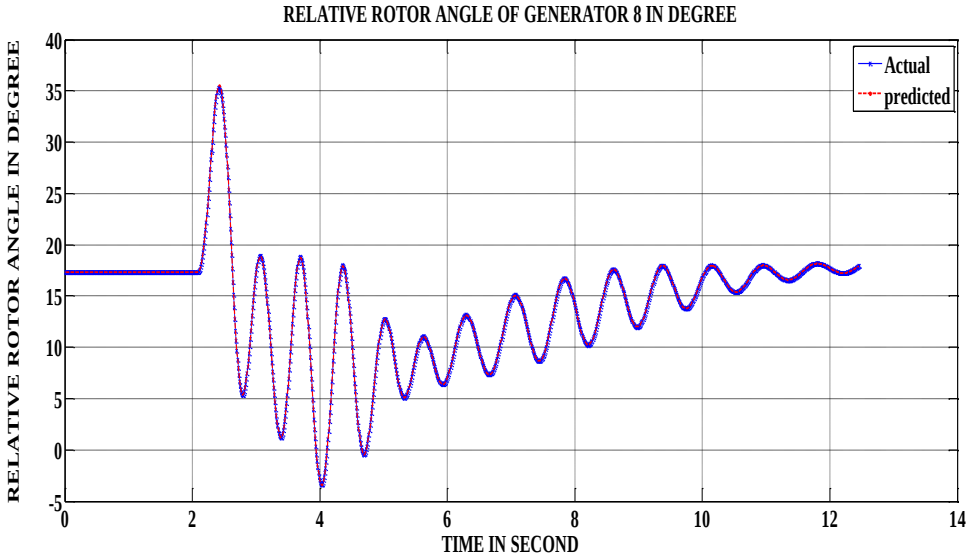

Fig 6.12: One step-ahead prediction of rotor angle of generator 8 during testing mode when HYBRID DFIG+ SOLAR PV+ SHP is connected to the grid (ANN3).

It is observed that ANN3 took 70ms for the training to be concluded. This is expected because learning/training usually takes a longer time. The longest testing time, which is 13ms was obtained when HYBRID DFIG+SOLAR PV+SHP was used. All the testing

results show a high correlation between the output and the predicted value. This indicates that the model has actually learned very well and could be used for prediction.

Table 6.7: Comparison during Training and Testing

DG/HDG INVESTIGATED	MSEREG	CORRELATION CO-EFFICIENT	TIME (ms)	REMARKS
Active Power of Solar PV	0.0321	0.9253	35	Training
Active Power of SHP	0.0351	0.9323	32	Training
Active Power of DFIG	0.4562	0.7847	40	Training
Rotor angle of generator 8 with HYBRID SOLAR PV +SHP	0.0173	0.9993	70	Training
Rotor angle of generator 8 with HYBRID SOLAR PV+SHP	0.012	0.9957	11	Testing
Rotor angle of generator 8 With HYBRID DFIG+SOLAR PV	0.0511	0.9998	10	Testing
Rotor angle of generator 8 with HYBRID DFIG+SHP	0.020	0.9963	11	Testing
Rotor angle of generator 8 with HYBRID DFIG+SOLAR PV + SHP	0.0414	0.9897	13	Testing

6.5.2 Impact of Penetration Level of HDG on Transient Stability using Trained RNN

In this section, the impact of HDG on the rotor angle is monitored by using RNN. The penetration level is increased from import mode, balanced mode to export mode.

Fig 6.13 shows the graph describing the impact of HDG (HYBRID SHP+SOLAR PV) penetration on rotor angle. The graph includes the case where there is no HDG as well as different penetration levels of the HDG (HYBRID SHP+SOLAR PV), namely, the import mode, balanced mode and export mode. The base case as shown in Fig 6.13 is

when there is no HDG integration. The simulation, which is conducted one-step ahead, takes 10ms to obtain the results using RNN. However, when TDS is used, it takes 5seconds to obtain the same results. From the figure, it indicates that as the penetration level increases, the instability also increases.

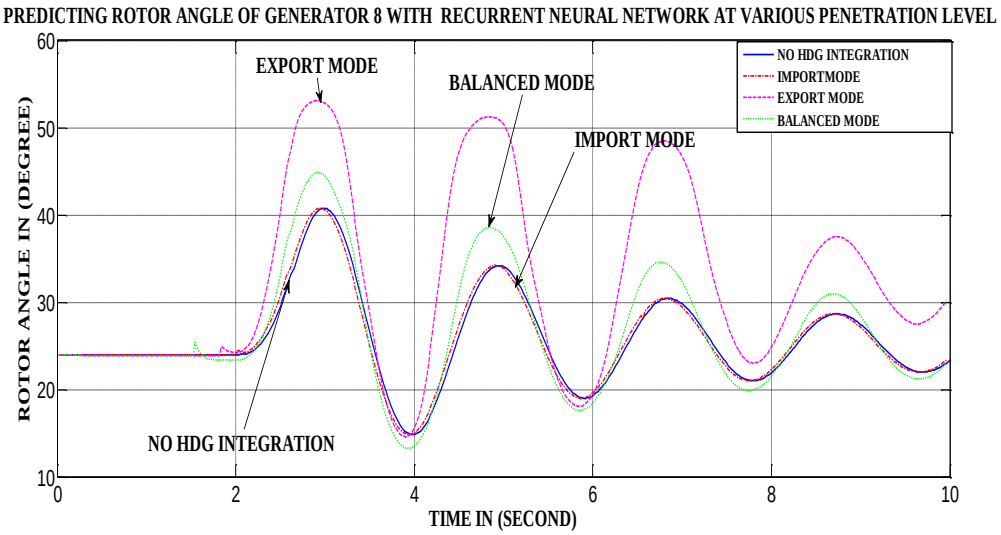

Fig 6.13: One step-ahead prediction showing the impact of HDG on rotor angle during testing mode when HYBRID SOLAR PV+SHP is used.

In Table 6.8, the accuracy of RNN in predicting one-step ahead was compared with Time Domain Simulation (TDS) in DIgSILENT. It is observed that RNN was able to predict the first swing of the rotor angle accurately, except for the export mode where the predicted angle is 53^0 instead of 50^0. The error in the prediction is about 6%, which is still acceptable. The accuracy of RNN prediction is 94.34%. It can also be seen that in all the cases shown in the Table, the RNN take a shorter time to predict the first swing rotor angle compared to 5s for TDS.

Table 6.8: Comparison of the Impact of HDG Using RNN with TDS

	RNN		**TDS**	
	First Swing Angle (degree)	**Time (ms)**	**First Swing Angle (degree)**	**Time (s)**
NO HDG INTEGRATION	41	10	41	5
IMPORT MODE	41	10	41	5
BALANCED MODE	45	10	45	5
EXPORT MODE	53	11	50	5

6.6 Impact of HDG Penetration on Critical clearing Time (CCT) using RNN

This section describes the impact of DG/HDG penetration on critical clearing time (CCT) using RNN. The data gathered for this training is obtained by calculating the CCT using TDS (in DIgSILENT) at different penetration levels (Import mode, balanced mode, and Export mode). The penetration of DG/HDG increases from 80MW (Import mode) to 160MW (Balanced mode) and to 240MW-400MW (export mode). Various disturbances such as three-phase fault, double-line-to-ground fault, line-to-line fault and single line-to-ground fault were applied on different transmission lines.

The faults were applied at the middle of the lines and cleared by removing the lines. The disconnected transmission lines are listed in Table 6.6 as discussed previously.

Tables 6.9-6.12 show the results of the impact of the HDG penetration on CCT using RNN when three-phase fault, double-line-to-ground fault, line-to-line fault and single line-to-ground fault were applied. For comparison, the results using TDS are also included in the Tables.

Table 6.9 shows the one-step prediction of CCT using RNN for the different HDG penetration level when a three-phase fault was applied. It can be seen that the prediction of the CCT by RNN is quite accurate. The errors in the prediction are very small and can

be neglected. For example, when HYBRID SOLAR PV+SHP supplied 80MW, the CCT value with TDS is 350ms. One-step prediction using RNN gives 345ms. The same is true for other penetration levels in Table 6.9 as well as for the various combinations of HDG. It shows that, RNN can be used to predict correctly the value of the CCT.

Table 6.10 shows the one-step prediction of CCT using RNN for different HDG penetration levels when a double-line–to-ground fault was applied. Comparison of the results in Table 6.9 with Table 6.10 shows that the values of the CCT in Table 6.10 are bigger than those in Table 6.9. This means that three-phase fault is the most severe. Table 6.11 and Table 6.12 show the results of the prediction of CCTs using RNN for a line-to-line fault and a single line-to- ground fault respectively. The same explanation used in Table 6.9 can be applied that is the single line –to-ground fault is the least severe fault for all the faults listed above.

Fig 6.14 shows the testing results when RNN was used to predict CCT value one-step ahead. The testing of the RNN was carried out with different input data. For example, at 0 output pattern, the CCT value using TDS is 410ms while the CCT predicted by RNN at 0.0167s is 409.6ms. The correlation coefficient value is 0.9990. It indicates that 99.9 % accuracy in predictions was made. The same argument can be used to explain the rest of the pattern in Fig 6.14. These results show that RNN can be used to monitor the system dynamics and make accurate prediction a one-step (0.0167s) ahead.

Table 6.9: One-Step Prediction of CCT with RNN during three-Phase Fault

		HYBRID SOLAR PV +SHP CCT in (ms)		HYBRID DFIG+SOLAR PV CCT in (ms)		HYBRID DFIG+SHP CCT(ms)	
S/N	ACTIVE POWER of HDG (MW)	TDS	RNN	TDS	RNN	TDS	RNN
1	80	350	345	340	335	337	335
2	160	345	345	338	337	335	335
3	240	340	342	320	321	333.5	333
4	320	335	335	310	310	332	332
5	400	333	331	280	280	330	331

Table 6.10: One-Step Prediction of CCT with RNN during Double-Line-to-Ground Fault

		HYBRID SOLAR PV +SHP CCT (ms)		HYBRID DFIG+SOLAR PV CCT (ms)		HYBRID DFIG+SHP CCT (ms)	
S/N	ACTIVE POWER of HDG (MW)	TDS	RNN	TDS	RNN	TDS	RNN
1	80	430	432	430	425	440	440
2	160	415	415	410	405	420	425
3	240	397	390	395	395	400	400
4	320	395	395	380	381	390	395
5	400	375	373	365	363	385	385

Table 6.11: One-Step Prediction of CCT with RNN during Line-to-Line Fault

		HYBRID SOLAR PV+SHP CCT (ms)		**HYBRID DFIG+SOLAR PV CCT (ms)**		**HYBRID DFIG+SHP CCT (ms)**	
S/N	**ACTIVE POWER of HDG (MW)**	**TDS**	**RNN**	**TDS**	**RNN**	**TDS**	**RNN**
1	**80**	**750**	**745**	720	725	**730**	**730**
2	**160**	**660**	**662**	630	630	**635**	**635**
3	**240**	**622**	**630**	625	625	**625**	**630**
4	**320**	**552**	**581**	565	552	**560**	**580**
5	**400**	**545**	**545**	560	562	**550**	**551**

Table 6.12: One-Step Prediction of CCT with RNN during Single Line-to-ground fault

		HYBRID SOLAR PV +SHP CCT (ms)		**HYBRID DFIG+SOLAR PV CCT (ms)**		**HYBRID DFIG+SHP CCT (ms)**	
S/N	**ACTIVE POWER of HDG (MW)**	**TDS**	**RNN)**	**TDS**	**RNN**	**TDS**	**RNN**
1	**80**	**900**	**901**	**700**	**700**	**750**	**752**
2	**160**	**875**	**875**	**650**	**650**	**700**	**700**
3	**240**	**800**	**805**	**630**	**635**	**650**	**652**
4	**320**	**750**	**755**	**620**	**620**	**600**	**600**
5	**400**	**700**	**702**	**600**	**605**	**550**	**550**

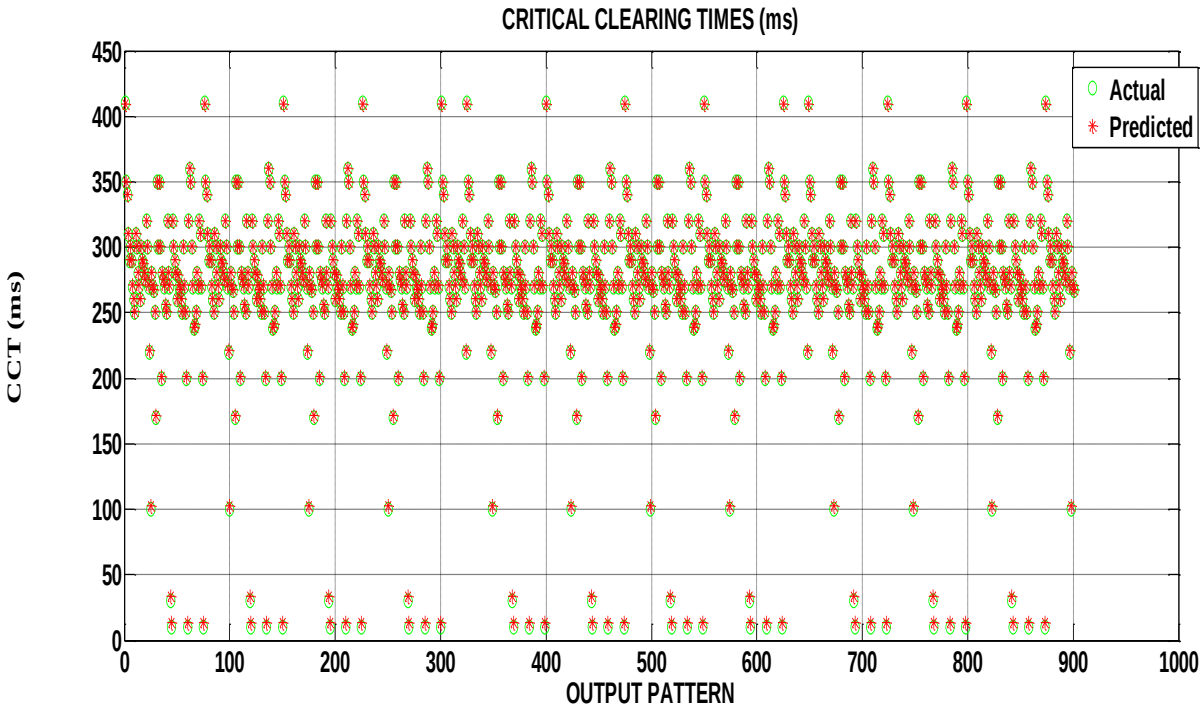

Fig 6.14**:** One step-ahead prediction of CCT during testing**.**

6.7 Determining CCT (Stability Status) Using Other Neural Networks (MLFNN, RBF, GRNN and SOFM)

This section uses four neural networks to predict the CCT. The results are explained in the next section.

6.8 Simulation Results for Critical Clearing Time prediction using MLFNN, RBF, GRNN and SOFM

This section uses four neural networks based on the model in Fig 6.3 and Fig 6.4 to determine the CCT in a modified IEEE 39-bus system. The same data used to train RNN in the previous section is also used in this section.

The training was done using a wide range of data gathered by applying different types of fault and simultaneously, the penetration of HYBRID SHP+SOLAR PV increases from 80MW to 400MW. The training data contains 70% of the entire data and the testing data is 15% while 15% was used for validation. ANN3 in Fig 6.3 was replaced with any of (MLFNN, RBF, GRNN, and SOFM) alternatively. RNN was used throughout as ANN1&ANN2 for various neural networks classifiers. When ANN3 is replaced with RNN, there is no further training and testing done because this has been conducted in the previous section. Only the discussion is given. Therefore, in this sub-section, only the four ANNs applied as ANN3 are trained and tested. During the testing, only the results of the CCT when three-phase fault was applied are described in the next sub-section.

6.8.1 Multi-Layer Feed-Forward Neural Network (MLFNN)

Table 6.13 shows the testing results conducted with the trained MLFNN. The results of the training are not shown. The CCT values when TDS is used and the predicted values obtained from the MLFNN 0.01667s ahead of time and the MSEREG values are listed in the Table (see Table 6.13). The MSEREG shows that there are little differences between the predicted CCT and the TDS values. For example, when the penetration level is 80MW, the CCT by TDS is 350ms and the predicted CCT is 351ms. Fig 6.15 is the comparison of predicted CCT using MLFNN and CCT using TDS. It can be observed

from Fig 6.15 that as the penetration increases, the CCT is worsened (i.e., the stability margin is reduced).

Table 6.13: The critical clearing time prediction using MLFNN

PENETRATION MW	**CCT USING TIME DOMAIN SIMULATION**	**PREDICTION OF CCT USING MLFNN**	**MSEREG**
80	**350**	351	0.0031
160	**345**	350	0.033
240	**340**	342	0.035
320	**335**	337	0.0134
400	**333**	330	0.0332

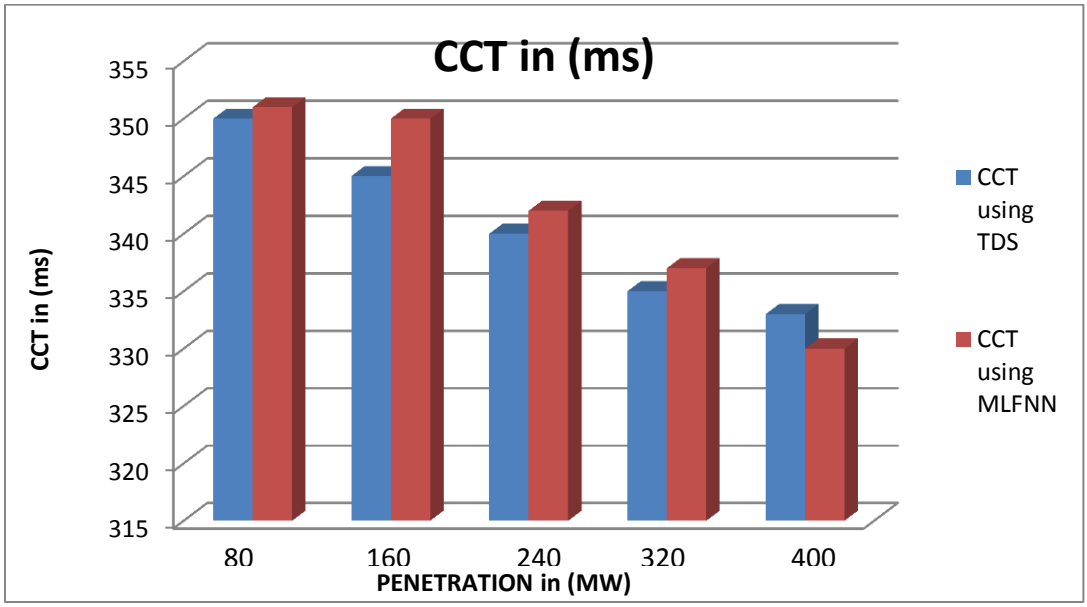

Fig 6.15: Comparison of Predicted CCT using MLFNN and CCT with TDS

The regression graph in Fig 6.16 shows the correlation between the predicted CCT and the actual CCT.

From correlation values in Fig 6.16, it can be seen that 84.9% of CCT was correctly predicted and 15.1% was inaccurately predicted. The time for training is 8.56 seconds while the testing is 0.06 seconds which is faster compared to that of RNN.

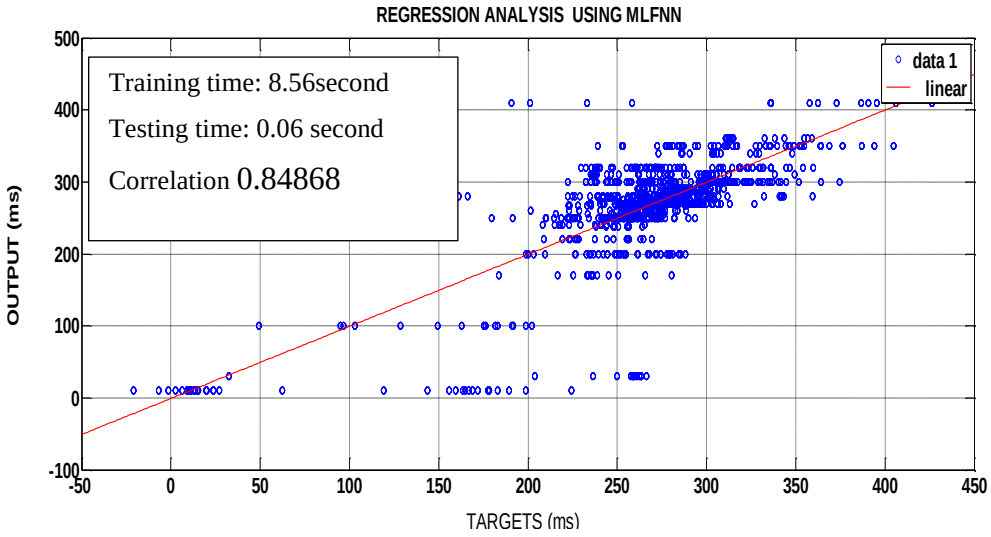

Fig 6.16: Regression graph during CCT Prediction using MLFNN (ANN3)

6.8.2 Recurrent Neural Network (RNN)

In this network, the analysis of the testing is reported since it has been trained and tested in the previous section.

Table 6.14 shows the results during RNN testing. The predicted values are closer to those obtained using TDS. For example, when the penetration is 80MW, the CCT using TDS is 350ms while the CCT using RNN is 345ms which is 98.6% accuracy of prediction. Fig 6.17 shows the graph indicating the prediction using RNN compared to when TDS is used.

Table 6.14: The critical clearing time prediction Recurrent Neural Network (RNN)

PENETRATION	CCT USING TIME DOMAIN SIMULATION	PREDICTION OF CCT USING RNN	MSEREG
80	**350**	**345**	0.0312
160	**345**	**345**	0.0144
240	**340**	**342**	0.0342
320	**335**	**335**	0.0152
400	**333**	**331**	0.0253

It takes 12.48 seconds for training while it takes 0.68 seconds to complete the testing. Fig 6.18 shows the regression graph. Rather than giving the accuracy of one predicted CCT, the regression analysis gives the overall correlation analysis. According to the graph, only 10.4% was inaccurately predicted while 89.6% was predicted accurately. The prediction is better than the prediction made using MLFNN which has an accuracy of 84.9%. Compare the time with that of MLFNN, RNN is slower.

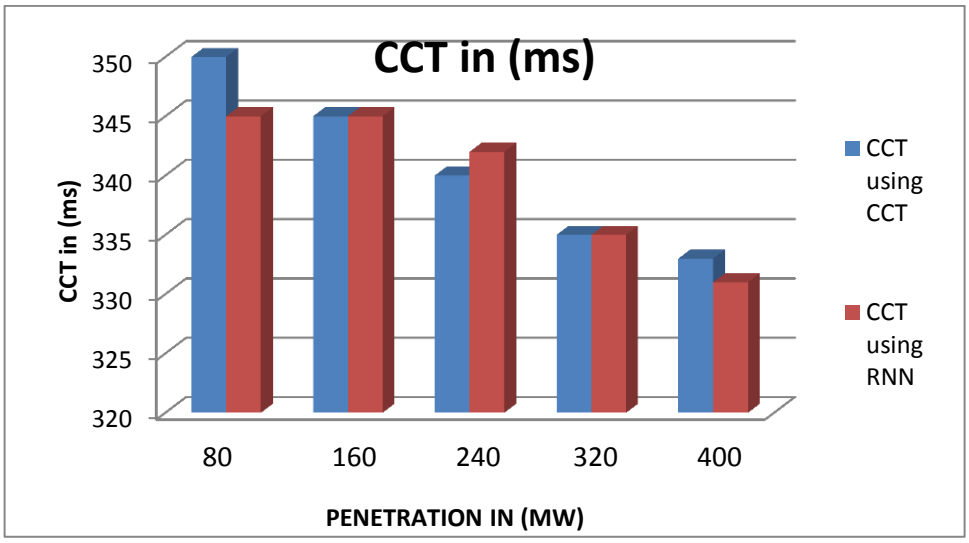

Fig 6.17: Comparison of Predicted CCT using RNN and CCT with TDS

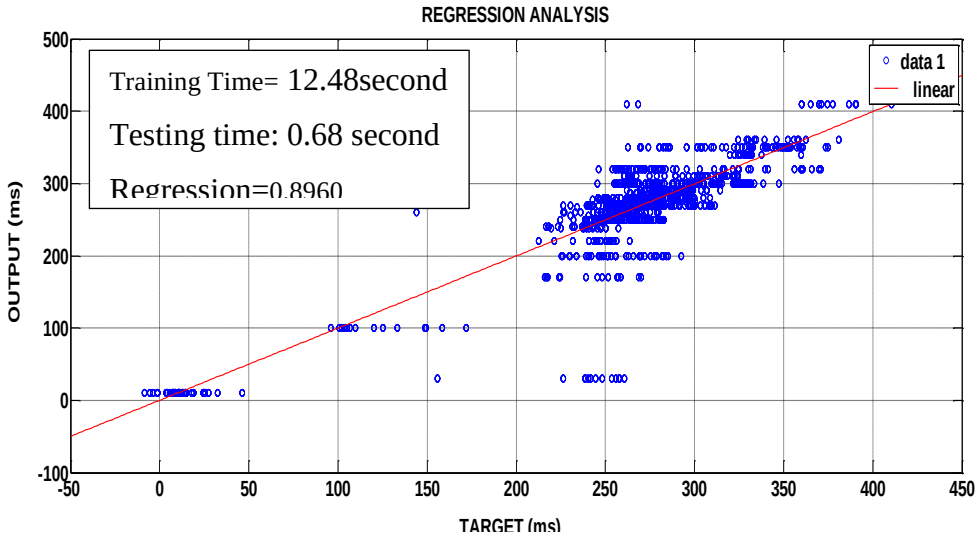

Fig 6.18: Regression graph during CCT Prediction Using RNN

6.8.3 Radial Basis Function (RBF)

Table 6.15 shows the testing results using RBF. As it can be seen in Table 6.15, the prediction results are accurate. For example, when the penetration was 80MW, the CCT using TDS was 350ms while the predicted CCT was 352ms. With this example, 99.4% accuracy was obtained and 0.6% not accurately predicted. The low MSEREG value shows that the prediction is accurate. Fig 6.19 shows that as the penetration increases the stability margin reduces. The predicted and the actual values of the CCT are closer as the penetration increases.

Table 6.15: The critical clearing time prediction Radial Basis Function

PENETRATION in (MW)	**CCT USING TIME DOMAIN SIMULATION**	**PREDICTION OF CCT USING RBF**	**MSEREG**
80	**350**	352	0.0122
160	**345**	347	0.0231
240	**340**	340	0.0101
320	**335**	335	0.0015
400	**333**	334	0.0162

The training time is 8.01seconds and the testing time is 0.065second. The overall accuracy is high as it can be seen on the Table. The correlation coefficient is 0.9959 (not shown in graph) which means that 99.6 % was accurately predicted while just 0.04% was inaccurately predicted. It is observed that RBF is slower than MLFNN and faster than RNN.

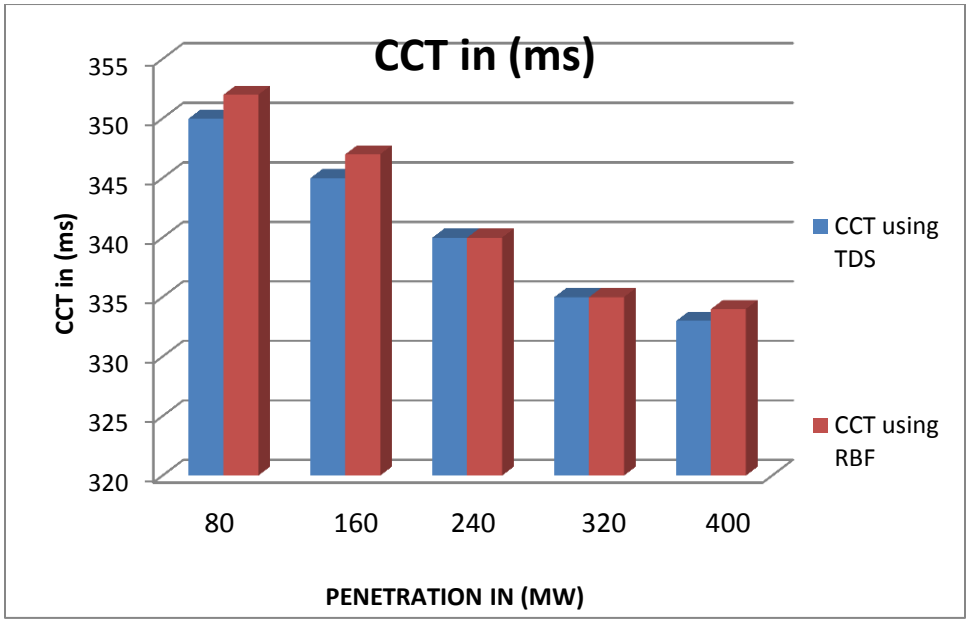

Fig 6.19: Comparison of Predicted CCT using RBF and CCT using TDS

6.8.4 Generalized Regression Neural Network (GRNN)

Table 6.16 shows the results when GRNN was used in the prediction. The accuracy of the prediction with MSEREG is shown in Table 6.16. When the penetration is 80 MW, CCT with TDS is 350ms while the predicted value using GRNN is 340ms. In this example, CCT is 97.1% accurately predicted and 2.9% inaccurately predicted. Using the regression analysis, the correlation coefficient is found to be 0.6773. It was observed that 67.7% was accurately predicted and 32.3% was inaccurately predicted. This value (inaccurate prediction) is high compared to MLFNN (15.1%) RNN (10.4%) and RBF (0.04%). It can be observed from Fig 6.20 that when the penetration increases, the CCT values using GRNN decreases as the penetration level increases except at 400MW where it increases

slightly. This is due to high inaccurate prediction that occurs in GRNN. It takes 12seconds for the training and 0.15second for the testing

Table 6.16: The critical clearing time prediction generalized regression neural networks

PENETRATION in (MW)	CCT USING TIME DOMAIN SIMULATION	PREDICTION OF CCT USING GRNN	MSEREG
80	**350**	340	0.2512
160	**345**	340	0.0532
240	**340**	342	0.0243
320	**335**	330	0.0434
400	**333**	335	0.0356

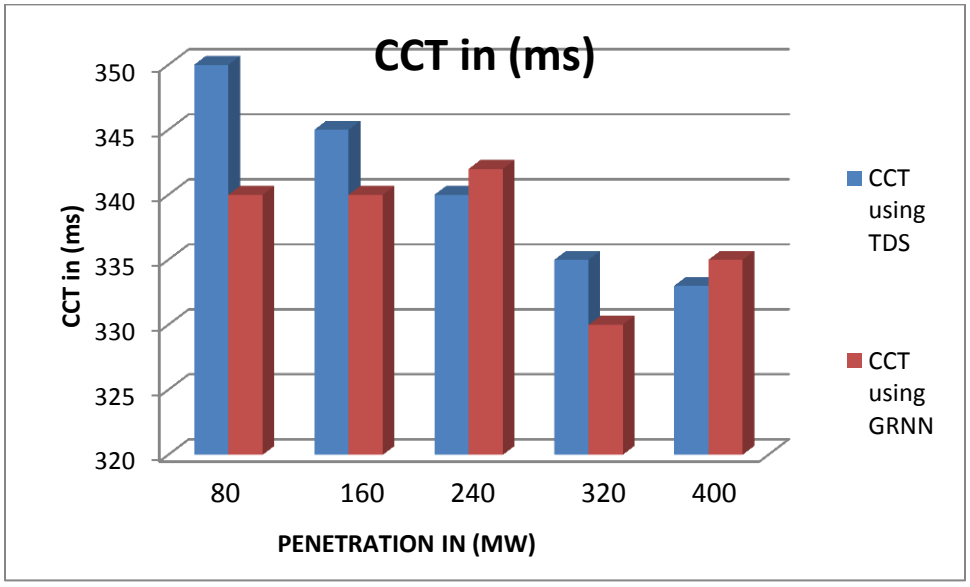

Fig 6.20: Comparison of Predicted CCT using GRNN and CCT using TDS

6.8.5 Self-Organized Map (SOFM)

Fig 6.21 shows the patterns using SOFM. It can be seen that there are five clusters in the figure. Input 1, input 4 and input 5 form one cluster. Input 2 forms another cluster. Input 3 forms the third cluster. Input 6 forms the fourth cluster while inputs 7 and 8 form the fifth cluster. The properties of the clusters are identified by analyzing the weight vectors

associated with the neurons in the clusters and comparing them with CCT. They are the visualization of the weight that connects each input to each 100 neurons in the 10x10 grid. The CCT is formed from the weight shown in Fig 6.22. The weight is a vector quantity. The neuron is represented by a red round object while the greenish objects are the training vectors. The blue line represents the distance between the vectors. The weight of the cluster neurons can be measured and relate it to the CCT. The results are shown in Table 6.17 and Fig 6.23. The first three input weights are displayed in three-dimensional patterns. Each neuron can be associated with its weight vector which represents a class of input vectors. Some neurons never classified any input vectors. Therefore, each component of a weight vector represents the critical clearing time (CCT). The time for the prediction is 0.78seconds.

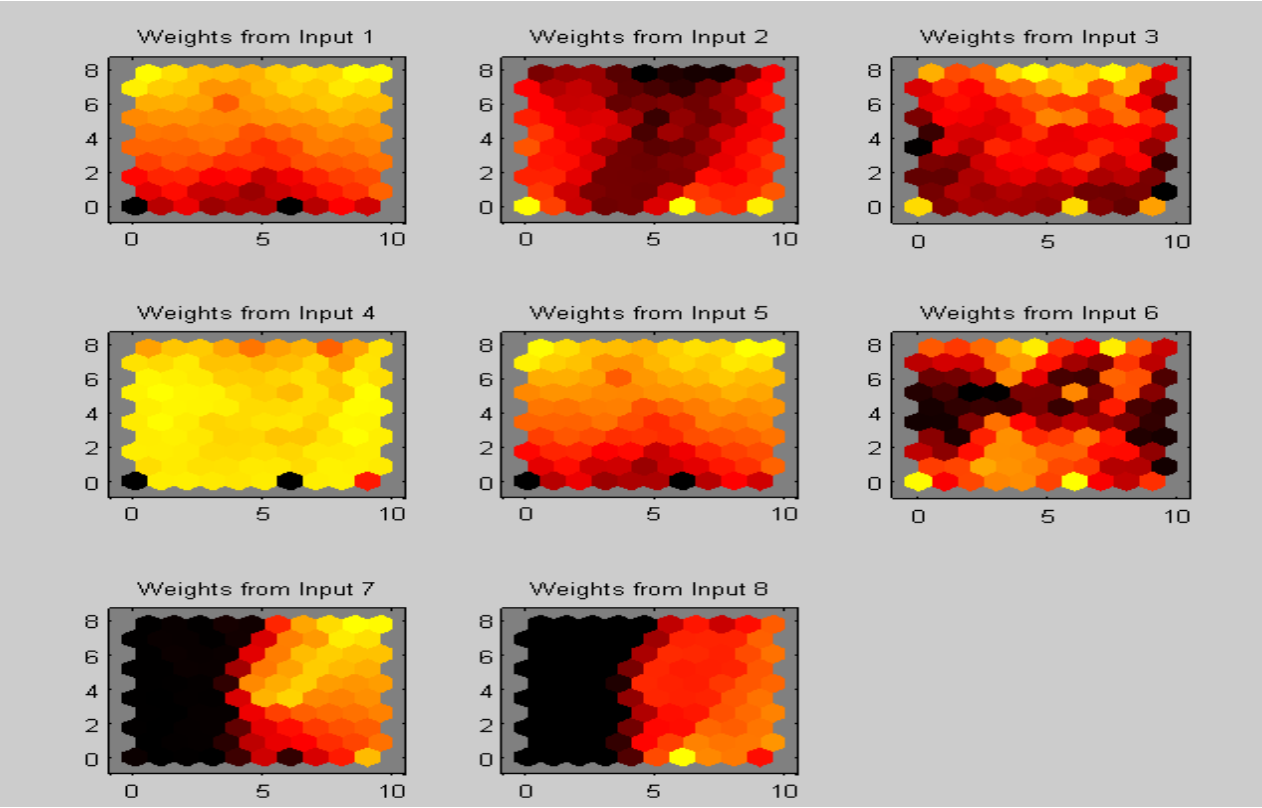

Fig 6.21: Input Weight of SOFM

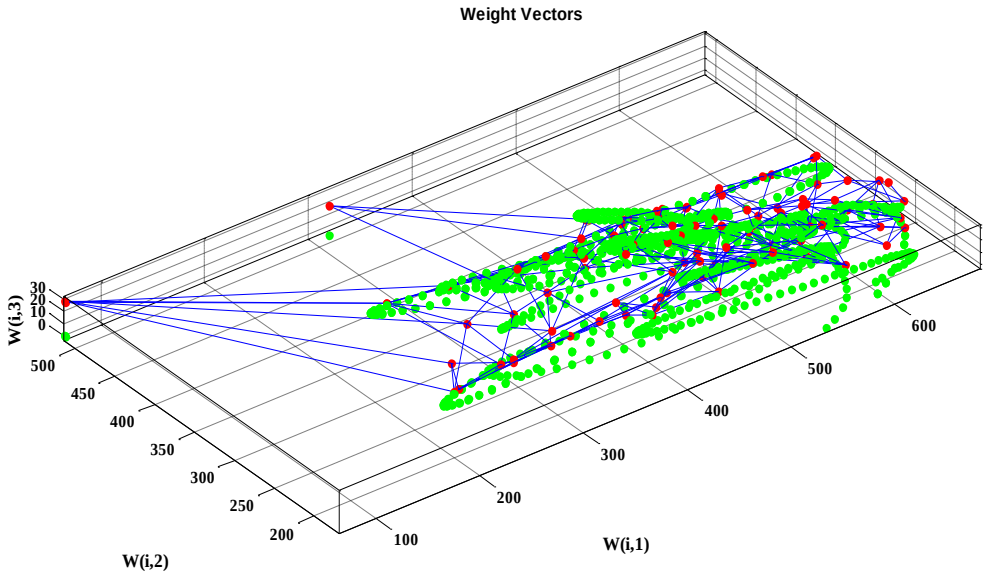

Fig 6.22: Weight Positions of SOFM

Table 6.17: The critical clearing time prediction Self Organizing Feature Map

PENETRATION LEVEL	CCT USING TIME DOMAIN SIMULATION	PREDICTION OF CCT USING SOFM	MSEREG
80	**350**	334	0.0524
160	**345**	320	0.0233
240	**340**	315	0.0352
320	**335**	320	0.0142
400	**333**	339	0.0221

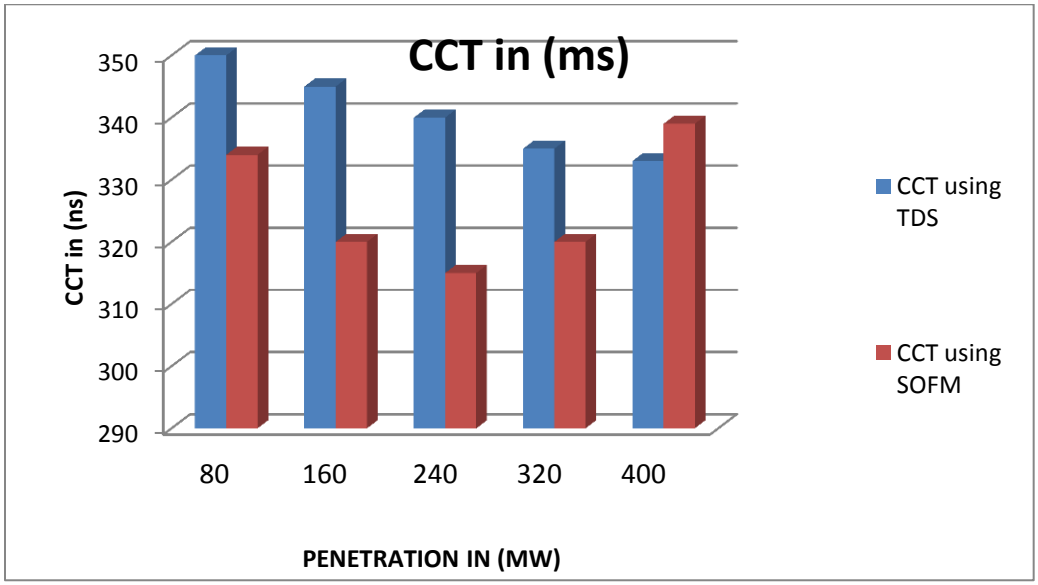

Fig 6.23: Comparison of Predicted CCT and CCT with TDS

Comparison was made between the five neural networks as shown in Fig 6.24. In Fig 6.24, the blue line indicates the CCT value when TDS is used while others are as indicated in the figure. At 80MW penetration, the CCT using time domain simulation is

350ms, while that of MLFNN is 351ms, CCT using RNN is 345ms, CCT using RBF is 352ms, CCT using GRNN is 340ms and for SOFM is 334ms. The closest CCT value to CCT using TDS is when RBF is used followed by MLFNN. Again at sample pattern 4, the CCT is for MLFNN is 337ms, RNN is 335ms, RBF is 335ms, GRNN is 330ms, SOFM is 320ms and TDS is 335ms. Therefore, when the prediction is compared with the TDS in all the tables, the CCT values predicted by RBF shows the closest values to the TDS and SOFM shows the worst CCT prediction.

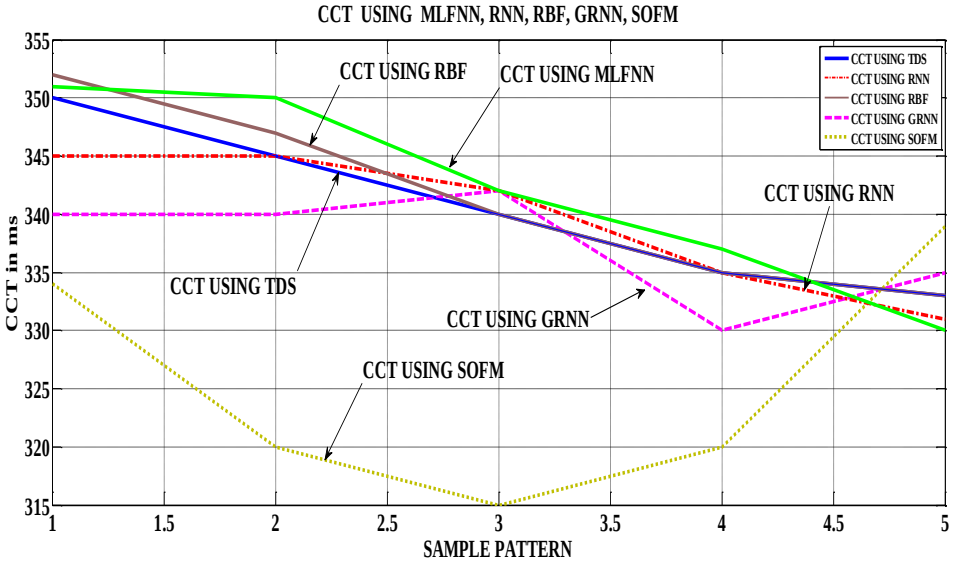

.

Fig 6.24: Comparison of CCT among the five neural networks

- **Time comparison of ANNS with Time domain simulations**

The time used by each ANNs during testing to predict instability are compared and presented in Table 6.18. In Table 6.18, the fault clearing time is increased from 0.1s to 0.3s and the rotor angle is monitored to see what time the loss of synchronism takes place in DIgSILENT. The time it takes the artificial neural networks to predict the loss of synchronism as the penetration of HYBRID SOLAR PV+SHP increases from 80MW to 400MW is also shown in Table 6.18. It shows that SOFM is the slowest in predicting instability while MLFNN is the fastest in predicting instability.

Table 6.18: Time comparison with Time domain simulations

Time to Predict Instability (s)							**HDG (HYBRID SOLAR PV+SHP) Penetration (MW)**
Fault Clearing Time (s)	Time Of Loss Of Synchronism (DIgSILENT) (s)	MLFNN	RNN	RBF	GRNN	SOFM	HDG (HYBRID SOLAR PV+SHP) PENETRATION
0.1	10	0.05	0.290	0.230	0.315	0.45	Export mode
0.15	12	0.08	0.311	0.230	0.315	0.475	Export mode
0.2	14	0.07	0.311	0.232	0.314	0.475	Export mode
0.25	15	0.06	0.412	0.228	0.313	0.475	Balanced mode
0.3	17	0.05	0.410	0.23	0.312	0.475	Import Mode

The five ANNs were also used to classify the state of the system into a stable (1) and unstable (0) states. The results are shown in Tables E1-E3 in Appendix E. It can be seen that RBF gives the best result in term of accuracy of prediction. Followed by MLFNN, then GRNN. SOFM performs generally worst during classification which is followed by RNN.(see Table E3 of Appendix E).

Chapter 7

Real Time Modelling and Estimation of Critical Clearing Time

As mentioned in chapter 6, critical clearing time is not a static stability index but a non-linear index that depends on varying operating conditions [32]. Using CCT as a fixed index and monitor the system based on this in order to take decision during system operation could lead to unwanted outcome. Sometime false alarm could be instigated indicating instability when actually the system is stable. In order to overcome this challenge, computational intelligence approach which can predict ahead of time and also generalised the training was also implemented. The whole simulation was conducted offline by using DIgSILENT power factory and Matlab neural network toolbox and m-file codes. This chapter discusses the wide area monitoring of CCT and rotor angle in real time. Wide area monitoring approach is motivated by the growing needs for real time monitoring and control of power system transient stability and the availability of installed Phasor Measurement Units (PMUs) for direct measurements of real power systems.

Phasor Measurement Units (PMUs) measure the dynamic states of the power system in real time and allow response to be made timely to an event in progress. The advent of Global Positioning System (GPS) has made it possible to synchronized data together. GPS provides geographical coordinates and time synchronization. By synchronized sampling of microprocessor-based systems, phasor calculation can be placed on a common reference to achieve synchronized phasor measurement units. This emerging technology will output the synchrophasor such as phasor voltages and currents as well, as their angles.

However synchronous time frame rotor angle cannot be obtained by direct measurements. The estimation can be carried out from the synchrophasor measurements from the PMU. The measurements carried out by PMUs are represented in synchronous time-frame at normal frequency but to compute the rotor angle or the CCT at the same reference frame

and also compute a prediction of this parameter at the next time-steps requires the use of more advanced method such as artificial neural networks. A recurrent neural network is used in this chapter to provide a step-ahead prediction of CCT and rotor angle of individual generators considering the fact that RNN can cope with various modelling uncertainties. RNN accepts data input to make a temporal characteristic pattern and takes both long time and short time decisions. The accuracy of the result is based on the learning rule or the training algorithm. This neural network uses back propagation (BP) implemented with a Levenberg Marquardt algorithm which is based on gradient descent.

The idea of calculating CCT for each generator becomes necessary considering the fact that each generator in a multi-machine system is equipped with a protective system. Instead of representing the entire system with one CCT value calculated by reducing the machines to a single machine, in this research, the calculation is based on individual generator's CCT and the smallest CCT value is taken as the system CCT value.

However, CCT depends on so many factors such as initial operating condition, inertia, the length of the transmission line, the loading of the generator, the type of generators, etc. It is important to design a model that will learn these characteristics and make appropriate decisions. To capture the behavior of the system accurately and the effect of these changing parameters on CCT together with the step-ahead prediction, a recurrent neural network model is developed. The recurrent neural network (RNN) is distributed across the network. Each generator has an attached RNN model to monitor the CCT in real time. As a result, the RNNs are considered to be distributed across the network and locally makes use of the PMU data. This method is fast and accurate. Once properly trained, it can follow the step changes of CCT as the operating condition changes. Using RNN in the control room will enhance an efficient operation of the power system by providing timely and intelligent dynamic monitoring with high level of precision and accuracy.

In order to collect appropriate real time data for neural network training, modelling and the simulations of the test system (68-Bus system) are done with a Real Time Digital Simulator (RTDS). RTDS integrated with PMU is used because it provides real time data for the RNN training and testing.

7.1 Modified 68-Bus System

Fig 7.1 shows the modified 68-bus system. For this thesis, the 68-bus system is modified to include HDG and PMUs. The modified 68-bus system consists of 16 centralized generators (CG) represented as (G1-G3, G5-G16, HDG), 68 buses, 16 PMUs located at the high voltage side of the generator's transformers. In the modified power system, GEN4 is replaced by HDG (SOLAR PV and SHP). Note that in this work, we did not attempt to optimally place the PMUs. Each generator is modelled as a two-axis (dq) model of a synchronous machine and is equipped with an excitation system (AVR) and a turbine governor. GEN13 which is connected to bus 65 is used as the common reference generator or slack generator. The choice of GEN13 as a reference generator is because of its higher inertia and higher capacity (3591MW). The transmission lines are modelled as π networks and the loads as constant power. Table 7.1 shows the characteristics of the modified 68-bus system.

Table 7.1**:** Characteristics of the Modified 68-Bus System

System Characteristics	**Value**
No of generators (Including the HDG)	17
No of buses	68
Transformer	18
PMUs	16
HDG (SHP, Solar PV, DFIG)	3(8+j4MVA each)

The modelling approach is based on common reference to estimate the rotor angle [174], ,[175]. The advantage of common reference is that it is easy to implement with simple equations [141]. Every other generator is referred to the common reference generator when calculating the rotor angle.

The system's data are listed in Tables A9-A13 of Appendix A.

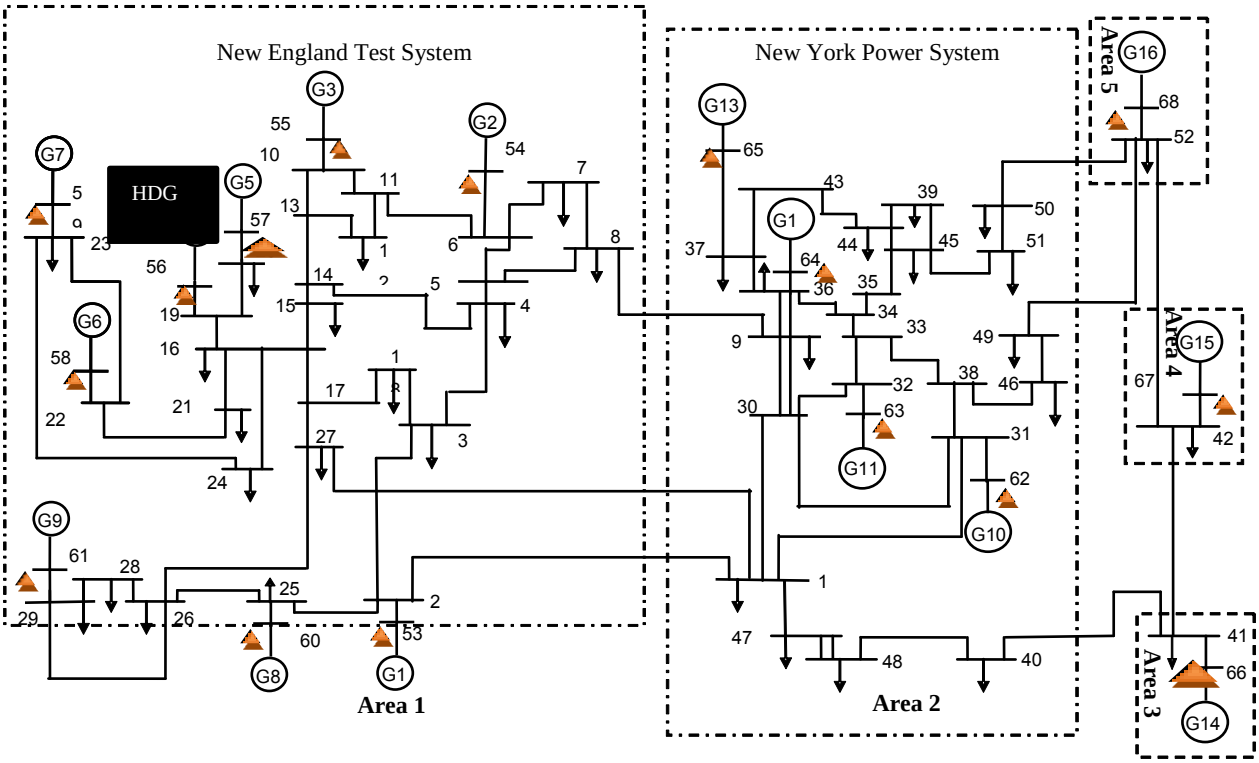

Fig 7.1: Modified 68-bus New England/New York power system

PMU Location

7.2 Recurrent Neural Network model

Fig 7.2 describes the architecture of the recurrent neural networks model used which consist of four inputs features from PMU measurements which are voltage, current and their angles, 8 hidden neurons, a delay unit, bias and the output ($P_m(t)$ or $\delta(t)$). The proposed architecture consists of two similar RNNs (RNNA and RNNB) wired together. The output of RNNA which is mechanical power or rotor angle is used as an additional input for RNNB. RNNB consists of 5 inputs (4 outputs of PMU and one additional input from the output of RNNA). The reason two ANNs were used is because RNNA is needed to track the continuous changes in the mechanical power $P_m\,(t)$ or $\delta(t)$ as the stability swing continues. Note that the rotor angle cannot be directly measured, therefore it is necessary to monitor the rotor angle or mechanical power as it changes with time. The

successive relative angle measurements is used to estimate the shift in P_m and $\delta(t)$. Once the new P_m or $\delta(t)$ is determined, the synchronized critical clearing time can be estimated from the output of RNNB [176]. Predicting the mechanical power ahead of time enhances the accuracy of prediction of CCT.

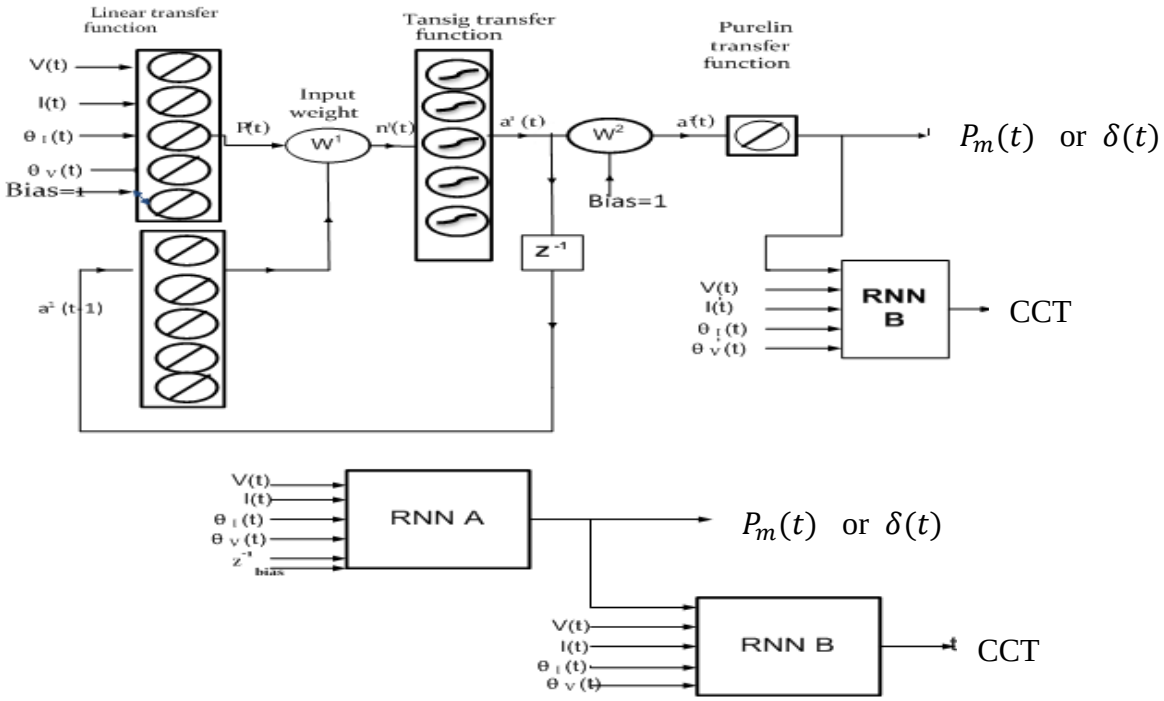

Fig 7.2: Proposed RNN Architecture for the 68-Bus System

7.3 Design of RNN Network Model for Real Time Prediction

Fig 7.3 shows the simple connection describing the flow of data from the PMU to the recurrent neural networks (RNNA and RNNB). These simple ANNs (RNNA and RNNB) will be incorporated with each generator in order to monitor the rotor angle and subsequently the CCT. As such, there will be 16 samples of the simple networks. The prediction is based on one-step ahead which is 0.0167s (one cycle of the fundamental frequency). The goal is to be able to determine the status of the system at 0.0167s ahead of time.

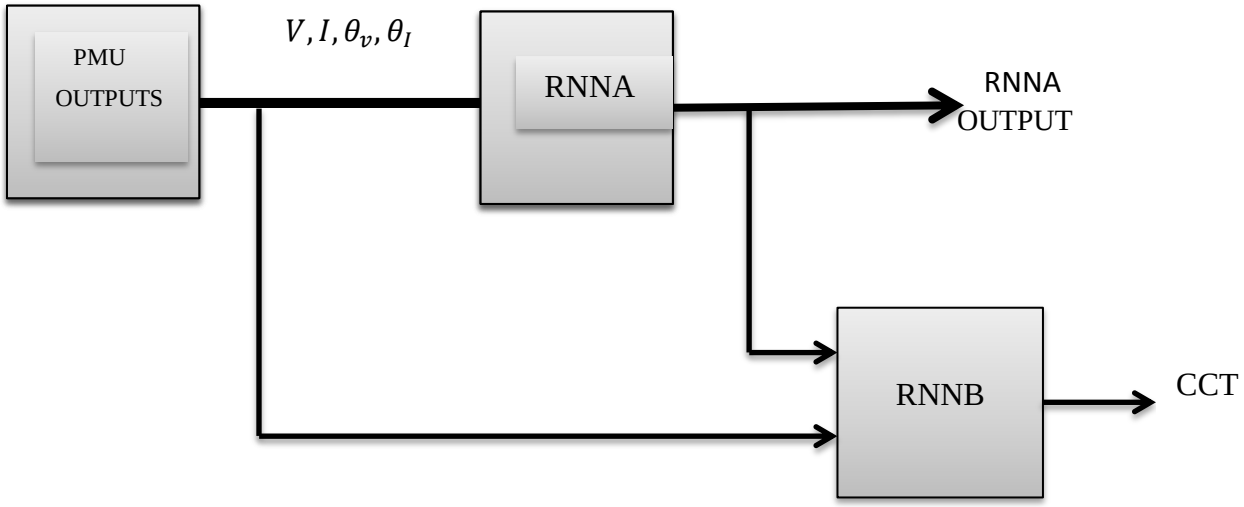

Fig 7.3: Simple connection for real time data flow

- **System's Critical Clearing Time**

Since every generator is equipped with a protection system, there will be 16 CCTs. The block diagram in Fig 7.4 shows how the CCT of the system is obtained. The minimum of the CCTs (CCT1-CCT16) is the system CCT.

In Fig 7.4, CCT1–CCT16 are the predicted value from the RNN. This is calculated for each generator and the minimum value is calculated for the entire network called the system's critical clearing time.

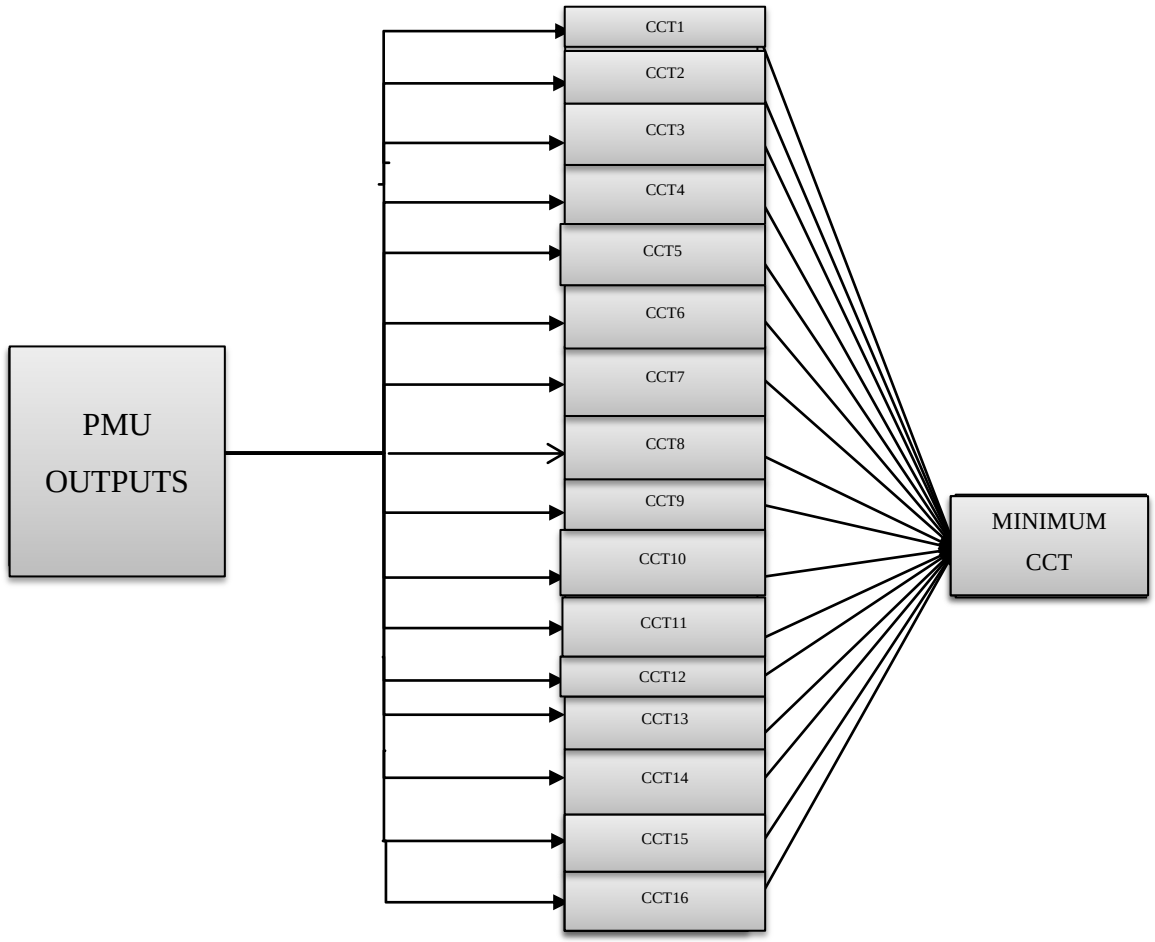

Fig 7.4: Predicted 16 CCTs from Recurrent Neural Networks

7.4 Data Collection and Preparation

A large number of data were generated by applying three-phase faults for simplicity. However, other types of fault can also be applied. There are two scenarios describing the types of fault applied. They are:

- Single – Contingency (Three-phase fault only)
- Multi- Contingencies (Three-phase fault and loss of generation)

The single contingency only considers the three-phase fault. For the multi-contingencies, the three-phase fault was applied on some selected lines while at the same time certain

generators were disconnected from the system. However, in order to investigate the impact of HDG on the system, generator 4 is replaced with HYBRID SOLAR PV+SHP. Generator 4 is rated 800 MW and so the total capacity of the HDG is 800MW. The fault was applied and cleared after 200ms by removing the line. Forty contingencies distributed across the major areas of the network were considered and time domain simulations were conducted in RTDS to collect the data for the training. The post fault data were collected 2seconds after the fault.

7.5 Rotor Angle Measurement Using PMU

The first step is to determine the rotor angle from the output of the PMUs since the rotor angle cannot be directly measured. The results are shown in the next section.

Fig 7.5 and Fig 7.6 show the results of the generator's rotor angle measured using PMU output results. The output data from the PMU are collected in steps of 0.01667 seconds, which is 1 cycle of fundamental frequency of the synchronous generator when a three-phase fault was applied and cleared after 200ms.

It can be seen that the rotor angle curves of the generator can be reconstructed using PMU data. The graphs show the accuracy and capability of PMU in measuring the rotor angle of generators using the voltages and currents from the output of the PMU.

Fig 7.7 shows the behavior of generators when the system was disturbed with three-phase fault and a loss of generators (5,6, 7 and 16).

During the real time operation, the active power can be directly measured without using PMU. However, PMU can also be used to measure the active power. The ability of PMU in measuring the active power is compared with the direct measurement from RTDS.

Fig 7.8 shows the graphs of the active power of some selected generators (not all the generators are shown) compared with the PMU measurements. There is no difference in the measurement as can be seen in Fig 7.8.

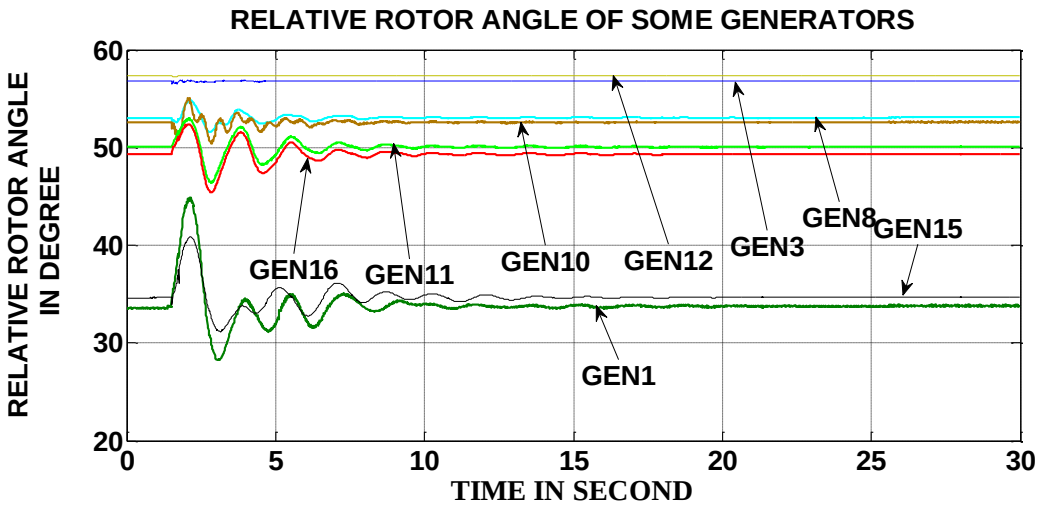

Fig 7.5: Rotor Angle Measurement of some Selected Generators Using PMU

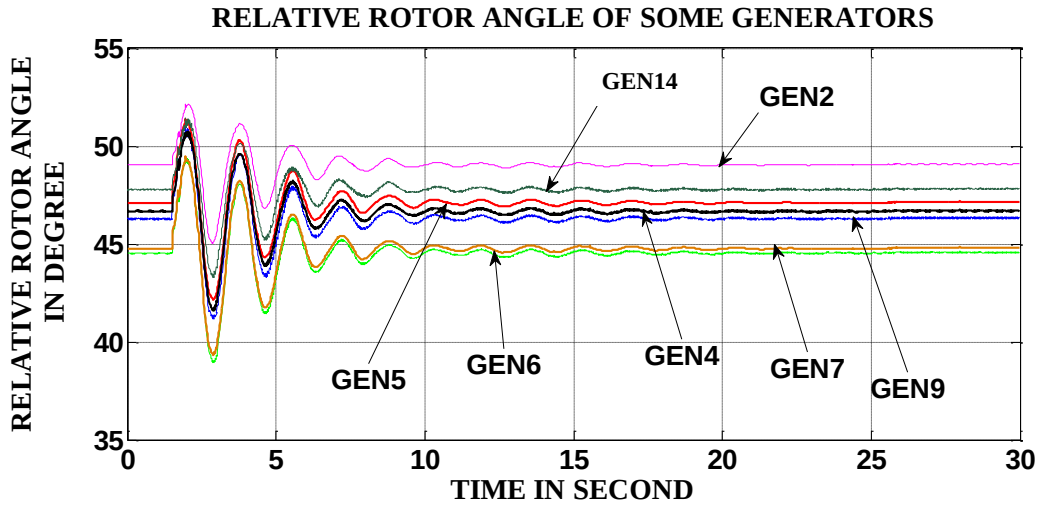

Fig 7.6: Rotor Angle Measurement of some Selected Generators Using PMU

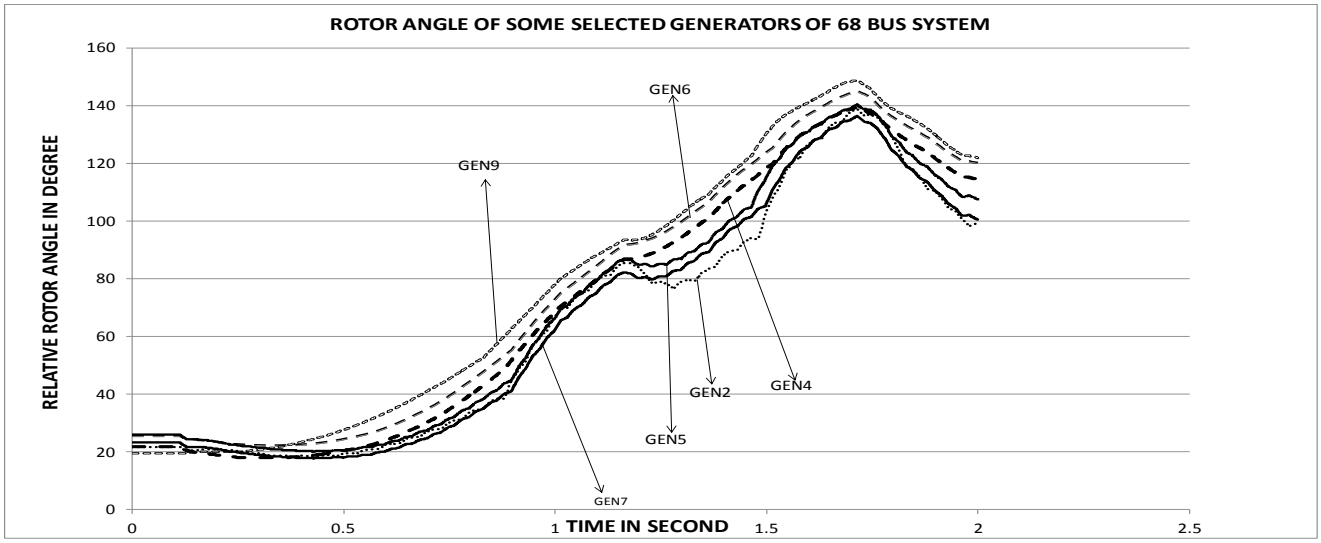

Fig 7.7 : Unstable Rotor Angle Measurement PMU of Generators Using PMU

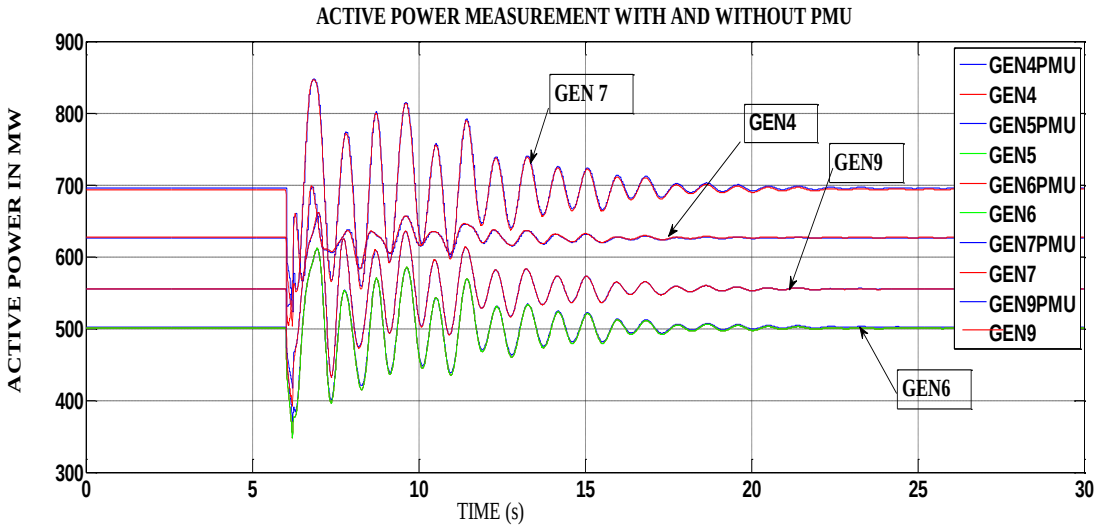

Fig 7.8: Active Power Measurement Of some selected Generator With and Without PMU

.

Based on the accuracy of the above results, RNN can now be used to model the dynamic of the system and make prediction 0.0167 seconds ahead in order to take an accurate decision in case of instability.

It should be mentioned that RTDS provides real time or near real time results with time-step of 50 μs where an hour in real world is equal to an hour in the simulator. However,

RTDS alone cannot be used to predict the stability status of the power system ahead of time. This is why RNN should be used.

7.6 Training of RNN

Accurate modelling with RNN depends on the structure of the RNN network together with the hidden neurons. The choice of the number of neurons and the training algorithm is determined by trial by error and shown in Appendix F. The training is based on the data collected. After the training of each RNN based on the four input data from the PMU, the mechanical power or rotor angle is determined. The mechanical power or rotor angle also serves as input for the determination of the CCT. With five inputs to the RNN B, the critical clearing time of each generator is obtained. On each epoch, the training data are each submitted to the network for training (i.e online training).

Fig7.9 shows the actual and the predicted rotor angle during training mode while Fig 7.10 shows the actual and the predicted rotor angle during testing mode.

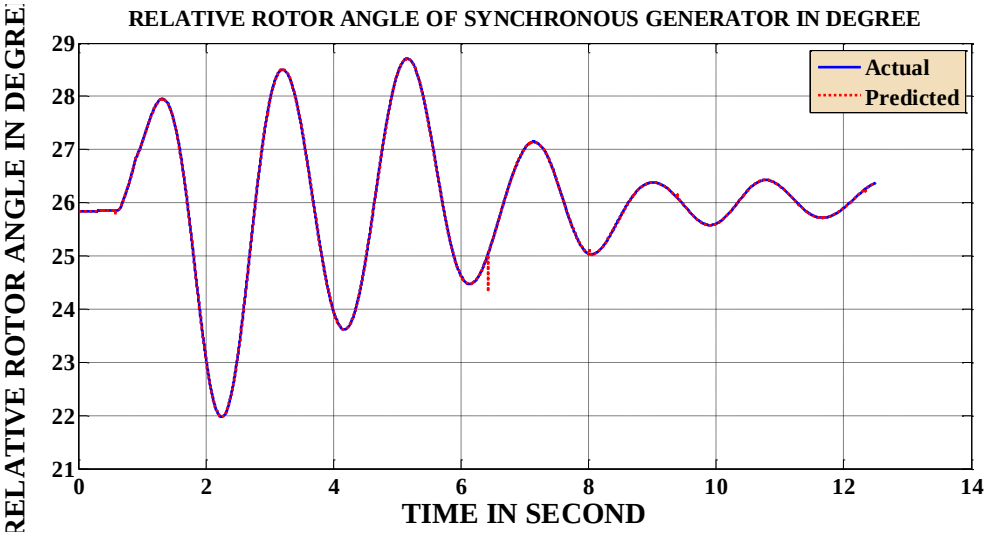

Fig 7.9: One Step Prediction of Rotor Angle of Generator 1during Training

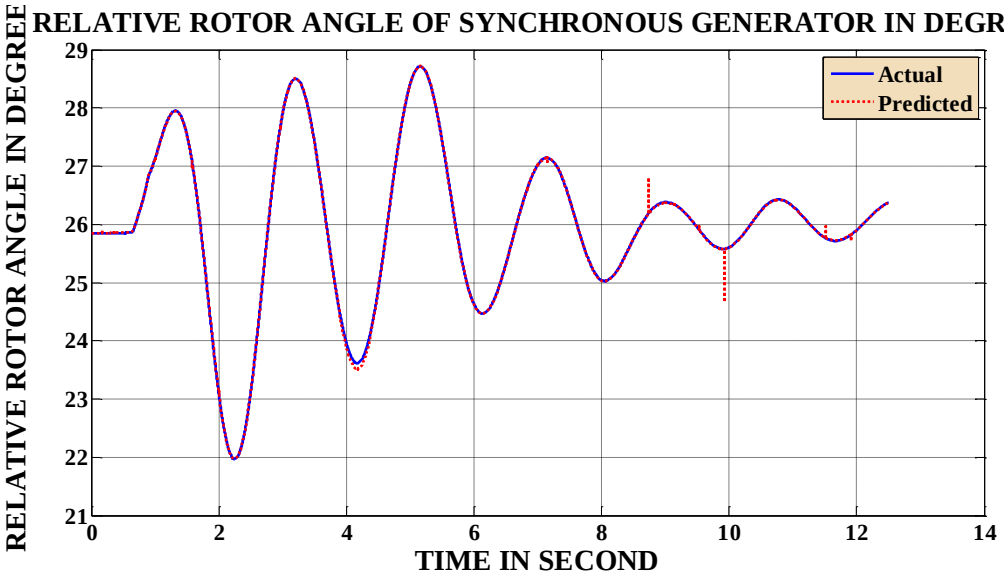

Fig 7.10: One-Step Prediction of Rotor Angle of Generator 1 during Testing

The time it takes for the training is 1minute and 53seconds (i.e 1.53s) while the time for the testing is 70ms. The MSEREG during the training is 1.25×10^{-7} while MSEREG during testing is 3.78×10^{-7}. The values of the MSEREG for both training and testing indicates that the model can perform the task of one-step prediction of rotor angle accurately and timely. The testing is faster compare to the time for the training. This is expected considering the fact that it requires more time for learning than for testing. The time it takes for RTDS in Fig 7.10 is 13s while for RNN is 70ms. This indicates that RNN provides faster simulation compares to RTDS.

7.6.1 Determination of CCT during Training of RNN when Single Contingency is applied

The training was conducted with 10240 post fault data. The data were distributed as follows; 70% was used for training, 15% for testing and 15% for validation. During the training, different hidden neurons were tested in order to find the appropriate number of hidden neurons for solving this problem. It was discovered that 8 hidden neurons was appropriate because it gives the smallest errors with good time scale enough for the prediction. Fig 7.11, shows the output of RNN and the actual CCT during training while Fig 7.12 and Fig 7.13 show the percentage error and the regression analysis, respectively. These two graphs (Fig 7.12 and Fig 7.13) show a high degree of accuracy and precision

that is good enough to be used for real time prediction. The correlation coefficient shown in the regression analysis graph (Fig 7.13) is 0.9987. The correlation coefficient shows that 99.87% was accurately predicted with only 0.13% inaccurately predicted. The time for prediction in case of single contingency is 85ms.

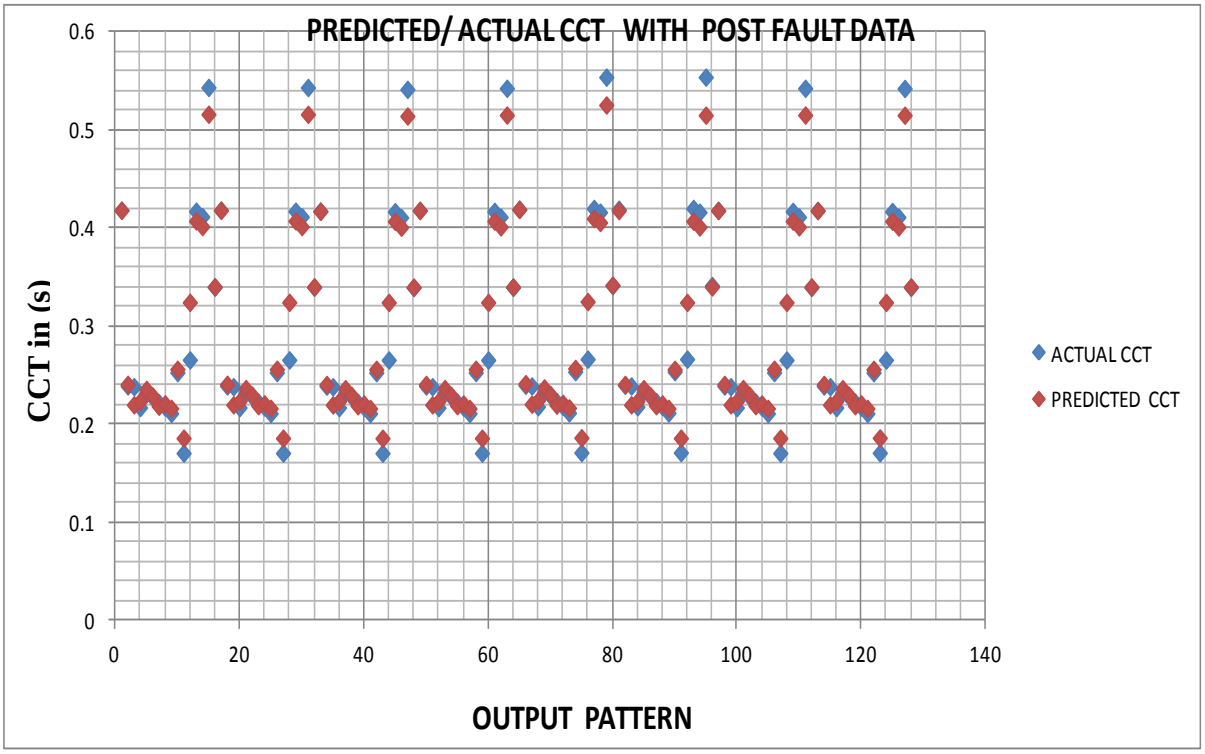

Fig 7.11: RNN Training considering Single-Contigency

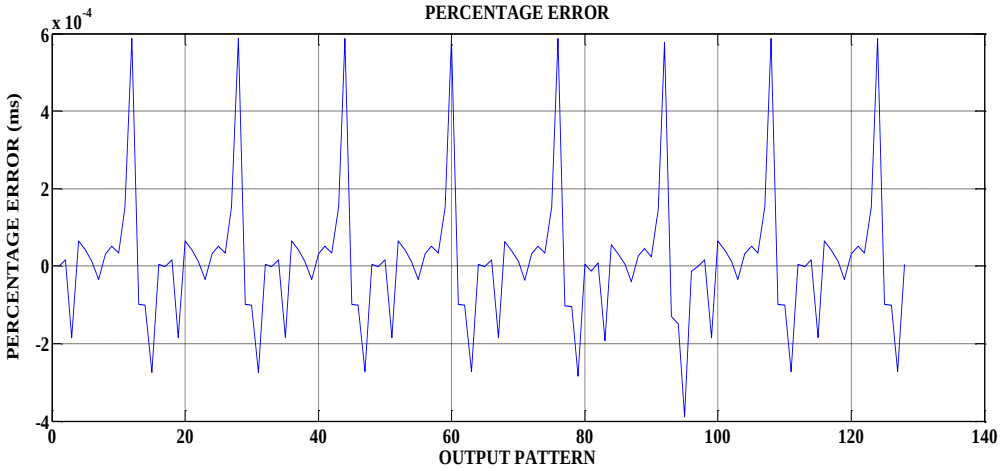

Fig 7.12: Percentage error of single-contingency

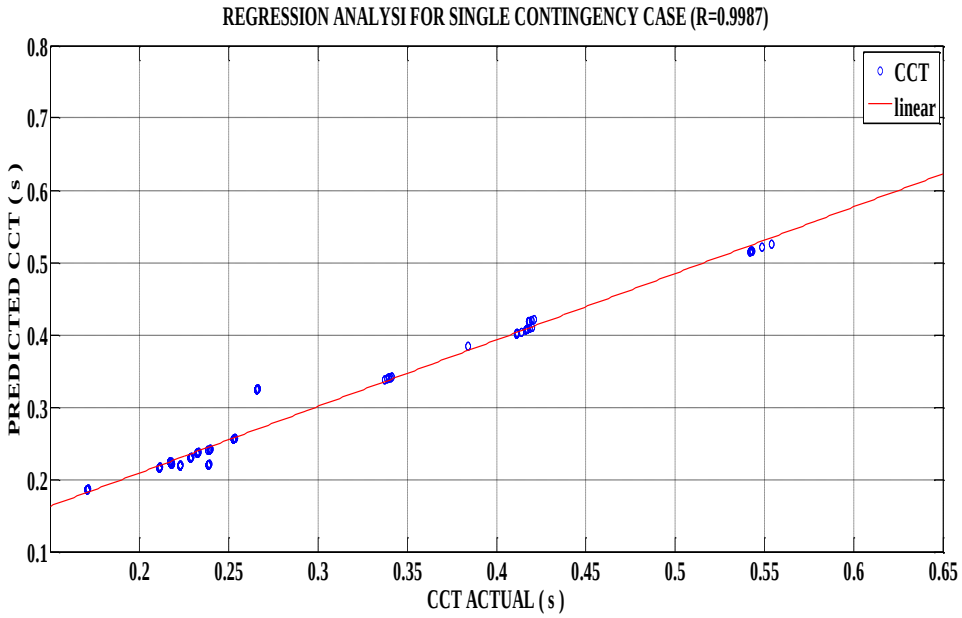

Fig 7.13: Regression analysis for single-contingency

7.6.2 Determination of CCT during Training of RNN when Multi-Contingencies is applied

In case of multi- contingencies, the behaviour of the system is observed when a three-phase fault and a loss of generation were considered. Generator 5, 6, 7 and 16 were switched off alternatively with the three-phase fault. Fig 7.14 shows the actual and the predicted value of the CCT. The accuracy of the predicted values was also determined by the percentage error and mean square error with regularization. As it can be seen in Fig 7.14, the predicted values are very close to the actual values. Figs 7.15 and Fig 7.16 show the detail of the performance index for the multi-contingencies case. The correlation coefficient shown in the regression analysis graph (Fig 7.14) is 0.9986. It is observed that only 0.14% was inaccurately predicted and 99.86% was accurately predicted. The time for prediction in case of multi-contingencies is 110ms.

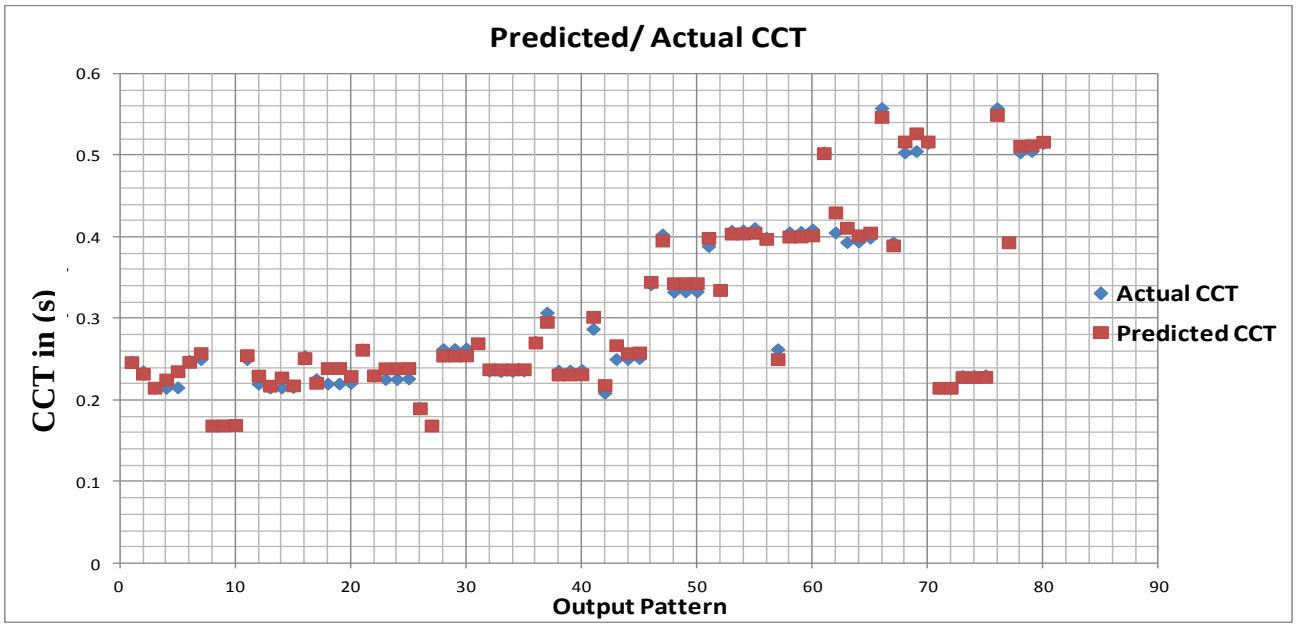

Fig 7.14: Predicted CCT with Multi-Contigencies

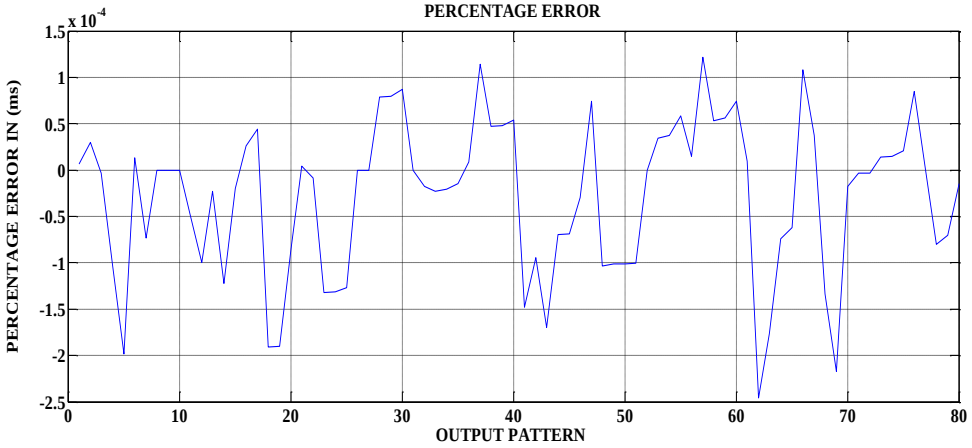

Fig 7.15: Percentage error with Multi-contingencies

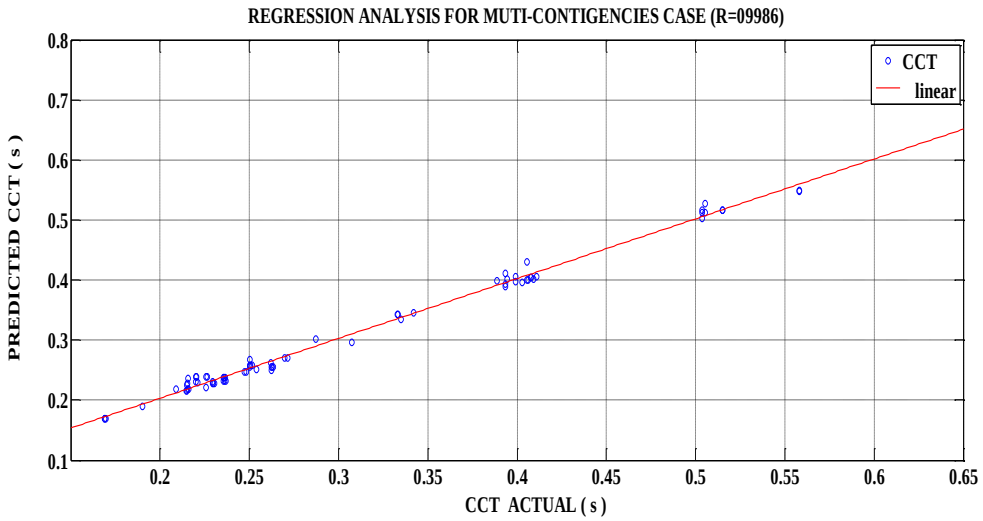

Fig 7.16: Regression Analysis with Multi-Contingencies

The error in both cases indicates that the model has been well trained. The error in case of multi contingencies is much higher than the error in the single contingency.

Critical clearing time prediction in real time using recurrent neural network is accurate and timely.

7.7 Investigating the Impact of HDG on the Critical Clearing Time with RNN

As discussed previously, the impact of HDG is investigated by replacing generator 4 with HYBRID SOLAR PV+ SHP. Table 7.2 and Table 7.3 show the CCT values when a three-phase fault and a loss of generation were considered.

Two case studies were investigated in the simulations. The first case study was when there is no HDG integration and the second case study is when there is HDG integration. The situation when there is no HDG integration indicates that the original conventional generator was retained as generator 4. Different disturbances were considered such a loss of generators and lines disconnection due to three phase fault. For example, in the second and third columns, generator 5 was disconnected and the CCT is calculated when NO HDG is connected and when HDG is integrated. In columns 4 and 5, it was a transmission line that was disconnected.

There are 16 values of CCTs which means each generator has its own CCT. Zero in Tables 7.2 and 7.3 show that the generator is disconnected from the system for

contingency analysis. Data were gathered for each case study in order to train RNN. The training also follows the same step as stated in section 7.6. The results of the RNN for one-step predictions are shown in Tables 7.2 and 7.3. It is observed from Tables 7.2 and 7.3 that the system stability is worsened when HDG is used to replace conventional generator (including generator 4). The approach of replacing the conventional generators with DG/HDG will definitely create serious stability issues.

Table 7.2: CCT with HDG and without HDG (RNN results)

	CCT (s) When GEN 5 is disconnected		**CCT (s) When a line disconnected**		**CCT (s) When a line is disconnected**		**CCT (s) When a line is disconnected**		**CCT (s) When a line is disconnected**	
No of Generators	**No HDG**	**WITH HDG**	**No HDG**	**WITH HDG**	**No HDG**	**WITH HDG**	**No HDG**	**WITH HDG**	**No HDG**	**WITH HDG**
1	0.3888	0.3881	0.4182	0.4184	0.3823	0.3821	0.4075	0.4197	0.4202	0.4075
2	0.2715	0.2711	0.2408	0.2392	0.2692	0.2691	0.2361	0.2397	0.2397	0.2361
3	0.2697	0.2693	0.2199	0.2384	0.2674	0.2673	0.2354	0.2389	0.2389	0.2354
4	0.2472	0.2457	0.2236	0.2172	0.2442	0.2441	0.2149	0.2179	0.2179	0.2149
5	0	0	0.2364	0.2324	0.265	0.2649	0.2296	0.2327	0.2329	0.2296
6	0.2664	0.2622	0.2297	0.2285	0.2601	0.26	0.2258	0.2288	0.2289	0.2258
7	0.2541	0.2534	0.2191	0.2226	0.2522	0.2521	0.2202	0.2229	0.223	0.2202
8	0.2502	0.2499	0.2208	0.2177	0.2484	0.2484	0.2154	0.218	0.2181	0.2154
9	0.2435	0.2432	0.2163	0.2112	0.2418	0.2417	0.209	0.2114	0.2115	0.209
10	0.2873	0.2869	0.2561	0.2528	0.2845	0.2844	0.2503	0.2544	0.2546	0.2503
11	0.2482	0.2479	0.1859	0.1707	0.2464	0.2464	0.1689	0.1709	0.171	0.1689
12	0.2647	0.2644	0.3243	0.2657	0.2626	0.2625	0.2625	0.2661	0.2662	0.2625
13	0.3991	0.3979	0.4073	0.4173	0.3917	0.3913	0.4057	0.4187	0.4193	0.4057
14	0.5037	0.5013	0.4016	0.4117	0.4889	0.4882	0.3936	0.414	0.4149	0.3936
15	0.658	0.6527	0.5160	0.5434	0.6259	0.6246	0.5036	0.5486	0.5507	0.5036
16	0.342	0.3413	0.3377	0.3373	0.3373	0.3371	0.3329	0.3407	0.341	0.3329
System stability	0.2435	0.2432	0.1859	0.1707	0.2418	0.2417	0.1689	0.1709	0.171	0.1689

Table 7.3: CCT with HDG and without HDG continue (RNN results)

	CCT (s) When a line is disconnected		**CCT (s) When a line is disconnected**		**CCT (s) When a line is disconnected**		**CCT (s) When a line is disconnected**		**CCT (s) When Generator16 is disconnected**	
No of Generators	**No HDG**	**WITH HDG**	**No HDG**	**WITH HDG**	**No HDG**	**WITH HDG**	**No HDG**	**WITH HDG**	**No HDG**	**WITH HDG**
1	0.4184	0.4181	0.4182	0.4179	0.4184	0.4181	0.4182	0.4179	0.4109	0.4073
2	0.2392	0.2391	0.2408	0.2407	0.2392	0.2391	0.2408	0.2407	0.237	0.236
3	0.2384	0.2384	0.2199	0.2199	0.2384	0.2384	0.2199	0.2199	0.2364	0.2354
4	0.2172	0.2171	0.2236	0.2235	0.2172	0.2171	0.2236	0.2235	0.2156	0.2148
5	0.2323	0.2315	0.2356	0.2363	0.2324	0.2323	0.2364	0.2363	0.2305	0.2295
6	0.2284	0.2276	0.2296	0.2288	0.2285	0.2284	0.2297	0.2296	0.2266	0.2257
7	0.222	0.2226	0.2190	0.2185	0.2226	0.2226	0.2190	0.2190	0.221	0.2201
8	0.2177	0.2176	0.2208	0.2207	0.2177	0.2177	0.2208	0.2208	0.2161	0.2154
9	0.2112	0.2111	0.2163	0.2162	0.2112	0.2111	0.2163	0.2162	0.2097	0.209
10	0.2528	0.2527	0.2561	0.2560	0.2528	0.2527	0.2561	0.2560	0.2515	0.2503
11	0.1707	0.1707	0.1859	0.1859	0.1707	0.1707	0.1859	0.1859	0.1695	0.1689
12	0.2657	0.2656	0.3243	0.3242	0.2657	0.2656	0.3243	0.3242	0.2635	0.2624
13	0.4173	0.417	0.4073	0.4071	0.4173	0.417	0.4073	0.4071	0.4093	0.4055
14	0.4118	0.4112	0.4017	0.4011	0.4117	0.4113	0.4016	0.4012	0.3991	0.3934
15	0.5435	0.5421	0.5161	0.5148	0.5434	0.5424	0.5160	0.5151	0.5152	0.503
16	0.3399	0.3396	0.3403	0.3400	0.3398	0.3397	0.3402	0.3401	0	0
System stability	0.1707	0.1707	0.1859	0.1859	0.1707	0.1707	0.1859	0.1859	0.1695	0.1689

It can be concluded that PMU can be used to measure the rotor angle. At the same time RNN is also an effective tool capable of predicting the CCT and the rotor angle ahead of time (0.0167s) in order to avert possible blackouts. Besides, when HDG is used to replace the original conventional generator, the system CCT is reduced. It means the stability margin is worsened. This is different from a situation where the DG/HDG is used to supply the increasing load demand without reducing the number of conventional generators.

7.8 Summary

In this chapter, the wide area monitoring using PMU integrated into RTDS was investigated. The method here is to calculate the CCT for each generator in real time. Each generator has one PMU and RNNs attached to it. There are 16 PMUs and RNNs in all. The result shows the potential of using PMUs to measure the rotor angle. The outputs of the PMUs were used for the training of the RNN. In the training, there are only four variables available. They are the voltage, current and the respective angles.

Chapter 8

Conclusions and Recommendations for Future Works

8.1 Conclusion

The new technologies such as DG/HDG, power electronic interface circuits, hybrid electric vehicles, advanced controllers, etc., have introduced additional dynamics into the grid thereby making the grid more complex. With the advent of distributed generation (DG) and hybrid distributed generation (HDG), the grids will further experience increasing stress and risks. This is due to intermittent behavior of most renewable energies, especially wind generator and solar PV. Hence the security margin is compromised.

Under such operating conditions, blackout due to transient instabilities become inevitable if a major disturbance takes place or large amount of megawatt is transferred across transmission and distribution corridor. When these changes occur, instabilities developed almost instantly, leaving no time to react. In order to avoid the risk of blackout due to instability, the state of the system must be predicted ahead of time rather than using a fixed stability margin based on offline simulation (analytical approach).

In this thesis, a Computational Intelligence (CI) approach based on ANNs has been developed. CI approach has been combined with offline analytical approach based on DIgSILENT and online Real Time Digital Simulator (RTDS) to monitor and predict CCT.

The dynamic impact of grid-integrated HDG on transient stability is investigated. The following DGs were used.

- Wind turbine (Double fed- synchronous generation (DFIG))
- Small Hydropower System (SHP)

- Solar PV

The above DGs were combined to form Hybrid DGs such as HYBRID SOLAR PV+ SHP, HYBRID DFIG+SOLAR PV, HYBRID DFIG+SHP, HYBRID DFIG+SOLAR PV+SHP.

Analytical Approach

Simulation results obtained using the analytical approach show that the impact of HDG on transient stability depends on the:

1. Penetration level of HDG, HDG (Solar PV, SHP, DFIG) and fault location.
2. Load conditions (Annual increase in load)
3. Location of the HDG (Dispersed or concentrated HDG)
4. Transmission line length.

The following conclusions were drawn from the simulations conducted:

- When DFIG alone is used, the first swing of the rotor angle of GEN 2 is higher compared to SOLAR PV alone and SHP alone are used. In terms of settling time, SHP alone gives the fastest settling time, followed by SOLAR PV alone, while DFIG alone gives the worst performance. This means that among the three DGs that were used, SHP alone gives the best performance. This is probably because SHP is able to supply reactive power during the fault.
- Comparing the Hybrid DG with a single source under the export mode only, it can be seen that HYBRID SOLAR PV+SHP has slight better performance than SHP alone, SOLAR PV alone and DFIG alone. The settling time of the rotor angle of GEN 2 when HYBRID SOLAR PV+SHP and HYBRID DFIG+SHP are used is faster compared to when DFIG alone or SOLAR PV alone is used.
- Under the export mode, it can be deduced from all the simulations that the highest first swing (2.21°) occurs when HYBRID DFIG+SOLAR PV+SHP was integrated into the grid. The second highest first swing (-1.24°) is when HYBRID DFIG+SOLAR PV is used. It can be seen from the results that HYBRID SOALR PV+SHP gives the best performances (-13.45^{0}), followed by HYBRID

DFIG+SHP (-5.103°). It is also observed that the stability margin is reduced if three DGs are combined together (DFIG inclusive), compared to when two DGs are combined.

- Additional simulations were conducted using CDSG instead of DFIG. It was observed that when CDSG is used in combination with SOLAR PV and SHP, the stability improves compared to when two DGs are combined together.

- The Transient stability is improved (in respect of CCT) when HYBRID SOLAR PV+SHP is used to supply additional and base loads than when DFIG is combined with other DGs to supply the additional and base loads. In addition, transient stability is improved when SHP alone supplies the yearly load increase compared to when SOLAR PV alone supplies the base load.

- The transient stability improves when dispersed HDGs (i.e., HDG located close to the loads), compared to when concentrated HDGs (i.e., HDG located on a single site, possibly far from the loads). This is because more voltage drop will occurs on long lines compared to short lines which will impact negatively on the transient stability.

- Increasing the penetration level of HDG leads to a decrease in CCT values (transient stability reduces). It is shown that power system network with SOLAR PV alone or SHP alone has higher CCT values than the system with DFIG alone which gives the worst case scenario. The CCT values are higher when HYBRID SOLAR PV+SHP is used compared to when HYBRID DFIG+SOLAR PV, or HYBRIDDFIG+SHP is used.

One of the disadvantages of the analytical approach to transient stability is that it is slow. Therefore, it is suitable for offline studies and inadequate for real time/online transient stability.

Computational Intelligence Approach

The impact of HDG on transient stability was investigated using five Artificial Neural Networks (ANNs) to predict the CCT. The ANNs used are:

- Multilayer Feed-Forward neural networks (MLFNN)
- Recurrent neural networks (RNN)
- Radial basis function neural networks (RBF)
- Generalized regression neural networks (GRNN)
- Self-organizing map neural networks (SOFM).

It was concluded that:

- Transient stability problems can be detected and the state of the system monitored in real time using ANNs with high accuracy and precision. However, the time of prediction and the level of accuracy depends on the ANNs used. From the simulation results, it is shown that RBF provides the most accurate prediction of the CCT values. In term of time, RBF used 0.065s for predicting the CCT compared to 0.06s for MLFNN, 0.68s for RNN, 0.15s for GRNN and 0.78s for SOFM. Among the five ANNs used in the study, MLFNN is the fastest while SOFM has the slowest performance in predicting instability. This may be due to the fact that SOFM is an unsupervised learning that performs clustering without requiring a teacher. So it takes more time to perform the clustering. On the other hand, MLFNN is the fastest, because it does not require feedbacks compared to RNN.

- RNN predicts CCT accurately than MLFNN. However, it has a slower prediction time compared to MLFNN.

Wide Area Monitoring of Critical Clearing Time (CCT)

It was discovered that real time monitoring should be based on real time data collected using Phasor Measurement Units (PMUs). The simulation conducted using output data of the PMUs integrated into RTDS shows that:

- Rotor angle can be monitored using data from the PMUs which cannot be directly measured in real life.
- RNN can be trained and prediction is done using data from PMU. The transient stability status prediction is done ahead of time using RNN trained with real time data which are gathered from PMUs device.
- The CCT values are determined in real time and online but monitored using RNN in offline.
- It is discovered that, RNN is faster than the RTDS. It shows that RNN or ANN in general can be used to smarting the smart grid.

The analytical approach to transient stability cannot be used to predict the state of the system ahead of time because of its slowness. The analytical approach often uses modelling reduction in order to improves its speed and accuracy. The demerit of modelling reduction and the slow rate of simulation when analytical approach is used makes it unsuitable for real time operation. Hence analytical approach is slower for real time stability studies than the computational intelligence approach. For example, when DIgSILENT is used, small time-step cannot be accommodated without slowing down the simulation time. On the other hand, computational intelligence can easily accommodate small time-step without the simulation time being significantly affected. An advantage of RTDS over offline simulation tools such as DIgSILENT is that, it uses a time-step of 50micro-seconds which allows real time or near real time simulations. As a result of this, RTDS addresses most of the limitations arising from analytical approach. However, one of the limitations of RTDS is that it cannot predict ahead of time without the use of ANN.

In this research, ANN models are successfully developed for monitoring the critical clearing time and the rotor angle of hybrid distributed generation in real time.

8.2 Recommendations for Future Work

- The focus in the near future will be on dynamic optimization for scheduling and load sharing among the HDG using computational intelligence, such as Particle Swarm Optimization, Population Based Incremental Learning and other optimization algorithms. In the scheduling process, decisions to commit or de-commit units to meet the varying system load demand and the amount of spinning reserve required will be made in a way that the overall power production cost is minimized. Also in the load sharing, attention is placed to both active power and reactive power among the various HDG.

- The impact of HDG on transient stability as well as small signal stability will be investigated on a large power system network considering the intermittent of the energy sources.

- The renewable energies used are stochastic in nature. So the output behavior solely depends on the environment. A robust transient stability models should be able to learn from the past event and improve itself as the environment changes. Application of reinforcement learning to transient stability assessment will be used to perform the task and capture the uncertainty in the energy sources.

- Besides, an application of a hybrid intelligent system can be used to proffer a better solution incorporating improved algorithm in order to enhance faster transient stability assessment with improved precision.
- Further research is needed on online/real time implementation of neural networks based modelling, monitoring, optimization and control of HDG in RTDS. The modelling will involve transient and small signal stability in order to investigate the impact of HDG on transient stability and small signal stability in real time and online.

- Further research is necessary on modelling and control of DFIG in order to improve on the dynamic behavior during fault. If this improvement is achieved it will give a better result.

Appendix

Appendix A

Table A1: Data for Single Machine Infinite Bus

	Active Power (MW)	**Reactive Power (MVAr)**	**Voltage (kV)**	**Length (km)**
Load 1	80	40	230	
Load 2	80	40	230	
Centralized Generator (GEN2)	80	60	13.8	
Grid (Voltage Source)	Infinite		230	
HDG	8 *	4*	0.7	
Transmission Line (Line 1&Line 2)	-	-	230	100
Transmission Line (LINE 3)	-	-	230	40
Transformer (T1)	100MVA		13.8/230	
Transformer (T2)	100MVA		11/230	

Note that the * is indicating that the values are varied throughout the simulations

Table A2: Generator Data GEN2 and SHP

	Synchronous generator's Data (GEN 2 and SHP)
Rs	0.03 pu
Xl	0.13 pu
Xd	1.2 pu
Xq	0.7 pu
$Td0^{'}$	5s
$Tq0^{'}$	5s
$Xd^{'}$	0.30 pu
$Xq^{'}$	0.25 pu
$Td0^{''}$	0.04s
$Td0^{''}$	0.05s
$Xd^{''}$	0.22 pu
$Xq^{''}$	0.25 pu
H	4s

Rs is the stator resistance while xl is the leakage reactance

V_{base}=230kV

S_{base}= 100MVA

For the 100km and 40km lines

$Y=2.28x10^{-6}S/km$

$Z= [0.05+j0.436]\Omega/km$

Table A3.1: Doubly-Fed Induction Generator's (DFIG) Data

	DFIG Data
No of Pole	2
Nominal frequency	50/60Hz
Stator resistance	3.1 pu
Rotor resistance	0.01 pu
Rotor reactance	3.1 pu
Mutual reactance	0.1 pu
Inertia	2s

Table A3.2: SOLAR PV Data

	SOLAR PV Data
Nominal frequency	50/60Hz
V	0.7 (kV)
P	8 (MW)
T	25^0 c
Irradiance	$1000W/m^2$.

Table A4: Transformer's Data

Parameters	**Value**
Srated	130MVA
HV	230KV
LV	13.8KV
Frequency	50 Hz
X/R ratio	8
Connection	YN

Table A5: Bus and Generator data of IEEE 39-Bus New England bus system

Bus no	Volts(pu)	Load (MW)	Load(MVAr)	GEN(MW)	GEN(MVAr)
1		0.0	0.0		
2		0.0	0.0		
3		322.	0 2.4		
4		500.0	184.0		
5		0.0	0.0		
6		0.0	0.0		
7		233.8	84.0		
8		522.0	176.0		
9		0.0	0.0		
10		0.0	0.0		
11		0.0	0.0		
12		7.5	88.0		
13		0.0	0.0		
14		- 0.0	0.0		
15		- 320.0	153.0		
16		329.0	32.3		
17		0.0	0.0		
18		158.0	30.0		
19		0.0	0.0		
20		628.0	103.0		
21		274.0	115.0		
22		0.0	0.0		
23		247.5	84.6		
24		308.6	-92.2		
25		224.0	47.2		
26		139.0	17.0		
27		281.0	75.5		
28		206.0	27.6		

29		283.5	26.9		
30	1.0475	0.0	0.0		250
31	0.982	9.2	4.6		Slack bus Label as (GEN 10)
32	0.9831	0.0	0.0		650
33	0.9972	0.0	0.0		632
34	1.0123	0.0	0.0		508
35	1.0493	0.0	0.0		650
36	1.0635	0.0	0.0		560
37	1.0278	0.0	0.0		540
38	1.0265	0.0	0.0		830
39	1.03	114.0	250.0		1000

Table A6.1: Generator Data for IEEE 39-Bus New England bus system

Gen Num	Bus Num	Base kV	Base MVA	Xl (pu)	Rs (pu)	Xd (pu)	Xd' (pu)	Xd'' (pu)	Tdo' (s)
1	53	22	800	0.100	0.002	0.800	0.248	0.200	10.200
2	54	22	850	0.298	0.002	2.508	0.592	0.425	6.560
3	55	22	1000	0.304	0.002	2.495	0.531	0.450	5.700
4	56	22	800	0.236	0.002	2.096	0.349	0.280	5.690
5	57	22	750	0.203	0.002	2.475	0.495	0.375	5.400
6	58	22	1000	0.224	0.002	2.540	0.500	0.400	7.300
7	59	22	750	0.242	0.002	2.213	0.368	0.300	5.660
8	60	22	700	0.196	0.002	2.030	0.399	0.315	6.700
9	61	22	1000	0.298	0.002	2.106	0.570	0.450	4.790
10	62	22	875	0.174	0.002	1.479	0.400	0.350	9.370

Table A6: Generator Data for IEEE 39-Bus New England bus system continue

Gen Num	**Tdo''** (s)	**Xq (pu)**	**Xq' (pu)**	**Xq'' (pu)**	**Tqo' (pu)**	**Tqo'' (s)**	**H (s)**
1	0.050	0.552	0.224	0.200	1.500	0.035	5.250
2	0.050	2.397	0.510	0.425	1.500	0.035	3.553
3	0.050	2.370	0.500	0.450	1.500	0.035	3.580
4	0.050	2.064	0.320	0.280	1.500	0.035	3.575
5	0.050	2.325	0.450	0.375	0.440	0.035	3.467
6	0.050	2.410	0.450	0.400	0.400	0.035	3.480
7	0.050	2.190	0.338	0.300	1.500	0.035	3.520
8	0.050	1.960	0.350	0.315	0.410	0.035	3.471
9	0.050	2.050	0.500	0.450	1.960	0.035	3.450
10	0.050	1.006	0.394	0.350	1.500	0.035	3.543

Table A7: Excitation for IEEE 39-Bus New England bus system

Tr	0.02 (s)	Measurement Delay
Ka	200.0 (pu)	Controller Gain
Ta	0.03 (s)	Controller Time Constant
Ke	1.0 (pu)	Exciter Constant
Te	0.2 (s)	Exciter Time Constant
Kf	0.05 (pu)	Stabilization Path Gain
Tf	1.50 (s)	Stabilization Path Time Constant
E1	3.90 (pu)	Saturation Factor 1
Se1	0.10 (pu)	Saturation Factor 2
E2	5.20 (pu)	Saturation Factor 3
Se2	0.50 (pu)	Saturation Factor 4
Vrmin	-10.00 (pu)	Controller Output Minimum
Vrmax	10.00 (pu)	Controller Output Maximum
E2	5.20 (pu)	Saturation Factor 3
Se2	0.50 (pu)	Saturation Factor 4
Vrmin	-10.00 (pu)	Controller Output Minimum
Vrmax	10.00 (pu)	Controller Output Maximum

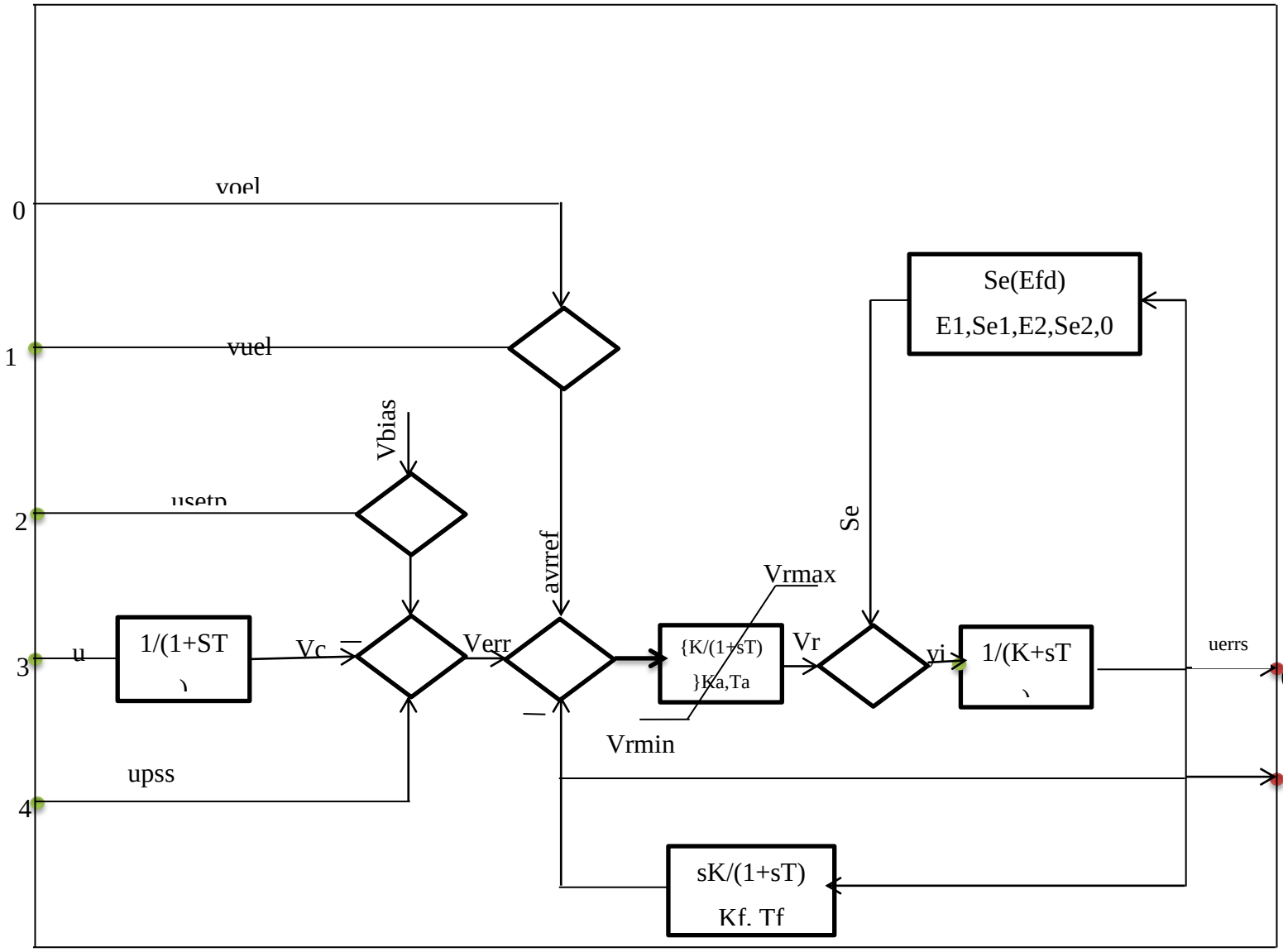

FigA.1: avr_IEEET1 Excitation System in DIgSILENT

TableA8: Line data of IEEE 39-Bus New England bus system

From Bus	To Bus	Resistance (pu)	Reactance (pu)	Susceptance (pu)	Transformer magnitude	Tap angle
1	2	0.0035	0.0411	0.6987	0	0
1	39	0.0010	0.0250	0.7500	0	0
2	3	0.0013	0.0151	0.2572	0	0
2	25	0.0070	0.0086	0.1460	0	0
3	4	0.0013	0.0213	0.2214	0	0
3	18	0.0011	0.0133	0.2138	0	0
4	5	0.0008	0.0128	0.1342	0	0
4	14	0.0008	0.0129	0.1382	0	0
5	6	0.0002	0.0026	0.0434	0	0
5	8	0.0008	0.0112	0.1476	0	0
6	7	0.0006	0.0092	0.1130	0	0
6	11	0.0007	0.0082	0.1389	0	0
7	8	0.0004	0.0046	0.0780	0	0
8	9	0.0023	0.0363	0.3804	0	0
9	39	0.0010	0.0250	1.2000	0	0
10	11	0.0004	0.0043	0.0729	0	0
10	13	0.0004	0.0043	0.0729	0	0
13	14	0.0009	0.0101	0.1723	0	0
14	15	0.0018	0.0217	0.3660	0	0
15	16	0.0009	0.0094	0.1710	0	0
16	17	0.0007	0.0089	0.1342	0	0
16	19	0.0016	0.0195	0.3040	0	0
16	21	0.0008	0.0135	0.2548	0	0
16	24	0.0003	0.0059	0.0680	0	0
17	18	0.0007	0.0082	0.1319	0	0
17	27	0.0013	0.0173	0.3216	0	0

21	22	0.0008	0.0140	0.2565	0	0
22	23	0.0006	0.0096	0.1846	0	0
23	24	0.0022	0.0350	0.3610	0	0
25	26	0.0032	0.0323	0.5130	0	0
26	27	0.0014	0.0147	0.2396	0	0
26	28	0.0043	0.0474	0.7802	0	0
26	29	0.0057	0.0625	1.0290	0	0
28	29	0.0014	0.0151	0.2490	0	0
12	11	0.0016	0.0435	0.0000	1.006	0
12	13	0.0016	0.0435	0.0000	1.006	0
6	31	0.0000	0.0250	0.0000	1.07	0
10	32	0.0000	0.0200	0.0000	1.07	0
19	33	0.0007	0.0142	0.0000	1.07	0
20	34	0.0009	0.0180	0.0000	1.009	0
22	35	0.0000	0.0143	0.0000	1.025	0
23	36	0.0005	0.0272	0.0000	1	0
25	37	0.0006	0.0232	0.0000	1.025	0
2	30	0.0000	0.0181	0.0000	1.025	0
29	38	0.0008	0.0156	0.0000	1.025	0
19	20	0.0007	0.0138	0.0000	1.06	0

TableA9: Bus and Generator data for 68-bus system on 100MVA base

Bus	**Volt (pu)**	**Pgen (MW)**	**Qgen (MVAr)**	**Pload (MW)**	**Qload (MVAr)**	**Generator's number**	**Bus name**
1	1	0	0	2.527	1.1856		
2	1	0	0	0	0		
3	1	0	0	3.22	0.02		
4	1	0	0	2	0.736		
5	1	0	0	0	0		
6	1	0	0	0	0		
7	1	0	0	2.34	0.84		
8	1	0	0	2.088	0.708		
9	1	0	0	1.04	1.25		
10	1	0	0	0	0		
11	1	0	0	0	0		
12	1	0	0	0.09	0.88		
13	1	0	0	0	0		
14	1	0	0	0	0		
15	1	0	0	3.2	1.53		
16	1	0	0	3.29	0.32		
17	1	0	0	0	0		
18	1	0	0	1.58	0.3		
19	1	0	0	0	0		
20	1	0	0	6.8	1.03		
21	1	0	0	2.74	1.15		
22	1	0	0	0	0		
23	1	0	0	2.48	0.85		
24	1	0	0	3.09	-0.92		
25	1	0	0	2.24	0.47		
26	1	0	0	1.39	0.17		

Bus	**Volt (pu)**	**Pgen (MW)**	**Qgen (MVAr)**	**Pload (MW)**	**Qload (MVAr)**	**Generator's number**	**Bus name**
27	1	0	0	2.81	0.76		
28	1	0	0	2.06	0.28		
29	1	0	0	2.84	0.27		
30	1	0	0	0	0		
31	1	0	0	0	0		
32	1	0	0	0	0		
33	1	0	0	1.12	0		
34	1	0	0	0	0		
35	1	0	0	0	0		
36	1	0	0	1.02	-0.1946		
37	1	0	0	60	3		
38	1	0	0	0	0		
39	1	0	0	2.67	0.126		
40	1	0	0	0.6563	0.2353		
41	1	0	0	10	2.5		
42	1	0	0	11.5	2.5		
43	1	0	0	0	0		
44	1	0	0	2.6755	0.0484		
45	1	0	0	2.08	0.21		
46	1	0	0	1.507	0.285		
47	1	0	0	2.0312	0.3259		
48	1	0	0	2.412	0.022		
49	1	0	0	1.64	0.29		
50	1	0	0	1	-1.47		
51	1	0	0	3.37	-1.22		
52	1	0	0	24.7	1.23		
53	1	2.5	0	0	0	1	
54	0.98	5.45	0	0	0	2	
55	0.983	6.5	0	0	0	3	

56	0.997	6.32	0	0	0	4	
57	1.011	5.052	0	0	0	5	
58	1.02	7	0	0	0	6	
59	1.02	5.6	0	0	0	7	
60	1	5.4	0	0	0	8	
61	1.01	8	0	0	0	9	
62	1	5	0	0	0	10	
63	1	10	0	0	0	11	
64	1	13.5	0	0	0	12	
65	1.011	35.91	0	0	0	13	Slack
66	1	17.85	0	0	0	14	
67	1	10	0	0	0	15	
68	1	40	0	0	0	16	

Bus Data					
From Bus	**To Bus**	**R(pu)**	**Xl(pu)**	**B(pu)**	**Tap ratio**
1	2	0.007	0.0822	0.34935	0
1	2	0.007	0.0822	0.34935	0
1	30	0.0008	0.0074	0.48	0
2	3	0.0013	0.0151	0.2572	0
2	25	0.007	0.0086	0.146	0
2	53	0	0.0181	0	1
3	4	0.0013	0.0213	0.2214	0
3	18	0.0011	0.0133	0.2138	0
4	5	0.0008	0.0128	0.1342	0
4	14	0.0008	0.0129	0.1382	0
5	6	0.0002	0.0026	0.0434	0
5	8	0.0008	0.0112	0.1476	0
6	7	0.0006	0.0092	0.113	0
6	11	0.0007	0.0082	0.1389	0
6	54	0	0.025	0	1.07
7	8	0.0004	0.0046	0.078	0
8	9	0.0046	0.0726	0.1902	0
8	9	0.0046	0.0726	0.1902	0
9	30	0.0019	0.0183	0.29	0
9	30	0.0019	0.0183	0.29	0
10	11	0.0004	0.0043	0.0729	0
10	13	0.0004	0.0043	0.0729	0
10	55	0	0.02	0	1.07

TableA10: Line data for 68-Bus system

Bus Data					
From Bus	**To Bus**	**R(pu)**	**Xl(pu)**	**B(pu)**	**Tap ratio**
12	11	0.0016	0.0435	0	1.02
12	13	0.0016	0.0435	0	1.02
13	14	0.0009	0.0101	0.1723	0
14	15	0.0018	0.0217	0.366	0
15	16	0.0009	0.0094	0.171	0
16	17	0.0007	0.0089	0.1342	0
16	19	0.0016	0.0195	0.304	0
16	21	0.0008	0.0135	0.2548	0
16	24	0.0003	0.0059	0.068	0
17	18	0.0007	0.0082	0.1319	0
17	27	0.0013	0.0173	0.3216	0
19	20	0.0007	0.0138	0	1.02
19	56	0.0007	0.0142	0	1.03
20	57	0.0009	0.018	0	1.009
21	22	0.0008	0.014	0.2565	0
22	23	0.0006	0.0096	0.1846	0
22	58	0	0.0143	0	1.01
23	24	0.0022	0.035	0.361	0
23	59	0.0005	0.0272	0	1
25	26	0.0032	0.0323	0.531	0
25	60	0.0006	0.0232	0	1.01
26	27	0.0014	0.0147	0.2396	0
26	28	0.0043	0.0474	0.7802	0

Bus Data					
From Bus	**To Bus**	**R(pu)**	**Xl(pu)**	**B(pu)**	**Tap ratio**
26	29	0.0057	0.0625	1.029	0
28	29	0.0014	0.0151	0.249	0
29	61	0.0008	0.0156	0	1.01
9	36	0.0022	0.0196	0.34	0
9	36	0.0022	0.0196	0.34	0
36	37	0.0005	0.0045	0.32	0
34	36	0.0033	0.0111	1.45	0
35	34	0.0001	0.0074	0	1
33	34	0.0011	0.0157	0.202	0
32	33	0.0008	0.0099	0.168	0
30	31	0.0013	0.0187	0.333	0
30	32	0.0024	0.0288	0.488	0
1	31	0.0016	0.0163	0.25	0
31	38	0.0011	0.0147	0.247	0
33	38	0.0036	0.0444	0.693	0
38	46	0.0022	0.0284	0.43	0
46	49	0.0018	0.0274	0.27	0
1	47	0.0013	0.0188	1.31	0
47	48	0.0025	0.0268	0.4	0
47	48	0.0025	0.0268	0.4	0
48	40	0.002	0.022	1.28	0
35	45	0.0007	0.0175	1.39	0

Bus Data					
From Bus	**To Bus**	**R(pu)**	**Xl(pu)**	**B(pu)**	**Tap ratio**
37	43	0.0005	0.0276	0	0
43	44	0.0001	0.0011	0	0
44	45	0.0025	0.073	0	0
39	44	0	0.0411	0	0
39	45	0	0.0839	0	0
45	51	0.0004	0.0105	0.72	0
50	52	0.0012	0.0288	2.06	0
50	51	0.0009	0.0221	1.62	0
49	52	0.0076	0.1141	1.16	0
52	42	0.004	0.06	2.25	0
42	41	0.004	0.06	2.25	0
41	40	0.006	0.084	3.15	0
31	62	0	0.026	0	1
32	63	0	0.013	0	1
36	64	0	0.0075	0	1
37	65	0	0.0033	0	1.02
41	66	0	0.0015	0	1
42	67	0	0.0015	0	1
52	68	0	0.003	0	1

Table A11.1: Generator Data for 68-Bus System

Gen Num	Bus Num	Base kV	Base MVA	Xl (pu)	Rs(pu)	Xd (pu)	Xd' (pu)	Xd" (pu)	Tdo' (s)
1	53	22	800	0.100	0.002	0.800	0.248	0.200	10.200
2	54	22	850	0.298	0.002	2.508	0.592	0.425	6.560
3	55	22	1000	0.304	0.002	2.495	0.531	0.450	5.700
4	56	22	800	0.236	0.002	2.096	0.349	0.280	5.690
5	57	22	750	0.203	0.002	2.475	0.495	0.375	5.400
6	58	22	1000	0.224	0.002	2.540	0.500	0.400	7.300
7	59	22	750	0.242	0.002	2.213	0.368	0.300	5.660
8	60	22	700	0.196	0.002	2.030	0.399	0.315	6.700
9	61	22	1000	0.298	0.002	2.106	0.570	0.450	4.790
10	62	22	875	0.174	0.002	1.479	0.400	0.350	9.370
11	63	22	1300	0.134	0.002	1.664	0.234	0.156	4.100
12	64	22	2000	0.440	0.002	2.020	0.620	0.500	7.400
13	65	345	10000	0.150	0.002	1.480	0.275	0.200	5.900
14	66	345	10000	0.170	0.002	1.800	0.285	0.230	4.100
15	67	345	10000	0.170	0.002	1.800	0.285	0.230	4.100
16	68	345	10000	0.205	0.002	1.780	0.355	0.275	7.800

Table A11.2: Generator Data for 68-Bus System continue

Gen Num	**Tdo''** (s)	**Xq** (pu)	**Xq'** (pu)	**Xq''** (pu)	**Tqo'** (s)	**Tqo''** (s)	**H (s)**
1	0.050	0.552	0.224	0.200	1.500	0.035	5.250
2	0.050	2.397	0.510	0.425	1.500	0.035	3.553
3	0.050	2.370	0.500	0.450	1.500	0.035	3.580
4	0.050	2.064	0.320	0.280	1.500	0.035	3.575
5	0.050	2.325	0.450	0.375	0.440	0.035	3.467
6	0.050	2.410	0.450	0.400	0.400	0.035	3.480
7	0.050	2.190	0.338	0.300	1.500	0.035	3.520
8	0.050	1.960	0.350	0.315	0.410	0.035	3.471
9	0.050	2.050	0.500	0.450	1.960	0.035	3.450
10	0.050	1.006	0.394	0.350	1.500	0.035	3.543
11	0.050	1.599	0.195	0.156	1.500	0.035	2.169
12	0.050	1.900	0.560	0.500	1.500	0.035	4.615
13	0.050	1.430	0.250	0.200	1.500	0.035	4.960
14	0.050	1.730	0.250	0.230	1.500	0.035	3.000
15	0.050	1.730	0.250	0.230	1.500	0.035	3.000
16	0.050	1.670	0.300	0.275	1.500	0.035	4.500

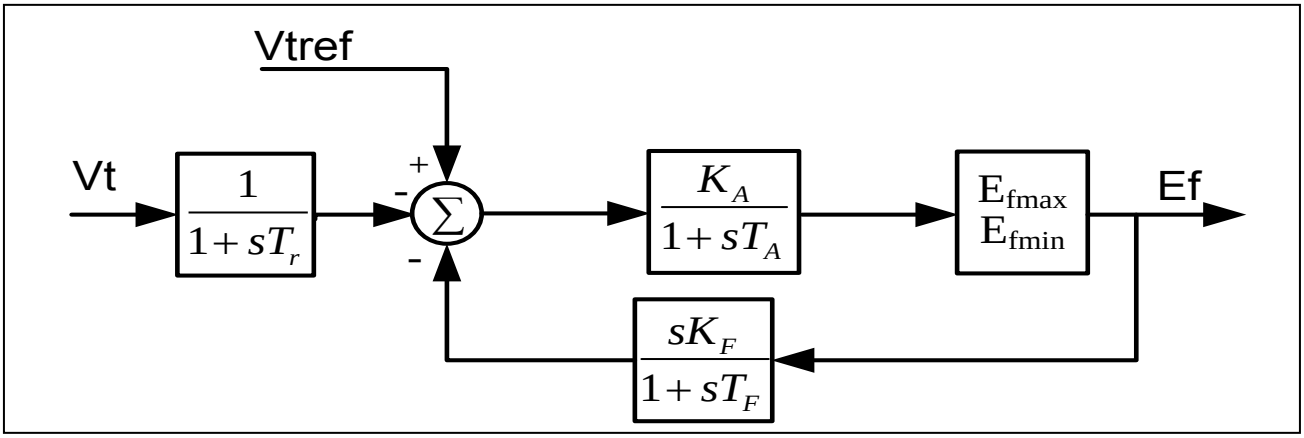

Fig A.1 : IEEE Exciter in RSCAD (user interface with (RTDS)

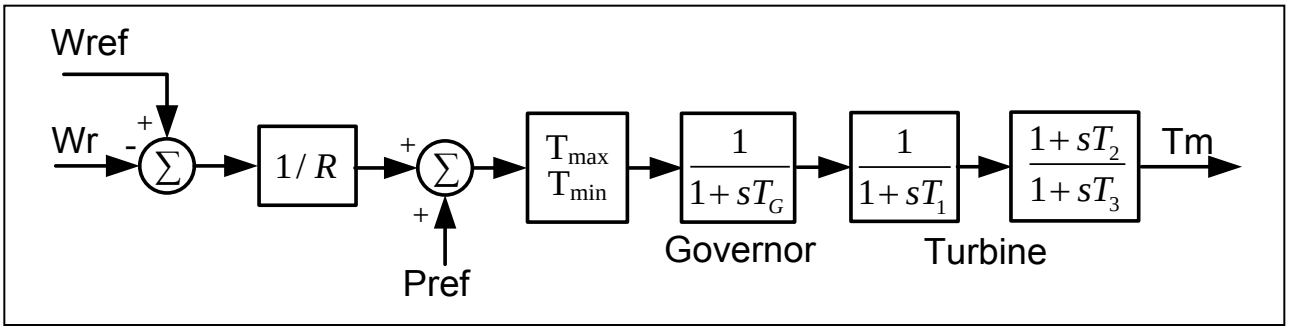

Fig A.2: Governor in RSCAD (user interface with RTDS)

Table A12: AVR Excitation System for 68-Bus system

Gen Num	Bus Num	T_r	K_A	T_A	K_F/T_F	TF	E_{fmax}	E_{fmin}
1	53	0.01	50	0.02	0.1	0.5	4	-4
2	54	0.01	25	0.02	0.2	0.5	4	-4
3	55	0.01	25	0.02	0.3	0.5	4	-4
4	56	0.01	20	0.02	0.3	0.5	4	-4
5	57	0.01	20	0.02	0.3	0.5	4	-4
6	58	0.01	20	0.02	0.3	0.5	4	-4
7	59	0.01	20	0.02	0.3	0.5	4	-4
8	60	0.01	50	0.02	0.05	0.5	4	-4
9	61	0.01	50	0.02	0.2	0.5	4	-4
10	62	0.01	25	0.02	0.3	0.5	4	-4
11	63	0.01	50	0.02	0.05	0.5	4	-4
12	64	0.01	50	0.02	0.2	0.5	4	-4
13	65	0.01	20	0.02	0.4	0.5	4	-4
14	66	0.01	25	0.02	0.3	0.5	4	-4
15	67	0.01	25	0.02	0.3	0.5	4	-4
16	68	0.01	25	0.02	0.3	0.5	4	-4

Table A13: **Turbine Speed Governor System for 68-Bus System**

Gen Num	Bus Num	1/R	T_{max}	T_{min}	T_G	T_1	T_2	T_3
1	53	20	1.1	0	0.2	0.1	2.5	8
2	54	20	1.1	0	0.2	0.1	2.5	8
3	55	20	1.1	0	0.2	0.1	2.5	8
4	56	20	1.1	0	0.2	0.1	2.5	8
5	57	20	1.1	0	0.2	0.1	2.5	8
6	58	20	1.1	0	0.2	0.1	2.5	8
7	59	20	1.1	0	0.2	0.1	2.5	8
8	60	20	1.1	0	0.2	0.1	2.5	8
9	61	20	1.1	0	0.2	0.1	2.5	8
10	62	20	1.1	0	0.2	0.1	2.5	8
11	63	20	1.1	0	0.2	0.1	2.5	8
12	64	20	1.1	0	0.2	0.1	2.5	8
13	65	20	1.1	0	0.2	0.1	2.5	8
14	66	20	1.1	0	0.2	0.1	2.5	8
15	67	20	1.1	0	0.2	0.1	2.5	8
16	68	20	1.1	0	0.2	0.1	2.5	8

Appendix B

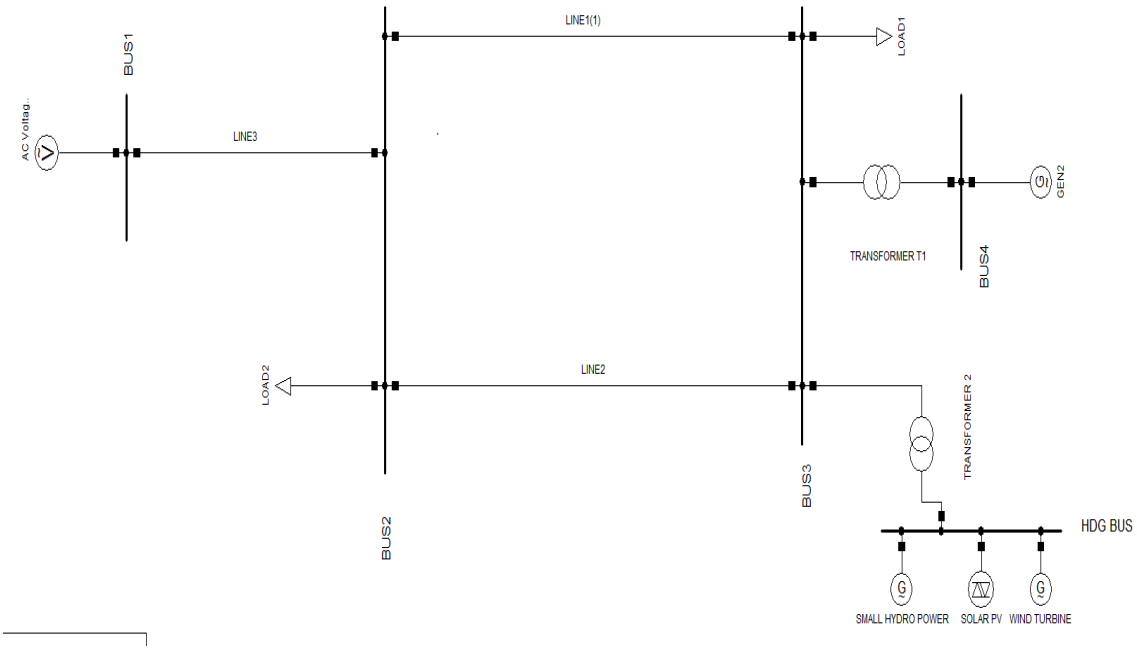

FigB.1: Single-line diagram of Single machine Infinite Bus System in DIgSILENT

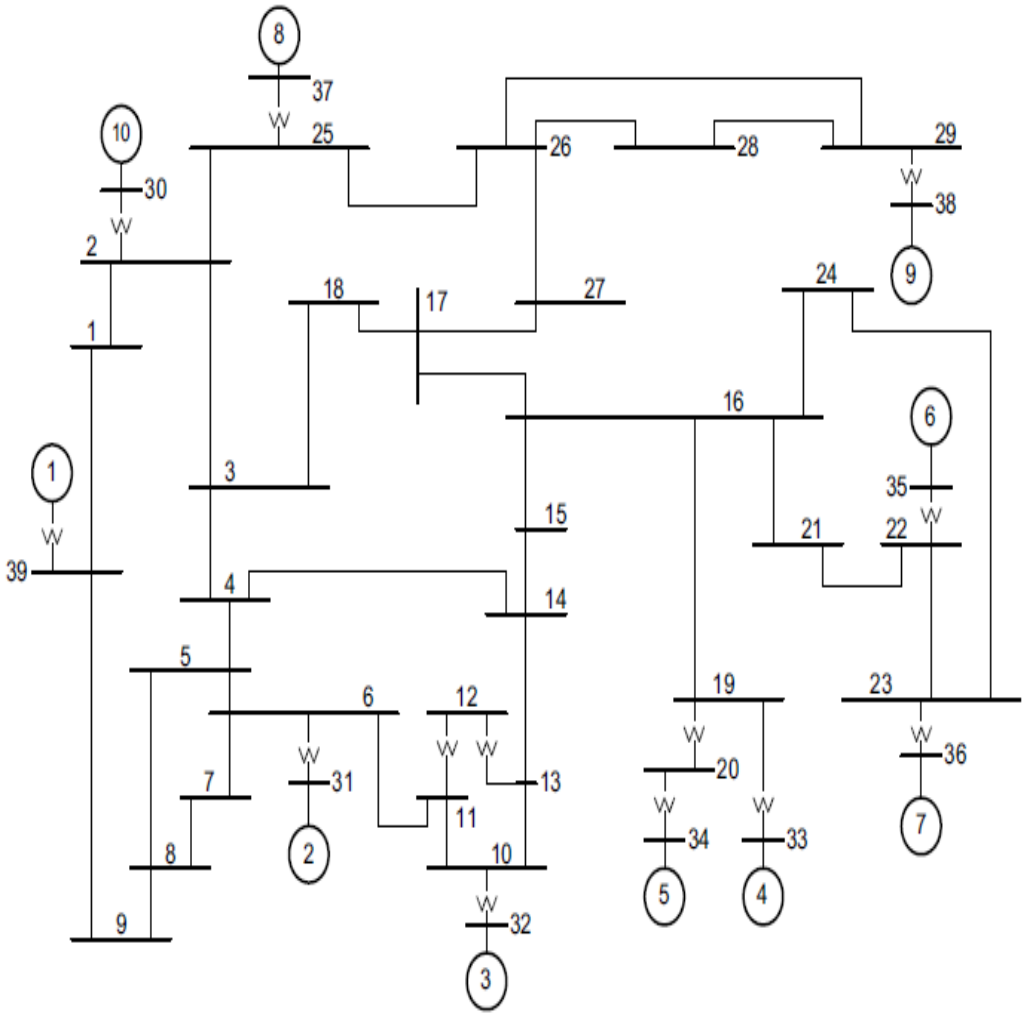

Fig B.2: Single-line diagram of the IEEE 39-bus New England Test System

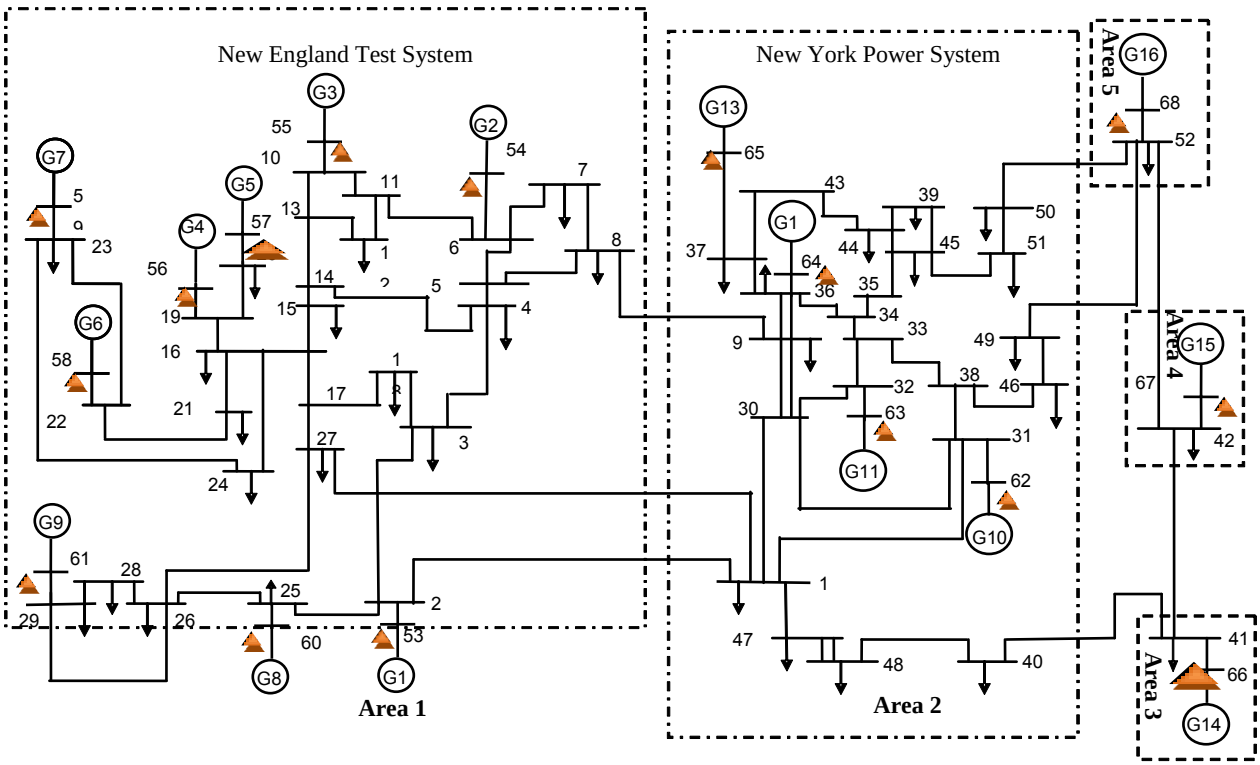

Fig B.3: Single-line diagram of IEEE 16-machine 68-bus system at 345 kV.

Appendix C

Appendix C1

Simulation Results With Converter Driven Synchronous Generator (CDSG).

The simulations conducted when CDSG is used alone and with other DGs are reported in this section. When HYBRID CDSG+SOLAR PV+ SHP is used, the rotor angle of GEN 2 has the least first swing oscillation compared to CDSG alone and HYBRID CDSG+ SOLAR PV. In this simulation, the first swing when HYBRID CDSG+SOLAR PV is used shows the highest.

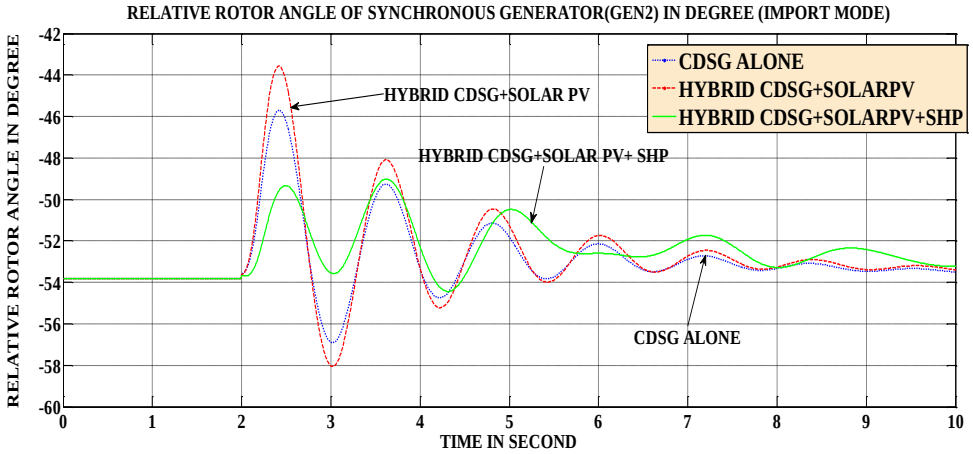

Fig C1.1 :Rotor angle comparison between CDSG alone, HYBRID CDSG +SOLAR PV and HYBRID CDSG+ SOLAR PV+SHP (Import mode).

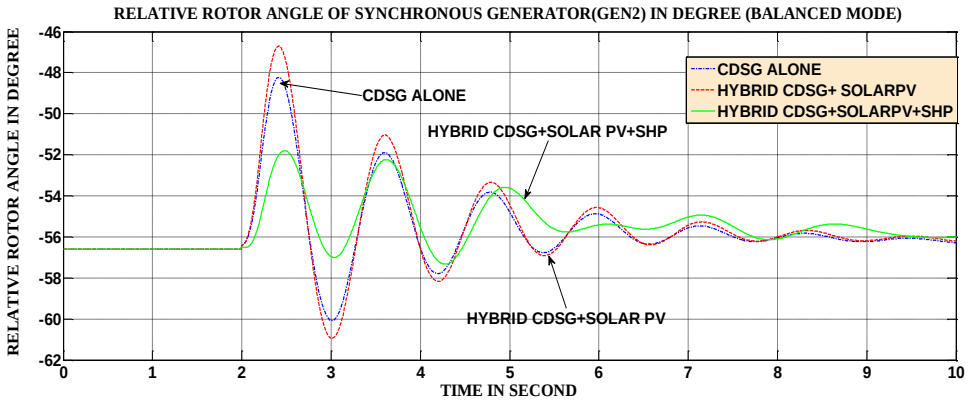

Fig C1.2: Rotor angle comparison between CDSG ALONE, SOLAR PV+ CDSG and Hybrid CDSG + SOLAR PV+SHP (Balanced mode)

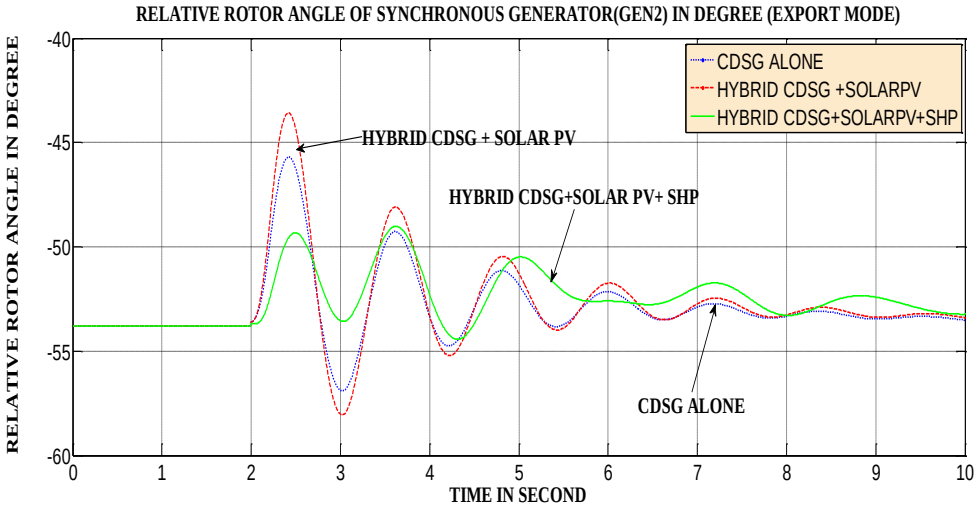

Fig C1.3: Rotor angle comparison between CDSG ALONE, SOLAR PV+ CDSG and HYBRID CDSG + SOLAR PV+SHP (Export mode)

Appendix C2

Table C2.1: The critical clearing time of synchronous generator with integrated CDSG Alone

Fault location	**Import mode**	**Balanced mode**	**Export mode**
In %	CCT(ms)	CCT(ms)	CCT(ms)
0	320	310	305
20	350	380	370
40	380	420	400
60	400	420	410
80	390	400	380
100	370	360	350
	Average (ms)		
	368.3	381.7	369.17

Table C2.2: The critical clearing time of synchronous generator with integrated HYBRID CDSG + SOLAR PV

Fault location	**Import mode**	**Balanced mode**	**Export mode**
In %	CCT(ms)	CCT(ms)	CCT(ms)
0	340	330	325
20	365	398	380
40	390	430	410
60	405	425	410
80	395	410	388
100	375	365	359
	Average (ms)		
	378.3	393	378.7

Table C2.3: The critical clearing time of synchronous generator With HYBRID CDSG +SOLAR PV+SHP.

Fault location	**Import mode**	**Balanced mode**	**Export mode**
In %	CCT(ms)	CCT(ms)	CCT(ms)
0	360	340	330
20	400	385	390
40	450	440	410
60	430	420	415
80	430	400	395
100	390	375	370
	Average (ms)		
	414	397	388

Appendix C3

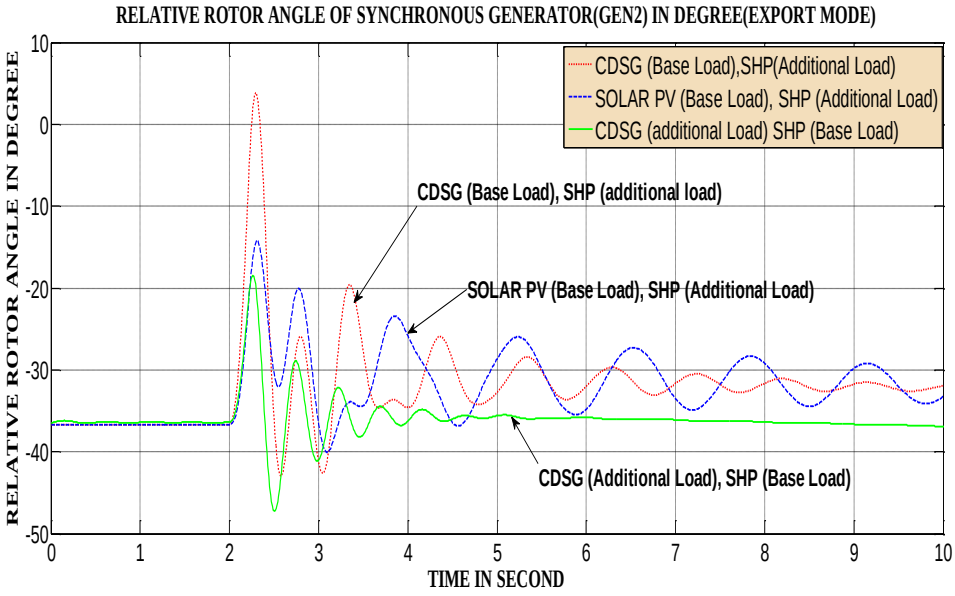

Fig C3: CDSG constant but SHP varies

Appendix C4

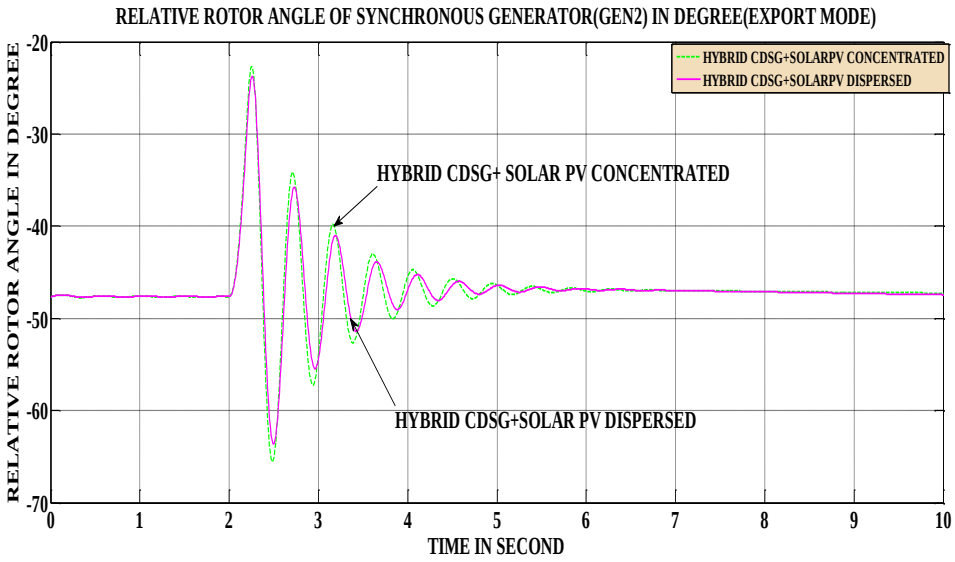

Fig C4.1: Rotor angle of synchronous generation with HYBRID CDSG+SOLAR PV (Dispersed and concentrated locations)

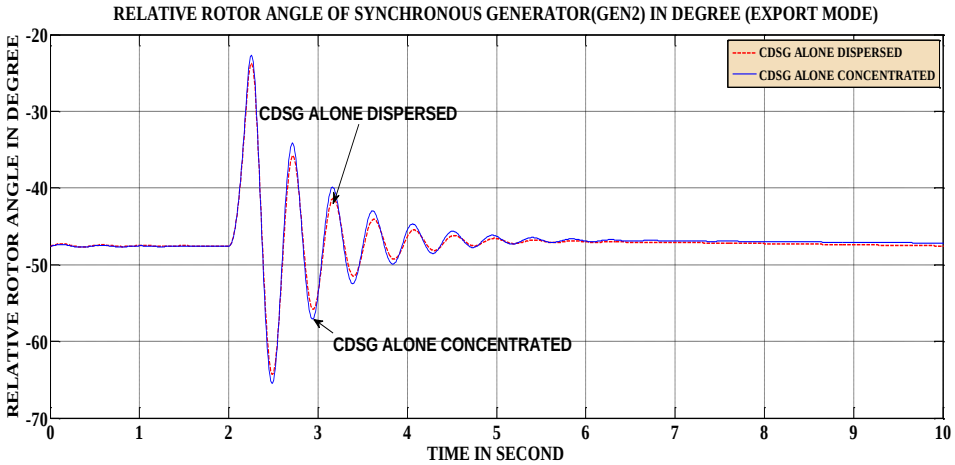

Fig C4.2: Rotor angle of synchronous generation with CDSG alone (Dispersed and Concentrated locations)

Appendix C5

Table C4: CCT OF CONCENTRTED AND DISPERSED HDG WITH CDSG AND SHP, SOLAR PV, DFIG

	CCT (ms) (Dispersed)	**CCT (ms) (Concentrated)**
HYBRID CDSG + DFIG	376	330
HYBRID CDSG +SOLAR PV	390	366
HYBRID CDSG + SHP	400	370
HYBRID CDSG+SHP+ SOLAR PV	410	375

Appendix C6

For clarity, the impact of single source DG and HDG is shown at different case studies. The following simulations are recorded for export mode only:

- Case study 2 is compared with each of the DG in case study 1
- Case study 3 is compared with each of the DG in case study1
- Case study4 is compared with each of the DG in case study 1
- Case study 5 is compared with each of the DG in case study1

CASE STUDY 2

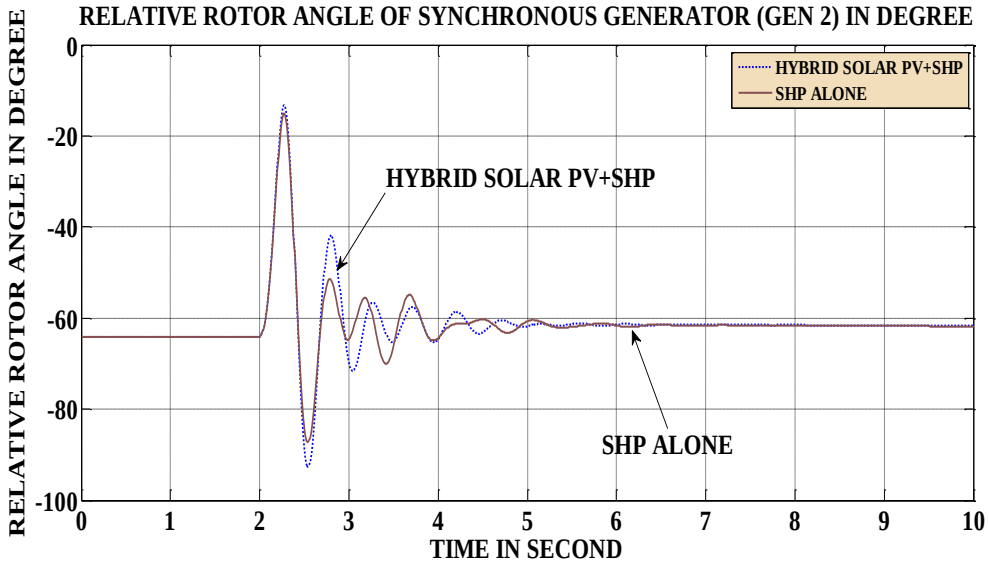

Fig C6.1: Comparison Of the impact of Hybrid SOLAR PV-SHP and SHP alone on the rotor angle of GEN2 (Export mode)

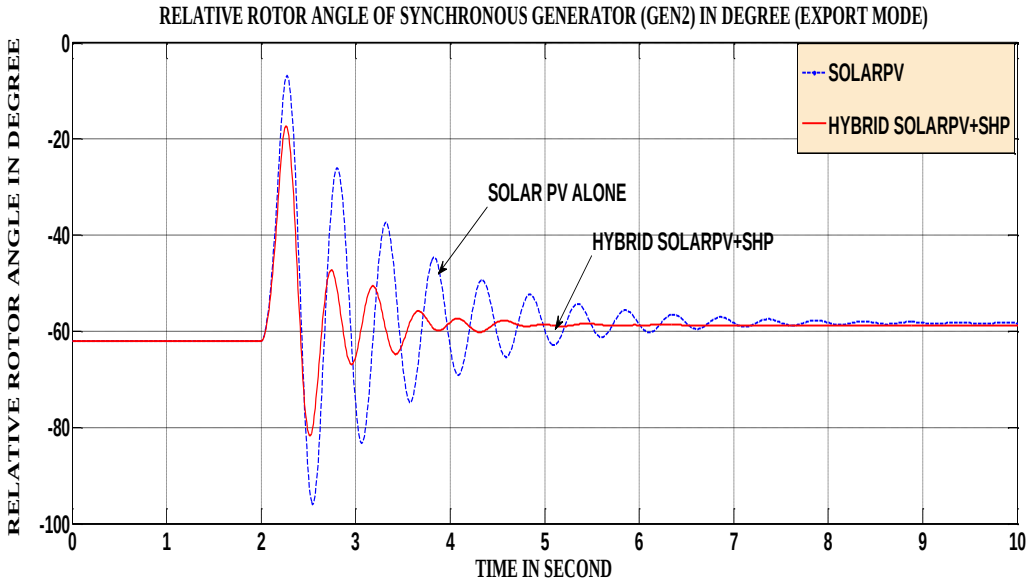

Fig C6.2: Comparison Of the impact of Hybrid Solar PV-SHP and solar PV alone on the rotor angle of GEN2 (Export mode)

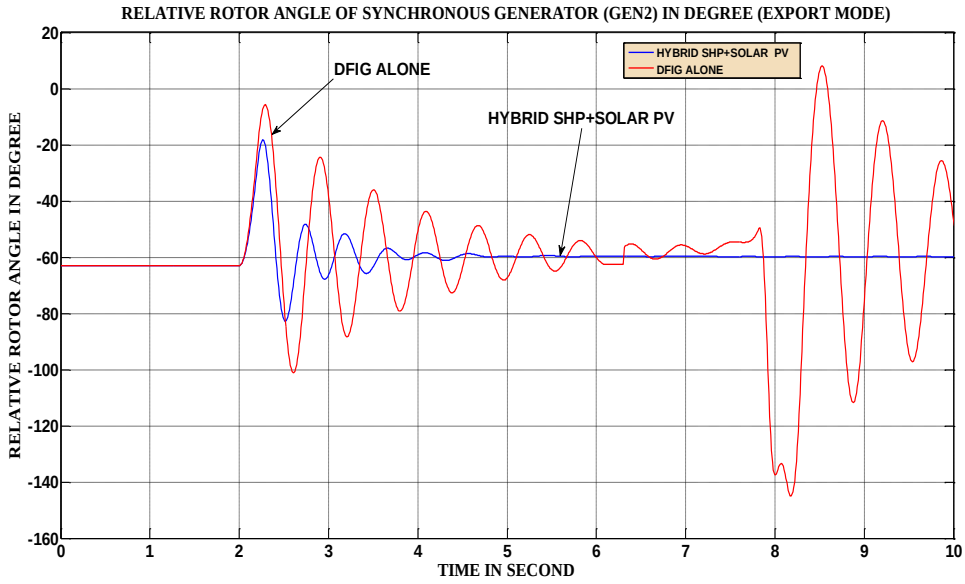

Fig C6.3: Comparison Of the impact of HYBRID SHP +SOLAR PV and DFIG alone on the rotor angle of GEN2 (Export mode)

CASE STUDY 3

The graphs in Fig C6D-C6F shows the graphs for case study 3 with case study 1

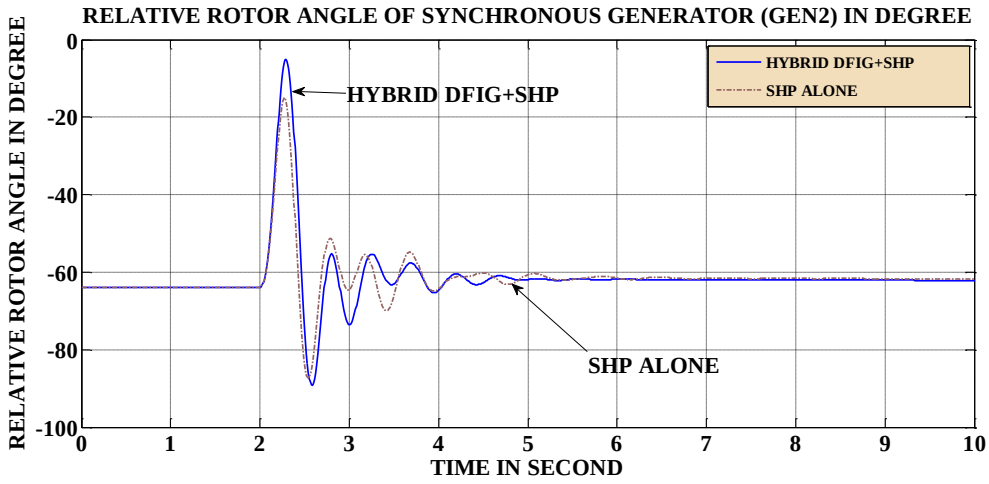

Fig C6.4: Comparison Of the impact of HYBRID DFIG+ SHP and SHP alone on the rotor angle of GEN2 (Export)

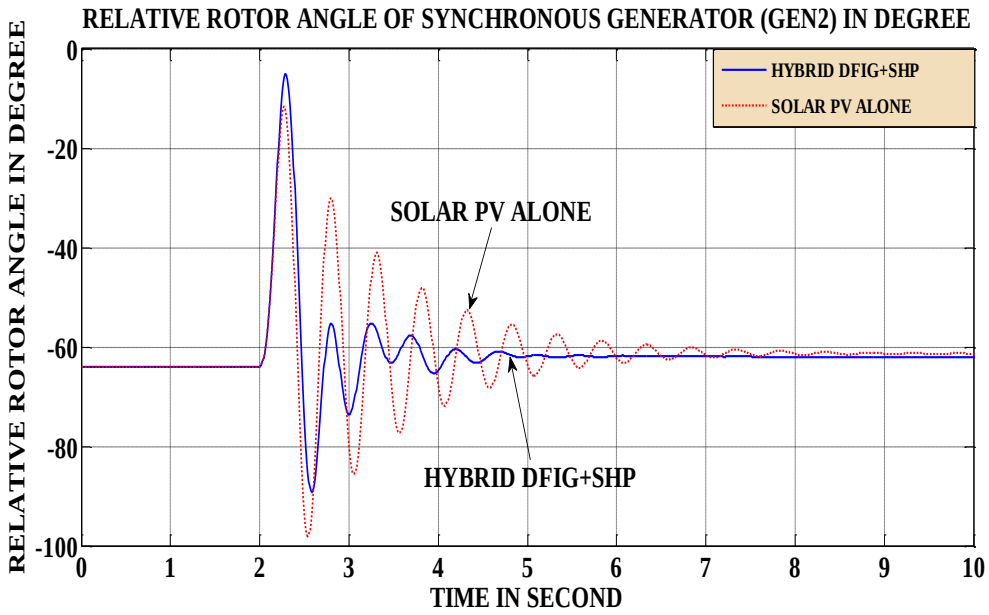

Fig C6.5: Comparison Of the impact of HYBRID DFIG+ SHP and SOLAR PV alone on the rotor angle of GEN2 (Export)

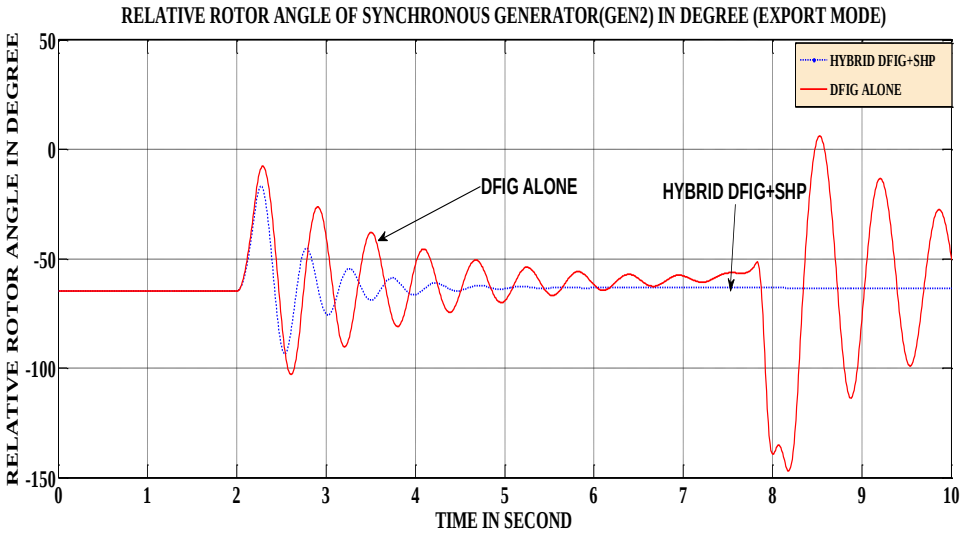

Fig C6.6: Comparison Of the impact of HYBRID DFIG+ SHP and DFIG alone on the rotor angle of GEN2 (Export)

CASE STUDY 4

The graphs in Fig C6G-C6I show the graphs for case study 4 with case study 1

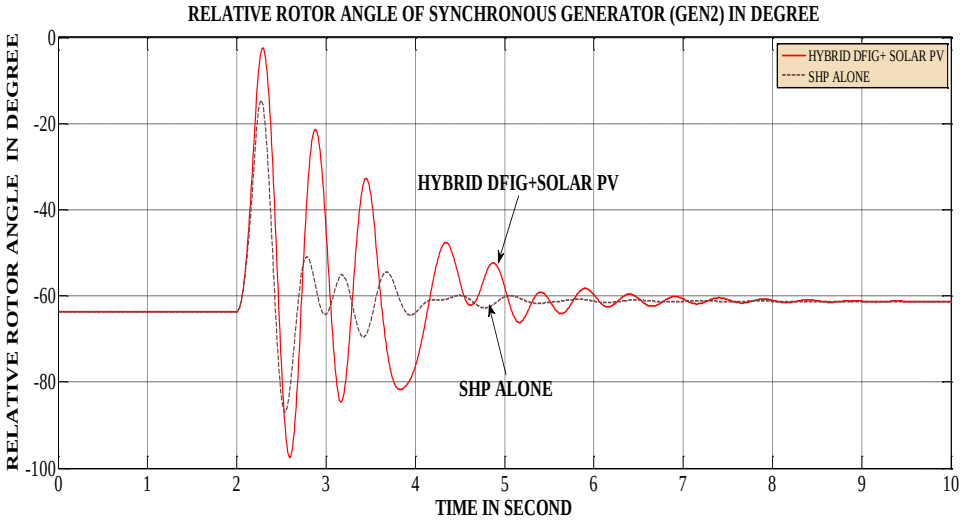

Fig C6.7: Comparison Of the impact of HYBRID DFIG+SOLAR PV and SHP alone on the rotor angle of GEN2 (Export)

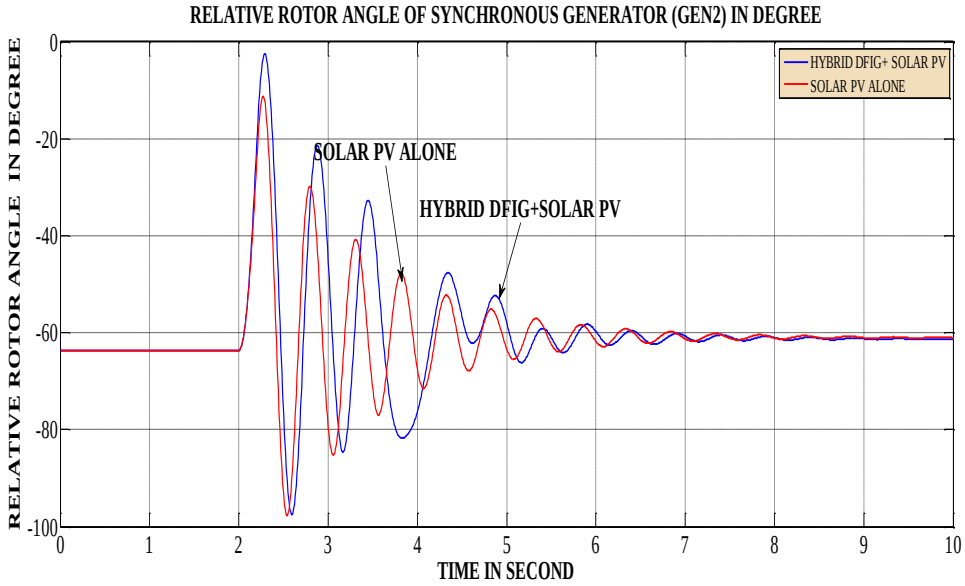

Fig C6.8: Comparison Of the impact of HYBRID DFIG+SOLAR PV and SOLAR PV alone on the rotor angle of GEN2 (Export)

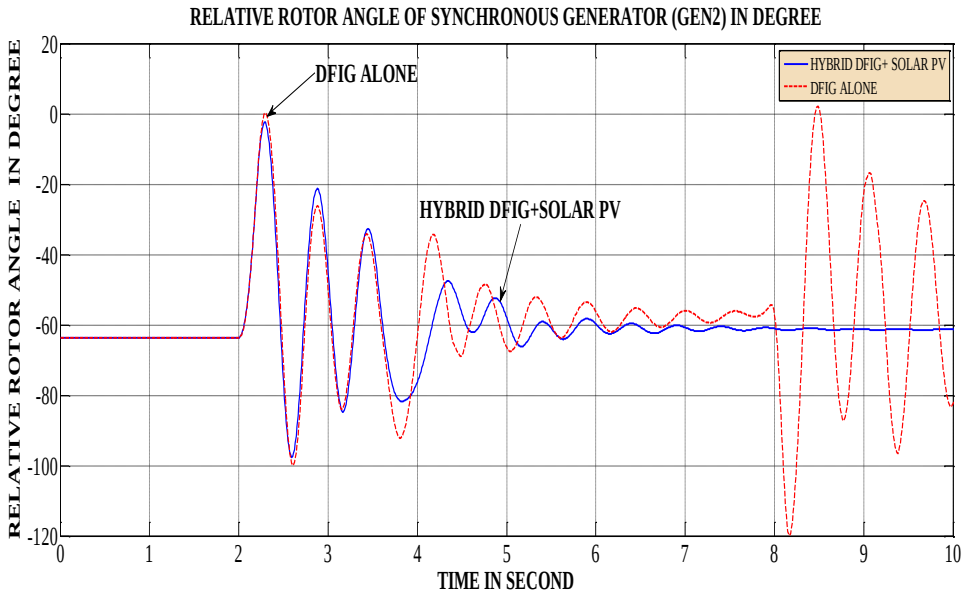

Fig C6.9: Comparison Of the impact of HYBRID SOLAR PV+DFIG and DFIG alone on the rotor angle of GEN2 (Export)

CASE STUDY 5

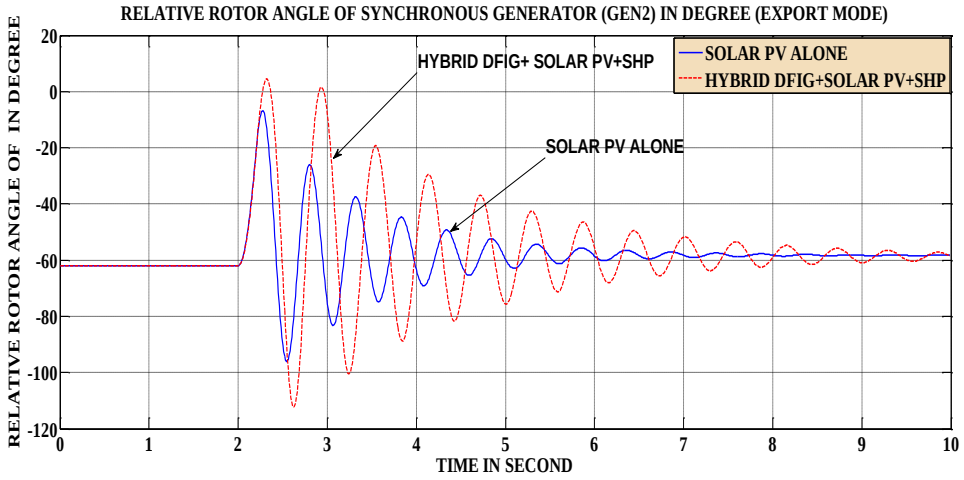

Fig C6.10: Comparison Of the impact of HYBRID DFIG+ SOLAR PV+SHP and SOLAR PV alone on the rotor angle of GEN2 (Export)

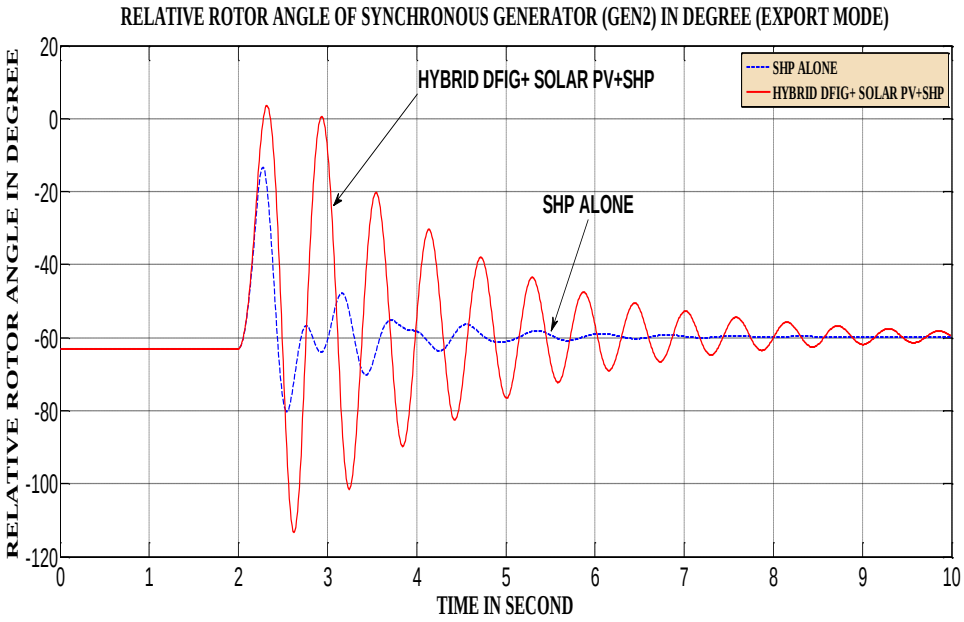

Fig C6.12: Comparison Of the impact of HYBRID DFIG+ SOLAR PV+SHP and SHP alone on the rotor angle of GEN2 (Export)

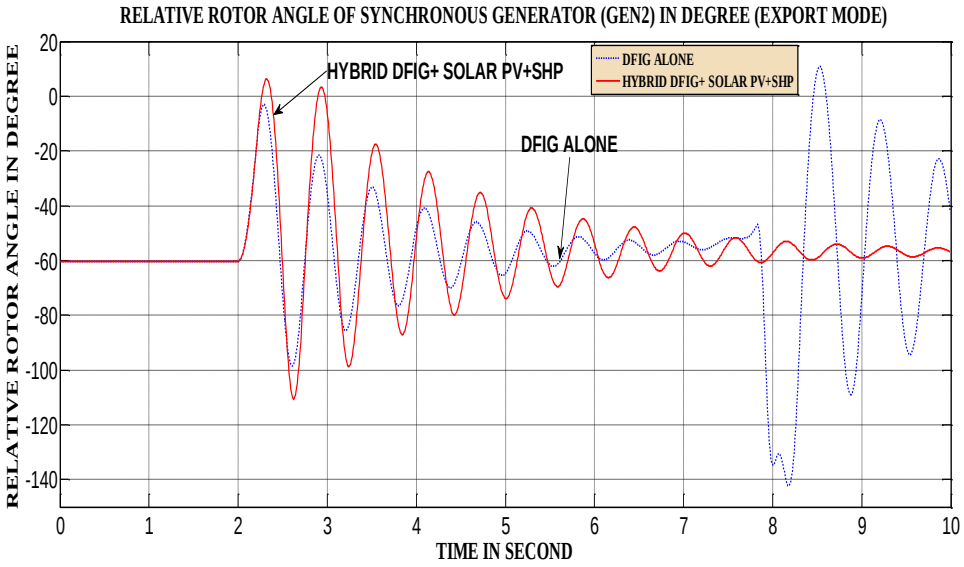

Fig C6.11: Comparison Of the impact of HYBRID DFIG+ SOLAR PV+SHP and DFIG alone on the rotor angle of GEN2 (Export)

.

Appendix D

Solar PV Simulation Result In Matlab

The output power of Solar PV depends on the temperature and the irradiance of the environment. The dependence of power generated by a PV array conditions can readily be seen in the current-voltage (I-V) and the power-voltage (P-V) characteristics of PV arrays as shown in Fig D.1-Fig D.3. The maximum power can be tracked from these diagrams. Fig D.1 shows the active Power/Voltage with varying temperatures while the irradiance is constant. The irradiance value is 1000W/m^2. Fig D.2 shows Current/Voltage with changing temperature and constant irradiance while Fig D.3 shows the current/voltage with variation in irradiance at constant temperature of 25^0c. As the temperature increases, the power also increases.

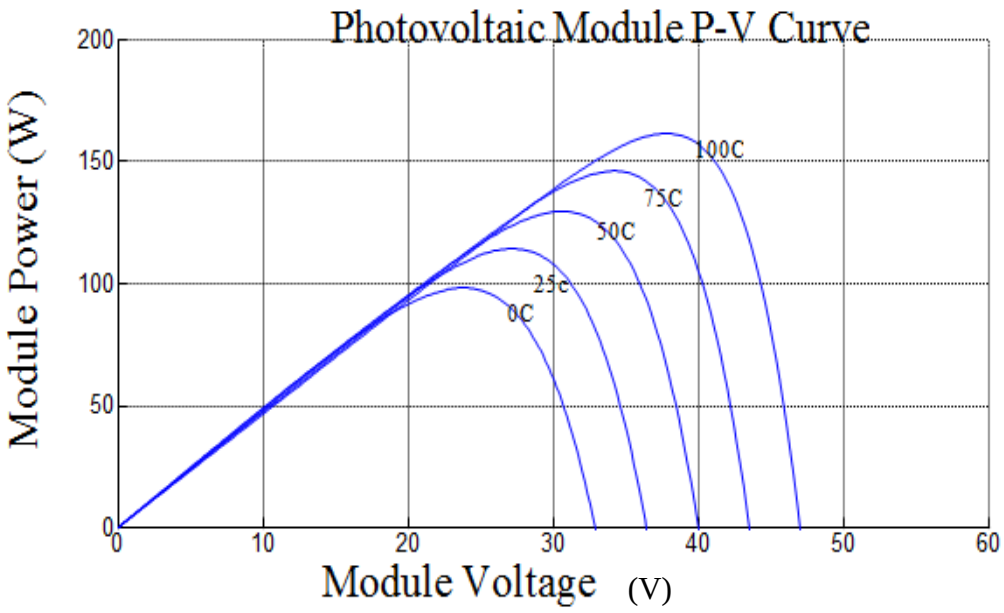

Fig D.1: Photovoltaic Module P-V Curve

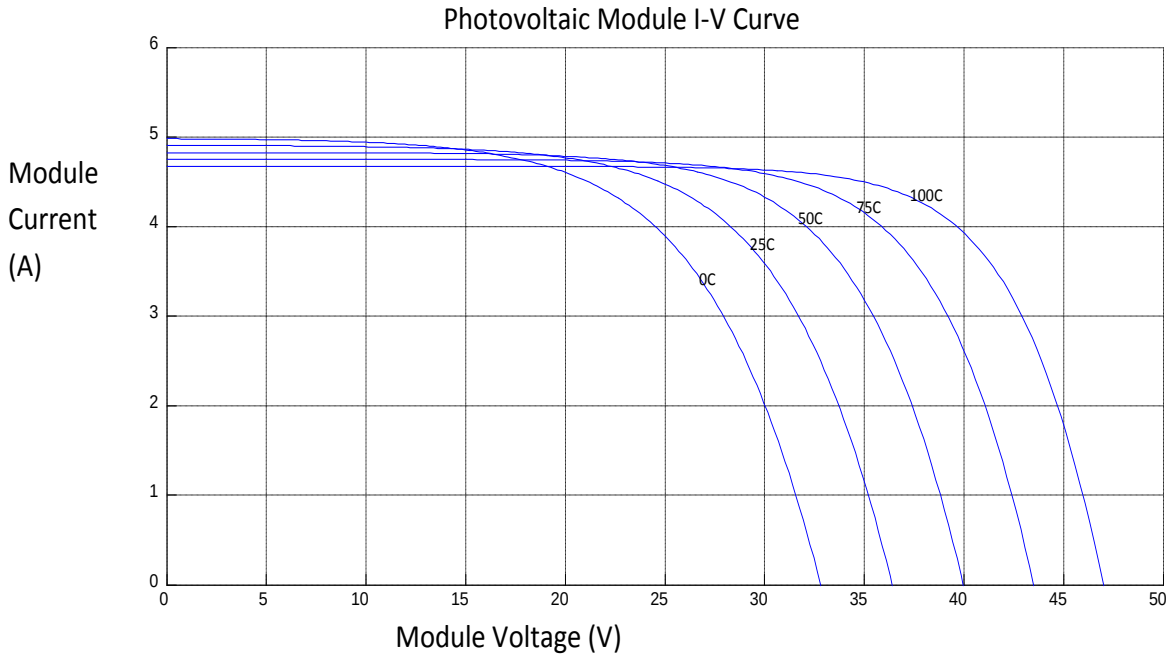

Fig D.2: Photovoltaic Module I-V Curve

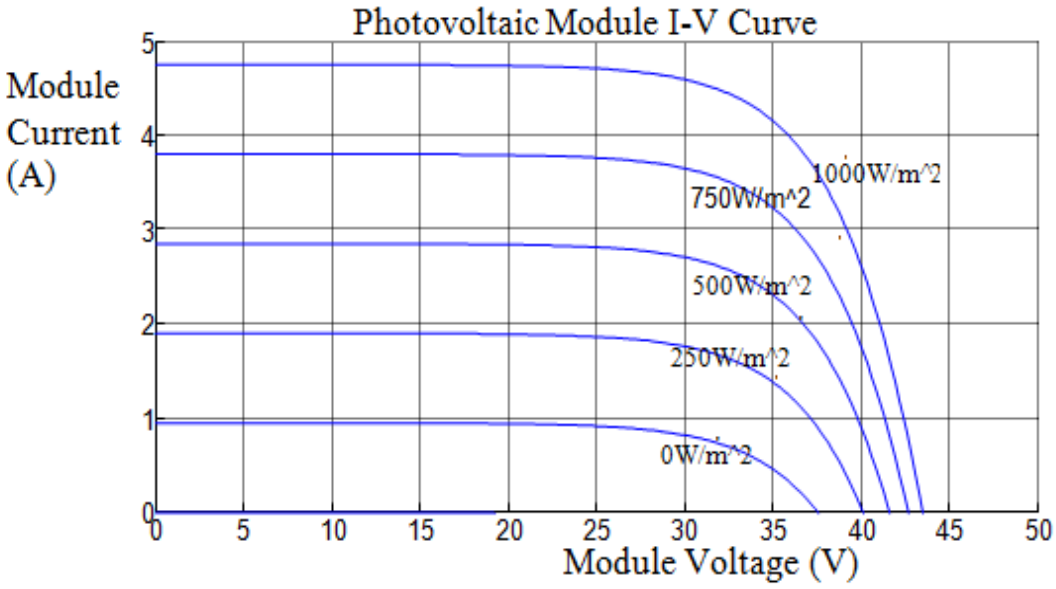

Fig D.3: Photovoltaic Module I-V Curve.

Appendix E

Binary Classification

The classification will group the status into stable (1) and unstable (0). It is either zero or one. The vertical column shows the penetration level of HDG while the horizontal column shows the fault duration. Table E.1 shows the time domain simulation results while Table E.2 shows the results with neural network.

Table E.1: **Time domain simulation**

Fault clearing time / HDG Penetration	100	150	200	250	300	350	380	400	410	500
0	1	1	1	1	1	1	1	1	1	0
80	1	1	1	1	1	1	0	0	0	0
160	1	1	1	1	1	1	0	0	0	0
240	1	1	1	1	1	1	0	0	0	0
320	**1**	**1**	**1**	**1**	**1**	**0**	**0**	**0**	**0**	**0**
400	**1**	**1**	**1**	**1**	**0**	**0**	**0**	**0**	**0**	**0**

Unstable Region

Table E.2: **RNN classification**

Fault clearing time / HDG Penetration	100	150	200	250	300	350	380	400	410	500
0	1	1	1	1	1	1	1	1	1	0
80	1	1	1	0	1	1	0	0	0	1
160	0	1	1	1	1	1	0	1	0	0
240	1	1	1	1	1	1	0	0	0	0
320	**1**	**1**	**1**	**1**	**1**	**0**	**0**	**0**	1	**0**
400	**1**	**1**	**1**	**1**	**0**	1	**0**	**0**	**0**	**0**

0 and 1 Misclassified points

In Table E.1, the fault duration in the horizontal level increases from 100ms to 500ms. The vertical column shows the increase in HDG penetration. When the penetration is 40, the system is stable till 350ms after which is no longer stable. In other word, the CCT is 350ms.Table E.2, the prediction with RNN shows correctly classified classes and misclassification. There are just six misclassifications as indicated in Table E.2 Four of them indicate 1 instead of 0 and two indicate 0 instead of 1. The classifications can be compared with other neural networks as shown in Table E.3

Table E.3: Classifications Comparison

Time the Fault is cleared(s)	Time Of Loss Of Synchronism (DIgSILENT) (s)	Percentage correctly Predicted				
		RNN	MLFNN	RBF	GRNN	SOFM
0.1	10	81.4	97.9	99	92	80
0.15	12	81.2	97.5	99	92	80
0.2	14	81.2	96	99	92	80
0.25	15	81.1	95	99	91.7	80
0.3	17	80	94	99	91.5	79.1

The results show that classification does not depend on the time of clearing the fault or on the time of loss of synchronism but rather on the number of neurons and training algorithm. SOFM shows the lowest classification compare to others. The classification is highest in RBF due to its ability to handle more data during training.

Appendix F

PRELIMINARY RESULTS

Mean square error (MSE) has been used for some-times, but a comparison is made here to find the accuracy of MSE (Fig F.1). It was discovered that mean square error with regularization (MSEREG) is smoother. Therefore MSEREG will be used. The performance index in term of mean square error and time in second are compared to make a choice of the number of neurons to use for the training (Figs F.2-Fig F.3). Levenberg-Marquardt is choosing because it gives minimum MSEREG and shorter computation time.

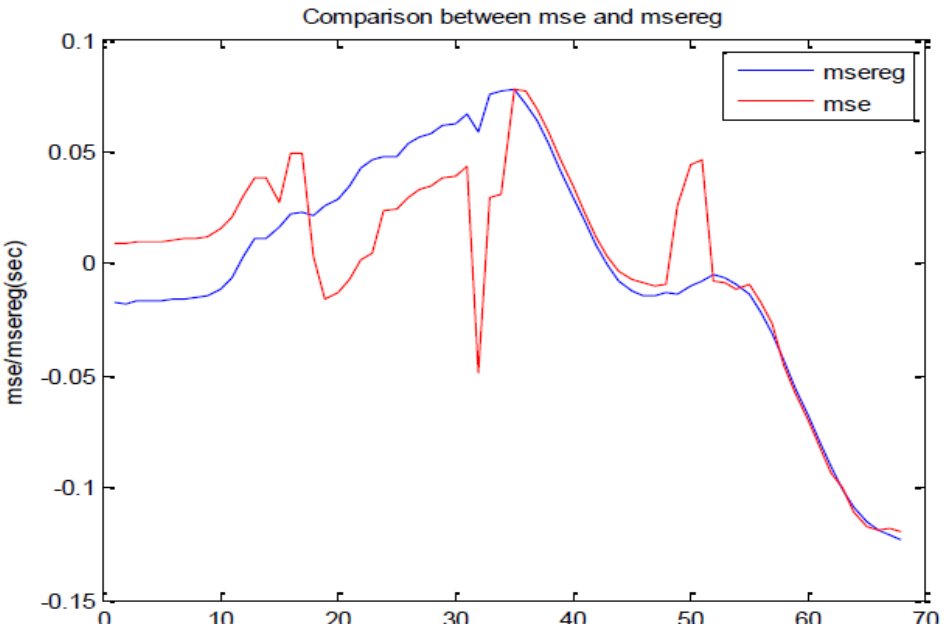

FigF.1: Comparison of MSE and MSEREG

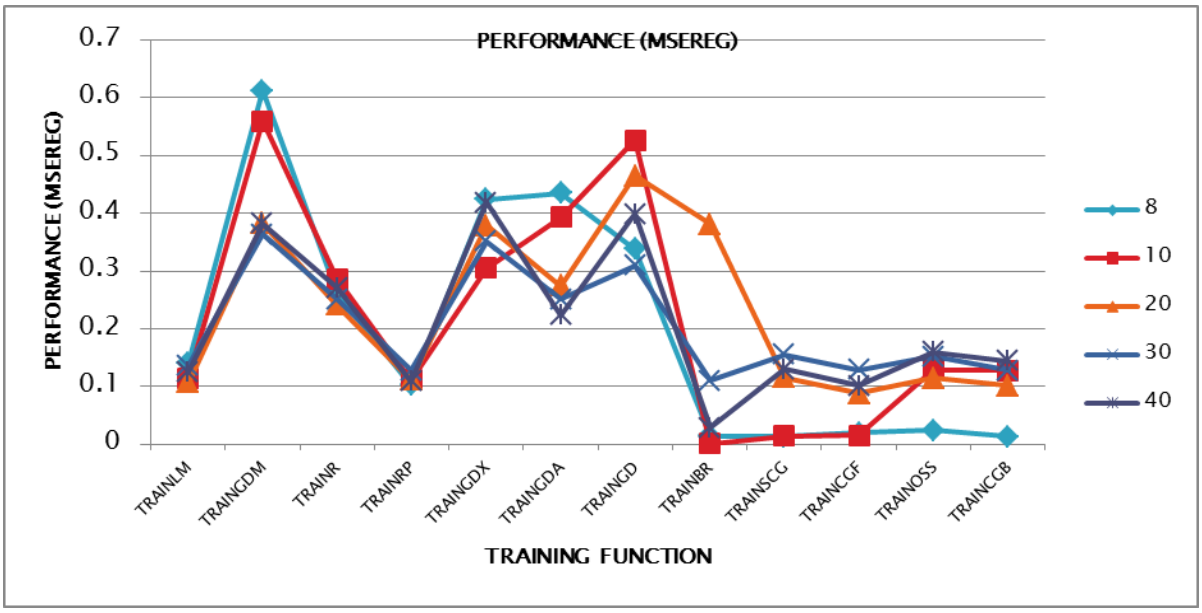

Fig F.2: Performance of Training Algorithm with MSEREG

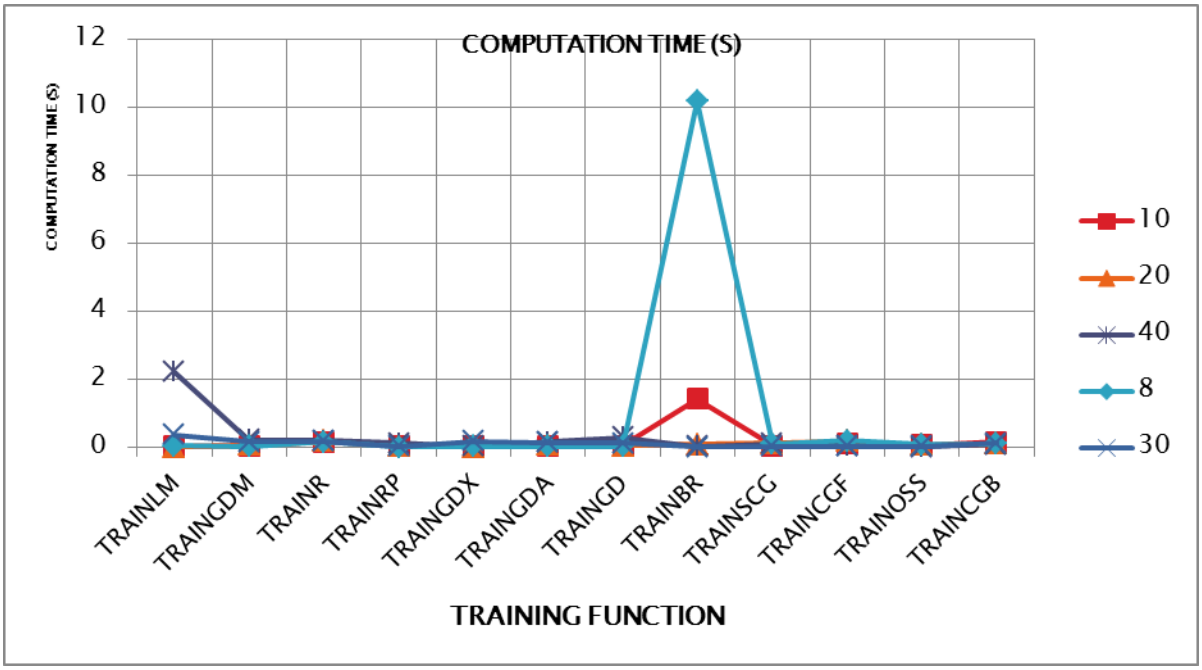

Fig F.3: Computation Time

Train	Train neural network
TRAINLM	Levenberg-Marquardt backpropagation
TRAINGDM	Gradient descent with momentum backpropagation
TRAINR	Random order incremental training with learning functions
TRAINRP	Resilient backpropagation
TRAINGDX	Gradient descent with momentum and adaptive learning rate backpropagation
TRAINGD	Gradient descent backpropagation
TRAINBR	Bayesian regulation backpropagation
TRAINSCG	Scaled conjugate gradient backpropagation
TRAINCGF	Conjugate gradient backpropagation with Fletcher-Reeves updates
TRAINOSS	One-step secant backpropagation
TRAINCGB	Conjugate gradient backpropagation with Powell-Beale restarts

.

CONFERENCE PAPER PUBLISHED/ACCEPTED

[1] P.K. Olulope, S.P. Chowdhury, S.Chowdhury, K.A.Folly, "Review of Distributed Generation, Modelling and its Impact on Power System Stability". Proceeding of the ninth IASTED European Conference Power & energy system (Euro2009), pp193-199.

[2] P.K.Olulope, K.A Folly,S.P Chowdhury,S. Chowdhury, 'Computational intelligence techniques applied to real time and offline power system stability assessment with distributed generation' Joint International conference on Power Electronics, drives and Energy Systems(PEDES) & 2010 Power India, 2010, pp1-10,,*Dec21*-23,2010.

[3] P.K. Olulope, S.Chowdhury, S.Chowdhury, K.A.Folly, "Dynamic Impact of Stability Of Power Systems with DG Penetration: A Review" UPEC Proceeding 2010.

[4] P.K.Olulope, K.A.Folly, S.Chowdhury, S.P. Chowdhury**,** 'Transient Stability Prediction Of Power System With Distributed Generation Using Recurrent Neural Network' SAUPEC 2011.

[5] K.Olulope, K.A.Folly, S.Chowdhury, S.P.Chowdhury, 'Prediction of Critical Clearing Time using Artificial Neural Network' 2011 IEEE Symposium on Computational Intelligence application in smart grid (CIASG) pp 1 – 5.

[6] P.K Olulope, Ganesh K. Venayagamoorthy, K.A Folly , S.Chowdhury, SP. Chowdhury 'Transient stability Prediction using Recurrent neural network' Poster presented at Power and Energy society General meeting, Renaissance Center in Detroit, Michigan, USA 24 – 28 July 2011**.**

[7] P.K Olulope, K.A Folly, 'Impact of Hybrid Distributed Generation On Transient Stability Of Power System' Power and Energy Systems Applications (PESA 2012), Las Vegas, USA, November 12 – 14, 2012, pp97-105**.**

[8] P.K Olulope, K.A Folly, Ganesh K. Venayagamoorthy, 'Modeling And Simulation Of Hybrid Distributed Generation And Its Impact On Transient Stability Of Power System, International conference on Industrial technology (ICIT) 2013, 25-27 February 2013.

[9] P.K Olulope, Ganesh K. Venayagamoorthy, K.A Folly, , 'Wide Area Monitoring Of Rotor Angle Based On Synchrophasor Measurements' IEEE PES Power Africa 2012 Conference and Exposition, Johannesburg, South Africa, 9-13 July 2012

JOURNAL PUBLISHED

[1] **P.K. Olulope,** K.A.Folly, S.Chowdhury, S.Chowdhury 'Transient stability Assessment using Artificial Neural Network Considering Fault Location' Iraq Journal. Electrical and Electronic Engineering, Vol.6 No.1, 2010.

[2] **P.K. Olulope,** K.A.Folly**,** 'Comparative Analysis Between Synchronous Wind Generator, Small HydroPower, Solar PV And Hybrid Power System for Distributed Generation Applications Journal **Accepted for publication** at International Journal of Advanced Renewable Energy Research (IJARER), 2012.

JOURNAL PAPERS ACCEPTED FOR PUBLICATION.

[1] **P.K. Olulope,** K.A Folly, ' Computational Intelligence Techniques Applied to Offline and Real time Power System Stability Assessment – A Review, **Accepted for publication** at Control and Intelligent Systems Journal.

[2] **P.K.Olulope,** K.A.Folly**,** 'Transient Stability Prediction of Power System with Distributed Generation Using Recurrent Neural Network' Journal **Accepted for publication** at International Journal of Soft Computing and Engineering,2012.

REFERENCES

[1] S.C.Savulescu, *Real time stability assessment in Modern power system control centres*. John Willey&Sons, Inc, Publication, 2009.

[2] S. C. Savulescu, *Real-Time Stability in Power Systems: Techniques for Early Detection of the Risk of Blackout*. Springer, 2005.

[3] G. Pepermans, J. Driesen, D. Haeseldonckx, R. Belmans, and W. D'haeseleer, "Distributed generation: definition, benefits and issues," *Energy Policy*, vol. 33, no. 6, pp. 787–798, Apr. 2005.

[4] "World Energy Resources and Consumption en.wilipedis.org." http://en.wikipedia.org/wiki/World_energy_consumption.

[5] K. A. Folly and S. Sheetekela, "Impact of fixed and variable speed wind generators on the transient stability of a power system network," in *Power Systems Conference and Exposition, 2009. PSCE '09. IEEE/PES*, 2009, pp. 1 –7.

[6] B. Eggertson, "Clear intentions? South Africa's transition towards renewable energy," *Refocus*, vol. 3, no. 5, pp. 42 – 44, 2002.

[7] P.K. Olulope, S.P.Chowdhury, S.Chowdhury, and K.A. Folly, "Review of Distributed Generation, Modeling and its impact on power system stability", Power and energy systems," in *Proceeding of the ninth IASTED European Conference Power & energy system (Euro2009),*, Spain, 2009, pp. 193–199.

[8] "Refocus 2002. South Africa Transition towards Renewable Energy Clear Intentions www.re-focus.net. Pretoria." 2002.

[9] Kenneth Bossong,, "Renewable Energy Provides 14% of US Electrical Generation During First Half of 2013," *Renewable Energy World*, 08-Nov-2013. [Online]. Available: http://www.renewableenergyworld.com/rea/news/article/2013/08/renewable-energy-tops-14-of-us-electrical-generation-during-first-half-of-2013. [Accessed: 08-Nov-2013].

[10] Ronald Hankey, "Electric Power Monthly with Data for August 2013." U.S. Department of Energy, Oct-2013.

[11] K. Huhn, "Market opportunities for distributed generation systems," in *in Proc. of the Seminar on Distributed Energy Systems*, 2003, vol. Vol 1.

[12] "Distributed Generation in Liberalised Electricity Markets. International Energy Agency," 2002.

[13] M. K. Donnelly, J. E. Dagle, D. J. Trudnowski, and G. J. Rogers, "Impacts of the distributed utility on transmission system stability," *IEEE Trans. Power Syst.*, vol. 11, no. 2, pp. 741 –746, May 1996.

[14] V. V. Thong, J. Driesen, and R. Belmans, "Transmission system operation concerns with high penetration level of distributed generation," in *Universities Power Engineering Conference, 2007. UPEC 2007. 42nd International*, 2007, pp. 867 –871.

[15] P. P. Barker and R. W. De Mello, "Determining the impact of distributed generation on power systems. I. Radial distribution systems," in *IEEE Power Engineering Society Summer Meeting, 2000*, 2000, vol. 3, pp. 1645 –1656 vol. 3.

[16] J.Momoh,G.D.Boswell, *Improving power Grid Efficiency using Distributed Generation*. JANUARY, 11-17.

[17] T. Ackermann, G. Andersson, and L. Söder, "Distributed generation: a definition," *Electr. Power Syst. Res.*, vol. 57, no. 3, pp. 195–204, Apr. 2001.

[18] J. Paska, P. Biczel, and M. Kłos, "Hybrid power systems – An effective way of utilising primary energy sources," *Renew. Energy*, vol. 34, no. 11, pp. 2414–2421, Nov. 2009.

[19] G. Chicco and P. Mancarella, "Distributed multi-generation: A comprehensive view," *Renew. Sustain. Energy Rev.*, vol. 13, no. 3, pp. 535–551, Apr. 2009.

[20] A. A. Servansing, M. Pahlevaninezhad, and P. K. Jain, "A review of hybrid distributed generation systems," in *Telecommunications Energy Conference (INTELEC), 2012 IEEE 34th International*, 2012, pp. 1–5.

[21] "The Role of Distributed Generation in Power Quality and Reliability."

[22] R. Hidalgo, C. Abbey, and G. Joos, "Technical and economic assessment of active distribution network technologies," in *2011 IEEE Power and Energy Society General Meeting*, 2011, pp. 1 –6.

[23] P. Chiradeja and R. Ramakumar, "An approach to quantify the technical benefits of distributed generation," *IEEE Trans. Energy Convers.*, vol. 19, no. 4, pp. 764 – 773, Dec. 2004.

[24] K. Darrow and B. Hedman, "The Role of Distributed Generation in Power Quality and Reliability." New York State Energy Research and Development Authority. Final Report, Dec-2005.

[25] J. G. Slootweg and W. L. Kling, "Impacts of distributed generation on power system transient stability," in *2002 IEEE Power Engineering Society Summer Meeting*, 2002, vol. 2, pp. 862 –867 vol.2.

[26] V. Knazkin, "Stability of Power Systems with Large Amounts of Distributed Generation." 2004.

[27] Z. Vale, G. K. Venayagamoorthy, J. Ferreira, and H. Morais, "Computational Intelligence Applications for Future Power Systems," in *Computational Intelligence for Engineering Systems*, Springer Netherlands, 2011, pp. 176–193.

[28] R.G.Harley and J Liang, "Computational Intelligence in Smart Grids," in *Symposium Series on Computational Intelligence (SSCI)*, 2011.

[29] G. K. Venayagamoorthy, "Potentials and promises of computational intelligence for smart grids," in *IEEE Power Energy Society General Meeting, 2009. PES '09*, 2009, pp. 1 –6.

[30] X. Chu and Y. Liu, "Real-time transient stability prediction using incremental learning algorithm," in *IEEE Power Engineering Society General Meeting, 2004*, 2004, pp. 1565 –1569 Vol.2.

[31] N. Amjady and S. F. Majedi, "Transient Stability Prediction by a Hybrid Intelligent System," *IEEE Trans. Power Syst.*, vol. 22, no. 3, pp. 1275 –1283, Aug. 2007.

[32] A. L. Bettiol, A. Souza, J. L. Todesco, and J. Tesch, J.R., "Estimation of critical clearing times using neural networks," in *Power Tech Conference Proceedings, 2003 IEEE Bologna*, 2003, vol. 3, p. 6 pp.

[33] A. H. M. A. Rahim and M. H. Haque, "A Simple Method of Computing Critical Clearing Time of a Multi-Machine Power System through Evaluation of System Rate of Change of Kinetic Energy," *Electr. Mach. Power Syst.*, vol. 17, no. 6, pp. 343–358, Jan. 1989.

[34] Y. Xue, T. Van Cutsem, and M. Ribbens-Pavella, "A simple direct method for fast transient stability assessment of large power systems," *IEEE Trans. Power Syst.*, vol. 3, no. 2, pp. 400 –412, May 1988.

[35] P. K. Olulope, K. A. Folly, S. Chowdhury, and S. P. Chowdhury, "Computational intelligence techniques applied to real time and off-line power system stability assessment with distributed generation -A review," in *2010 Joint International Conference on Power Electronics, Drives and Energy Systems (PEDES) 2010 Power India*, 2010, pp. 1 –10.

[36] L. Fang and Y. Ji-lai, "Transient stability analysis with equal area criterion directly used to a non-equivalent generator pair," in *International Conference on Power Engineering, Energy and Electrical Drives, 2009. POWERENG '09*, 2009, pp. 386 –389.

[37] J. A. Momoh and M. E. El-Hawary, *Electric Systems, Dynamics, and Stability with Artificial Intelligence Applications (Power Engineering*, 1st ed. CRC Press, 1999.

[38] P K Olulope, K. A. Folly, S.Chowdhury, and SP. Chowdhury, "Transient stability assessment using artificial neural network considering fault location," *Iraq J Electr. Electron. Eng.*, vol. Vol. 6, no. No 1, p. pp 67–72, 2010.

[39] J. Wang and G. Wu, "A multilayer recurrent neural network for solving continuous-time algebraic Riccati equations," *Neural Netw.*, vol. 11, no. 5, pp. 939–950, Jul. 1998.

[40] M.Azmy, *Simulation and Management of Distributed Generation units using intelligent techniques*. Department Electrical Engineering University of Duisburg-Essen: Ph.D Thesis submitted to the department Electrical Engineering University of Duisburg-Essen, 2005.

[41] H. Demuth, *Neural network toolbox for use with MATLAB: User's guide*. MathWorks, Inc, 1992.

[42] S. Haykin, *Neural Networks: A Comprehensive Foundation*, 2nd ed. Prentice Hall, 1998.

[43] *MATLAB Version 7.12 (R2011a)*. 2011.

[44] A. P. Engelbrecht, *Computational Intelligence: An Introduction*, 2nd ed. Wiley, 2007.

[45] K. S. Swarup and P. B. Corthis, "ANN approach assesses system security," *IEEE Comput. Appl. Power*, vol. 15, no. 3, pp. 32 –38, Jul. 2002.

[46] M. Reza, W. L. Kling, and L. van der Sluis, "Stability analysis of transmission system with high penetration of distributed generation." Dissertation at Delft University of Technology, 21-Dec-2006.

[47] J. A. P. Lopes, N. Hatziargyriou, J. Mutale, P. Djapic, and N. Jenkins, "Integrating distributed generation into electric power systems: A review of drivers, challenges and opportunities," *Electr. Power Syst. Res.*, vol. 77, no. 9, pp. 1189–1203, Jul. 2007.

[48] J. McDonald, "Adaptive intelligent power systems: Active distribution networks," *Energy Policy*, vol. 36, no. 12, pp. 4346–4351, Dec. 2008.

[49] A.-M. Borbely and J. F. Kreider, *Distributed Generation: The Power Paradigm for the New Millennium*. CRC Press, 2001.

[50] D. P. Kaundinya, P. Balachandra, and N. H. Ravindranath, "Grid-connected versus stand-alone energy systems for decentralized power—A review of literature," *Renew. Sustain. Energy Rev.*, vol. 13, no. 8, pp. 2041–2050, Oct. 2009.

[51] A. A. Bayod-Rújula, "Future development of the electricity systems with distributed generation," *Energy*, vol. 34, no. 3, pp. 377–383, Mar. 2009.

[52] Hassan Farhangi, "The Path of the Smart Grid," *IEEE power & energy magazine*, pp. 18–28, Jan-2010.

[53] A. Mellit and S. A. Kalogirou, "Artificial intelligence techniques for photovoltaic applications: A review," *Prog. Energy Combust. Sci.*, vol. 34, no. 5, pp. 574–632, Oct. 2008.

[54] "European Technology Platform SmartGrids http://www.smartgrids.eu/documents/SmartGrids_SDD_FINAL_APRIL2010.pdf." Apr-2010.

[55] G. K. Veneyagamoorthy, "IEEE Transaction on Smart Grid, Special Issue on Computational Intelligence Applications in Smart Grids." 2011.

[56] "NIST Framework and Roadmap for Smart Grid Interoperability Standards, Release 1.0." http://www.nist.gov/public_affairs/releases/upload/smartgrid_interoperability_final.pdf, Jan-2010.

[57] P. Zhang, F. Li, and N. Bhatt, "Next-Generation Monitoring, Analysis, and Control for the Future Smart Control Center," *IEEE Trans. Smart Grid*, vol. 1, no. 2, pp. 186 –192, Sep. 2010.

[58] S. Awerbuch and A.Preston, *The Virtual Utility: Accounting, Technology & Competitive Aspects of The Emerging Industry*. Kluwer Academic Publishers;, 1997.

[59] P. Nema, R. K. Nema, and S. Rangnekar, "A current and future state of art development of hybrid energy system using wind and PV-solar: A review," *Renew. Sustain. Energy Rev.*, vol. 13, no. 8, pp. 2096–2103, Oct. 2009.

[60] F. Katiraei and M. R. Iravani, "Power Management Strategies for a Microgrid With Multiple Distributed Generation Units," *IEEE Trans. Power Syst.*, vol. 21, no. 4, pp. 1821 –1831, Nov. 2006.

[61] Hatziargyriou, Nikos; Asano, Hiroshi; Iravani, Reza; Marnay, Chris, *Microgrids: An Overview of Ongoing Research, Development, and Demonstration Projects*. IEEE Power & Energy, 2007.

[62] C. L. Moreira, F. O. Resende, and J. A. P. Lopes, "Using Low Voltage MicroGrids for Service Restoration," *IEEE Trans. Power Syst.*, vol. 22, no. 1, pp. 395 –403, Feb. 2007.

[63] S. Abu-Sharkh, R. J. Arnold, J. Kohler, R. Li, T. Markvart, J. N. Ross, K. Steemers, P. Wilson, and R. Yao, "Can microgrids make a major contribution to UK energy supply?," *Renew. Sustain. Energy Rev.*, vol. 10, no. 2, pp. 78–127, Apr. 2006.

[64] P. LeMar, "Integrated Energy Systems (IES) for Buildings: A Market Assessment." Resource Dynamics Corporation, Aug-2002.

[65] A. Zaltash, A. Y. Petrov, D. T. Rizy, S. D. Labinov, E. A. Vineyard, and R. L. Linkous, "Laboratory R&D on integrated energy systems (IES)," *Appl. Therm. Eng.*, vol. 26, no. 1, pp. 28–35, Jan. 2006.

[66] M. Geidl, G. Koeppel, P. Favre-Perrod, B. Klockl, G. Andersson, and K. Frohlich, "Energy hubs for the future," *IEEE Power Energy Mag.*, vol. 5, no. 1, pp. 24 –30, Feb. 2007.

[67] P. R. Khatri, V. S. Jape, N. M. Lokhande, and B. S. Motling, "Improving power quality by distributed generation," in *Power Engineering Conference, 2005. IPEC 2005. The 7th International*, 2005, pp. 675–678 Vol. 2.

[68] W. G. Morsi and M. E. El-Hawary, "Effect of distributed generation on voltage flicker in distributed systems: A case study," in *Canadian Conference on*

Electrical and Computer Engineering, 2008. CCECE 2008, 2008, pp. 000065 – 000070.

[69] T. Ackermann and V. Knyazkin, "Interaction between distributed generation and the distribution network: operation aspects," in *Transmission and Distribution Conference and Exhibition 2002: Asia Pacific. IEEE/PES*, 2002, vol. 2, pp. 1357 – 1362 vol.2.

[70] P. P. Barker and B. K. Johnson, "Power system modeling requirements for rotating machine interfaced distributed resources," in *2002 IEEE Power Engineering Society Summer Meeting*, 2002, vol. 1, pp. 161 –166 vol.1.

[71] K. Maki, S,Repo, and P.Jarventausta, "Problems Related to Islanding Protection of Distributed Generation in the Distribution Network.," in . *Lausanne, Switzerland: Power Tech Conference*.

[72] S. P. Chowdhury, S. Chowdhury, and P. A. Crossley, "Islanding protection of active distribution networks with renewable distributed generators: A comprehensive survey," *Electr. Power Syst. Res.*, vol. 79, no. 6, pp. 984–992, Jun. 2009.

[73] M. M. Mijalili, A. R. Sedighi, and M. R. Haghifam, "Impact of DG location on protection coordination in distribution systems," in *2012 Proceedings of 17th Conference on Electrical Power Distribution Networks (EPDC)*, 2012, pp. 1 –6.

[74] M. T. Doyle, "Reviewing the impacts of distributed generation on distribution system protection," in *2002 IEEE Power Engineering Society Summer Meeting*, 2002, vol. 1, pp. 103 –105 vol.1.

[75] M. Kolhe, K. Agbossou, J. Hamelin, and T. K. Bose, "Analytical model for predicting the performance of photovoltaic array coupled with a wind turbine in a stand-alone renewable energy system based on hydrogen," *Renew. Energy*, vol. 28, no. 5, pp. 727–742, Apr. 2003.

[76] J. A. Momoh, M. Elfayoumy, B. Mittelstadt, and Y. V. Makarov, "Probabilistic angle stability index," in *IEEE Power Engineering Society Summer Meeting, 1999*, 1999, vol. 1, pp. 212–218 vol.1.

[77] S. H. Karaki, R. B. Chedid, and R. Ramadan, "Probabilistic performance assessment of autonomous solar-wind energy conversion systems," *IEEE Trans. Energy Convers.*, vol. 14, no. 3, pp. 766–772, 1999.

[78] H. Kim and C. Singh, "Probabilistic security analysis using SOM and Monte Carlo simulation," in *IEEE Power Engineering Society Winter Meeting, 2002*, 2002, vol. 2, pp. 755–760 vol.2.

[79] M. . Elhadidy and S. . Shaahid, "Role of hybrid (wind+diesel) power systems in meeting commercial loads," *Renew. Energy*, vol. 29, no. 1, pp. 109–118, Jan. 2004.

[80] R. Cossent, T. Gómez, and L. Olmos, "Large-scale integration of renewable and distributed generation of electricity in Spain: Current situation and future needs," *Energy Policy*, vol. 39, no. 12, pp. 8078–8087, Dec. 2011.

[81] F. Bonanno, A. Consoli, S. Lombardo, and A. Raciti, "A logistical model for performance evaluations of hybrid generation systems," in *Industrial and Commercial Power Systems Technical Conference, 1997. Conference Record, Papers Presented at the 1997 Annual Meeting., IEEE 1997*, 1997, pp. 177 –183.

[82] S. H. Karaki, R. B. Chedid, and R. Ramadan, "Probabilistic performance assessment of autonomous solar-wind energy conversion systems," *IEEE Trans. Energy Convers.*, vol. 14, no. 3, pp. 766 –772, Sep. 1999.

[83] F. Bonanno, A. Consoli, S. Lombardo, and A. Raciti, "A logistical model for performance evaluations of hybrid generation systems," in *Industrial and Commercial Power Systems Technical Conference, 1997. Conference Record, Papers Presented at the 1997 Annual Meeting., IEEE 1997*, 1997, pp. 177 –183.

[84] J. G. McGowan and J. F. Manwell, "Hybrid wind/PV/diesel system experiences," *Renew. Energy*, vol. 16, no. 1–4, pp. 928–933, Jan. 1999.

[85] M. K. Deshmukh and S. S. Deshmukh, "Modeling of hybrid renewable energy systems," *Renew. Sustain. Energy Rev.*, vol. 12, no. 1, pp. 235–249, Jan. 2008.

[86] T. Ackermann, Ed., *Wind Power in Power Systems*, 1st ed. Wiley, 2005.

[87] Mohamed El-Ashry, "REN21. 2009. Renewables Global Status Report: 2009 Update," 2009.

[88] Christine Lins, "REN21. 2013. Renewables Global Status Report: 2013 Update." 2013.

[89] L. L. Freris, *Wind energy conversion systems*. Prentice Hall, 1990.

[90] P. Sørensen, A. Hansen, Janosi,L, Bech, J, and Bak-Jensen, B, "Simulation of Interaction between Wind Farm and Power System." Dec-2001.

[91] M. V. A. Nunes, J. A. P. Lopes, H. H. Zurn, U. H. Bezerra, and R. G. Almeida, "Influence of the variable-speed wind generators in transient stability margin of the conventional generators integrated in electrical grids," *IEEE Trans. Energy Convers.*, vol. 19, no. 4, pp. 692 – 701, Dec. 2004.

[92] J. Morren and S. W. H. de Haan, "Ridethrough of wind turbines with doubly-fed induction generator during a voltage dip," *IEEE Trans. Energy Convers.*, vol. 20, no. 2, pp. 435 – 441, Jun. 2005.

[93] J. B. Ekanayake, L. Holdsworth, X. Wu, and N. Jenkins, "Dynamic modeling of doubly fed induction generator wind turbines," *IEEE Trans. Power Syst.*, vol. 18, no. 2, pp. 803 – 809, May 2003.

[94] M. A. Poller, "Doubly-fed induction machine models for stability assessment of wind farms," in *Power Tech Conference Proceedings, 2003 IEEE Bologna*, 2003, vol. 3, p. 6 pp. Vol.3.

[95] J. A. Carta, "2.18 - Wind Power Integration," in *Comprehensive Renewable Energy*, Ali Sayigh, Ed. Oxford: Elsevier, 2012, pp. 569–622.

[96] Mukund R. Patel, Ph.D., P.E., *Wind and Solar Power Systems*. United States of America: CRC Press.

[97] M. Singh and S. Santoso, "Dynamic Models for Wind Turbines and Wind Power Plants'." National renewable energy laboratory,, January2008-May2011.

[98] W. Qiao, "Dynamic modeling and control of doubly fed induction generators driven by wind turbines," in *Power Systems Conference and Exposition, 2009. PSCE '09. IEEE/PES*, 2009, pp. 1 –8.

[99] A. D. Hansen, Clemens Jauch, P. Sørensen, Florin Iov, and Frede Blaabjerg, "Dynamic wind turbine models in power system simulation tool DIgSILENT." Risø National Laboratory, Roskilde, Dec-2003.

[100] D. Gautam, V. Vittal, and T. Harbour, "Impact of increased penetration of DFIG based wind turbine generators on transient and small signal stability of power systems," in *2010 IEEE Power and Energy Society General Meeting*, 2010, p. 1.

[101] S. Achilles and M. Pöller, "Direct drive synchronous machine models for stability assessment of wind farms," in *in Proc. 4th Int. Workshop Large Scale Integration of Wind Power and Transmission Networks for Offshore Windfarm*, Billund, Denmark,, 2003.

[102] M.A Hemeida, A. W. Farag, and O.A. Mahgoub, "Modeling and Control of Direct Driven PMSG for Ultra Large Wind Turbines," in *World Academy of Science, Engineering and Technology*, 2011, vol. 59, pp. 918–924.

[103] A. D. Hansen, J. Clemens, P. Sørensen, F. Iov, and F. Blaabjerg, "Dynamic wind turbine models in power system simulation tool DIgSILENT," 2003.

[104] J. G. Slootweg, H. Polinder, and W. L. Kling, "Dynamic modelling of a wind turbine with doubly fed induction generator," in *Power Engineering Society Summer Meeting, 2001*, 2001, vol. 1, pp. 644 –649 vol.1.

[105] J. G. Slootweg, H. Polinder, and W. L. Kling, "Representing wind turbine electrical generating systems in fundamental frequency simulations," *IEEE Trans. Energy Convers.*, vol. 18, no. 4, pp. 516 – 524, Dec. 2003.

[106] C. Hamon, "Doubly-fed Induction Generator Modeling and Control in DigSilent Power Factory." KTH Schooll of Electrical Engineering, 2010.

[107] L. Gray,, *The physics of the solar cell A. Luque, S. Hegedus (Eds.), Handbook of Photovoltaic Science and Engineering, Wiley, New York (2003), pp. 61–111 (Chapter 3)*. Handbook of photovoltaic science and engineering, Wiley, New York: Wiley, New York, 2003.

[108] J.A Ramos Hernanz, J.J. Campayo Martín, Zamora Belver, I.1, , Larrañaga Lesaka, J.2, and , Zulueta Guerrero, E.3, "Modeling of photovoltaic module," presented at the International Conference on renewable Energies and Power Quality.

[109] M. . de Blas, J. . Torres, E. Prieto, and A. García, "Selecting a suitable model for characterizing photovoltaic devices," *Renew. Energy*, vol. 25, no. 3, pp. 371–380, Mar. 2002.

[110] R. Chenni, M. Makhlouf, T. Kerbache, and A. Bouzid, "A detailed modeling method for photovoltaic cells," *Energy*, vol. 32, no. 9, pp. 1724–1730, Sep. 2007.

[111] W. Xiao, W. G. Dunford, and A. Capel, "A novel modeling method for photovoltaic cells," in *Power Electronics Specialists Conference, 2004. PESC 04. 2004 IEEE 35th Annual*, 2004, vol. 3, pp. 1950 – 1956 Vol.3.

[112] J. Mondol, Y. Yohanis, and B. Norton, "Comparison of Measured and Predicted Long-Term Performance of a Grid Connected Photovoltaic System," 2007.

[113] "Statistical review of World energy 2009.www.bp.com/statistical review." 2009.

[114] Dolf Gielen, "Renewable Energy Technologies; Cost Analysis Series." IRENA International Renewable Energy Agency, Jun-2012.

[115] H. Ramos, "Guidlines For Design of Small Hydropower Plants." Jul-1999.

[116] "Small Hydropower Systems," e U.S. Department of Energy (DOE) by the National Renewable Energy Laboratory (NREL), Jul. 2001.

[117] "Hydropower basics http://www.microhydropower.net/basics/turbines.php." .

[118] L. Ye, H. B. Sun, X. R. Song, and L. C. Li, "Dynamic modeling of a hybrid wind/solar/hydro microgrid in EMTP/ATP," *Renew. Energy*, vol. 39, no. 1, pp. 96–106, Mar. 2012.

[119] Ali Khudhair M, "Dynamic System Identification Using Time-Delay Feedforward Neural Networks: Application to DC Motor," vol. Vol. 03, no. No 01, p. pp 65–79, Jun. 2010.

[120] R. Singh, M. Elizondo, and S. Lu, "A review of dynamic generator reduction methods for transient stability studies," 2011, pp. 1–8.

[121] G. K. Venayagamoorthy, "Potentials and promises of computational intelligence for smart grids," in *IEEE Power Energy Society General Meeting, 2009. PES '09*, 2009, pp. 1 –6.

[122] Payman S hamsollahi, *Adaptive power system stabilizer based on recurrent neural network",*. Calgary, Alberta: PhD Thesis submitted to the department of electrical and computer Engineering, 1998.
[123] E. Derya and M. beyli, "Case Studies for Applications of Elman Recurrent Neural Networks," in *Recurrent Neural Networks*, X. Hu and P. Balasubramaniam, Eds. InTech, 2008.
[124] R. Tadeusiewicz, "Neural networks: A comprehensive foundation," *Control Eng. Pract.*, vol. 3, no. 5, pp. 746–747, May 1995.
[125] P. Xiao, G. K. Venayagamoorthy, K. A. Corzine, and J. Huang, "Recurrent Neural Networks Based Impedance Measurement Technique for Power Electronic Systems," *IEEE Trans. Power Electron.*, vol. 25, no. 2, pp. 382 –390, Feb. 2010.
[126] H. Demuth, *Neural network toolbox for use with MATLAB: User's guide*. MathWorks, Inc, 1992.
[127] Ben Krose and P. Van der Smargt, *An Introduction to Neural networks*. 1996.
[128] *Matlab Version 7.9.0 (R2009b)*. 2009.
[129] T. G. Barbounis, J. B. Theocharis, M. C. Alexiadis, and P. S. Dokopoulos, "Long-term wind speed and power forecasting using local recurrent neural network models," *IEEE Trans. Energy Convers.*, vol. 21, no. 1, pp. 273 – 284, Mar. 2006.
[130] M. Bayrak, "Recurrent artificial neural network based islanding protection by using generator speed deviation," 2009, vol. 4, pp. 212–216.
[131] A. M. A. Haidar, M. W. Mustafa, F. A. F. Ibrahim, and I. A. Ahmed, "Transient stability evaluation of electrical power system using generalized regression neural networks," *Appl. Soft Comput.*, vol. 11, no. 4, pp. 3558–3570, Jun. 2011.
[132] John A. Bullinaria, "Self Organizing Maps: Fundamentals: Introduction to Neural Networks :," 2004.
[133] A. J. G. Dagmar Niebur, "Unsupervised neural net classification of power system static security states," *Int. J. Electr. Power Amp Energy Syst.*, pp. 233–242.
[134] S, Haykin, *Neural Networks: A comprehensive Foundation*, Second Edition. McMaster University,Canada: Pearson Education,Inc, 1999.
[135] A. Hoballah and I. Erlich, "PSO-ANN approach for transient stability constrained economic power generation," in *PowerTech, 2009 IEEE Bucharest*, 2009, pp. 1 –6.
[136] R. Rajendra, "Particle Swarm Optimization Algorithm vs Genetic Algorithm to Develop Integrated Scheme for Obtaining Optimal Mechanical Structure and Adaptive Controller of a Robot," *Intell. Control Autom.*, vol. 02, no. 04, pp. 430–449, 2011.
[137] M. Pavella, D. Ernst, and D. Ruiz-Vega, *Transient Stability of Power Systems: A Unified Approach to Assessment and Control*. Springer, 2000.
[138] L. S. Moulin, A. P. Alves da Silva, M. A. El-Sharkawi, and I. Marks, R.J., "Support vector machines for transient stability analysis of large-scale power systems," *IEEE Trans. Power Syst.*, vol. 19, no. 2, pp. 818–825, 2004.
[139] D. J. Sobajic and Y.-H. Pao, "Artificial neural-net based dynamic security assessment for electric power systems," *IEEE Trans. Power Syst.*, vol. 4, no. 1, pp. 220–228, Feb. 1989.
[140] D. Srinivasan, C. S. Chang, A. C. Liew, and K. C. Leong, "Power system security assessment and enhancement using artificial neural network," in *1998 International Conference on Energy Management and Power Delivery, 1998. Proceedings of EMPD '98*, 1998, vol. 2, pp. 582–587.

[141] A. G. Bahbah and A. A. Girgis, "New method for generators' angles and angular velocities prediction for transient stability assessment of multimachine power systems using recurrent artificial neural network," *IEEE Trans. Power Syst.*, vol. 19, no. 2, pp. 1015 – 1022, May 2004.

[142] A. Del Angel, P. Geurts, D. Ernst, M. Glavic, and L. Wehenkel, "Estimation of rotor angles of synchronous machines using artificial neural networks and local PMU-based quantities," *Neurocomputing*, vol. 70, no. 16–18, pp. 2668–2678, Oct. 2007.

[143] F. Hashiesh, H. E. Mostafa, I. Helal, and M. M. Mansour, "A wide area synchrophasor based ANN transient stability predictor for the Egyptian Power System," in *Innovative Smart Grid Technologies Conference Europe (ISGT Europe), 2010 IEEE PES*, 2010, pp. 1–7.

[144] J. T. C. -W. Liu, "Application of synchronised phasor measurements to real-time transient stability prediction," *Gener. Transm. Distrib. IEE Proc.-*, no. 4, pp. 355 – 360, 1995.

[145] M. Boudour and A. Hellal, "Combined use of supervised and unsupervised learning for power system dynamic security mapping," *Eng. Appl. Artif. Intell.*, vol. 18, no. 6, pp. 673–683, Sep. 2005.

[146] F. V. Gonçalves, L. H. Costa, and H. M. Ramos, "ANN for Hybrid Energy System Evaluation: Methodology and WSS Case Study," *Water Resour. Manag.*, vol. 25, no. 9, pp. 2295–2317, Jul. 2011.

[147] P. Kundur, J. Paserba, V. Ajjarapu, G. Andersson, A. Bose, C. Canizares, N. Hatziargyriou, D. Hill, A. Stankovic, C. Taylor, T. Van Cutsem, and V. Vittal, "Definition and classification of power system stability IEEE/CIGRE joint task force on stability terms and definitions," *IEEE Trans. Power Syst.*, vol. 19, no. 3, pp. 1387 – 1401, Aug. 2004.

[148] P. Kundur, *Power System Stability and Control*. McGraw-Hill Companies,Incorporated, 1994.

[149] M. R. Gent, "North American Electricity Reliability Council," Sep-2003.

[150] P. M. Anderson, A.-A. A. Fouad, and I. of E. and E. Engineers, *Power system control and stability*. IEEE Press, 2003.

[151] L. L. Grigsby, *Power System Stability and Control, Third Edition*. CRC Press, 2012.

[152] O. Samuelsson and S. Lindahl, "Discussion of 'Definition and classification of power system stability,'" *IEEE Trans. Power Syst.*, vol. 21, no. 1, p. 446, Feb. 2006.

[153] "Frequency Instability Problems in North American Interconnections." .

[154] C. Sharma and M. G. Ganness, "Determination of Power System Voltage Stability Using Modal Analysis," in *International Conference on Power Engineering, Energy and Electrical Drives, 2007. POWERENG 2007*, 2007, pp. 381 –387.

[155] M. Kowsalya, K. K. Ray, D. P. Kothari, A. Kumar, and A. Ghai, "A Fast Technique of Voltage Stability Analysis and Optimization in the Grid Network," in *IEEE Region 10 and the Third international Conference on Industrial and Information Systems, 2008. ICIIS 2008*, 2008, pp. 1 –6.

[156] C. Sharma and M. G. Ganness, "Determination of the applicability of using modal analysis for the prediction of voltage stability," in *Transmission and Distribution Conference and Exposition, 2008. T #x00026;D. IEEE/PES*, 2008, pp. 1 –7.

[157] G. K. Morison, B. Gao, and P. Kundur, "Voltage stability analysis using static and dynamic approaches," *IEEE Trans. Power Syst.*, vol. 8, no. 3, pp. 1159 –1171, Aug. 1993.

[158] M. S. Chih-Wen Liu, "Application of a novel fuzzy neural network to real-time transient stability swings prediction based on synchronized phasor measurements," *Power Syst. IEEE Trans. On*, no. 2, pp. 685 – 692, 1999.

[159] R. Billinton and P. R. S. Kuruganty, "A Probabilistic Index for Transient Stability," *IEEE Trans. Power Appar. Syst.*, vol. PAS-99, no. 1, pp. 195–206, 1980.

[160] K.E. Martin, "Phasor measurement systems in western North America," in *Relay Protection and Substation Automation of Modern Power Systems*, Cheboksary, 2007.

[161] M. Liu, H. Sun, B. Zhang, L. Yao, M. Han, and W. Wu, "PMU measurements and EMS models based transient stability on-line forecasting," in *IEEE Power Energy Society General Meeting, 2009. PES '09*, 2009, pp. 1 –8.

[162] M. Liu, H. Sun, B. Zhang, L. Yao, M. Han, and W. Wu, "PMU measurements and EMS models based transient stability on-line forecasting," in *IEEE Power Energy Society General Meeting, 2009. PES '09*, 2009, pp. 1 –8.

[163] "IEEE Standard for Synchrophasor Measurements for Power Systems," IEEE Std C37.118.1-2011 (Revision of IEEE Std C37.118-2005)," 2011.

[164] Y. Yare and G. K. Venayagamoorthy, "Real-time transient stability assessment of a power system during energy generation shortfall," 2010, pp. 1–9.

[165] J. Tong and L. Wang, "Design of a DSA Tool for Real Time System Operations," in *International Conference on Power System Technology, 2006. PowerCon 2006*, 2006, pp. 1 –5.

[166] F. Ding and C. D. Booth, "Applications of PMUs in Power Distribution Networks with Distributed Generation," *Univ. Power Eng. Conf. UPEC Proc. 2011 46th Int.*, pp. 1 –5, Sep. 2011.

[167] J. T. C. -W. Liu, "Application of synchronised phasor measurements to real-time transient stability prediction," *Gener. Transm. Distrib. IEE Proc.-*, no. 4, pp. 355 – 360, 1995.

[168] Q. Huang, N. N. Schulz, A. K. Srivastava, and T. Haupt, "Distributed state estimation with PMU using grid computing," in *IEEE Power Energy Society General Meeting, 2009. PES '09*, 2009, pp. 1 –7.

[169] A. G. Phadke and J. S. Thorp, *Synchronized Phasor Measurements and Their Applications*. Springer, 2008.

[170] M. A. P¨oller, "Power System Analysis Software DIGSILENT PowerFactory V14." .

[171] "Real time Digital Simulator, http://www.rtds.com/index/index.html." .

[172] A.G. Parlos, O.T. Rais, and A.F.Atiya, "Multi-step-ahead prediction using dynamic recurrent neural networks," *Neural Netw.*, vol. 13, pp. 765–786, 2000.

[173] M. A. Pai,, *Energy Function Analysis for Power System Stability*,. Kluwer Academic Publishers, 1989.

[174] X. Wu, J. Zhao, A. Xu, H. Deng, and P. Xu, "Review on transient stability prediction methods based on real time wide-area phasor measurements," in *2011 4th International Conference on Electric Utility Deregulation and Restructuring and Power Technologies (DRPT)*, 2011, pp. 320 –326.

[175] A.-A. A. Fouad and V. Vittal, *Power system transient stability analysis using the transient energy function method*. Prentice Hall, 1992.

[176] V. Centeno, A. G. Phadke, A. Edris, J. Benton, M. Gaudi, and G. Michel, "An adaptive out-of-step relay [for power system protection]," *IEEE Trans. Power Deliv.*, vol. 12, no. 1, pp. 61 –71, Jan. 1997.